Mechanical Vibrations

Mechanical Vibrations

Active and Passive Control

Tomasz Krysinski
François Malburet

iSTE

Adapted from “Origine et contrôle des vibrations mécaniques : méthodes passives et actives” published in France in 2003 by Hermès Science/Lavoisier
First published in Great Britain and the United States in 2007 by ISTE Ltd

ISTE Ltd
6 Fitzroy Square
London W1T 5DX
UK

ISTE USA
4308 Patrice Road
Newport Beach, CA 92663
USA

www.iste.co.uk

Library of Congress Cataloging-in-Publication Data

Krysinski, Tomasz.
[Origine et contrôle des vibrations mécaniques. English]
Mechanical vibrations: active and passive control/Tomasz Krysinski, François Malburet.
p. cm.
Includes bibliographical references and index.
ISBN 978-1-905209-29-3
1. Rotors--Vibration. 2. Damping (Mechanics) 3. Structural control. I. Malburet, François. II. Title.
TJ1058K79 2006
621.8'11--dc22

2007003333

British Library Cataloguing-in-Publication Data
A CIP record for this book is available from the British Library
ISBN 13: 978-1-905209-29-3

Printed and bound in Great Britain by Antony Rowe Ltd, Chippenham, Wiltshire.

Table of Contents

Foreword

For all rotating machines, the analysis of dynamic stress and of resultant vibrations represents, at all times, an important subject. This analysis becomes crucial in the case of helicopters and piston engines. Be it the design of parts working in fatigue or the lowering of the vibratory level, the success of a project lies mainly in the hands of dynamicists. Throughout the history of helicopters there are many examples of devices whose commercial career was shortened, even interrupted, because their designer did not know how to obtain either a sufficient vibratory comfort or components working in fatigue whose service lives could be compatible to a competitive usage.

We must acknowledge the fact that, until recently, this field was governed by the wrong type of empiricism; certain constructors have dealt with prototypes of piston engines, rotors or different transmissions, all of them bound to lead to frequent as well as inexplicable failures.

Two specialists in dynamics, Tomasz Krysinski, head of the design department of Eurocopter, and François Malburet, teacher at l'Ecole nationale superieure d'arts et metiers, combined their talents and used their experience to present a complete collection on this aspect. It would be a good idea to praise in this collaboration an example of cooperation between an engineer in the field and a teacher-researcher at a reputed school, collaboration that is often recommended by the decision-making leaders but very rarely encountered in practice.

This book, the first of its kind on this topic, without insisting on complicated mathematical modeling, will describe in concrete terms the essential dynamic phenomena and the way they can be observed in reality.

The writer of these lines can guarantee the authors' skill in solving the issues related to the vibration control of helicopters, having been tested several times during test flights. The permanent confrontation between measurements during flights and theoretical analysis has very often led to brilliant successes, such as the vibratory level of the Tigre helicopter, and to the avoidance of instabilities which would have been likely to compromise the safety of the flight.

After reading this book, the student in engineering wishing to specialize in this field or the engineer working in the design department or in test flights will be able to acquire the knowledge and modeling methods necessary to understand dynamic phenomena and to develop solutions able to eliminate negative effects.

P. ROUGIER
Tigre Departmental Head
of Eurocopter Test Flights

Preface

In standard ISO 2041 the International Standards Organization defines vibrations as follows [BIG 95]: *"The variation with time of the magnitude of a quantity which is descriptive of the motion or position of a mechanical system, when the magnitude is alternately greater and smaller than some average value or reference."*

Dynamics is the science that deals with variations of physical units associated with vibrations according to time. This discipline is equally important for science and technology. Galileo studied the movements of stars. Newton, Lagrange, Euler and D'Alembert outlined the first theoretical ideas. Poincaré, Stodola and Timoshenko were a part of the industrial boom.

A few examples of historical practical work carried out in the field of vibration control are available.

Balancing machine

The first balancing machine was built by Martinson in Canada, in 1870 [LAC 79]. This machine did not find any practical application; however, the need to reduce the dynamic stresses in the bearings of swiveling elements was already present.

The first serial manufacture of balancing machines was initiated by Schenck in Germany at the beginning of the 20^{th} century. The balancing technique was perfected by improving measurement techniques and by choosing better correction places. In particular, the theory on balancing flexible shafts enabled the increase of the rotation speed of machines.

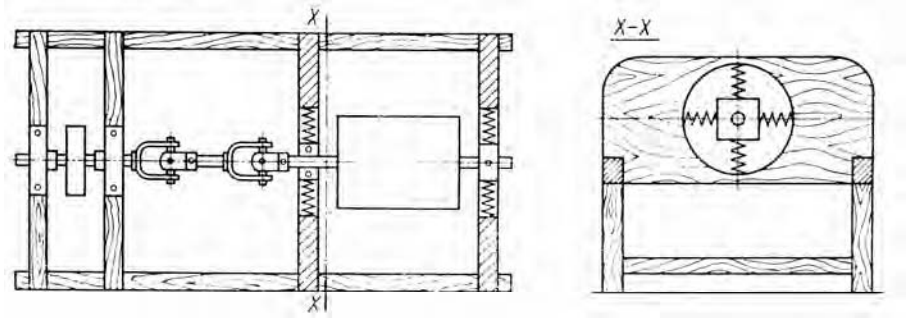

Figure 1. *The first balancing machine built by Martinson in 1870 [LAC 79]*

Dynamic absorber of torsional vibrations

The principle for a dynamic absorber comes from the need to process torsional vibrations on the crankshafts of a combustion engine. The first practical applications were carried out before World War II. In this respect, we can give the example of a torsional vibration absorber developed for an aeronautical engine by Havilland Engine Company between 1936 and 1938 [KER 68].

This absorber was used for the overcharged version of the Havilland "Gipsy" engine for versions 4 and 6 cylinders connected without an absorber and for version 6 cylinders connected with an absorber. This six cylinder engine with an absorber was the first mass production engine.

Nowadays, different versions of torsional dynamic absorbers are used for many combustion engines, such as some Formula 1 engines.

Suspensions and anti-vibration systems

Another significant example is the suspension of the transmission unit of a helicopter. This suspension was implemented for the first time on a Puma helicopter in France in the 1960s.

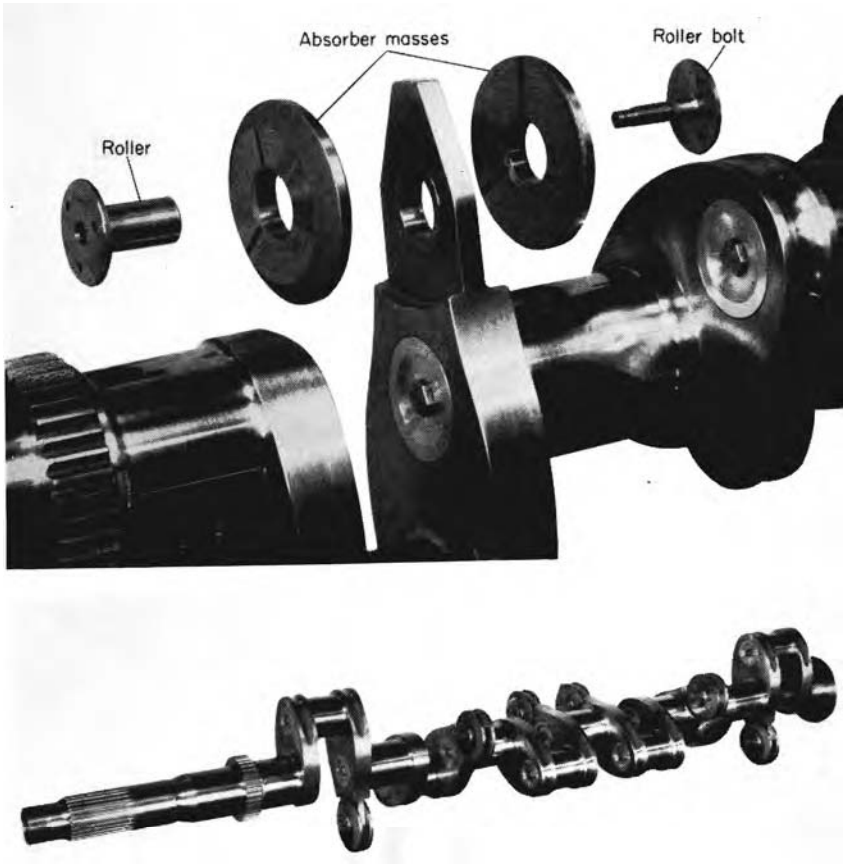

Figure 2. *Torsional dynamic absorber on an Havilland Engine Company engine [KER 68]*

The principle of insertion of a flexible element between two masses (the fuselage and the rotor) enables a significant improvement in cabin comfort.

These suspensions were largely enhanced by a better understanding of dynamic filtering techniques, by the introduction of elastomer elements, by the usage of resonators and by the arrival of semi-active and active systems.

The increasing need for comfort and the development of standards, particularly those pertaining to safety, urged industrialists to seek competitive solutions. The development of electronics and of digital systems constituted important elements in this rapid growth.

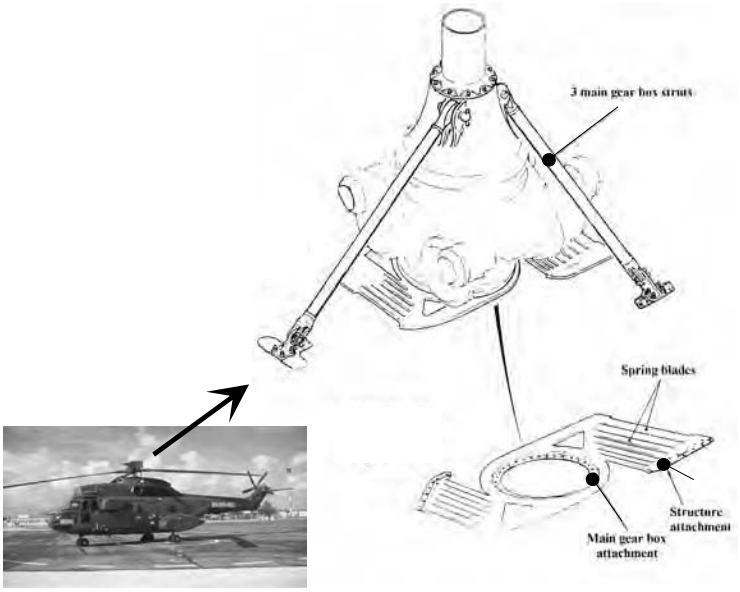

Figure 3. *First unit suspension on a Puma helicopter, 1965*

The helicopter was one of the first industrial applications to use active vibration control systems. For this, dynamic stresses are induced by actuators embedded in the structure. Figure 4 shows the embedded active systems on an EC725 helicopter.

The active and semi-active systems make it possible to correct certain mechanical systems defects and they produce better results than passive systems.

These few examples prove that dynamics is an innovative science that evolves continuously. The development of system requirements requires research for new solutions of phenomena modeling.

In the following chapters, the authors will provide examples of industrial problems of dynamics associated with their modeling and technical solutions.

The goal of this book is to outline certain elements which will enable an engineer to understand the problem of vibrations: it starts with the origin of excitations, continues with their minimization and concludes with passive and active filtering techniques.

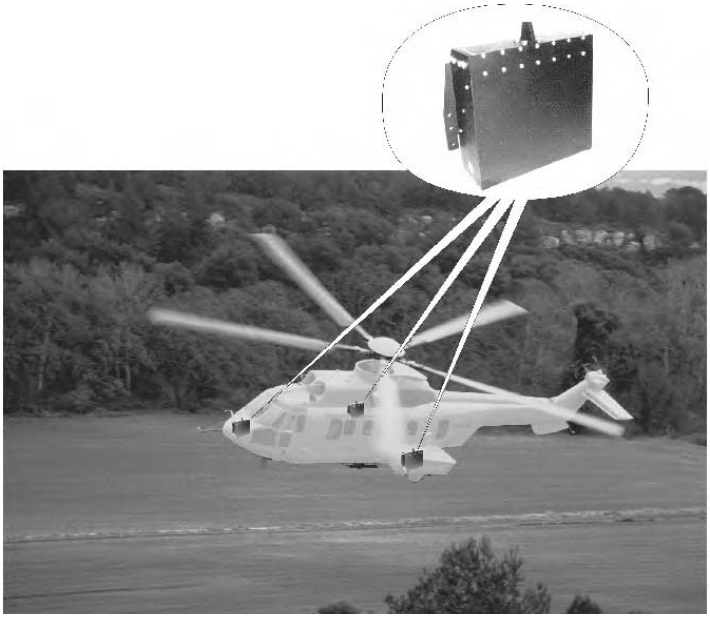

Figure 4. *EC725 helicopter with an active anti-vibration system. Photo C. Guarnieri (Eurocopter)*

D'Alembert's law proves the equality between inertial effects and stresses. Hence, for a solid non-deformable S, the fundamental principle of dynamics can be written in a torsorial form [AGA 86]:

$$\mathcal{D}\left(S/R_g\right) = \sum\left\{\overline{S} \to S\right\} \qquad [1]$$

with:

– $\mathcal{D}\left(S/R_g\right)$: dynamic torsor of solid S with respect to the R_g inertial frame,

– $\left\{\overline{S} \to S\right\}$: torsor of mechanical actions applied to the solid.

This can be also formulated in two vector equations:

$$\begin{cases} m(S)\,\vec{A}_{G\in S/R_g} = \vec{R}\left(\overline{S} \to S\right) \\ \vec{\delta}_M\left(S/R_g\right) = \vec{M}_M\left(\overline{S} \to S\right) \end{cases} \qquad [2]$$

with:

– m(S): mass of the solid,

– $\vec{A}_{G\in S/R_g}$: Galilean acceleration of center of inertia of S,

– $\vec{R}\left(\overline{S}\to S\right)$: resultant of mechanical actions outside of S,

– $\vec{\delta}_M\left(S/R_g\right)$: dynamic Galilean moment of S expressed in M,

– $\vec{M}_M\left(\overline{S}\to S\right)$: moment resulting from mechanical actions outside of S expressed in M.

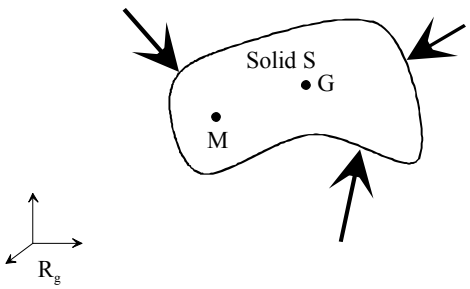

Figure 5. *The solid and its mechanical actions during its movement with respect to an inertial frame*

In dynamics, in order to generate vibrations represented by accelerations, there must be exterior mechanical actions, often called “excitations”. These excitations can be of different types: unbalance, connection stress, aerodynamic stress, electromagnetic stress, etc,

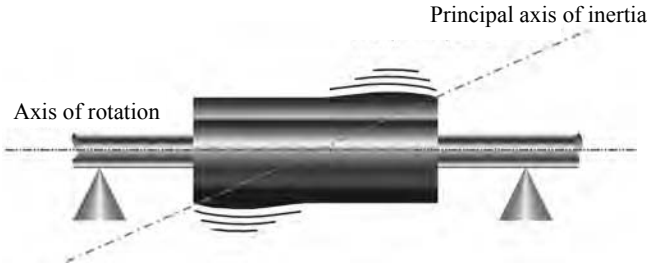

Figure 6. *Image of a non-balanced rotor, source of dynamic excitations. Photo C. Guarnieri (Eurocopter)*

Optimization of excitations is the main objective of engineers. However, it has its limits. The remaining dynamic stresses are often transmitted into the environment and this leads, in spite of everything, to pollution and damage. As a result, it is important to work on the transfer which constitutes a means of minimizing the negative effects of vibrations.

In order to avoid important dynamic constraints, natural frequencies of the structure must be positioned far from excitation harmonics. The Campbell diagram in Figure 7 shows the position of natural frequencies of helicopter rotor blades according to the speed of rotation of the rotor.

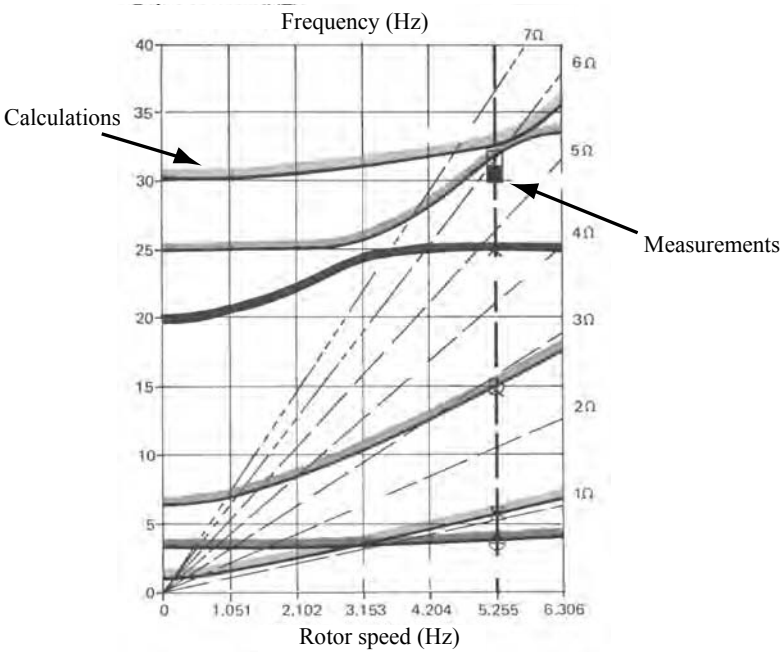

Figure 7. *Campbell diagram for a helicopter blade. Photo: C. Guarnieri (Eurocopter)*

The notion of transfer combines together the insulations, suspensions, anti-vibration systems and the dynamic matching of mechanical systems. In particular we intend to deal with active systems that allow optimizing the transfer.

Mechanical systems get deformed and this entails, in certain cases, the problem of dynamic amplification. This dynamic amplification is associated with the notion of natural frequency or critical flow. The vibrations of deforming systems can be

sufficiently important to cause destruction. When mechanical systems are exposed to increasing oscillations, they are referred to as unstable. Hence, it is important to study the stability of mechanical systems. The utilization field of modern mechanical systems is one in which the necessary stability margins are not enough and therefore active controls are needed.

Among industrial examples, the helicopter represents one of the most complex systems in terms of sources of vibrations. This fact is the consequence of its architecture and operating mode. This system comprises many swiveling systems with very different speeds of rotation, hence the problems related to unbalance, connections, rotors, aerodynamic excitations, etc. On this type of structure, the excitations stresses are relatively important in relation to the mass of the structure (fuselage). Aeronautical structures are light and therefore flexible. Natural frequencies can be close to excitation frequencies, which may entail problems of vibration comfort and alternate constraints in the mechanical parts. The problems of dynamic optimization of the rotor and structure are very important. This optimization may require the introduction of insulating elements, such as suspensions, anti-vibrators or vibration control systems for the blades. These systems can be passive, self-adaptive or active. Some examples will be developed here.

The authors wish to thank:

– Eurocopter for being kind enough to allow them to use in this book the knowledge, experience and know-how developed by its employees,

– the management of l'Ecole nationale superieure d'arts et metiers and la Societe d'etudes et recherches de l'Ecole nationale superieure d'arts et metiers for their help,

– the teachers and students of l'Ecole nationale superieure d'arts et metiers of Aix-en-Provence, who were able to take part in some of these studies.

PART I

Sources of Vibrations

Introduction

There is a very important number of different excitations. Ever since the beginning of time, human beings were confronted with violent winds and earthquakes which destroyed buildings and harvests. In addition, the principle of resonance was used in various musical instruments. The first signs of dynamic optimization were observed in the case of instruments used in fabric manufacturing, as shown in Figure 1.

In this application, a small flywheel made it possible to avoid shutdowns while the thread was winding on the spool.

The first mechanisms were manufactured by the Romans and the first gear systems have been dated from then (Vitruriusz 35 BC). 20 centuries had to pass before it was understood why gears that are bound to transmit static movement generate dynamic excitations which can be very destructive. The extremely fast development of steam engines (Newcoment, 1705, and especially Watt, 1769) met with the first engine failures, caused by uncontrolled dynamic excitations. This aspect is also dealt with in works on civil engineering. The main sources of excitation are earthquakes and weather stresses, particularly wind. The Tacoma bridge (USA), which was destroyed in a few hours in 1940, represents a valid example in this respect.

Analysis of excitations and optimization of mechanical systems represent the basis of engineering. In the first part of this work, we will provide a few examples of excitation:

– unbalancing of trees (Chapter 1),

– piston engines (Chapter 2),

– rotor blade movements (Chapter 3),

– the influence of the blades' movement on the structure (Chapter 4),

– shaft coupling (Chapter 5),

– aerodynamic stresses (Chapter 6).

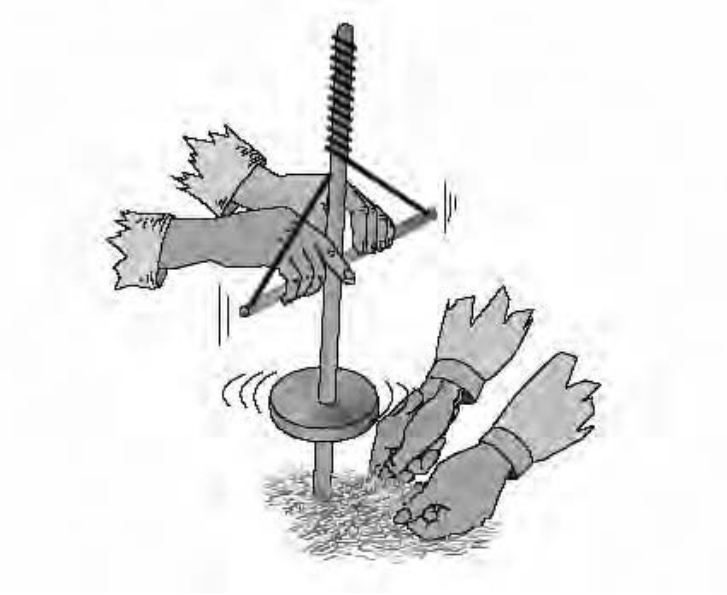

Figure 1. *Example of a flywheel utilization*

The goal of the choice made is to provide the reader with the potential to understand the origin of these excitations, to put forward a method of theoretical and experimental analysis and to present a few optimization techniques. We used accessible approaches which can also be applied to other fields.

Chapter 1

Unbalance and Gyroscopic Effects

1.1. Introduction

Unbalance is one of the conventional vibratory sources in rotating systems. The mass distribution of rotating parts around the axis of rotation may, in certain cases, generate inertial effects. These create vibrations in the carrier structure and cyclic loads in the links.

These loads are generally noticeable and important for structures rotating at high speeds or when the rotating structure, the rotor, has a large mass with an inappropriate mass distribution around the axis of rotation.

Current technical progress stems from the increase of the speed of rotation of machines (see [BIG 95, LAC 79]):

– the speeds of rotation of aviation turbines are often greater than 40,000 rpm,

– rotors of certain electric motors turn at the speed of 1,000,000 rpm,

– the speed of rotation of the perforators of dental drills reaches 500,000 rpm (microturbines on air bearings),

– certain elements of textile machines turn at the speed of 900,000 rpm,

– the rotors of gas microturbines turn at the speed of 2,000,000 rpm.

The dental drill without load in Figure 1.1 turns at the speed of 420,000 rpm. For a rotation speed of 240,000 rpm, the necessary power to cut one tooth is 7.5 watts. These high rotation speeds require very precise balancing.

This tendency to look for greater and greater speeds comes from the need for light structures and operational efficiency.

When the masses of rotating elements are distributed evenly around the axis of rotation, the resultant inertial effects are zero. Hence, we can say that these elements are in equilibrium. The machines in equilibrium do not generate vibration or noise.

These two parameters are essential for proper dynamic operation of the machines. For high rotation speeds, a slight asymmetry of the rotating parts is enough to generate an unbalance that causes dynamic reactions at the bearings.

A very simple analysis shows that a rotation speed of 6,000 rpm and an offset of the center of inertia of 25 μm cause dynamic reactions in the bearing equal to the shaft weight. For the same offset and for a speed of 30,000 rpm, the reaction at the bearing will be 25 times the shaft weight.

The "mechanical design" engineer, whose task is to decrease these negative effects, must overcome the origin of unbalance.

Figure 1.1. *Dental drill, microturbine with gas bearing (420,000 rpm). Photo: J. Szabela*

Figure 1.2. *Transmission system on a helicopter that needs balancing. Photo: Eurocopter*

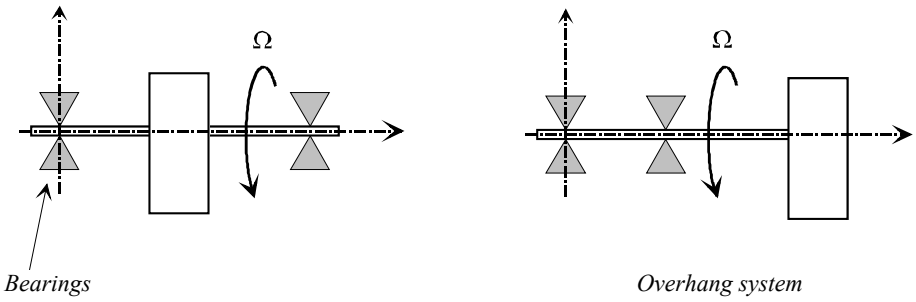

Figure 1.3. *Modeling of a rotation system with its bearings*

1.1.1. *Physico-mathematical model of a rotating system*

In order to analyze the origin of unbalance, modeling consists of the rotating system attached to a non-bending solid in rotation around a fixed axis. The bearings constituting the pivot link are considered to be without clearance or friction.

Among the models used, we can distinguish between those with the center of inertia positioned between the two bearings and those with an overhang. The position of the bearings does not modify the phenomenon studied, and only the interpretation of the results will be different. In this chapter only the first model will be developed.

The theory of balance distinguishes between situations in which the effects of bending of the rotating system are negligible or not. Firstly, we will consider the fact that the effects of bending of the rotating part are negligible.

1.1.2. *Formation of equations and analysis*

The set of rotating elements is associated with a non-bending solid marked S. Rotation is parameterized by the angle $\alpha(t)$ such that $\alpha(t) = \Omega t$. Ω represents the rotation speed of the solid, and is considered constant.

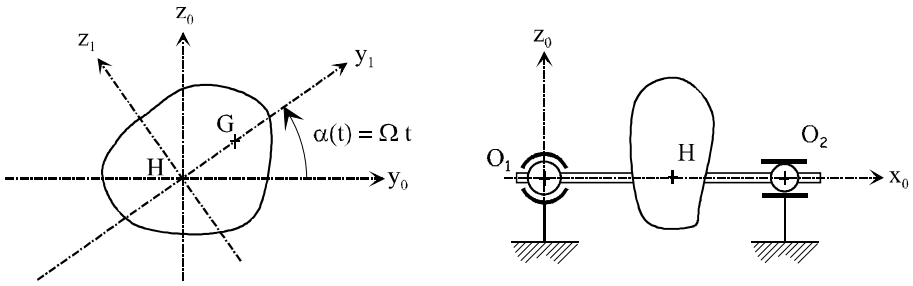

Figure 1.4. *Parametric transformation associated with the solid in rotation*

The points O_1 and O_2 define the link centers of the two bearings. G is the center of inertia of the rotating system. The geometric dimensions are defined by:

$$\overrightarrow{O_1O_2} = L\,\vec{x}_0 \quad \overrightarrow{O_1H} = l\,\vec{x}_0 \quad \overrightarrow{HG} = e\,\vec{y}_1 \qquad [1.1]$$

The hypotheses are as follows:

– links are without friction,

– weight effects are ignored in view of other effects,

– the rotating solid has a certain shape,

– the mechanical action of the engine and all resistant mechanical actions are modeled by pure pairs represented by $\vec{x}_0$,

– mechanical actions transmitted through links are modeled at the geometric center of the link by a pure resultant.

The rotor inertial matrix is defined as follows:

$$\bar{\bar{I}}_G(S) = \begin{bmatrix} I_{xx} & -I_{xy} & -I_{xz} \\ -I_{xy} & I_{yy} & -I_{yz} \\ -I_{xz} & -I_{yz} & I_{zz} \end{bmatrix}_{(\vec{x}_1,\vec{y}_1,\vec{z}_1)} \qquad [1.2]$$

The loads in the links are obtained through the fundamental principle of dynamics, applied to the solid S. Let:

$$\begin{cases} \text{m(S)}\ \vec{A}_{G,S/R_g} = \vec{F}(\text{bearing1} \to \text{S}) + \vec{F}(\text{bearing2} \to \text{S}) + \ldots \\ \qquad\qquad \ldots + \vec{F}(\text{engine} \to \text{S}) + \vec{F}(\text{receiver} \to \text{S}) \\ \vec{\delta}_{O_1}(\text{S}/R_g) = \vec{M}_{O_1}(\text{bearing1} \to \text{S}) + \vec{M}_{O_1}(\text{bearing2} \to \text{S}) + \ldots \\ \qquad\qquad \ldots + \vec{M}_{O_1}(\text{engine} \to \text{S}) + \vec{M}_{O_1}(\text{receiver} \to \text{S}) \end{cases} \quad [1.3]$$

Only the resultant equation in projection on $\vec{y}_0$ and $\vec{z}_0$ and the momentum equation in projection on $\vec{y}_0$ and $\vec{z}_0$ provide the equations necessary to the study.

The result of load expressions at the level of link centers is as follows:

$$\begin{cases} \left(F_{O_2}\right)_z = \dfrac{I_{xz}}{L}\Omega^2 \cos(\Omega t) - \left(\dfrac{I_{xz}}{L} + \dfrac{me\ \ l}{L}\right)\Omega^2 \sin(\Omega t) \\ \left(F_{O_2}\right)_y = \dfrac{I_{xz}}{L}\Omega^2 \sin(\Omega t) + \left(\dfrac{I_{xz}}{L} + \dfrac{me\ \ l}{L}\right)\Omega^2 \cos(\Omega t) \\ \left(F_{O_1}\right)_y = -\left(\dfrac{I_{xy}}{L} + \dfrac{me\ \ (l-L)}{L}\right)\Omega^2 \cos(\Omega t) - \left(\dfrac{I_{xz}}{L}\right)\Omega^2 \sin(\Omega t) \\ \left(F_{O_1}\right)_z = \left(\dfrac{I_{xy}}{L} + \dfrac{me\ \ (l-L)}{L}\right)\Omega^2 \sin(\Omega t) - \left(\dfrac{I_{xz}}{L}\right)\Omega^2 \cos(\Omega t) \end{cases} \quad [1.4]$$

These equations lead to several observations:

– harmonic function. The angular frequency corresponds to the speed of rotation. We talk of excitation in 1 Ω. Loads are proportional to Ω^2,

– the "m e" product is an important feature of unbalance. The effect induced by this term is called "static unbalance". This underlines the fact that the center of inertia may not be on the axis of rotation ($e \neq 0$),

– the products of inertia of the matrix of inertia I_{xy} and I_{xz} are the other characteristics of unbalance. The effect induced by these terms is called, by contrast, "dynamic unbalance". They suggest the fact that the axis of rotation is not aligned with a principal axis of inertia.

1.2. Theory of balancing

Unbalance is the combination between "static" unbalance and "dynamic" unbalance.

To obtain equilibrium – to avoid unbalance – we have to ensure that the center of inertia is on the axis of rotation and the axis of rotation is a principal axis of inertia.

Mathematically, and for the model developed, this is translated by:

– the "m e" product is zero,

– the terms I_{xy} and I_{xz} are zero.

The problem lies in knowing how to physically balance an existing system. Despite taking great care during design and manufacture, rotating parts or systems are not necessarily balanced. In many instances, the resultant unbalance is not desirable. This is the case in crankshafts, car wheels, and pins of machine tools, etc.

At times, unbalance can be the result of complex and numerous assemblies whose defects cannot be handled.

To obtain balance, the solution consists of adding or removing mass from the rotating system in order to modify the mass distribution in space. Most often the added or removed mass has a smaller volume than the volume of the rotor. In fact, the added or removed masses are considered punctual.

Two masses m_1 and m_2 are added to the respective points M_1 and M_2. The position of each mass m_i is defined by:

$$\overrightarrow{O_1M_i} = a_i\ \vec{x}_0 + b_i\ \vec{y}_1 + c_i\ \vec{z}_1 \qquad [1.5]$$

Balance is obtained if the inertial effects entailed by the rotor and by the masses m_1 and m_2 are canceled, or if the following equations are verified:

$$\begin{cases} m(S)\ \vec{A}_{G,S/R_g} + m_1\ \vec{A}_{M_1/R_g} + m_2\ \vec{A}_{M_2/R_g} = \vec{0} \\ \vec{\delta}_{O_1}(S/R_g) + O_1M_1 \wedge \left(m_1\ \vec{A}_{M_1/R_g}\right) + O_2M_2 \wedge \left(m_2\ \vec{A}_{M_2/R_g}\right) = \vec{0} \end{cases} \qquad [1.6]$$

After projection, the following equations are obtained:

$$\begin{cases} m\,e + m_1\,b_1 + m_2\,b_2 = 0 \\ m_1\,c_1 + m_2\,c_2 = 0 \\ I_{xz} + m\,e\,l + m_1\,a_1\,b_1 + m_2\,a_2\,b_2 = 0 \\ I_{xz} + m_1\,a_1\,c_1 + m_2\,a_2\,c_2 = 0 \end{cases} \quad [1.7]$$

We notice that there are four equations to solve, with eight parameters (m_1, m_2, a_1, a_2, b_1, b_2, c_1, c_2). Hence, in order to choose the set of values, other criteria can be introduced (inertia, mass, etc.).

It is noticed that if the term of inertia I_{xz} is non-zero, it is impossible to ensure balance with $a_1 = a_2$. Therefore, in order to obtain both "static and dynamic" balance, it is essential to act in two distinct planes perpendicular to the axis of rotation.

For example, on car wheels, the distances a_1 and a_2 are imposed because balancing masses are positioned inside and outside the rims. Also, they must be located at a precise diameter. The value of the masses and their angular positions are the only ones left to be calculated.

To obtain balance, it is necessary to know the position of the center of inertia and the mass distribution on the system. The value of parameters e, m, 1, I_{xy}, I_{xz} must be determined. One of the methods is to measure the loads in the bearings, or their effects, in order to identify the features of the existing system.

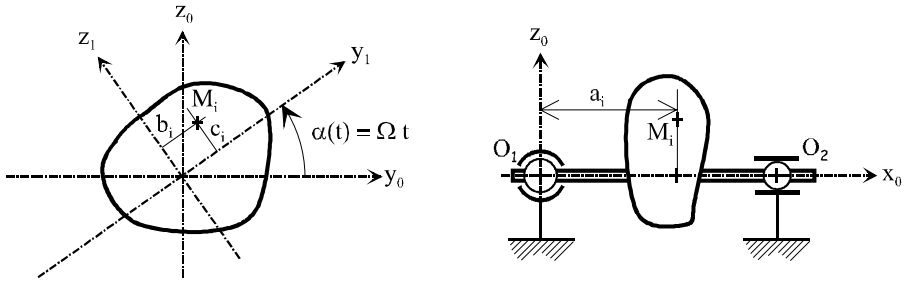

Figure 1.5. *Geometric definition of the position of balancing masses*

If the system can be disassembled, a "balancing" machine is generally used. If the system is too complex and therefore cannot be placed on a balancer, a method *in situ* will be used. This method implies that all necessary measurements are taken directly on the system in order to determine the features of balancing masses.

1.2.1. *Balancing machine or "balancer"*

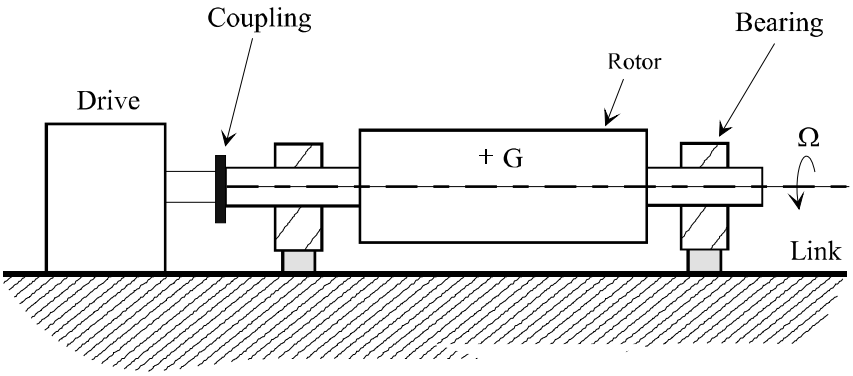

Figure 1.6. *Diagram of a balancing machine*

In technology, there are two types of balancing machines classified according to their link to the ground:

– the soft-bearing machine,

– the hard-bearing machine.

1.2.1.1. *The soft-bearing machine*

The link to the ground is very soft; it follows an axis, generally the vertical one. This softness is due to one part which is more bent than the others. In fact, bendings of other parts (bearings, connection with the drive system, etc.) are negligible.

Symmetrically, the balancing machine can be reduced to a system of 1 degree of freedom. The dynamic resultant due to unbalance is marked F. Its amplitude is proportional to m, e and Ω^2.

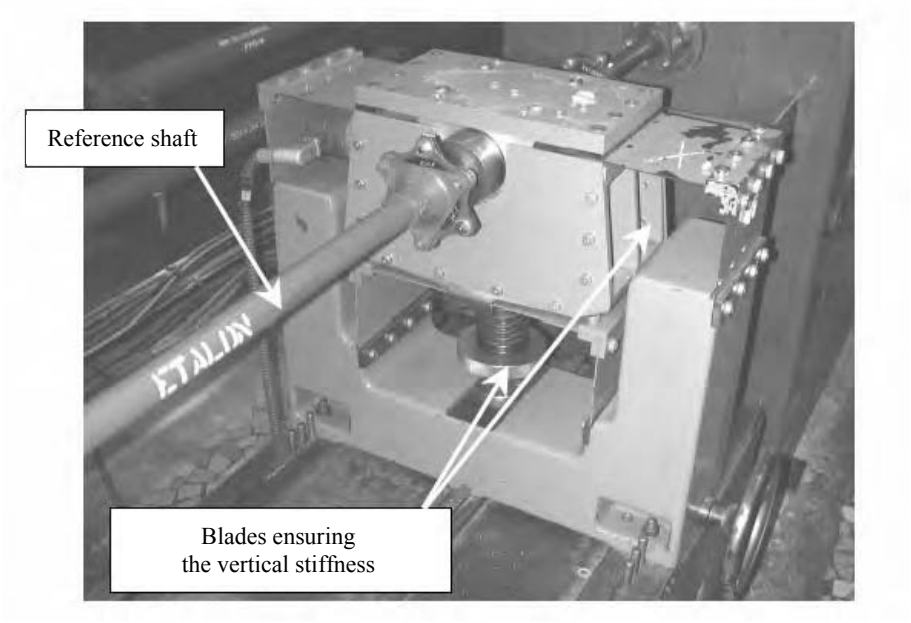

Figure 1.7. *Soft-bearing balancing machine. Photo: Eurocopter*

With the help of modeling in Figure 1.8, the equation of motion around the stable angle following the vertical axis is as follows:

$$M\,\ddot{z} + c\,\dot{z} + k\,z = m\Omega^2\ e\sin(\Omega\ t) \qquad [1.8]$$

with:

– m: rotating mass,

– M: suspended mass,

– k: suspension stiffness,

– e: offset,

– Ω: speed of rotation.

Let the natural angular frequency ω_p and the reduced damping λ be defined by:

$$\omega_p = \sqrt{\frac{k}{M}} \qquad \lambda = \frac{c}{c_{cr}} = \frac{c}{2\sqrt{kM}} \qquad [1.9]$$

The constant c_{cr} is called critical damping. It represents the damping that the system needs in order to obtain balance as fast as possible after a certain disturbance.

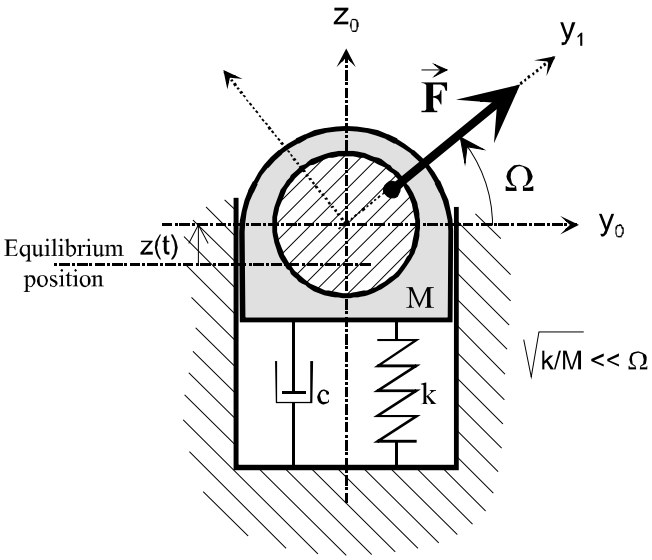

Figure 1.8. *Bearing modeling for a soft-bearing balancing machine*

Reduced damping is very often used as a parameter in characterizing oscillating systems.

In the case of unbalance, we are looking for the particular solution of the differential equation [1.8]. Let:

$$z = z_0 \sin(\Omega t + \varphi) \qquad [1.10]$$

with:

– z_0: amplitude of motion,

– φ: phase difference between motion and excitation.

The following complex variable transform is used:

$$z(t) \rightarrow \overline{z}_0 \; e^{j\Omega t} \qquad [1.11]$$

Substituting [1.11] in the equation of motion [1.8]:

$$\left(\text{k-M}\Omega^2 + \text{i c}\Omega\right)\ \bar{z}_0\ e^{\text{i}(\Omega t)} = \text{m e}\ \Omega^2\ e^{\text{i}(\Omega t)} \qquad [1.12]$$

By identification, the complex amplitude of displacement is obtained:

$$\bar{z}_0 = \frac{\text{m e}\ \Omega^2}{\left[\left(\text{k-M}\ \Omega^2\right) + \text{i c}\ \Omega\right]} \qquad [1.13]$$

Let:

$$\begin{cases} z_0 = \left|\bar{z}_0\right| = \dfrac{\text{m e}\ \Omega^2}{\sqrt{\left[\left(\text{k-M}\ \Omega^2\right)^2 + (\text{c}\ \Omega)^2\right]}} = \dfrac{\text{e}\ \dfrac{\text{m}}{\text{M}}\ \omega_r^2}{\sqrt{\left[\left(1-\omega_r^2\right)^2 + (2\lambda\omega_r)^2\right]}} \\ \text{tg}(\varphi) = \arg\left(\bar{z}_0\right) = -\dfrac{\text{c}\ \Omega}{\text{k-M}\ \Omega^2} = -\dfrac{2\lambda\omega_r}{1-\omega_r^2} \end{cases} \qquad [1.14]$$

with: $\omega_r = \dfrac{\omega}{\omega_p}$.

The magnitude $e_r = e\dfrac{m}{M}$ is called relative unbalance. The reduced displacement of the shaft is characterized:

$$\begin{cases} \dfrac{z_0}{e_r} = \dfrac{\omega_r^2}{\sqrt{\left[\left(1-\omega_r^2\right)^2 + (2\lambda\omega_r)^2\right]}} \quad \text{Reduced amplitude of motion} \\ \text{tg}(\varphi) = -\dfrac{2\lambda\omega_r}{1-\omega_r^2} \end{cases} \qquad [1.15]$$

A “soft-bearing machine” is a machine whose natural angular frequency ω_p is less than the speed of rotation Ω.

The analysis of reduced amplitude of motion for soft-bearing balancing machines shows that, for pulsations far greater than the pulsation ω_p, a displacement z_0 is obtained close to the relative offset e_r.

Therefore, the measurement of displacements and phases at the right of the bearings makes it possible to define the value of e and the position of the center of inertia.

The advantages of this type of machine are its simple implementation and relatively low price.

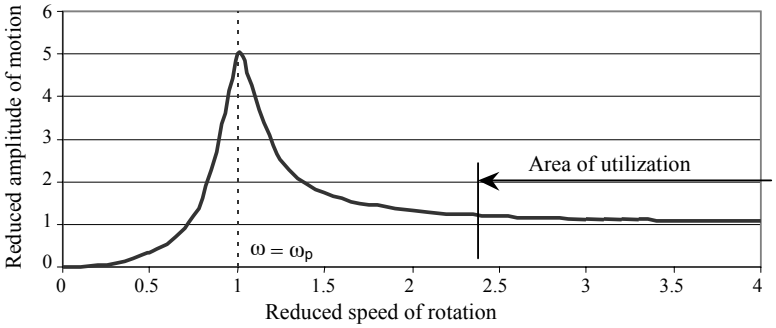

Figure 1.9. *The amplitude/frequency feature of a balancing machine*

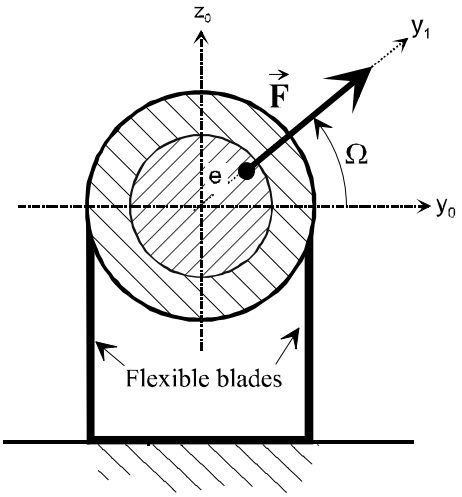

Figure 1.10. *Hard-bearing balancing machine*

1.2.1.2. *The hard-bearing machine*

For hard-bearing machines, balance is obtained by measuring the reactions at the bearings.

This device is often called "subcritical balancing machine" because balance is obtained at a speed of rotation less than the natural angular frequency ω_p. Reactions at the bearings are proportional to Ω^2. For this type of machines, high balancing speeds are used in order to improve measurement precision.

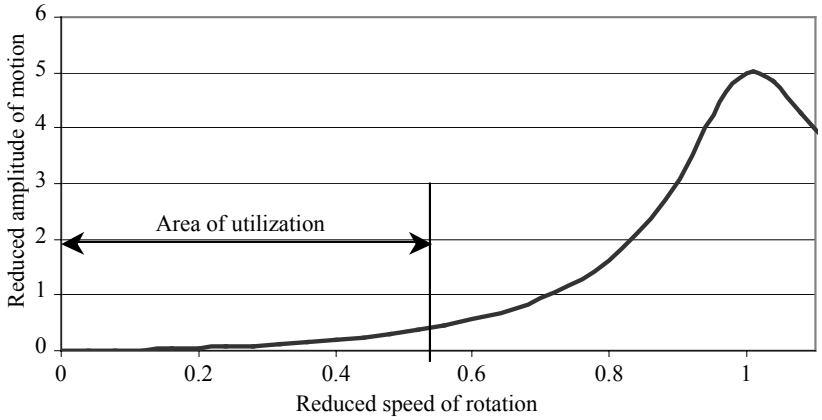

Figure 1.11. *The amplitude/frequency feature of a hard-bearing balancing machine*

The balancing speed cannot get close to the first critical angular frequency in order to avoid the effect of dynamic amplification. The bearings of this type of machine must be very rigid in order to fix the first critical angular frequency as being very high.

For hard-bearing balancing machines, the phase difference between the direction of unbalance and the reaction in the bearing is close to zero, which improves the balance precision.

1.2.2. *Balancing in situ*

In certain cases it is difficult, impractical and even impossible to dismantle a rotor to be balanced. Hence, it is very important to be able to do on site balancing.

There is a method called *in situ* that makes it possible to overcome this difficulty [EDF 70].

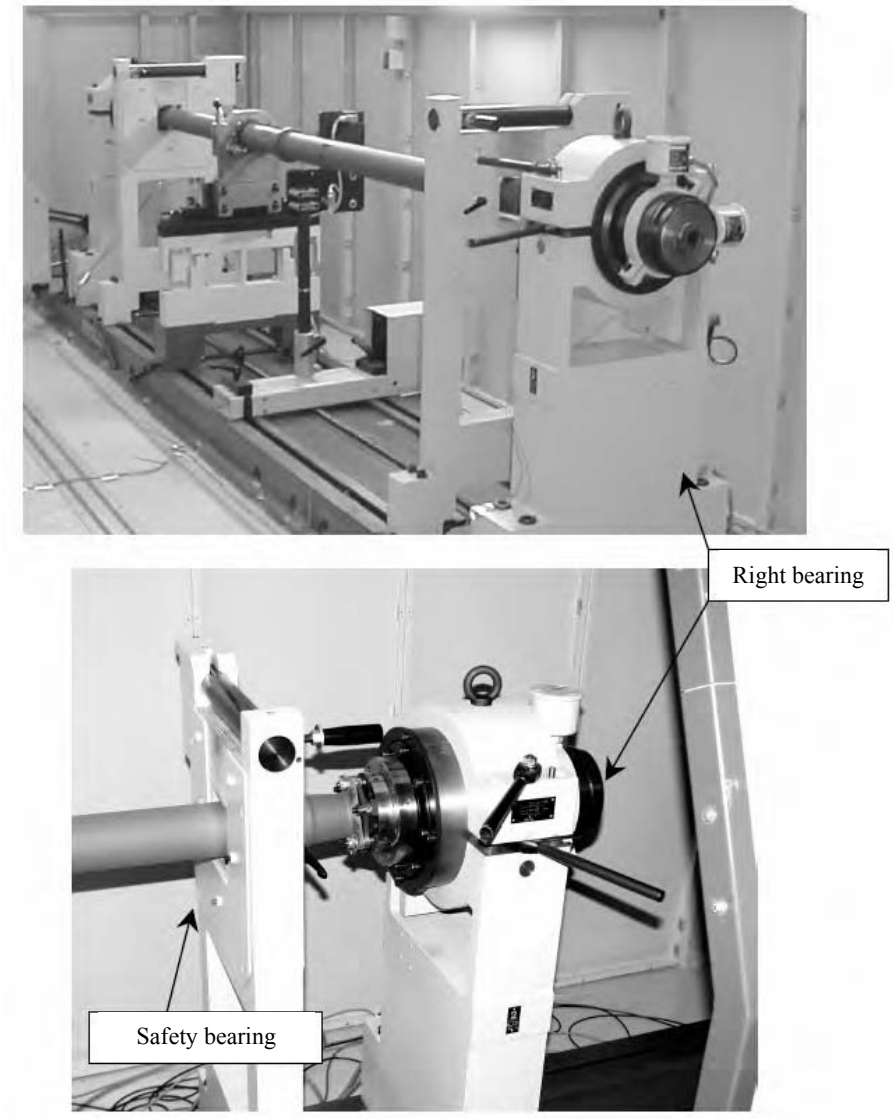

Figure 1.12. *Hard-bearing balancing machine.*
Photo: Eurocopter Deutschland

Two planes perpendicular to the axis of rotation, where the balancing masses will be placed, are attached to each bearing. They are referred to as “balancing planes”.

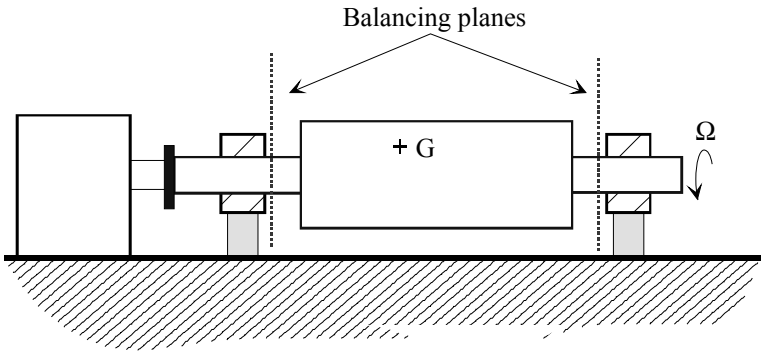

Figure 1.13. *Definition of balancing planes*

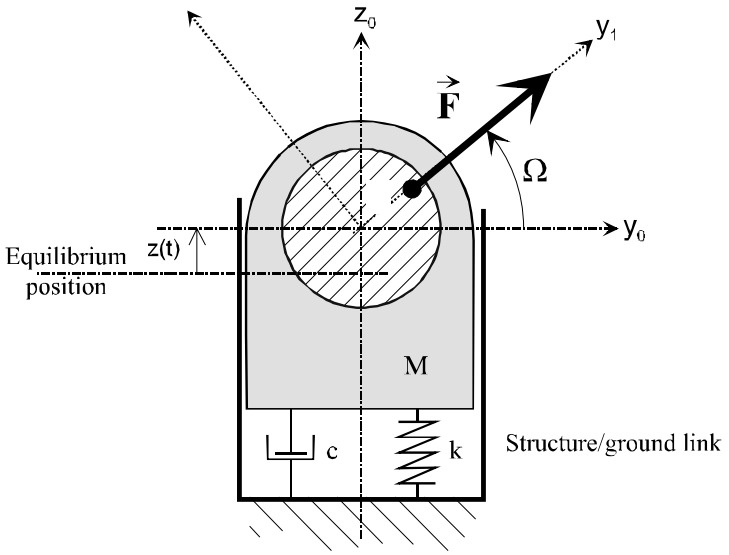

Figure 1.14. *Modeling of a bearing*

1.2.2.1. *The method of separate planes*

1.2.2.1.1. Principle of a bearing

The rotating system consists of bearings. For each bearing we consider only the effect of a rotating force which is proportional to the speed of rotation, defined by:

$$\vec{F} = F_0 \ \Omega^2 \ \vec{y}_1 \qquad [1.16]$$

Starting from the model in Figure 1.14, we define the equation of small motions around the stable angle following the vertical axis:

$$M\,\ddot{z} + c\,\dot{z} + k\,z = F_0\,\Omega^2\,\sin(\Omega\,t) \qquad [1.17]$$

In order to solve this equation, we use the following complex variable transform:

$$\begin{aligned} &z(t) \rightarrow \overline{Z}_0\; e^{j\,\Omega\,t} \\ &F_0\,\Omega^2\,\sin(\Omega\,t) \rightarrow \overline{F}_0\; e^{j\,\Omega\,t} \end{aligned} \qquad [1.18]$$

The obtained equation shows the complex relationship between vibration and excitation:

$$\overline{Z}_0 = \frac{\overline{F}_0}{k - M\,\Omega^2 + j\,c\,\Omega} = \overline{H}(\Omega)\,\overline{F}_0 \qquad [1.19]$$

with:

$$\overline{H}(\Omega) = \frac{1}{k - M\,\Omega^2 + j\,c\,\Omega} \qquad [1.20]$$

Based on the measurement of vibration $\overline{Z}_0$, it would have been interesting to be able to define the unbalance $\overline{F}_0$ in order to determine the mass to be added near the bearing. That requires knowing the bearing features (k and c), which is not always obvious to measure or model. The suggested method makes it possible to overcome this difficulty.

We suggest adding a test mass noted m_e to a position randomly chosen. We measure the vibration m_e entailed by the effect of the initial unbalance and the created unbalance. This is represented by:

$$\overline{Z}_1 = \overline{H}\left(\overline{F}_0 + \overline{R}_e\right) \qquad [1.21]$$

with $\overline{R}_e$ as the unbalance of the test mass such that:

$$\overline{R}_e = m_e\ r_e\ \Omega^2\ e^{j\,\varphi_e} \qquad [1.22]$$

with:

– m_e: test mass,

– r_e and φ_e: polar coordinates of the test mass.

By combining equations [1.19] and [1.21] we can obtain the expression $\overline{\overline{F}}_0$:

$$\begin{cases} \overline{Z}_1 - \overline{Z}_0 = \overline{\overline{H}}\,\overline{R}_e \\ \overline{Z}_0 = \overline{\overline{H}}\,\overline{F}_0 \end{cases} \quad \text{if } \overline{F}_0 = \frac{\overline{Z}_0}{\overline{\overline{Z}}_1 - \overline{Z}_0}\,\overline{R}_e \qquad [1.23]$$

1.2.2.1.2. Experimental implementation

Since the vibration measurements are done within a fixed frame of reference and since the unbalance is defined within a rotating frame of reference, it is imperative to use a sensor which links the fixed frame of reference to the rotating one. Hence, an optical sensor and an optical target placed on the rotor are very often used.

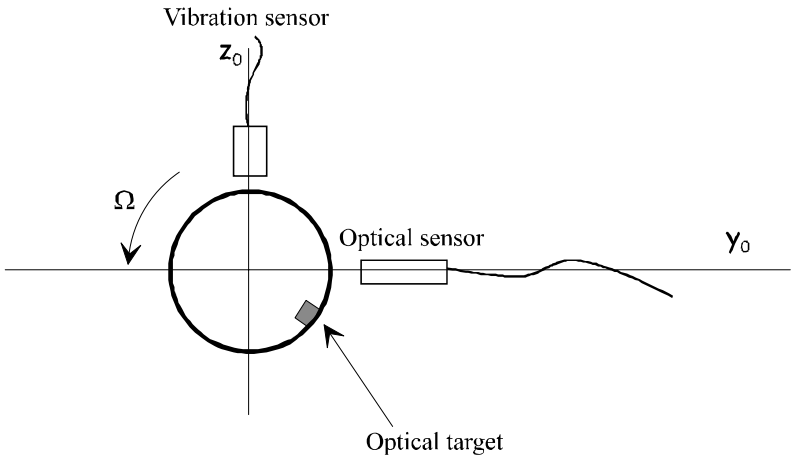

Figure 1.15. *Experimentation: location of the sensors*

Measurements (Figure 1.16) make it possible to identify the amplitude of vibration |Z| and the phase difference φ. The latter is defined based on the measurement of time T and t_φ, such that:

$$\varphi = 2\,\pi\,\frac{t_\varphi}{T} \qquad [1.24]$$

With the help of equation [1.23], two relations can be defined:

$$\begin{cases} \left|\overline{F}_0\right| = \left|\dfrac{\overline{Z}_0}{\overline{Z}_1 - \overline{Z}_0}\right| m_e\ r_e \\ \arg\left(\overline{F}_0\right) = \arg\left(\dfrac{\overline{Z}_0}{\overline{Z}_1 - \overline{Z}_0}\right) + \arg\left(\overline{R}_e\right) \end{cases} \qquad [1.25]$$

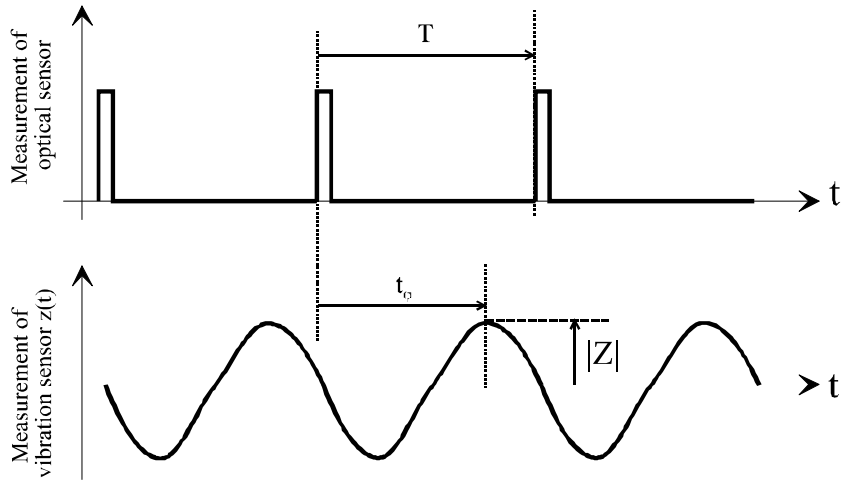

Figure 1.16. *Diagram of experimental measurements*

The mass to be added in order to eliminate the unbalance must verify the relation:

$$\overline{R}_s = m_s\ r_s\ \Omega^2\ e^{j\varphi_s} = -\overline{F_0} \qquad [1.26]$$

In fact, it is shown that:

$$\begin{cases} m_s\ r_s = m_e\ r_e\ \dfrac{\left|\bar{Z}_0\right|}{\left|\bar{Z}_1\text{-}\bar{Z}_0\right|} \\ \Delta\varphi = \varphi_s - \varphi_e = -\arg\left(\dfrac{\bar{Z}_0}{\bar{Z}_1\text{-}\bar{Z}_0}\right) \end{cases} \quad [1.27]$$

These two relations make it possible to calculate the value of the mass to be added (m_s) and its position (r_s and φ_s). We notice that there are three variables for two equations. We often set one of the parameters, $r = r_e = r_s$.

1.2.2.1.3. Numerical example

For example, the following was measured at bearing 1:

$$\begin{cases} \text{amplitude to } 75\ \mu\text{m} \\ \text{phase difference/pip to } +35^\circ \end{cases} \quad [1.28]$$

Then with a 10 g test mass to a radius r_e placed at 0^o (Figure 1.17):

$$\begin{cases} \text{amplitude to } 54\ \mu\text{m} \\ \text{phase difference/pip to } -21^\circ \end{cases} \quad [1.29]$$

Hence we define:

$$\begin{cases} \bar{Z}_0 = \left[75, +35^\circ\right] = 75\ e^{+i35^\circ} \\ \bar{Z}_0 = \left[54, -21^\circ\right] = 54\ e^{-i21^\circ} \\ \bar{R}_e = \left[10,\ 0^\circ\right] = 10 \end{cases} \quad [1.30]$$

Then, according to [1.27]:

$$\begin{cases} m_s = m_e\ \dfrac{\left|\bar{Z}_0\right|}{\left|\bar{Z}_1\text{-}\bar{Z}_0\right|} = 10\ \dfrac{75}{\left|54\ e^{\text{-}i21^\circ}\text{-}75\ e^{+i35^\circ}\right|} = 11.8\ \text{g} \\ \Delta\varphi = \varphi_s\text{-}\varphi_e = \text{-}\arg\left(\dfrac{\bar{Z}_0}{\bar{Z}_1 - \bar{Z}_0}\right) = +45^\circ \end{cases} \quad [1.31]$$

In order to eliminate the vibrations at bearing 1, a mass of 11.8 g must be added, moved away with + 45° from the test mass.

1.2.2.1.4. Principle for the set of bearings

A series of this type of measurements must be taken for each bearing. Each bearing is analyzed successively. Unfortunately, adding a mass in the balancing plane of a bearing will disturb the other bearings. The method consists of establishing a vibration threshold value (criterion depending on the application). Afterwards, by iteration, the bearings are balanced until the vibrations of the set of bearings are below the threshold.

This method can be used only if it rapidly converges to a solution. We can say that this condition is fulfilled if the distance between a balancing plane and its bearing is small compared to the distance between bearings. The advantage of this method is the simplicity of its implementation and calculation. The disadvantage lies in this condition of convergence and in the requirement for iteration which, if there are several bearings, may take a lot of time.

An alternative to this method is the method of simultaneous planes.

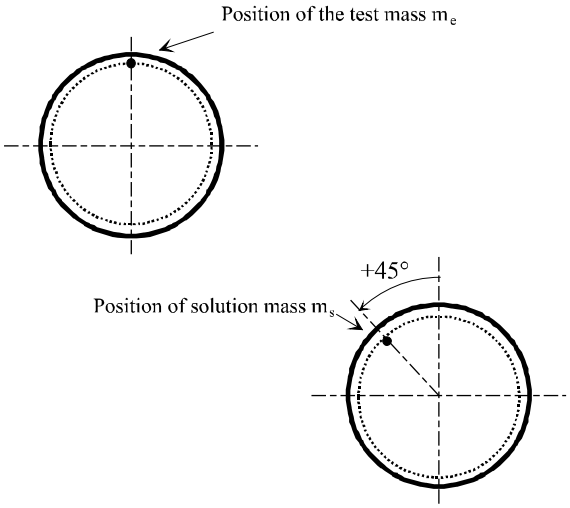

Figure 1.17. *Position of balancing mass*

1.2.2.2. *The method of simultaneous planes – influence coefficients*

Vibrations at the right of the bearings shall be measured. These vibrations are function of the vibratory source, which is the unbalance in our case, and of the

structure behavior, function of transfer. It is supposed that behavior in small motion is linear. We use the following equation which links the vibrations to the unbalance:

$$\begin{bmatrix} \overline{Z}_1 \\ \overline{Z}_2 \end{bmatrix} = \begin{bmatrix} \overline{H}_{11} & \overline{H}_{12} \\ \overline{H}_{21} & \overline{H}_{22} \end{bmatrix} \begin{bmatrix} \overline{F}_1 \\ \overline{F}_2 \end{bmatrix} \qquad [1.32]$$

$\overline{Z}_1$ and $\overline{Z}_2$ represent the vibrations at bearings 1 and 2. $\overline{F}_1$ and $\overline{F}_2$ represent the contribution of unbalance as "seen" by the bearings. H_{ij}, called influence coefficient, represents the behavior of the structure (we find here the influence of the bearing mass, its stiffness and damping):

– no load test:

$$\begin{bmatrix} \overline{Z}_{10} \\ \overline{Z}_{20} \end{bmatrix} = \begin{bmatrix} \overline{H}_{11} & \overline{H}_{12} \\ \overline{H}_{21} & \overline{H}_{22} \end{bmatrix} \begin{bmatrix} \overline{F}_1 \\ \overline{F}_2 \end{bmatrix} \qquad [1.33]$$

– test with a test mass m_{e1} at bearing 1:

$$\begin{bmatrix} \overline{Z}_{11} \\ \overline{Z}_{21} \end{bmatrix} = \begin{bmatrix} \overline{H}_{11} & \overline{H}_{12} \\ \overline{H}_{21} & \overline{H}_{22} \end{bmatrix} \begin{bmatrix} \overline{F}_1 + \overline{R}_{e1} \\ \overline{F}_2 \end{bmatrix} \qquad [1.34]$$

– test with a test mass m_{e2} at bearing 2:

$$\begin{bmatrix} \overline{Z}_{12} \\ \overline{Z}_{22} \end{bmatrix} = \begin{bmatrix} \overline{H}_{11} & \overline{H}_{12} \\ \overline{H}_{21} & \overline{H}_{22} \end{bmatrix} \begin{bmatrix} \overline{F}_1 \\ \overline{F}_2 + \overline{R}_{e2} \end{bmatrix} \qquad [1.35]$$

$\overline{R}_{ei}$: unbalance created by the test mass m_{ei} (see [1.22]).

Through the combination of equations [1.33], [1.34] and [1.35], we can show that:

$$\overline{H}_{ij} = \frac{(\overline{Z}_{ij} - \overline{Z}_{i0})}{\overline{R}_{ej}} \qquad i, j = 1,2 \qquad [1.36]$$

The value of the masses to be added and their locations, masses whose effects must oppose the original unbalance, are defined by the relation:

$$\left[\overline{R}_{sj}\right] = -[F_i] = -\left[\overline{H_{ij}}\right]^{-1} \left[\overline{Z}_{i0}\right] \qquad [1.37]$$

In certain cases, due to technical reasons, it is impossible to have as many balancing planes as bearings to balance.

Through the least squares method, the method consists of minimizing the ensemble of residual vibrations on the set of bearings.

The residual vibrations are defined by:

$$\left[\bar{R}_{rj}\right] = \left[\bar{Z}_{i0}\right] - \left[\overline{H_{ij}}\right]^{-1}\left[\bar{Z}_{sj}\right] \qquad [1.38]$$

We can show that minimizing these vibrations makes it possible to establish the solution for balancing:

$$\left[\bar{R}_{sj}\right] = -\left[\left[\bar{H}_{ij}\right]^{T}\ \left[\overline{H_{ij}}\right]\right]^{-1}\ \left(\left[\bar{H}_{ij}\right]\ \left[\bar{Z}_{i0}\right]\right) \qquad [1.39]$$

1.2.3. *Example of application: the main rotor of a helicopter*

The rotor of a helicopter, consisting of a hub and its blades, represents a rotating system whose balance is extremely important for its good operation and for the comfort of the passengers.

Differences in the blades may occur due to manufacturing errors or to various damages. Despite being a product with an industrial basis, the blades, made of composites, largely depend on the expertise and skill of employees to obtain the required quality. Numerous checks are performed at each manufacturing stage (weight, mechanical property, mold temperature, holographic check, etc.). Nevertheless, each blade is slightly different from the others.

These imperfections can be of different types: mass variation, variation of the location of the center of inertia in the direction of the blade span and the chord, variation in the mass distribution in the direction of the blade span, variation in the airfoil shape (blade torsion, shape of the leading and trailing edges). All these imperfections can have consequences on dynamic behavior. Consequently, blade balancing is necessary.

Balancing is done in several phases. One phase is away from the aircraft, consisting of obtaining static balancing as well as dynamic balancing. Another phase is the one in which the blades are assembled on the device; this phase takes place on the ground and then in flight.

1.2.3.1. *Bench test phase on the ground*

1.2.3.1.1. Static balancing

This adjustment is done on a balance and must be very accurate. Its objective is to guarantee the same centrifugal force for all blades. This implies that the center of inertia of the set of blades is shifted on the axis of rotation.

In order to do that, adjustable counterweights are attached at the blade edge and along the variation axis of the pitch (at 25% from the chord), as illustrated in Figure 1.18.

1.2.3.1.2. Dynamic balancing

The blade is then tested on a whirl test bench. This bench consists of three blades: the blade that needs balancing, the master blade and the accompanying blade. This bench is also used for helicopters which have more than three blades.

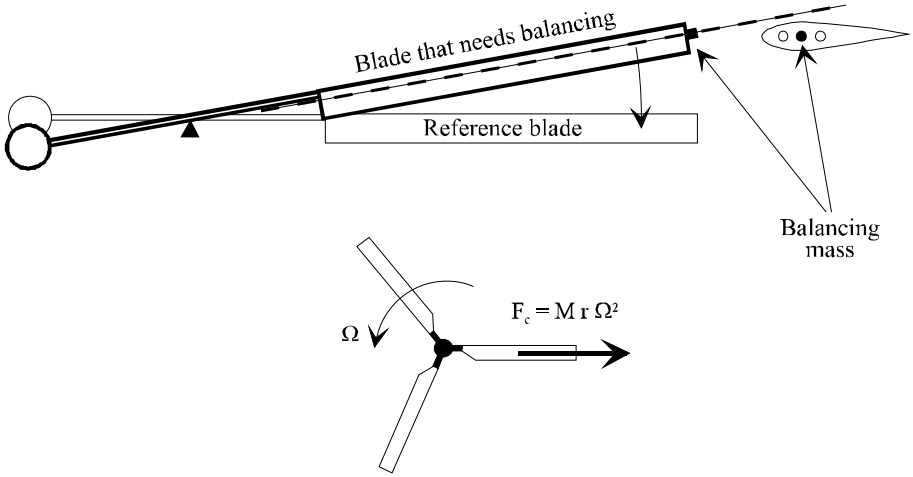

with:

– M: blade mass

– r: distance between the center of inertia and the axis of the rotor

– Ω: rotation angular speed of the rotor

Figure 1.18. *Static blade balancing*

The master blade is representative for the serial manufacture blades (average characteristics). Its reference role makes it an important element that must be

protected against rain and dust. The accompanying blade is less important; it makes it possible to control possible variations in the behavior of the rotor.

The objective is to obtain the same alignment for all blades (vertical clearance) and the same rotor control loads for any range of pitch variations. Hence, we can add a certain mass on the blade root, on the length of the pitch link (pitch incidence change) and on the tabs (a small flap on the blade that modifies its aerodynamic features).

At low pitch, the length of the pitch link is set to enable the test blade to have the same alignment as the others. The alignment is then recorded again at high pitch.

Also, at high pitch, the inclination of the tab is modified in order to obtain accurate control loads. The tab inclination does not have any direct consequences on the lift, but it entails blade torsions and pitch variations, which affect the control pressures (pitch down for a tab inclination towards the bottom).

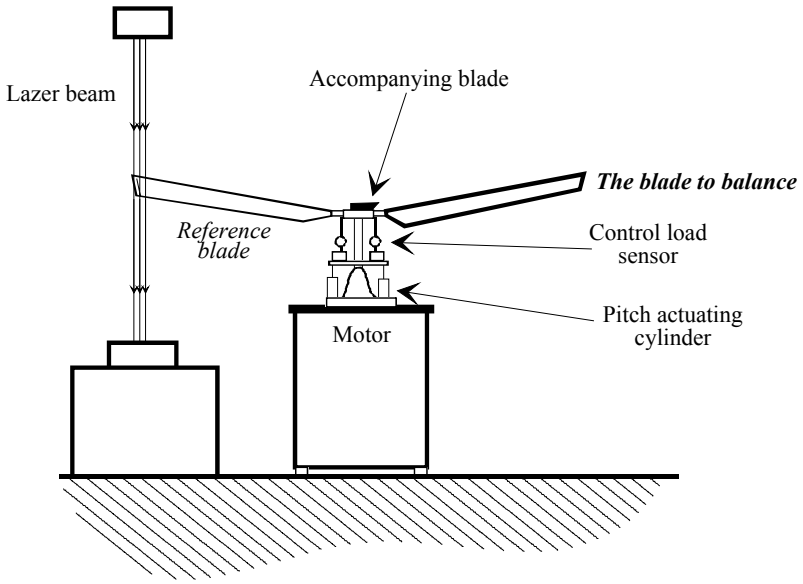

Figure 1.19. *Specific balancing machine*

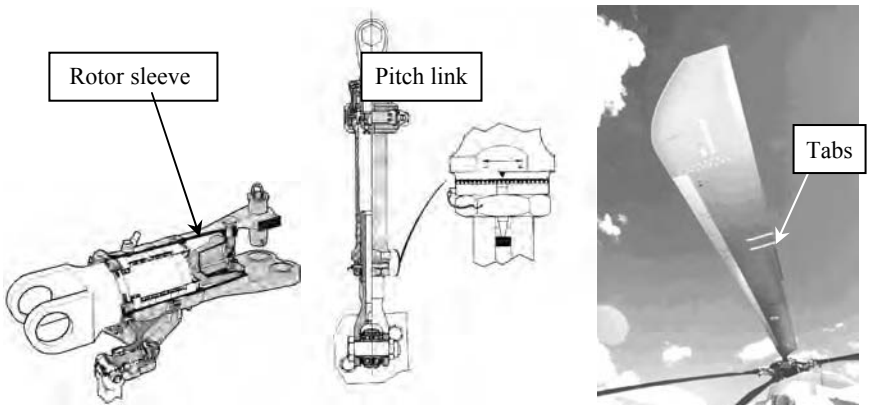

Figure 1.20. *Rotor parameters used for rotor turning*

At high pitch, other counterweights, called "dynamic", are placed in such a way that the same alignment and the same control loads are obtained on the blades. They are positioned at the blade extremity, symmetrically to the pitch axis. The counterweights generate a moment proportional to the pitch, due to centrifugal forces applied to them (moment to pitch down when the counterweights are moved forward).

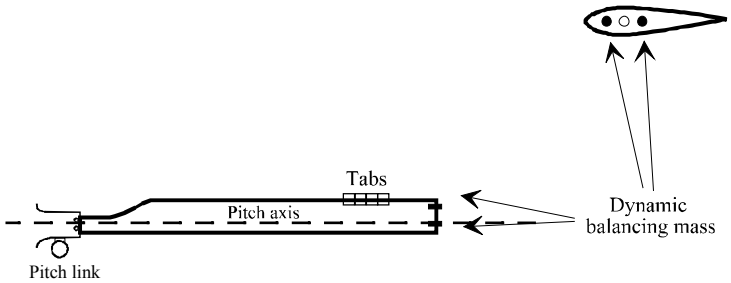

Figure 1.21. *Way of setting the rotor: pitch link, dynamic masses*

At low pitch, the centrifugal forces are actually parallel to the blade and they do not cause any torsion moment.

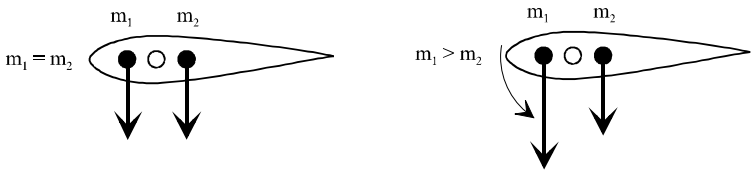

Figure 1.22. *Influence of dynamic counterweights*

A perfect adjustment is very rare. However, a compromise on the set of parameters makes it possible to obtain for all practical purposes a very satisfactory behavior, irrespective of the pitch.

1.2.3.2. *Test phase on a helicopter in flight*

Despite the accuracy of these tests, minor corrections of the pitch link and of the tab deflection are necessary once the blades are mounted on the device.

The balancing of a helicopter rotor is done for several operating conditions such as ground configuration, hovering flight, ground effect and out of ground effect, high speed level flight and high speed maneuvers.

As has been mentioned before, the three ways to balance the rotor are the length of the pitch link, the tabs and the counterweights on the rotor sleeves.

It is difficult to obtain a perfect balancing for all flight operating conditions. The adjustment often supposes a compromise.

All types of imperfections do not create the same unbalance over the entire speed range. A rotor that is perfectly balanced in a hovering flight can cause problems in a level flight.

There are two methods of rotor non-balancing:

– one method consists of observing the vertical alignment of the blades through a camera or a stroboscope,

– another method is based on the measurement of accelerations in the cabin.

The method based on the accelerations in the cabin performs better as far as the vibratory comfort in the fuselage is concerned [FRE 01].

This method uses the measurement of accelerations along three directions in certain points of the device. Since the blade alignment measurement is not necessary, the implementation is very simple. The values of the adjustments provided fully meet the manufacturer's specifications.

This technique is based on learning and adjustment through the neural network technique, which makes it possible to minimize the vibrations of fuselage for the harmonics of the rotor speed.

The analysis of in-flight test results shows that:

– after balancing the main rotor, the vibratory levels in the cabin are very low, for example, less than 0.08 inch/s (if 5.7 10^{-3} g) along the Y and Z axis, for a 10 ton device,

– the residual misalignment of the blades is very low,

– no constraint increase was noticed on the supports of the main transmission unit, pitch controls or the cyclic swash plates.

The following reports (Figures 1.23 and 1.24) enable us to compare the results for different flight configurations.

Hence, flight number 1 provides the vibratory level in the cabin according to the axis indicated for a heavy device (10 ton class) adjusted through traditional methods, flight number 2, the level obtained after deliberate maladjustment of the rotor and finally, for flight number 3, the level after correction according to the indications provided by neural network learning and adjustment.

An artificial neural network is a system of data processing based on the neurophysiologic functioning of the brains. It basically refers to interconnected "mathematical neurons" whose configuration of links gives the network the skill of learning and memorizing [TOU 92]. This method can also be applied to the tail rotor or to aircraft propellers.

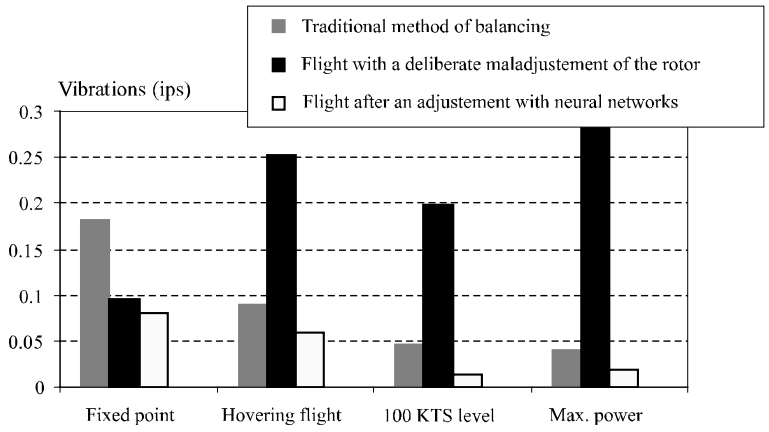

Figure 1.23. *Copilot side vibrations following the vertical axis Z (frequency 4.4 Hz (1 Ω))*

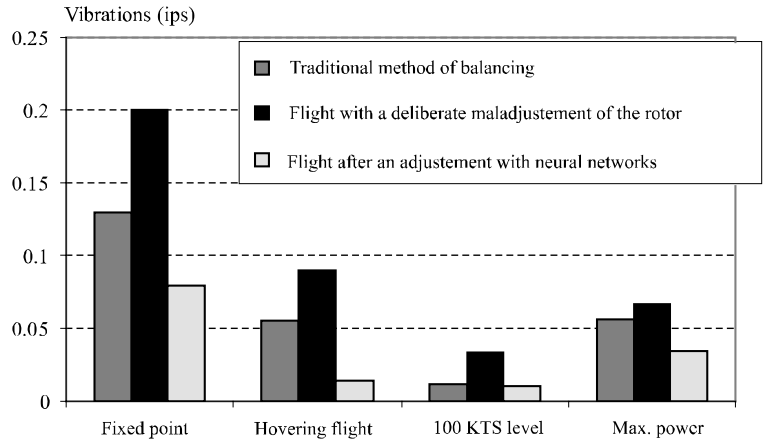

Figure 1.24. *Copilot side vibrations following the lateral axis Y (frequency 4.4 Hz (1 Ω))*

1.3. Influence of shaft bending

We wish to analyze the influence on balancing of the shaft bending [PAR 88]. Let us consider the following example:

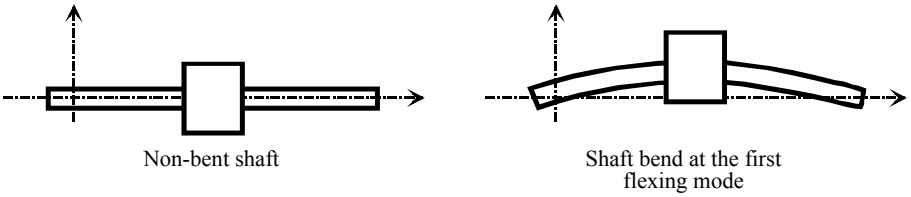

Figure 1.25. *Shaft bending*

Shaft bending implies that the center of inertia is no longer situated on the axis of rotation. This location depends on the speed of rotation. In fact, balancing, which consists of shifting the center of inertia from the rotating part to the axis of rotation, also depends on the speed of rotation.

In reality not all shafts are considered flexible. Following the methods previously described, the shaft is usually balanced at low speeds, above its first critical frequency. If the vibrations due to unbalance are higher than the values allowed for high speeds of rotation, that shaft is considered a flexible shaft.

1.3.1. *The notion of critical speed*

Balancing at low speeds cancels out the loads at the bearings because the shaft is bent very little.

At greater speeds, when the speed of rotation gets close to the first bending frequency, the moment of bending in the shaft leads to the bending of the shaft. Since the center of inertia is no longer on the axis of rotation, a new unbalance appears.

For greater speeds, this phenomenon can occur for higher critical frequencies. Flexible shafts are usually used for machines that rotate very fast. When the system is used at speeds higher than the first critical frequency, we call them "supercritical shafts".

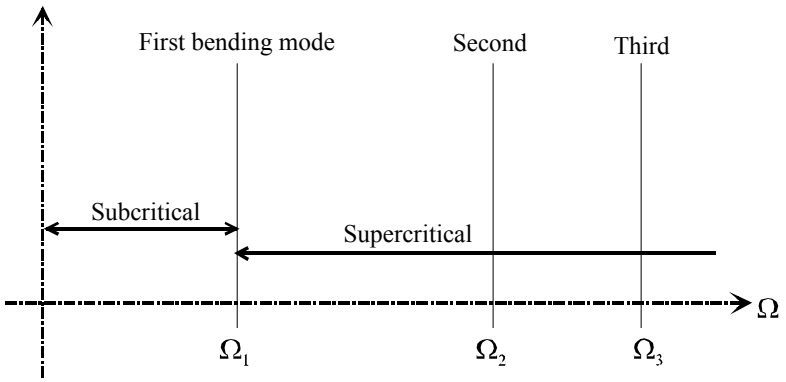

Figure 1.26. *Different types of rotor speeds*

Using supercritical shafts in power transmission decreases the reactions at the bearings and consequently the amplitudes of vibrations.

We will examine the case of a flexible shaft attached to a non-bending body modeled by a disk. We will suppose that the inertial effects of the shaft are negligible compared to the effects of the disk and that the bendings of the bearings are negligible compared to the bending of the shaft. This hypothetical case does not systematically correspond to the rotating shafts as they are in reality, but enables us to illustrate the phenomenon.

For this model, the disk moves perpendicularly to the shaft, which eliminates the gyroscopic effect (see section 1.4).

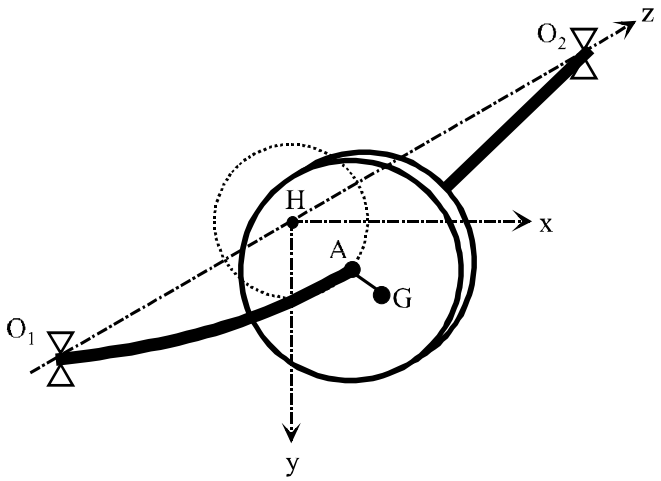

Figure 1.27. *Shaft bending*

The bending of the shaft while idle is ignored. The center of inertia of the disk is moved from the rotation axis of the shaft by a distance noted as e. Since the motion of the disk is planar, the model is provided in Figure 1.28.

The equivalent stiffness of the shaft strongly depends on the way the shaft is bent. A flexible shaft has an infinite variety of distinctive frequencies whose shapes correspond to different natural modes.

For the first frequency (the lowest), we will suppose that the bending "resembles" a sinusoidal form (it is not necessarily the most accurate form, but it is easy to integrate).

Therefore, the bending is written as follows:

$$\text{def}(z) = A \sin\left(\frac{\pi z}{L}\right) \qquad [1.40]$$

with:

– z: axial position,

– L: shaft length,

– A: amplitude of bending.

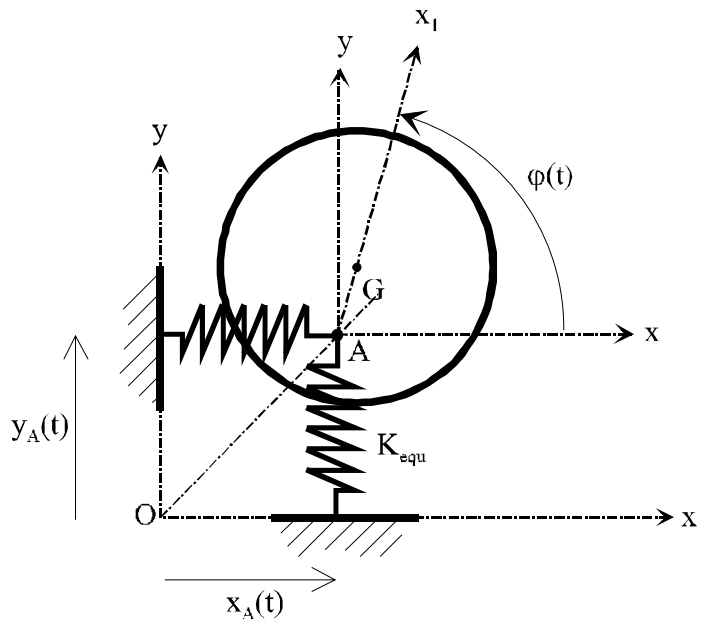

with:

– K_{equ} : equivalent stiffness of the shaft

– e: offset

Figure 1.28. *Shaft and rotor modeling*

Traditionally, the calculation of the equivalent stiffness can be done by using an energetic equivalence. It is shown that for the particular case when the disk is in the middle of the two bearings:

$$K_{equ} = \frac{\pi^4 \, E \, I}{2 \, L^3} \qquad [1.41]$$

with:

– E: elasticity modulus of the shaft material,

– I: moment of inertia of the shaft bending.

In reality, during the pre-design of a rotating shaft, we are usually interested in finding the first natural frequency. It is wise to model the shaft mass by a mass concentrated in its environment and then to overlay it on the mass M of the rotor:

$$m = M + \mu \frac{L}{2} \qquad [1.42]$$

where μ is the mass per unit length of the shaft.

In the case of the first bending mode, only half of the shaft mass takes part in this modeling [LAN 86].

The dynamic behavior of the shaft having the hypotheses mentioned above can be brought to a system with two degrees of freedom characterized by the displacements x_A and y_A (Figure 1.28). They are measured in relation to the static position.

For torsion, the equation of motion can be formulated as follows:

$$I\,\ddot{\varphi} = K_{equ}\ y_A\ e\sin(\varphi) - K_{equ}\ x_A\ e\cos(\varphi) - M_R + M_E \qquad [1.43]$$

with:

– M_R: resistance moment,

– M_E: drive moment.

If we suppose that the resistance moment and the drive moment are equal, we can also prove that bending and torsion motions are coupled by the equation:

$$\ddot{\varphi} = K_{equ}\ y_A\ \frac{e}{I}\sin(\varphi) - K_{equ}\ x_A\ \frac{e}{I}\cos(\varphi) \qquad [1.44]$$

In the case of systems allowing strong bending, the coupling between bending and torsion can be important. In common cases, the values *e*/I are very low and hence this relationship is negligible.

Another problematic case is the transfer of the resonance. If the difference $(M_E - M_R)$ is small, the system may be blocked during the increase in speed on the bending or torsion frequency. In this case, the entire external energy is absorbed by the bending and torsion vibrations: resonance is impossible to overcome. These phenomena occur in the case of certain drive trains paired with a piston engine

during the passage of torsional critical frequencies. It is necessary then to use torsional dampers (see Chapter 12).

For many applications, the rule is to keep the speed of rotation of the shaft constant. Hence:

$$\dot{\varphi} = \Omega \qquad [1.45]$$

The equations of motion of the disk, obtained by projection on x and y, are defined by:

$$m\,\vec{A}_{G,S/R_g} = \sum \vec{F}_{ext\to S} \quad \Rightarrow \quad \begin{cases} m\,\ddot{x} + c\,\dot{x}_A + K_{equ}\,x_A = 0 \\ m\,\ddot{y} + c\,\dot{x}_A + K_{equ}\,y_A = 0 \end{cases} \qquad [1.46]$$

with:

$$\begin{cases} x(t) = x_A + e\cos(\Omega\,t) \\ y(t) = y_A + e\sin(\Omega\,t) \end{cases} \qquad [1.47]$$

then [1.46] becomes:

$$\begin{cases} m\,\ddot{x}_A + c\,\dot{x}_A + K_{equ}\,x_A = m\,e\,\Omega^2\cos(\Omega\,t) \\ m\,\ddot{y}_A + c\,\dot{x}_A + K_{equ}\,y_A = m\,e\,\Omega^2\sin(\Omega\,t) \end{cases} \qquad [1.48]$$

If we consider $d(t) = x_A + i\,y_A$, the following equivalence is obtained:

$$m\,\ddot{d} + c\,\dot{d} + K_{equi}\,d = m\,e\,\Omega^2\,e^{i\,\Omega\,t} \qquad [1.49]$$

We write $d(t) = d_0\,e^{i\,(\Omega\,t-\varphi)}$, the solution for a forced response. Hence, equation [1.49] shows that:

$$\begin{cases} d_0 = \dfrac{e}{\sqrt{\left(1-\omega_{cr}^2\right)^2 + \left(2\,\lambda\,\omega_{cr}\right)^2}} \\ \varphi = \operatorname{atan}\left(\dfrac{2\,\lambda\,\omega_{cr}}{1-\omega_{cr}^2}\right) \end{cases} \qquad [1.50]$$

with:

$$\omega_{cr} = \frac{\omega_p}{\Omega} \qquad \omega_p = \sqrt{\frac{K_{equi}}{m}} \qquad \lambda = \frac{c}{2\, m\, \omega_{cr}}$$

It should be noted that the motion of the flexible shaft consists of two motions:

– the motion of rotation of the elastic center A around the axis of the bearings at the rotation frequency and in the direction of the rotation of the shaft,

– the motion of rotation of the center of inertia of the disk around the elastic center at the rotation frequency. This motion is a phase ahead compared to the previous motion.

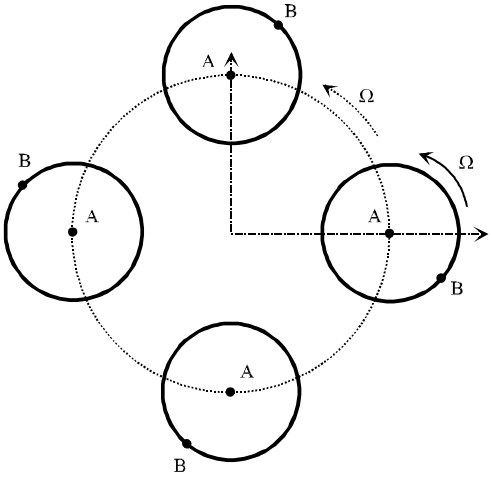

Figure 1.29. *Phenomenon of precession*

This motion combination is called *forward precession of the flexible shaft* [LAC 79]. Forward precession is represented by the diagram in Figure 1.29.

1.3.2. *Forward precession of the flexible shaft*

It is noticed that the distance between a certain point of the shaft B and the axis A does not vary in time. The two motions of rotation have the same frequency. In fact, the forward precession does not induce dynamic constraints in the shaft but only static ones.

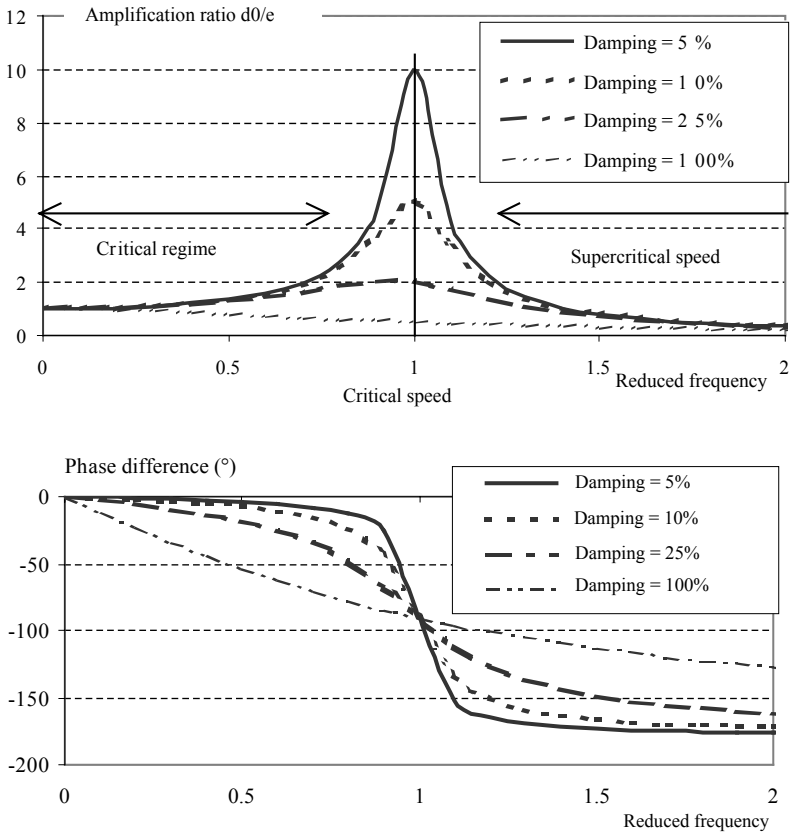

Figure 1.30. *Frequency response to unbalance of a flexible shaft for different damping ratios*

When the two motions are performed in opposite directions, we have what is called nostalgic precession. This type of precession cannot be triggered by unbalance. The backward precession can be caused only by external loads which act in a direction opposite to the rotation of the shaft. The dynamic response of the flexible shaft under the effect of unbalance can be shown graphically (see Figure 1.30). Hence, we can distinguish two possibilities.

1.3.2.1. *Subcritical speed* $(\Omega < \omega_{cr})$

For a low speed, below critical frequency, the angle φ is between 0 and 90°.

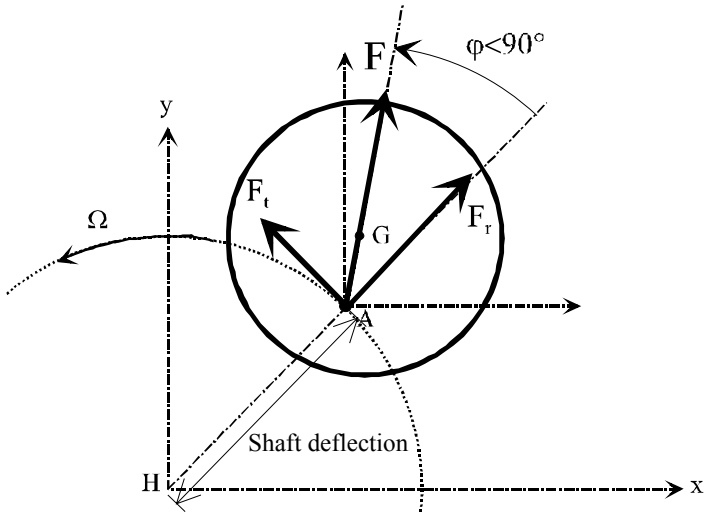

Figure 1.31. *Response for subcritical speed*

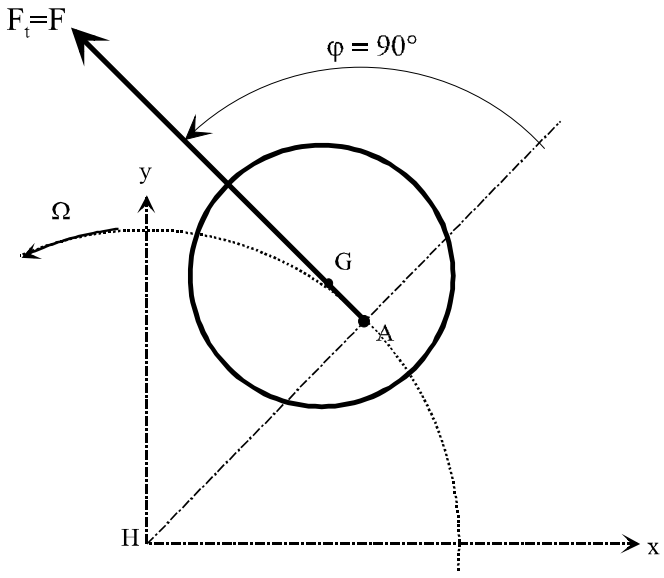

Figure 1.32. *Response to resonance*

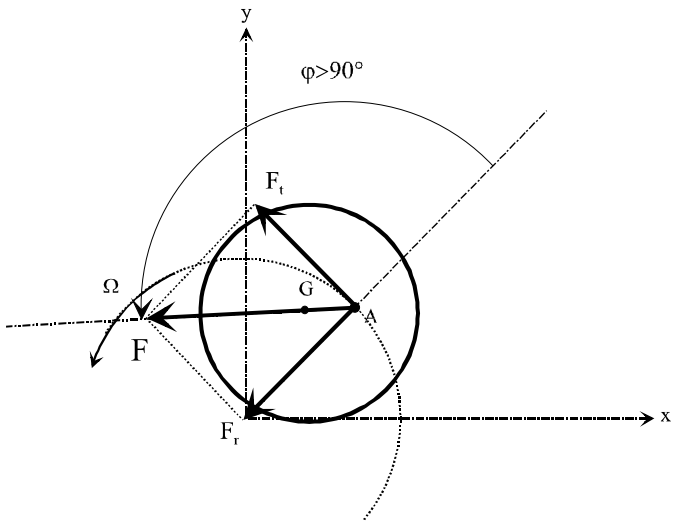

Figure 1.33. *Response for supercritical speed*

The radial component F_r of the centrifugal force leads to shaft deflection and the tangential component F_t entails the shaft precession. During the passage of critical frequency, the centrifugal force is perpendicular to the shaft deflection.

1.3.2.2. *Resonance* $(\Omega = \omega_{cr})$

The amplitude of shaft deflection is highest during passage through critical frequency. This phenomenon resembles the phenomenon of resonance even though the shaft is subjected to static constraints. Vibrations at the bearings appear at the shaft rotation frequency and they are highest during the passage of critical frequency.

Thus there is a certain analogy between the precession of a flexible shaft and the theory of the beams, but the two phenomena are fundamentally different.

1.3.2.3. *Supercritical speed* $(\Omega > \omega_{cr})$

When the speed of rotation is greater than the critical frequency, the centrifugal load tends to lower the bending deflection of the shaft up to the point where the center of inertia of the shaft is on the axis of rotation of the shaft.

This phenomenon of autocentering of the supercritical shaft often gives the advantage to supercritical shafts over subcritical shafts by reducing the reactions at the bearings.

1.3.3. *Balancing flexible shafts*

Balancing a flexible shaft is more difficult than balancing a rigid one. For this type of balancing, apart from reducing the reactions at the bearings, it is also required to minimize the shaft static deflections at the passage of its critical speeds. A good balancing must be carried out for the entire range of shaft operations, by taking into account all critical frequencies occurring for this range. The balancing technique for a flexible shaft will be illustrated as an example on a shaft which, during operation, allows two critical frequencies.

Balancing will be carried out at a low speed of rotation when the shaft will behave like a rigid element and at a high speed when the shaft will get bent. For balancing at a low speed, we correct the static and dynamic unbalances as shown in Figure 1.34. The static and dynamic balancing can be reached by simply adding certain masses in planes 1 and 5, as in Figures 1.35 and 1.36.

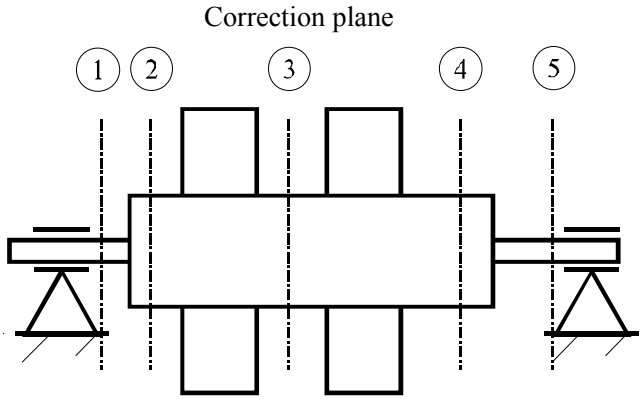

Figure 1.34. *Example of balancing planes for a flexible rotor*

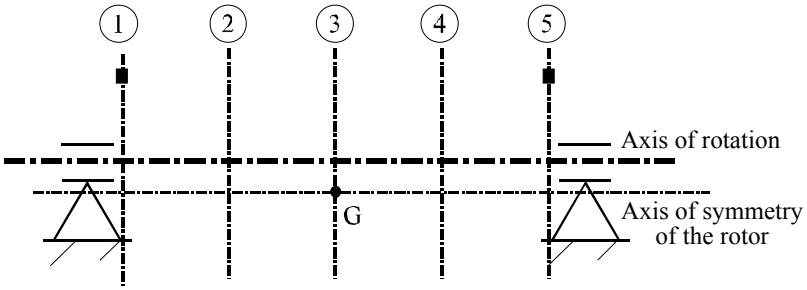

Figure 1.35. *Example of static balancing for low speeds*

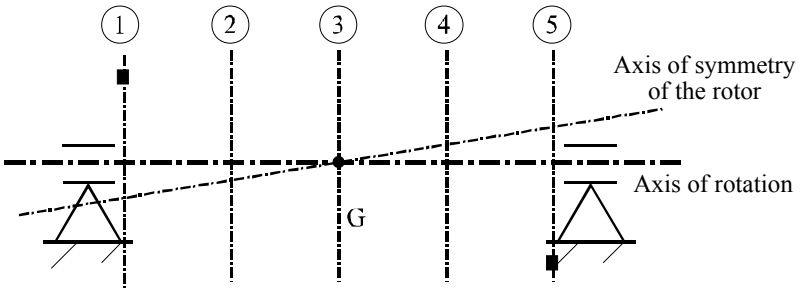

Figure 1.36. *Example of dynamic balancing for low speeds*

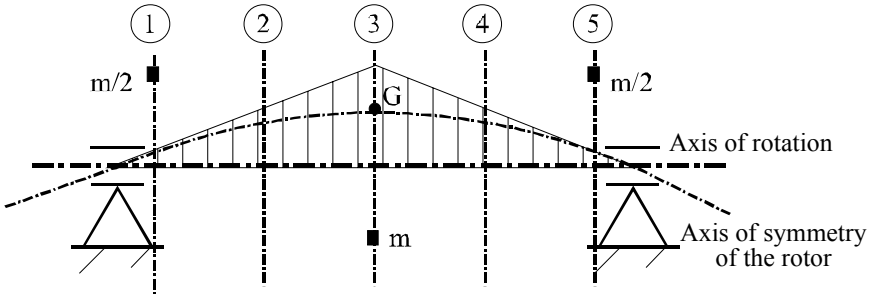

Figure 1.37. *Example of balancing for the first critical frequency*

Corrections at high and low speeds are overlapping and independent.

The flexible balancing is carried out at a speed for which the shaft can no longer be considered as a rigid element. For this type of balancing, the bearings must be more rigid than the shaft flexibility.

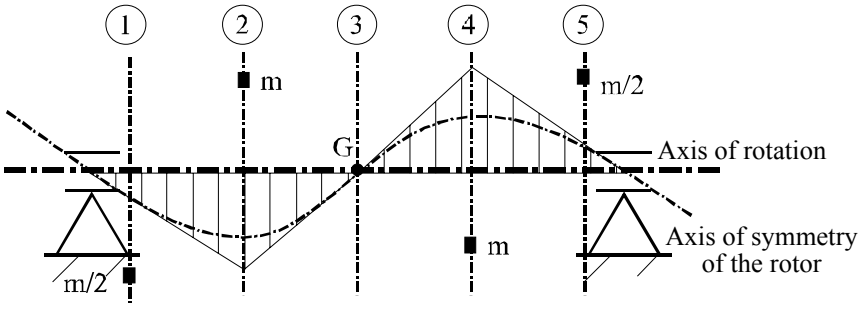

Figure 1.38. *Example of balancing for the second critical frequency*

In Figures 1.37 and 1.38, we notice that balancing masses are placed in such a way as to "correct" each critical frequency. The static deflections of the shaft during critical frequencies are reduced. The modal bendings of different critical frequencies are orthogonal and the balancing masses for a certain mode are placed so that they do not modify another mode.

1.3.4. *Example of application: transmission shaft of the tail rotor of a helicopter*

The objective of this section is to show the balancing of flexible shafts through an industrial example: the rear transmission shafts of a helicopter. They allow power to be brought to the tail rotor.

These shafts have slender shapes and they rotate at high speeds (5,000 rpm). There are two types of technology, i.e. subcritical shafts (which have many bearings; Figure 1.39) and supercritical shafts with very few bearings.

This phenomenon implies that in practice we have to take into consideration the shaft bending during balancing.

The nominal speed of rotation of the tail transmission is located between the first and second critical frequencies. It is necessary to add masses in three different planes. The first two are situated near the bearings. The third one is between the two bearings as shown in Figure 1.40.

In order to carry out the balancing process, the shafts must be mounted on a balancing machine.

The counterweights are added on a precise plane and at a precise radius. The tests consist of determining the value of the mass and the angular position.

1.4. Gyroscopic effects

1.4.1. *Forward or backward motion*

In the previous section, the model used enables us to define a natural bending frequency which does not depend on the speed of rotation of the shaft. It is important to know that for certain systems, bending frequency depends on the speed of rotation because of gyroscopic effects [LAN 97, PAR 88].

To illustrate this phenomenon, we will present the case of a rotor consisting of an overhang disk and whose shaft becomes very flexible.

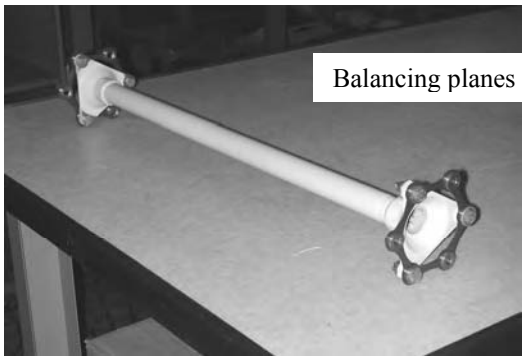

Figure 1.39. *Flexible shaft for tail transmission: example of subcritical shaft. Photo: Eurocopter*

Figure 1.40. *Location of counterweights for the balancing of subcritical transmission. Photo: Eurocopter Deutschland*

For this study we give the following hypotheses:

– the effects of the shaft weight are negligible,

– the Young modulus E and the shaft section are constant,

– the bearings are infinitely rigid.

The combination of a disk of non-zero inertia and the rotary bending of a shaft entails a gyroscopic torque caused by the disk inclination with respect to the plane perpendicular to the geometrical axis of rotation.

The motion comprises the rotation of the shaft around the neutral axis Z_1 at the speed Ω and the rotation of the neutral axis Z_1 around the geometrical axis Z at the speed W.

Depending on the characteristics of the disk, the speeds W and Ω can be in the same direction or in opposite directions:

– when $\Omega = W$, we have the case of *forward precession*,

– when $\Omega = -W$, we have the case of *backward precession*.

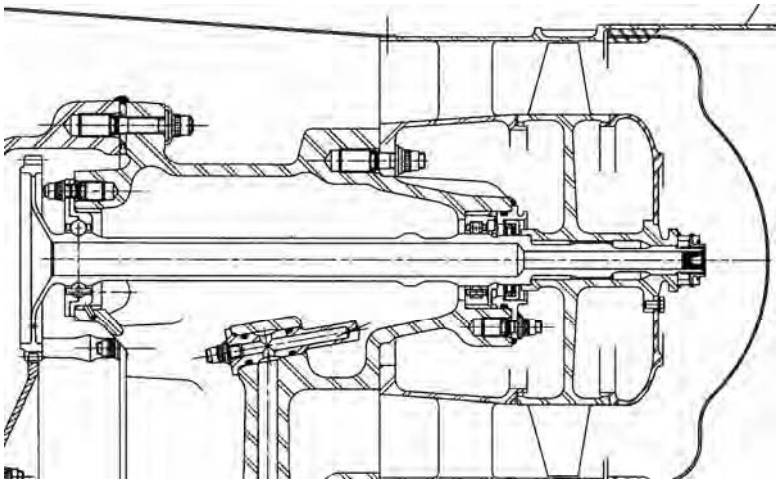

Figure 1.41. *Cooling fan of transfer unit*

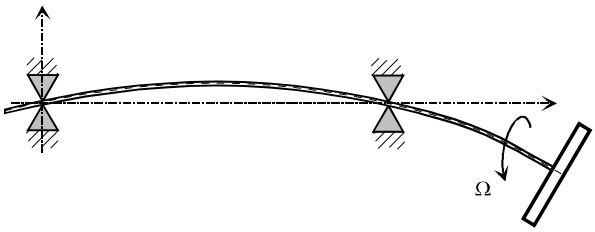

Figure 1.42. *Simplified modeling of cooling fan*

These shaft behaviors may cause two types of critical speeds to appear. A forward whirl appears when the corresponding mode is a forward precession motion, and when the mode is a backward whirl motion, a backward critical speed appears. Forward whirl speeds are the most dangerous because they are excited by the unbalances always present in a rotating structure.

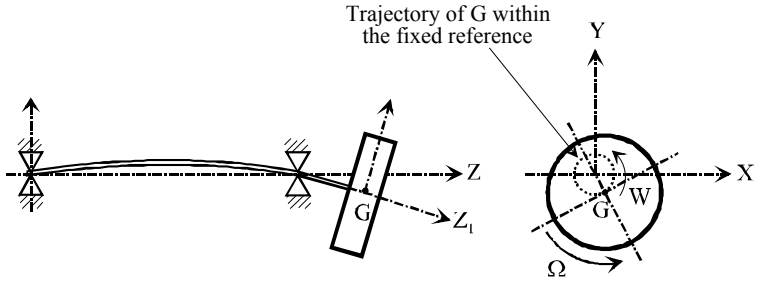

Figure 1.43. *Forward or backward motion of the cooling fan*

In the case of a forward whirl, the gyroscopic moment has the tendency to increase the shaft stiffness, hence to increase its natural frequency. On the contrary, in the case of a backward whirl, the shaft becomes flexible and its natural frequency decreases.

1.4.2. *Equations of motion*

The objective of this section is to create equations of gyroscopic effects in order to study them and to show their consequences.

The following hypotheses will apply to the entire study: the axial bendings of the shaft and the torsion bendings will be ignored, the shaft has a constant speed of rotation marked Ω, the bearings are infinitely rigid and the mass of the shaft is negligible.

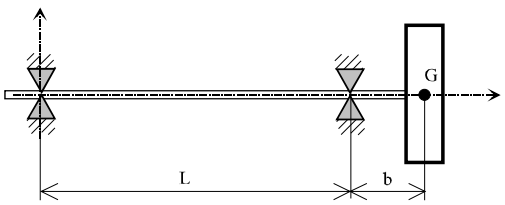

Figure 1.44. *Rotor geometry*

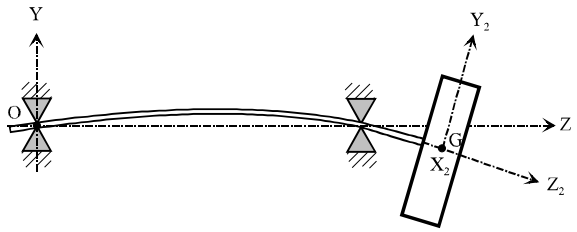

Figure 1.45. *Parametric transform and location*

Let $R = (O, \vec{X}, \vec{Y}, \vec{Z})$ be an inertial frame and $R_2 = (G, \overrightarrow{X_2}, \overrightarrow{Y_2}, \overrightarrow{Z_2})$ a frame of reference linked to the rotor disk. The fundamental principle of dynamics applied to the rotor disk S is written as follows:

$$\begin{cases} m\,\vec{\Gamma}_{(G\in S/R)} = \vec{R}\left(\overline{S} \to S\right) \\ \vec{\delta}_G(S/R) = \overrightarrow{M}_G\left(\vec{R}\left(\overline{S} \to S\right)\right) \end{cases} \quad [1.51]$$

The action of the shaft on the rotor is defined by:

$$\{\text{shaft} \to \text{rotor}\} : \begin{Bmatrix} \vec{R}\left(\overline{S} \to S\right) \\ \overrightarrow{M}_G\left(\overline{S} \to S\right) \end{Bmatrix} \quad [1.52]$$

The center of inertia G is expected to remain in the plane $(O, \vec{X}, \vec{Y})$. Also:

$$\overrightarrow{\Omega}_{2/0} = W_x\,\vec{x} + W_y\,\vec{y} + \Omega\,\vec{z}_1 \quad [1.53]$$

The matrix of inertia of the disk is defined, in its center of inertia, by:

$$\overset{\approx}{I}_G(S) = \begin{bmatrix} J & 0 & 0 \\ 0 & J & 0 \\ 0 & 0 & I \end{bmatrix}_{(\vec{x}_2, \vec{y}_2, \vec{z}_2)} \quad [1.54]$$

Hence, by defining the angular momentum in the center of inertia G is expressed by:

$$\vec{\sigma}_G(S/R) = \overset{=}{I}_G(S)\,\overrightarrow{\Omega}_{2/0} = J\,W_X\,\vec{x} + J\,W_y\,\vec{y} + I\,\Omega\,\vec{z}_2 \quad [1.55]$$

Thus:

$$\begin{aligned}\vec{\delta}_G(S/R) &= J\frac{d\,W_x}{dt}\,\vec{x} + J\frac{d\,W_y}{dt}\,\vec{y} + I\,\Omega\,\frac{d\,\vec{z}_2}{dt}\Bigg)_R \\ &= J\frac{d\,W_x}{dt}\,\vec{x} + J\frac{d\,W_y}{dt}\,\vec{y} + I\,\Omega\,\left(\vec{\Omega}_{2/0}\wedge\vec{z}_2\right) \\ &= \left(J\frac{d\,W_x}{dt} + I\,\Omega\,W_y\right)\vec{x} + \left(J\frac{d\,W_y}{dt} - I\,\Omega\,W_x\right)\vec{y}\end{aligned} \qquad [1.56]$$

and after projection:

$$\begin{cases} J\dfrac{d\,W_x}{dt} + I\,\Omega\,W_y = M_x \\ J\dfrac{d\,W_y}{dt} - I\,\Omega\,W_x = M_y \end{cases} \qquad [1.57]$$

We obtain a system of linear equations which link the motion of the rotor and the actions of the shaft on the rotor. Let be:

- ψ_X, the angular displacement defined by $\dfrac{d\,\Psi_x}{dt} = W_x$,
- ψ_Y, the angular displacement defined by $\dfrac{d\,\Psi_y}{dt} = W_y$.

The fundamental principle of dynamics provides the following expressions:

$$\begin{cases} M\dfrac{d^2X_G}{dt^2} = R_x \\ M\dfrac{d^2Y_G}{dt^2} = R_y \end{cases} \qquad [1.58]$$

and

$$\begin{cases} J\dfrac{d^2\Psi_x}{dt^2} + I\,\dfrac{d\Psi_x}{dt}\Omega\ = M_x \\ J\dfrac{d^2\Psi_y}{dt^2} - I\,\dfrac{d\Psi_y}{dt}\Omega\ = M_y \end{cases} \qquad [1.59]$$

We say:

$$\begin{aligned}\bar{Z} &= X_G + i\, Y_G \\ \bar{\Psi} &= \Psi_x + i\Psi_y \\ \bar{R} &= R_G + i\, R_G \\ \bar{M} &= M_x + iM_y\end{aligned} \qquad [1.60]$$

The equations can be reduced to:

$$\begin{cases} M\dfrac{d^2\bar{Z}}{dt^2} = \bar{R} \\ J\dfrac{d^2\bar{\Psi}}{dt^2} - i\, I\, \Omega\, \dfrac{\overline{d\Psi}}{dt} = \bar{M} \end{cases} \qquad [1.61]$$

The actions on the disk are the actions of the shaft. These actions are modeled by a stiffness matrix:

$$\begin{bmatrix}\bar{R} \\ \bar{M}\end{bmatrix} = -\begin{bmatrix}k_{11} & k_{12} \\ k_{21} & k_{22}\end{bmatrix}\begin{bmatrix}\bar{Z} \\ \bar{\Psi}\end{bmatrix}$$

let:

$$\begin{bmatrix}M & 0 \\ 0 & J\end{bmatrix}\begin{bmatrix}\ddot{\bar{Z}} \\ \ddot{\bar{\Psi}}\end{bmatrix} + \begin{bmatrix}0 & 0 \\ 0 & -i\, I\, \Omega\end{bmatrix}\begin{bmatrix}\dot{\bar{Z}} \\ \dot{\bar{\Psi}}\end{bmatrix} + \begin{bmatrix}k_{11} & k_{12} \\ k_{21} & k_{22}\end{bmatrix}\begin{bmatrix}\bar{Z} \\ \bar{\Psi}\end{bmatrix} = \begin{bmatrix}0 \\ 0\end{bmatrix} \qquad [1.62]$$

The complex solution has the following form:

$$\begin{bmatrix}\bar{Z} \\ \bar{\Psi}\end{bmatrix} = \begin{bmatrix}\bar{Z}_0 \\ \bar{\Psi}_0\end{bmatrix} e^{i\,(\omega\, t)} \qquad [1.63]$$

hence, equation [1.62] is written:

$$\begin{bmatrix}k_{11} - M\,\omega^2 & k_{12} \\ k_{21} & k_{22} + I\,\Omega\,\omega - J\,\omega^2\end{bmatrix}\begin{bmatrix}\bar{Z}_0 \\ \bar{\Psi}_0\end{bmatrix} = \begin{bmatrix}0 \\ 0\end{bmatrix} \qquad [1.64]$$

The solution of this equation must verify (provided that M and J are zero):

$$\omega^4 - \frac{I}{J}\,\Omega\,\omega^3 - \left(\frac{k_{11}}{M} + \frac{k_{22}}{J}\right)\omega^2 + \frac{I\,k_{11}\,\Omega}{J\,M}\omega + \frac{k_{11}\,k_{22} - k_{12}\,k_{21}}{J\,M} = 0 \qquad [1.65]$$

There are three interesting particular cases to study.

1.4.2.1. *Natural angular frequencies (shaft off motion)*

Natural frequencies represent the free oscillations of the shaft, in other words, when the speed of rotation is zero.

Hence it is enough to introduce $\Omega = 0$:

$$\omega^4 - \left(\frac{k_{11}}{M} + \frac{k_{22}}{J}\right)\omega^2 + \frac{k_{11}\,k_{22} - k_{12}\,k_{21}}{M\,J} = 0 \qquad [1.66]$$

1.4.2.2. *Critical speeds during forward precession*

These speeds represent the forced oscillations of the shaft, when it rotates the geometrical axis and itself at the same speed.

Hence it is enough to introduce $\Omega = \omega$:

$$\left(1 - \frac{I}{J}\right)\omega^4 - \left(\left(1 - \frac{I}{J}\right)\frac{k_{11}}{M} + \frac{k_{22}}{J}\right)\omega^2 + \frac{k_{11}\,k_{22} - k_{12}\,k_{21}}{M\,J} = 0 \qquad [1.67]$$

1.4.2.3. *Critical speeds during backward precession*

These speeds represent the forced oscillations of the shaft, when it turns around the geometrical axis and on itself at different speeds.

Hence it is enough to introduce $\Omega = -\omega$:

$$\left(1 + \frac{I}{J}\right)\omega^4 - \left(\left(1 + \frac{I}{J}\right)\frac{k_{11}}{M} + \frac{k_{22}}{J}\right)\omega^2 + \frac{k_{11}\,k_{22} - k_{12}\,k_{21}}{M\,J} = 0 \qquad [1.68]$$

The solution of equation [1.66] can be carried out graphically. For each value of Ω, the solution of [1.66] is searched for and marked. Hence, four curves are obtained.

The values of natural angular frequencies (ω_P) are obtained as a result of their intersection with the axis of ordinates ($\Omega = 0$). The values of forward whirl (ω_d) are obtained as a result of their intersection with the first bisector line ($\Omega = \omega$), the values of backward whirl (ω_r) as a result of their intersection with the second bisector line ($\Omega = -\omega$).

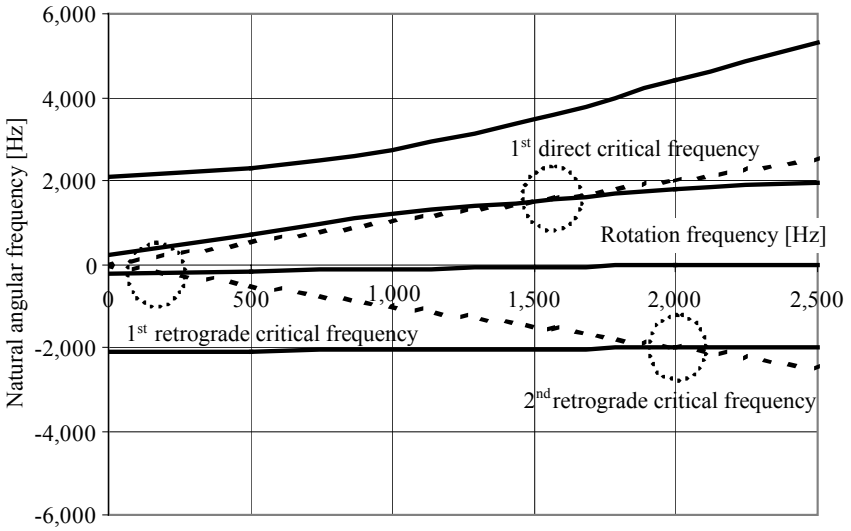

Figure 1.46. *Diagram of critical speeds of the cooling fan*

Note: for this example, the first frequency of the forward precession is at 1,569 Hz and it may be caused by the unbalance.

The natural frequencies corresponding to the backward whirl can be excited only if the excitation has a component which is in the opposite direction of the rotor. This hypothetical case can be the consequence of either a dynamic load applied within a fixed reference and transmitted to the shaft through the pivot link, or a crank-rod system.

Chapter 2

Piston Engines

2.1. Introduction

For terrestrial vehicles, vibratory discomfort is mainly caused by road roughness, wheel unbalances, streamline flow on the vehicle, or drive system. Hence, engines, particularly piston engines, generate disturbing excitations.

Road roughness causes excitations in the frequency band, ranging from 0.5 to 250 Hz. Engine excitations cover a very similar frequency band. Aerodynamic frequencies cover much more sizeable frequencies that can go up to 18,000 Hz.

This chapter will particularly deal with conventional piston engines. Specific engine technologies will not be discussed here.

Typical examples for this kind of application are line shafting of ships, terrestrial vehicles such as cars and trucks, helicopters and aircraft started by a piston engine like the TB 20, manufactured by the SOCATA company.

The installations powered with a piston engine are subjected to torque excitations generated by the effects of sudden variation of the pressure in the combustion chamber, and from the inertial effects of various moving masses. The link between the core engine and its chassis is also subjected to variable loads of the same origin. When the engine is integrated on the chassis, it is necessary to know the loads involved.

Thus, in the case of the SOCATA TB aircraft, the engine is integrated in a cantilever position by a DYNAFOCAL suspension system (see Figure 2.1).

This integration, apart from its esthetic attribute, guarantees a perfect dynamic decoupling between the fuselage and the engine (see Chapter 7), while preserving the properties of lightness. Dimensioning this link was possible by analyzing the dynamic effects coming from the engine.

Figure 2.1. *Engine integration on the SOCATA TB 20. Photo: SOCATA*

2.2. Excitations generated by a piston engine

The moving element of the engine consisting of rods and pistons is one of the first vibratory sources of the engines [BRU 84, RAH 88, OUZ 62, SWO 84, TEC 00]. The objective of this chapter is to illustrate a model that makes the analysis of specific excitations for this type of application possible.

The rod-crank system consists of elements which may be considered to be non-distorting. The links are supposed to be without friction or clearance. Our goal is to determine the visible engine torque provided by a piston engine.

We have (Figure 2.2):

– r: crankshaft eccentricity (crank length),

– L: rod length.

Let the angular position of the crankshaft be:

$$\theta = (\vec{x}_0, \vec{x}_1) = (\vec{y}_0, \vec{y}_1) \text{ with } \omega_{10} = \dot{\theta}(t) \qquad [2.1]$$

Consequently, we will suppose that the speed of rotation of the crankshaft is constant.

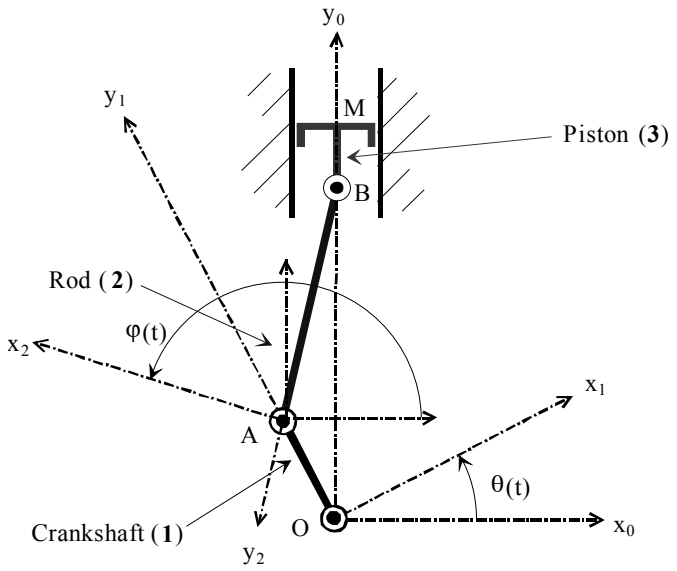

Figure 2.2. *Modeling of a piston-rod-crankshaft system*

2.2.1. *Analytic determination of an engine torque*

We mark Σ the system composed of the rod (3), the piston (2) and the crankshaft (1). The external actions on the system Σ are the actions of the gas on the piston, the pump torque on the crankshaft, and the linkage with the core engine.

The Galilean forces of mechanical actions applied on the system Σ are by definition:

$$\begin{cases} P(\text{receiver} \rightarrow 1/R_g) = \vec{C}_{\text{receiver}\rightarrow 1}.\vec{\Omega}_{1/0} = -C_r\ \omega_{10} \\ P(\text{gas} \rightarrow 3/R_g) = \vec{F}_{\text{gas}\rightarrow 3}.\vec{V}_{M,3/Rg} = F_{gas}V \\ P(\text{core engine} \rightarrow \Sigma/R_g) = 0 \end{cases} \quad [2.2]$$

The rotation speed of the crankshaft ω_{10} is linked to the traveling speed V of the piston. In order to obtain this relation, it is sufficient to write the following geometrical relationship:

$$\overrightarrow{OB} = r\vec{y}_1 - L\vec{y}_2 = \left[-r\sin(\theta) + L\sin(\varphi)\right]\vec{x}_0 + \left[r\cos(\theta) - L\cos(\varphi)\right]\vec{y}_0 \quad [2.3]$$

This vector being dependent only on $\vec{y}_0$, we obtain the relationship:

$$-r\sin(\theta) + L\sin(\varphi) = 0 \Rightarrow \sin(\varphi) = \frac{r}{L}\sin(\theta) = \frac{\sin(\theta)}{\lambda} \quad [2.4]$$

with:

$$\lambda = \frac{L}{r} \quad [2.5]$$

After deriving relationship [2.4], we obtain:

$$\cos(\varphi)\ \dot{\varphi} = \frac{\cos(\theta)}{\lambda}\ \dot{\theta} \quad [2.6]$$

If:

$$\dot{\varphi} = \frac{1}{\lambda}\frac{\cos(\theta)}{\cos(\varphi)}\ \dot{\theta} = \frac{1}{\lambda}\frac{\cos\theta}{\sqrt{1-\left(\frac{1}{\lambda}\right)^2\sin^2(\theta)}}\dot{\theta} \quad [2.7]$$

A relationship that will be preserved as follows:

$$\dot{\varphi}(t) = f(\theta)\ \dot{\theta}(t) \quad \text{with} \quad f(\theta) = \frac{r}{L}\frac{\cos(\theta)}{\sqrt{1-\left(\frac{r}{L}\right)^2\sin^2(\theta)}} \quad [2.8]$$

We can calculate the speed of the piston based on the speed of rotation $\dot{\theta}$, with the help of equations [2.3] and [2.8]:

$$\vec{V}_{B,3/0} = V\vec{y}_0 = \left.\frac{d\overrightarrow{OB}}{dt}\right)_{Rg} = \left[-r\,\dot{\theta}\sin(\theta) + L\,\dot{\varphi}\sin(\varphi)\right]\vec{y}_0 \quad [2.9]$$

Based on equation [2.8], let the relationship between the speed of the piston (3) and the rotation speed of the crankshaft (1) be:

$$V = [f(\theta)-1]\ r\sin(\theta)\ \dot{\theta} \quad [2.10]$$

We notice that the speed ratio is not sinusoidal, but that it is modulated by the function $\left(f(\theta)-1\right)$.

We mark by $T\left(S/R_g\right)$ the kinetic energy of the system Σ with respect to the inertial frame:

$$T\left(\Sigma/R_g\right) = T\left(\text{rod}/R_g\right) + T\left(\text{piston}/R_g\right) + T\left(\text{crankshaft}/R_g\right) \quad [2.11]$$

The inertial effects of the rod (2) and of the crankshaft (1) are ignored:

$$\begin{cases} T\left(3/R_g\right) = \frac{1}{2}MV^2 = \frac{1}{2}M\left[f(\theta)-1\right]^2 r^2 \sin^2(\theta)\dot{\theta}^2 \\ T\left(2/R_g\right) = 0 \\ T\left(1/R_g\right) = 0 \end{cases} \quad [2.12]$$

Hence, supposing that the speed of rotation is constant:

$$\frac{d}{dt}\left(T\left(\Sigma/R_g\right)\right) = g(\theta)\ M\ r^2\ \dot{\theta}^3 \quad [2.13]$$

with:

$$g(\theta) = \left[f(\theta)-1\right]\sin(\theta)\left(f'(\theta)\sin(\theta) + \left[f(\theta)-1\right]\cos(\theta)\right) \quad [2.14]$$

The theorem of kinetic energy applied to the system Σ makes it possible to establish the relationship linking the resisting torque to the gas effects. Hence:

$$\frac{d}{dt}\left(T(\Sigma/R_g)\right) = \sum p\left(\text{external} \rightarrow \Sigma/R_g\right) \quad [2.15]$$

if:

$$C_r(\theta) = \underbrace{[f(\theta)-1]\ \sin(\theta)\ r\ F_{gas}}_{\text{gas effects}} - \underbrace{g(\theta)\ M\ r^2\ \dot{\theta}^2}_{\text{inertial effects}} \quad [2.16]$$

We notice the following:

– the torque is variable during a turn because it represents the position θ and the gas action which occurs only during combustion,

– the torque represents the overlapping of gas action and inertial effects. It is the gas part that generates a medium non-zero torque.

We will draw the value of the instantaneous torque C_r for two turns in Figure 2.4. The shape of the gas pressure during one work cycle is illustrated in Figure 2.3.

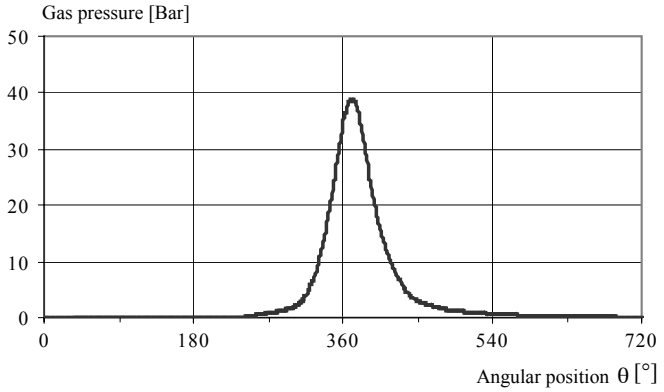

Figure 2.3. *Gas pressure according to the angular position of the crankshaft*

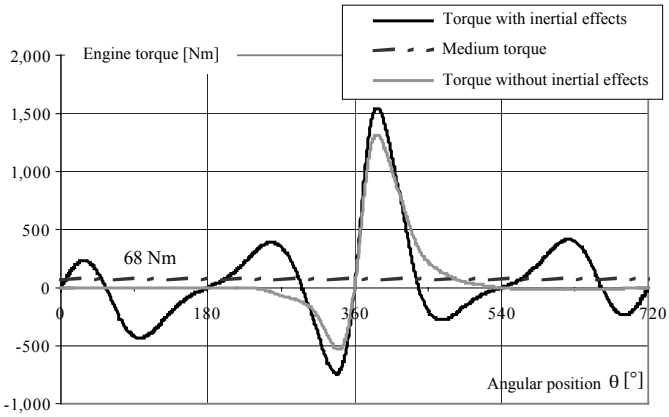

Figure 2.4. *Monocylinder engine torque with inertial effects*

The same analysis can be carried out for a multicylinder engine. The visible torque at the engine output is the total sum of the torques provided by each piston.

Thus, for a four cylinder engine, we have drawn the value of the torque according to the angular position of the crankshaft for one work cycle (Figure 2.5).

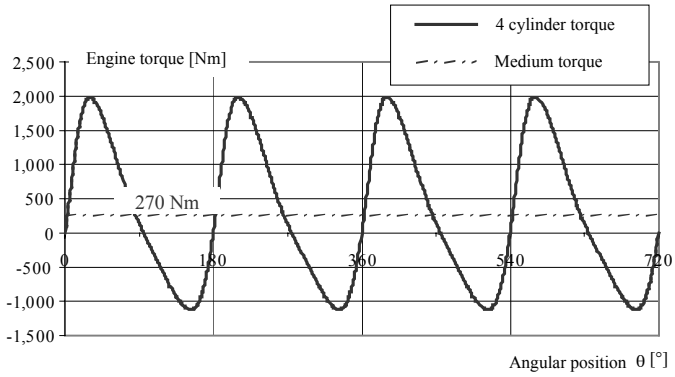

Figure 2.5. *Engine torque for a four cylinder engine with inertial effects*

2.2.2. *Engine excitations on the chassis frame*

It is important to keep in mind that there are other excitations at the origin of the vibrations generated by the engine and, in particular, those that pass through the link between the engine and the chassis.

Hence, we can provide a few definitions used to describe these loads which are defined according to the axis of rotation of the engine.

By definition, and using the definition of axes given in Figure 2.6, the resultant projection on $\vec{x}_0$ is called a shaking or dangling load and that on $\vec{y}_0$ is called a knocking load.

The torque around $\vec{x}_0$ is called galloping or pitch torque (*pitching*), that around $\vec{y}_0$ is called a yaw torque (*yawing*) and that around $\vec{z}_0$ is called a tilt or roll torque (*rolling*).

To determine components in the resultant and torque of the mechanical action of the piston-rod-crankshaft system, it is sufficient to isolate the group Σ. If we ignore the mass of rod 2, we can write:

$$\begin{cases} m(\Sigma)\ \vec{A}_{G_\Sigma,\Sigma/R_g+} = \vec{R}(\text{chassis frame} \to \Sigma) + \vec{R}(\text{receiver} \to \Sigma) + \vec{R}(\text{gas} \to \Sigma) \\ \vec{\delta}_O\left(\Sigma / R_g\right) = \vec{M}_O(\text{chassis frame} \to \Sigma) + \vec{M}_O(\text{receiver} \to \Sigma) + \vec{M}_O(\text{gas} \to \Sigma) \end{cases} \quad [2.17]$$

We intend to develop only knocking and galloping actions.

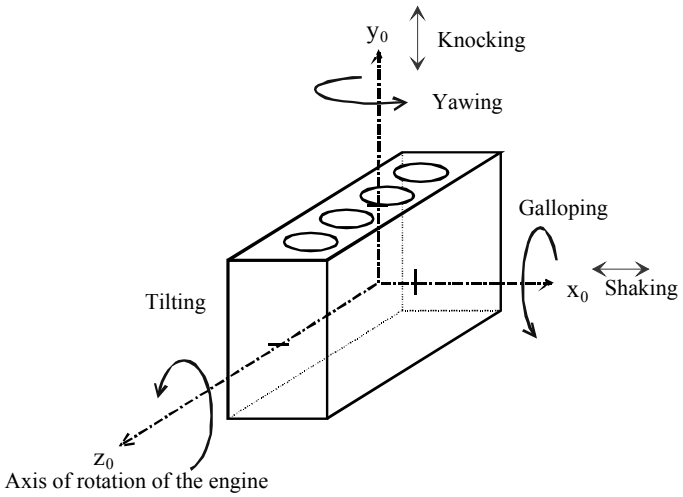

Figure 2.6. *Benchmark associated with the engine*

2.2.2.1. *Knocking load*

For a monocylinder engine, the resultant equation derived from equation [2.17] in projection on y_0 is given by:

$$M\ \vec{A}_{M.3/R_g} \cdot \vec{y}_0 = \vec{R}(\text{chassis frame} \rightarrow \Sigma) \cdot \vec{y}_0 + \vec{R}(\text{gas} \rightarrow \Sigma) \cdot \vec{y}_0 \qquad [2.18]$$

Or, by definition, the knocking load is defined by:

$$F_p = \vec{R}(\text{chassis frame} \rightarrow \Sigma) \cdot \vec{y}_0 \qquad [2.19]$$

In addition, we can show that the gas action is, because of the principle of reaction-counter reaction:

$$\vec{R}(\text{gas} \rightarrow \Sigma) \cdot \vec{y}_0 = 0 \qquad [2.20]$$

Hence, the analysis of equation [2.18] leads to:

$$F_p = M\ \vec{A}_{M.3/R_g} \cdot \vec{y}_0 \qquad [2.21]$$

and using the results from [2.10], we obtain:

$$\vec{A}_{M.3/R_g}.\vec{y}_0 = \frac{d\,V}{dt} = r\,h(\theta)\,\dot{\theta}^2 \qquad [2.22]$$

with:

$$h(\theta) = \left[-\cos(\theta) + \left(\frac{d\,f(\theta)}{d\theta}\,\sin(\theta) + f(\theta)^2 \sqrt{1-\left(\frac{r}{L}\right)^2\,\sin(\theta)^2} \right) \right] \qquad [2.23]$$

Therefore, based on [2.21] and [2.22], the knocking action is defined by:

$$F_p = h(\theta)\,M\,r\,\dot{\theta}^2 \qquad [2.24]$$

We notice that this action is linked to the action of inertial effects of mobile elements (only the piston in our case). Hence, we can draw the shape of the knocking load F_p for two turns (Figure 2.7). The cyclic variations of this type of action can easily be observed.

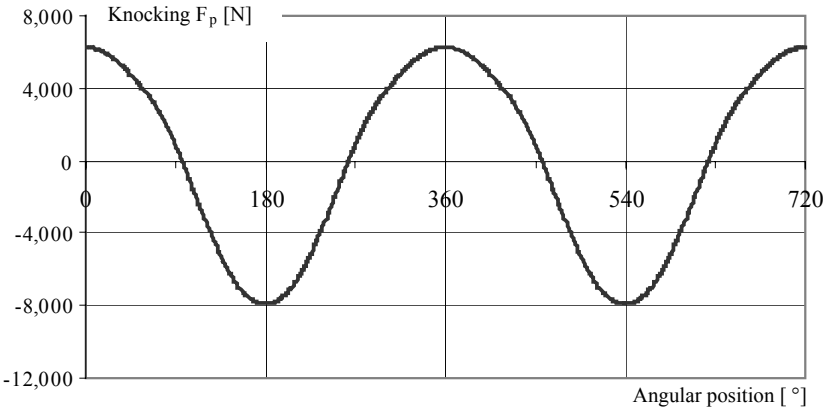

Figure 2.7. *Knocking loads for a monocylinder engine with inertial effects*

For a multi-cylinder engine, the knocking load is the sum of actions coming from each one of the cylinders. The engine geometry (four flat cylinders, four cylinders in V, etc.) has a crucial role in this overlapping of effects.

We will analyze a four flat cylinder engine (Figure 2.8).

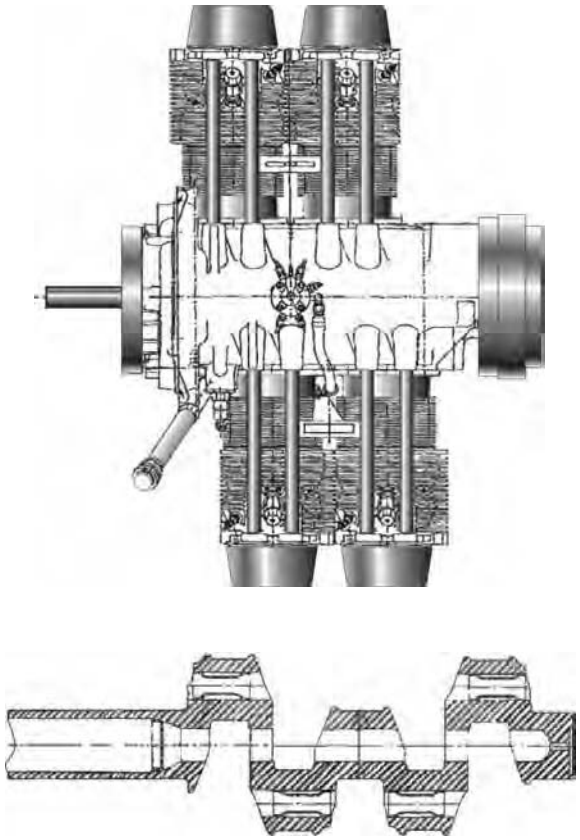

Figure 2.8. *Example of a four flat cylinder engine and the associated crankshaft. Photo: C. Guarnieri (Eurocopter)*

For this type of engine, it is possible to notice that the effects of each cylinder compensate each other. The overall knocking load is zero.

An analogical study can be carried out for the other actions too (galloping, shaking, yawing, etc.). The relationship between the chassis and the engine must be determined based on these results (see Chapter 7).

2.2.2.2. *Pitch torque*

We mark:

– a: the distance between cylinders 1 and 2, and cylinders 3 and 4,

– 2 a: the distance between cylinders 2 and 3,

– O: the geometrical center of the crankshaft belonging to the median plane.

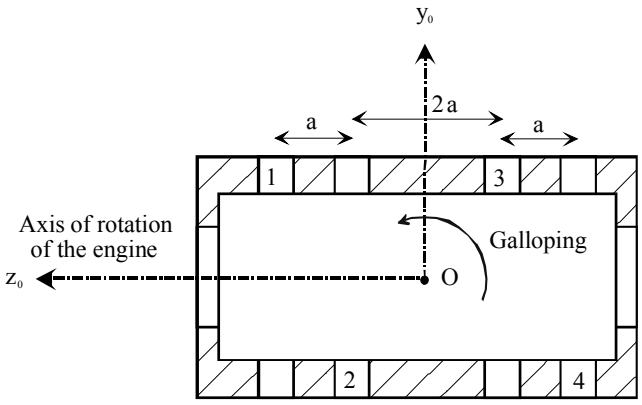

Figure 2.9. *Position of the cylinders on a four flat cylinder engine*

Hence,

$$\begin{aligned}\left(C_{galloping}\right)_{n^{th}order} = a\,A_n\,M\,r\,[2\cos(n\,\theta) - \cos(n\,(\theta+\pi)) + \ldots \\ \ldots - \cos(n\,(\theta+2\pi)) + 2\cos(n\,(\theta+3\pi))]\,\dot{\theta}^2\end{aligned} \quad [2.25]$$

We notice that, following the harmonics order n, the actions have different amplitudes. Thus:

$$\begin{aligned}&\text{order 1} \quad \left(C_{galloping}\right)_1 = 0 \\ &\text{order 2} \quad \left(C_{galloping}\right)_2 = 2a\,A_2\,M\,r\cos(2\theta)\,\dot{\theta}^2 \\ &\text{order 3} \quad \left(C_{galloping}\right)_3 = 0 \\ &\text{order 4} \quad \left(C_{galloping}\right)_4 = 2a\,A_4\,M\,r\cos(4\theta)\,\dot{\theta}^2\end{aligned} \quad [2.26]$$

2.2.2.3. *Review of actions for a four phase cylinder engine*

Shaking	Knocking	Yawing	Galloping
0			Order 1 = 0
			order 2 = A_2 M r $\left[2 \text{ a } \cos(2\theta)\right] \dot{\theta}^2$
			order 4 = $-A_4$ M r $\left[2 \text{ a } \cos(4\theta)\right] \dot{\theta}^2$

Table 2.1. *Review of excitations for a four flat cylinder engine*

2.2.3. *The notion of engine balancing*

The actions analyzed above can be minimized by balancing the engine. This can be done by adding masses to the system in motion in order to create inertial effects which can counteract the problematic effects.

Nevertheless, to define the masses to be added, it is necessary to analyze in the best possible way the cyclic character of mechanical actions. We intend to illustrate this through the study of knocking or galloping.

2.2.3.1. *Balancing the knocking loads*

2.2.3.1.1. The case of a monocylinder engine

The results of equation [2.24] showed that the knocking load for a monocylinder engine has the following form:

$$F_p = M \, \vec{A}_{M.3/R_g} \cdot \vec{y}_0 - \vec{R}(\text{gas} \rightarrow \Sigma) \cdot \vec{y}_0 \qquad [2.27]$$

Hence, the study of the cyclic character can be carried out through the study of piston acceleration.

The effects of the gas actions are zero [2.20].

Therefore, according to the definition of a piston point position [2.3] and using equation [2.4]:

$$\overrightarrow{OB}\cdot\vec{y}_0 = r\cos(\theta) + L\sqrt{1+\left(\frac{1}{\lambda}\right)^2 \sin(\theta)^2} \qquad [2.28]$$

If we suppose that the rod ratio L is large, then we can break it down using limited expansions:

$$\overrightarrow{OB}\cdot\vec{y}_0 = r\cos(\theta) + L\left(1-\frac{1}{2}\frac{\sin(\theta)^2}{\lambda^2}-\frac{1}{8}\frac{\sin(\theta)^4}{\lambda^4}-\frac{1}{16}\frac{\sin(\theta)^6}{\lambda^6}+\cdots\right) \qquad [2.29]$$

By using the properties of trigonometric functions, it is shown that:

$$\overrightarrow{OB}\cdot\vec{y}_0 = r\cos(\theta)+\ldots \\ \ldots+L\left(\left[1-\frac{1}{4}\left(\frac{1}{\lambda}\right)^2+\ldots\right]+\left[\frac{1}{4}\left(\frac{1}{\lambda}\right)^2+\frac{1}{16}\left(\frac{1}{\lambda}\right)^4+\ldots\right]\cos(2\theta)+\cdots\right) \qquad [2.30]$$

By derivation, we obtain:

$$\vec{A}_{B.3/R_g}.\vec{y}_0 = -r\left[\cos(\theta)+\left(\left[\left(\frac{1}{\lambda}\right)+\frac{1}{4}\left(\frac{1}{\lambda}\right)^3+\ldots\right]\cos(2\theta)+\ldots\right)\right]\dot{\theta}^2 \qquad [2.31]$$

In fact, the knocking load is represented by:

$$F_p = M\,r\left[\cos(\theta)+\left(\left[\left(\frac{1}{\lambda}\right)+\frac{1}{4}\left(\frac{1}{\lambda}\right)^3+\ldots\right]\cos(2\theta)+\ldots\right)\right]\dot{\theta}^2 \qquad [2.32]$$

if:

$$F_p = M\,r\left[A_1\cos(\theta)+A_2\cos(2\theta)+\ldots\right]\dot{\theta}^2 \qquad [2.33]$$

We notice that, if the engine turns at a constant rotation speed Ω, the knocking load is cyclic in 1Ω, 2Ω, 3Ω, 4Ω, etc.

To perfectly balance the system, each order has to be balanced separately according to the principle of equivalence between an alternative mass and two rotary masses. Hence, for a knocking load of order n, we can place two masses, generally equal, on two balancing shafts turning at n times the speed of the crankshaft, as shown in Figure 2.10.

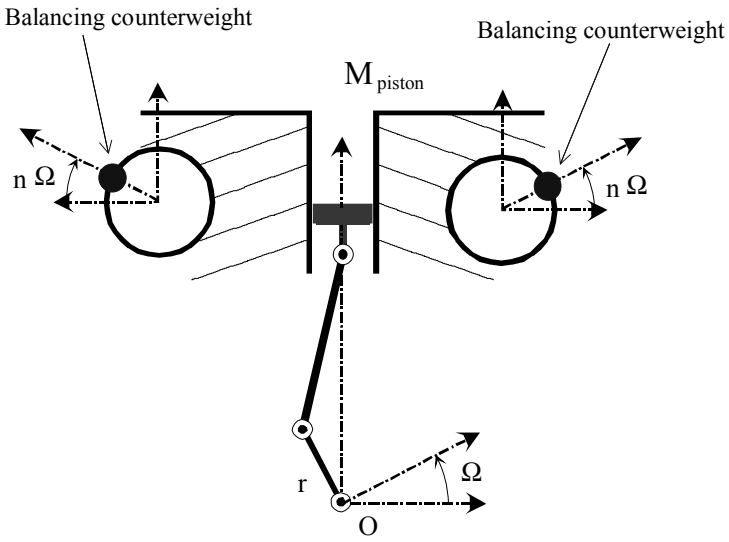

Figure 2.10. *Balancing of knocking load of the order n*

If this method is used for the second order, it is called the Lanchester method [SWO 84].

2.2.3.1.2. The case of a four flat cylinder engine

The knocking load of order n for a four flat cylinder engine will be:

$$\left(F_p\right)_{n^{th}\text{order}} = \sum_{j=0}^{3} A_n \; M\, r\left[\cos\left(n(\theta + j\,\pi)\right)\right] \dot{\theta}^2 \qquad [2.34]$$

Hence, it is shown that:

$$\left(F_p\right)_{n^{th}order} = 0 \qquad [2.35]$$

For a four flat, four phase cylinder engine the knocking loads are zero, irrespective of the order.

2.2.3.2. *Balancing the galloping torque*

The galloping torque of order n can be balanced by rotating two shafts of the off-centered center of inertia set in opposing phase and rotating in the opposite direction to the speed $n\,\Omega$ [SWO 84].

These shafts must rotate parallel to the crankshaft. The setting of the shafts must be adjusted to the angular position of the crankshaft.

Due to the complexity of this solution in most applications, this type of balancing is usually avoided. The disturbing effect of the galloping torque is compensated by the suspension of the engine on the chassis frame.

2.3. Line shafting tuning

2.3.1. *The notion of tuning*

The engine is by all means a part of the power transmission chain. This fact has certain consequences.

In particular, it is important to analyze the correspondence between the excitations in the engine torque and the behavior of the set of elements of the transmission chain. This analysis is called line shafting tuning.

Wrong tuning is usually the cause of gear, key and generally line shafting damage.

A clear example of this type of problem is a small helicopter powered by a piston engine.

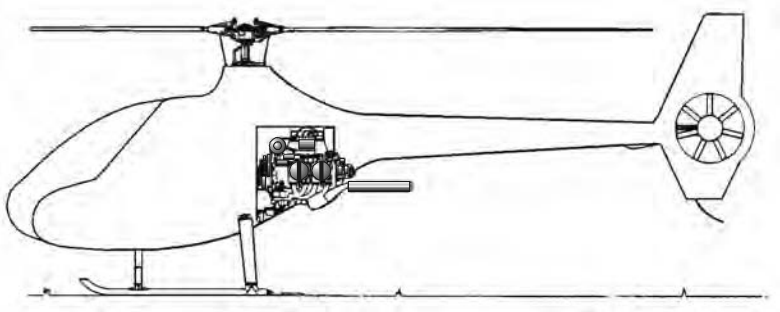

Figure 2.11. *Two-seater helicopter powered by a piston engine (photo: C. Guarnieri, Eurocopter)*

The transmission chain consists of a heat engine, long shafts, gears, pulleys, belts and rotors (main and tail).

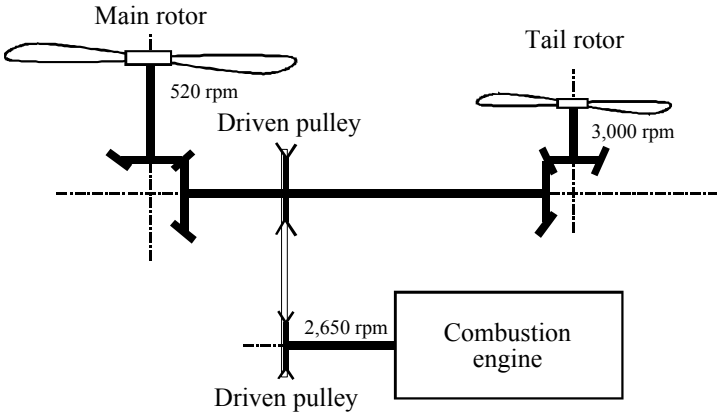

Figure 2.12. *Diagram of the transmission chain*

2.3.2. *Creation of the equations*

The industrial models used for this type of analysis are usually analytical. They consist of determining the number of degrees of freedom, inertia, and twist stiffness which make it possible to cover the corresponding frequency band.

For this application, the degrees of freedom selected are illustrated in Figure 2.13 and Figure 2.14.

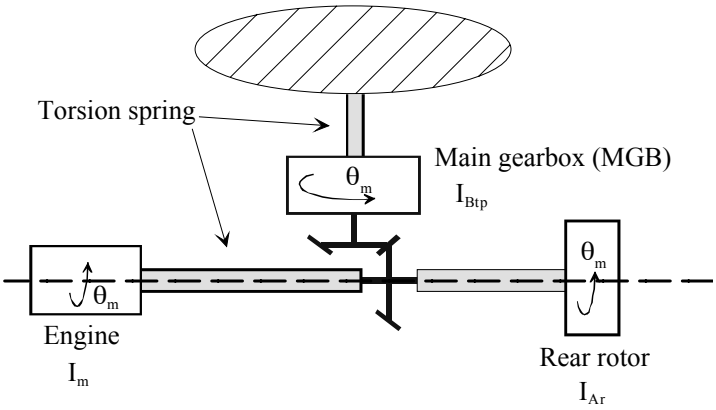

Figure 2.13. *Modeling of the transmission chain*

The search for the equations of motions can be performed with the help of the Lagrange equation method for the case of b blades.

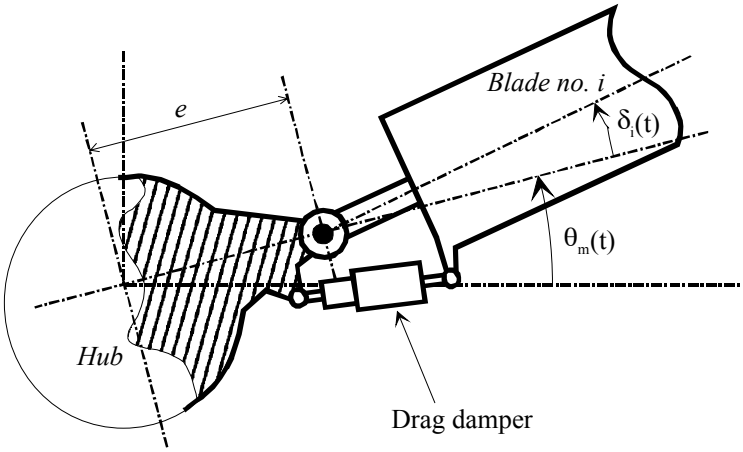

Figure 2.14. *Modeling of the main rotor: example of a blade*

Thus, we can define the kinetic energies of different elements of the system:

$$\begin{cases} T(\text{Blade no. i}/R_g) = \dfrac{1}{2}\left[I_\delta \ \dot{\delta}_i^2 + 2(e\ m_s + I_\delta)\ \dot{\theta}_m \ \dot{\delta}_i \right] \\ T(\text{Hub}/R_g) = \dfrac{1}{2} I_m \ \dot{\theta}_m^2 \\ T(\text{Tail rotor}/R_g) = \dfrac{1}{2} I_{Ar} \ \dot{\theta}_{Ar}^2 \\ T(\text{Engine}/R_g) = \dfrac{1}{2} I_{Btp} \ \dot{\theta}_{Btp}^2 \end{cases} \quad [2.36]$$

with:

– I_δ: blade drag inertia in the pivot point,

– m_s: blade static moment in the pivot point,

– e: pivot eccentricity,

– I_m: hub inertia,

– I_{Ar}: inertia of the tail rotor,

– I_{Btp}: equivalent inertia of the main transmission unit.

We can define the potential energy linked to the torsion springs and the drag dampers:

$$\begin{cases} U\left(\text{Rotor} \rightarrow \text{MGB}/R_g\right) = \dfrac{1}{2} K_{hm} \left(\theta_{MGB} - \theta_{mr}\right)^2 \\ U\left(\text{Tail rotor} \rightarrow \text{MGB}/R_g\right) = \dfrac{1}{2} K_{Ar} \left(\theta_{MGB} - \theta_{Ar}\right)^2 \\ U\left(\text{Engine} \rightarrow \text{MGB}/R_g\right) = \dfrac{1}{2} K_m \left(\theta_{MGB} - \theta_{engine}\right)^2 \\ U\left(\text{Blade no. i} \rightarrow \text{Hub}/R_g\right) = \dfrac{1}{2} K_\delta \ {\delta_i}^2 \end{cases} \quad [2.37]$$

with:

– K_{hm}: equivalent stiffness of the main shaft between the rotor and MGB,

– K_{Ar}: equivalent stiffness of the transmission shafts to the tail rotor,

– K_m: equivalent stiffness of the transmission shafts between the engine and the MGB,

– K_δ: equivalent stiffness of the drag damper.

With the help of Lagrange equations, we can obtain the equations of motion which have been put in a matrix form:

$$M\,\ddot{X} + K\,X = F \qquad [2.38]$$

with the position vector and the excitation vector:

$$X = \begin{Bmatrix} \delta \\ \theta_m \\ \theta_{Ar} \\ \theta_{Btp} \end{Bmatrix} \qquad K = \begin{Bmatrix} 0 \\ 0 \\ 0 \\ K_m\ \theta_m \end{Bmatrix} \qquad [2.39]$$

and the matrices:

$$M = \begin{bmatrix} b\,I_\delta & b\,(I_\delta + e\,m_s) & 0 & 0 \\ b\,(I_\delta + e\,m_s) & I_{mr} & 0 & 0 \\ 0 & 0 & I_{Ar} & 0 \\ 0 & 0 & 0 & I_{MGB} \end{bmatrix} \qquad [2.40]$$

$$K = \begin{bmatrix} b\left(K_\delta + e\,m_s\,\Omega^2\right) & 0 & 0 & 0 \\ 0 & K_{hm} & 0 & -K_{hm} \\ 0 & 0 & K_{Ar} & -K_{Ar} \\ 0 & -K_{hm} & -K_{Ar} & (K_{hm} + K_{Ar} + K_m) \end{bmatrix} \qquad [2.41]$$

The analysis of equations [2.38] makes it possible to calculate the natural frequencies of the system.

The risk is to obtain natural frequencies close to the excitation frequencies of the rotor. The choice of engine and of transmission parameters makes it possible to optimize tuning of the frequencies.

2.3.3. *Line shafting optimization*

2.3.3.1. *Results for a non-optimized line shafting*

The Campbell diagram (Figure 2.15) enables us to identify the evolution of natural frequencies based on the rotation speed of the engine, and thus to analyze the

tuning. For the chosen application, the engine is set at 2,650 rpm ±5% (Ω_N). We notice that the third torsion mode can be excited by the second harmonics of the rotation speed. This can lead to very strong oscillations of the dynamic chain, and to destruction of the most loaded elements.

Hence, we notice that for these data there is a coincidence between the excitation frequencies of the piston engine and the resonant frequencies of the system.

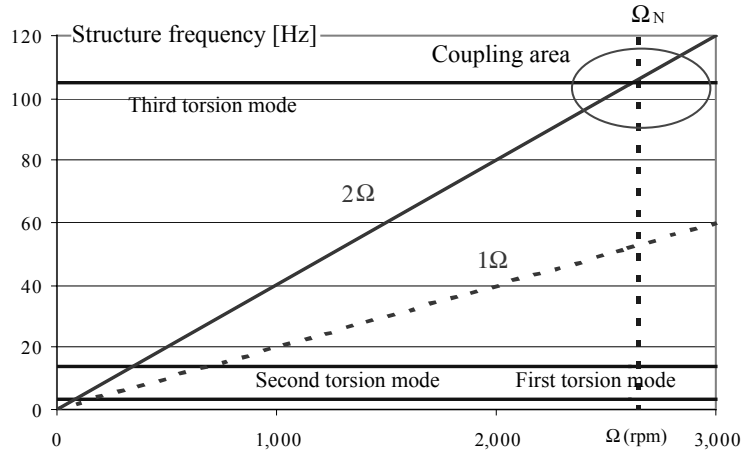

Figure 2.15. *Campbell diagram for a non-optimized line shafting*

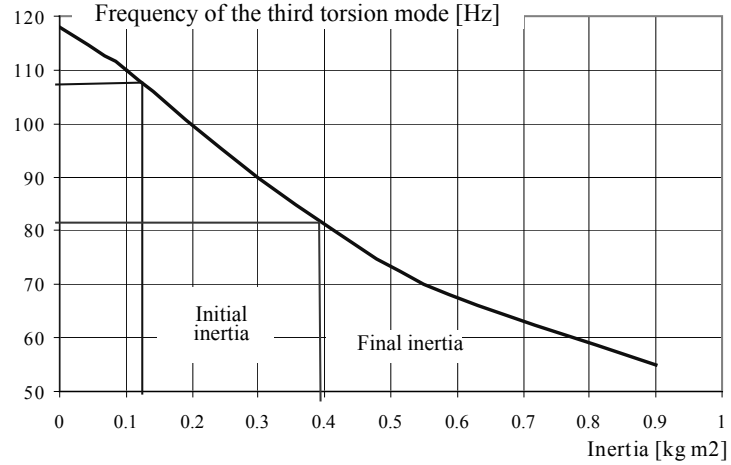

Figure 2.16. *Inertial influence on the position of the third torsion mode*

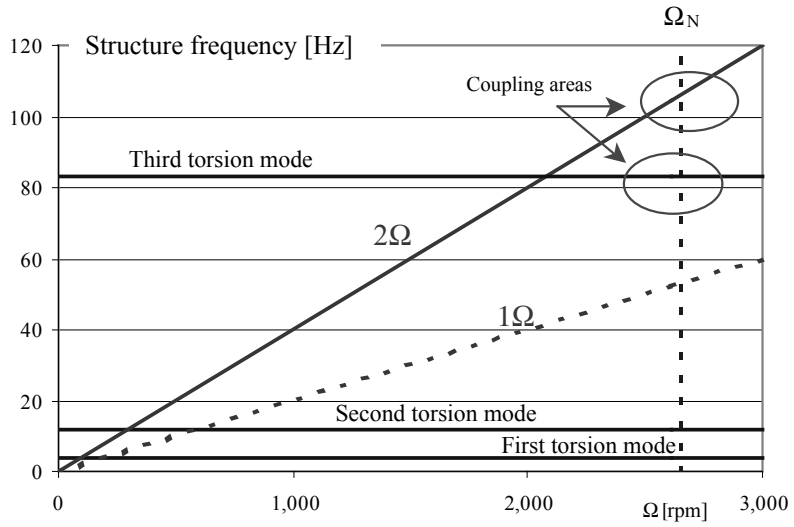

Figure 2.17. *Campbell diagram for an optimized system*

2.3.3.2. *Results for an optimized line shafting*

When considering the risk of resonance, the manufacturer has to rethink the design of his product. It is important to carry out parametric scanning in order to determine the physical parameters of the mechanical system, which induce disturbing torsion frequency.

The example of the previous kinematic diagram illustrates this strategy. Figure 2.16 shows the inertial influence of the driven pulley on the position of the third natural torsion frequency.

Following a dynamic study, the inertial value of the driven pulley was increased, which makes it possible to decrease the third critical frequency.

Figure 2.17 shows the final position of torsion frequencies after the increase of inertia of the driven pulley.

Chapter 3

Dynamics of a Rotor

3.1. Introduction

Helicopters, certain aircraft and ships, as well as industrial ventilation systems are driven by propellers. In the aeronautical field, they are usually called rotors.

These rotors produce very specific vibrations which require a very detailed analysis. We will analyze this type of excitation for a helicopter rotor which, due to its complexity, represents a general case covering the entire set of various applications. The helicopter is a complex structure subjected to a variety of flight conditions: hovering flight, ascending or descending forward flight, etc.

The study of forward flight is sufficient to analyze the dynamic behavior of a rotor: the aerodynamic excitations are variable. They are then transmitted to the cabin through the links between the main transmission unit and the fuselage. These aerodynamic excitations have important consequences on the comfort and functioning of mechanical parts.

3.2. Description of the blade/hub relationship

3.2.1. *Some historical data*

In 1784, at the Science Academy, Launoy and Beinvenue built a model capable of lifting itself into the air thanks to a vertical axis propeller [LIB 98].

Gustave de Ponton d'Amecourt was the first to invent the term "helicopter", derived from the Greek words *hélix* and *pteron*, which mean "propeller blades". He was also the first to explain the fundamental principles of aerodynamics and flight mechanics applied to a helicopter.

The models used, with coaxial rotors in order to counteract the torque effect, were firstly motorized by a spring, and then by a steam engine. Since they were too heavy, it was only in 1877 that a model of this type, manufactured by Forlanini, managed to fly for around 20 seconds.

Then, at the beginning of the 20th century, the Breguet brothers and others built machines meant to be controlled by a pilot.

In 1907, the device built by Paul Cornu left the ground with a pilot inside it and did not have any contact with the ground. Nevertheless, the flight was short because the engine was not very reliable or easy to handle.

The Breguet brothers carried out a lot of work before the First World War. In 1941, Ygor Sikorsky manufactured the first mass production helicopter. The architecture of this machine, an R-4 model, is at the origin of all modern devices.

The rotor has a fundamental role in the functioning of a helicopter. Hence, the link between the blades and the rotor hub has always been a very important subject of study. The introduction of these hinges and their technology led to the existence of many rotor concepts. We will analyze a few examples.

3.2.2. Hinge link of the blade and the hub

On a helicopter rotor it is very important to have a link between the blade and the hub composed of three rotations [GES 99, LEG 68] (see Chapter 4). These can be materialized either by three hinges (articulated rotor), or by obtaining the same degrees of freedom of motion from flexible link elements for bending and torsion and rigidity for traction (hingeless rotor).

One of the rotations is imposed by the pilot. It corresponds to the natural rotation of the blade around its longitudinal axis which thus controls the pitch. The other two possible rotations are called drag and flapping. They are related to the aerodynamic loads applied to the lead-lag of the blade during motion.

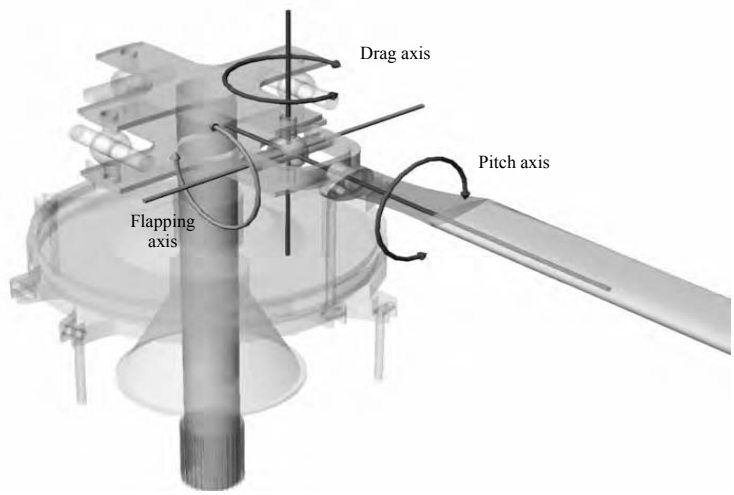

Figure 3.1. *Motion axes of the blade*

3.2.2.1. *Formation of the equations for blade motion*

3.2.2.1.1. Definition of coordinates and parametric transformation

The coordinates and the parametric transformation are shown in Figure 3.2.

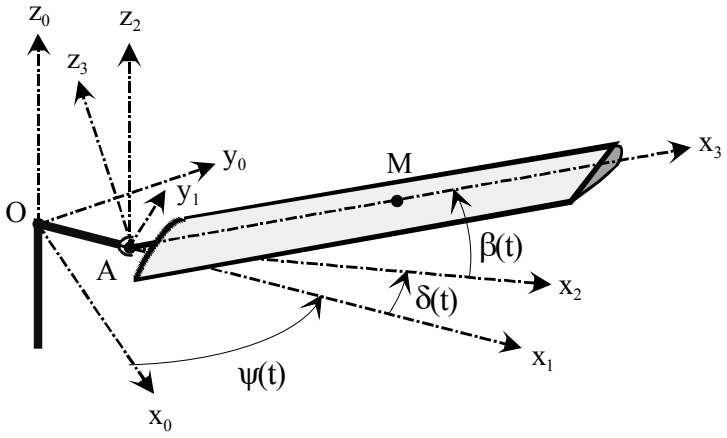

Figure 3.2. *Parametric transformation of blade motion*

The blade motion with respect to the coordinates of the fuselage (R_σ in this study) is defined by:

$$\psi(t) = (\widehat{\vec{x}_0,\vec{x}_1}) = (\widehat{\vec{y}_0,\vec{y}_1}) \text{ rotation angle of the rotor,}$$

$$\delta(t) = (\widehat{\vec{x}_1,\vec{x}_2}) = (\widehat{\vec{y}_1,\vec{y}2}) \text{ lag angle,} \qquad [3.1]$$

$$\beta(t) = (\widehat{\vec{x}_2,\vec{x}_3}) = (\widehat{\vec{z}_2,\vec{z}_3}) \text{ flap angle.}$$

The coordinate $R_g = (O,\vec{x}_0,\vec{y}_0,\vec{z}_0)$ is considered an inertial frame and the coordinate $R_3 = (A,\vec{x}_3,\vec{y}_3,\vec{z}_3)$ is linked to the blade.

We note the geometrical quantities:

$$\begin{aligned} \overrightarrow{OA} &= e\,\vec{x}_1 \\ \overrightarrow{AM} &= r\,\vec{x}_3 \end{aligned} \qquad [3.2]$$

The speed of point M of the blade is given by:

$$\begin{aligned} \vec{V}_{M,blade/R_g} &= \frac{d\overrightarrow{OM}}{dt} = e\frac{d\vec{x}_1}{dt}\Big)_{R_g} + r\frac{d\vec{x}_3}{dt}\Big)_{R_g} \\ &= e\,\Omega\,\vec{y}_1 + r(\dot{\delta}+\Omega)\cos(\beta)\,\vec{y}_2 - r\,\dot{\beta}\,\vec{z}_3 \end{aligned} \qquad [3.3]$$

For this study we have the following hypotheses:

– flap eccentricity and drag eccentricity are negligible,

– flap inertia and lag inertia are identical.

The equation of small flapping or drag is obtained with the help of the Lagrange equation method. Thus, the Galilean kinetic energy of the blade can be defined by:

$$T(blade/R_g) = \int_{blade} \frac{1}{2}\vec{V}^2_{M,blade/R_g}\,dm \qquad [3.4]$$

Let:

$$T(\text{blade}/R_g) = \int_{\text{blade}} \frac{1}{2} \left(e\Omega\, \vec{y}_1 + r\,(\dot{\delta} + \Omega) \cos(\beta)\, \vec{y}_2 - r\,\dot{\beta}\, \vec{z}_3 \right)^2 dm \qquad [3.5]$$

Let:

$$\begin{aligned} T(\text{blade}/R_g) = {} & \frac{1}{2}\left(m_p\, e^2\, \Omega^2 + I_p (\dot{\delta} + \Omega)^2\, \cos^2(\beta) + I_p\, \dot{\beta}^2 \right) + \ldots \\ & + e m_s\, \Omega(\dot{\delta} + \Omega) \cos(\beta) \cos(\delta) - m_s e\, \Omega\, \dot{\beta} \sin(\beta)\, \sin(\delta) \end{aligned} \qquad [3.6.]$$

with:

– I_p: flap or lag inertia of the rotor with respect to the hinge,

– m_p: blade mass,

– m_s: static moment,

– *e*: rotor eccentricity.

The potential function associated with the action of the drag damper (modeled by two different springs for flapping and lag) has the following form:

$$U(\text{adapter} \rightarrow \text{blade}/R_g) = \frac{1}{2} K_\beta\, \beta^2 + \frac{1}{2} K_\delta\, \delta^2 \qquad [3.7]$$

with:

– K_β: flapping stiffness of the damper,

– K_δ: lag stiffness of the damper.

3.2.2.1.2. Flapping equation

The generalized loads associated with aerodynamic loads are for parameter β:

$$\begin{aligned} Q_\beta(\text{aero} \rightarrow \text{blade}) &= \vec{M}_0(\text{aero} \rightarrow \text{blade}) \cdot \frac{d\, \vec{\Omega}_{3/0}}{d\dot{\beta}} \Bigg)_0 \\ &= -\vec{M}_0(\text{aero} \rightarrow \text{blade}) \cdot \vec{y}_3 \end{aligned} \qquad [3.8]$$

The momentum in O caused by aerodynamic loads is characterized by:

$$\overrightarrow{M}_A(\text{aero} \rightarrow \text{blade}) \cdot \vec{y}_3 = \int_{\text{blade}} \overrightarrow{AM} \wedge d\vec{F}_{\text{Aero}} \cdot \vec{y}_3 \qquad [3.9]$$

if:

$$\overrightarrow{M}_A(\text{aero} \rightarrow \text{blade}) \cdot \vec{y}_3 = -\int_0^R \frac{1}{2} r^3 \rho \, a \, C_{zp}(r) \, \Omega^2 dr \qquad [3.10]$$

with:

– ρ: air density,

– a: profile chord,

– C_{zp}: local lift coefficient.

We assume that the lift coefficient C_{zp} is, within the usage interval, a linear function of the angle of attack i (Figure 3.19).

Taking into account the relative speed of the wind, the angle of attack of the blade is defined through the analysis of the relative speed of the wind:

$$\begin{aligned} \vec{V}_{M,\text{blade/air}} &= \vec{V}_{M,\text{blade/hub}} + \vec{V}_{M,\text{hub/fuselage}} + V_{M,\text{fuselage/air}} \\ &= -r\,\dot{\beta}\,\vec{z}_1 + (e + r\cos(\beta))\,\Omega\,\vec{y}_1 + \vec{V}_{M,\text{fuselage/air}} \end{aligned} \qquad [3.11]$$

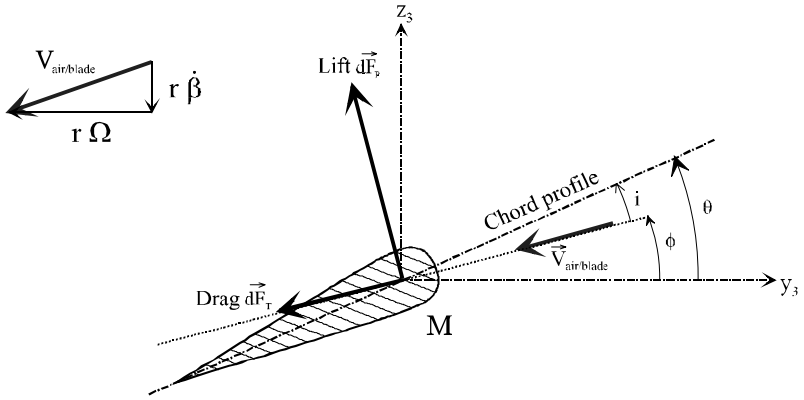

Figure 3.3. *Diagram of the air speed angle of attack for a blade in hovering flight*

Considering all quantities brought into play and ignoring the induced speed, we can have the following approximation:

$$\vec{V}_{M,blade/air} \approx -r\,\dot{\beta}\,\vec{z}_1 + r\,\Omega\,\vec{y}_1 \qquad [3.12]$$

Hence, the angle of attack can be defined by:

$$i = \theta - \phi \approx \theta - \frac{r\,\dot{\beta}}{r\,\Omega} \qquad [3.13]$$

Therefore, the expression of lift is defined by:

$$C_{zp}(r) = \frac{\partial C_p}{\partial i} i = \frac{\partial C_p}{\partial i}\left(\theta - \frac{\dot{\beta}}{\Omega}\right) \qquad [3.14]$$

We assume that $\frac{\partial Cp}{\partial i}$ is constant along the blade. After integration of the blade, equation [3.10] then becomes:

$$\left|\overrightarrow{M}_A(aero \rightarrow blade).\vec{y}_3\right| = M_{aero/\beta} = \frac{1}{2}\rho\, a \frac{\partial C_p}{\partial i}\left(\theta - \frac{\dot{\beta}}{\Omega}\right)\Omega^2 \frac{R^4}{4} \qquad [3.15]$$

We call γ Lock's number, representing the ratio between aerodynamic loads and inertial loads:

$$\gamma = \frac{\rho\, a}{I_p}\frac{\partial C_p}{\partial i} R^4 \qquad [3.16]$$

Thus, the moment due to aerodynamic loads in A following $\vec{x}_1$ is written:

$$M_{aero/\beta} = \frac{\gamma I_p \Omega^2}{8}\left(\theta - \frac{\dot{\beta}}{\Omega}\right) \qquad [3.17]$$

Therefore, the flapping equation is given by:

$$I_p\ \ddot{\beta} + \frac{\gamma I_p \Omega^2}{8}\dot{\beta} + \left((I_p + m_s\ e)\ \Omega^2 + K_\beta\right)\ \beta = \frac{\gamma I_p \Omega^2}{8}\theta \qquad [3.18]$$

The flapping angular frequency of the blade is defined by:

$$\omega_\beta{}^2 = \left(1 + \frac{e\ m_s}{I_p}\right)\ \Omega^2 + \frac{K_\beta}{I_p} \qquad [3.19]$$

We assume that flapping stiffness is very low if $K_\beta = 0$. In addition, for a blade of constant mass per unit length, we have:

$$\frac{e\ m_s}{I_p} = \frac{3}{2}\left(\frac{e}{R - e}\right) \qquad [3.20]$$

Then the natural angular frequency becomes:

$$\omega_\beta = \Omega\sqrt{1 + \frac{3}{2}\left(\frac{1}{\left(\frac{R}{e} - 1\right)}\right)} \approx \Omega\sqrt{1 + \frac{3}{2}\frac{e}{R}} \qquad [3.21]$$

Note that the natural angular frequency is proportional to the rotation speed of the rotor. The R/e ratio is generally high; in fact we can say that the flapping angular frequency is close to the rotation speed Ω. The blade performs a flapping movement (ascent and descent), which is called a flapping cyclic motion. Hence, the flapping equation is reduced to:

$$\ddot{\beta} + \frac{\gamma\Omega^2}{8}\dot{\beta} + \Omega^2\ \beta = \frac{\gamma\Omega^2}{8}\theta \qquad [3.22]$$

For the sake of piloting needs, the pitch has the following form (see Chapter 4):

$$\theta(t) = \theta_0 - \theta_{1c}\ \cos\left(\psi(t)\right) - \theta_{1s}\ \sin\left(\psi(t)\right) \qquad [3.23]$$

The solution of equation [3.22] has the form:

$$\beta(t) = \beta_0 - \beta_{1c}\ \cos\left(\psi(t)\right) - \beta_{1s}\ \sin\left(\psi(t)\right) \qquad [3.24]$$

Note that blade flapping represents a superposition of a static position (β_0) and a cyclic motion of the frequency of rotation of the rotor β_{1c} and β_{1s}.

3.2.2.1.3. Drag equation

The generalized loads associated with the aerodynamic loads for parameter δ are:

$$\begin{aligned} Q_\delta(\text{aero} \rightarrow \text{blade}) &= \vec{M}_0(\text{aero} \rightarrow \text{blade}) \cdot \left.\frac{d\vec{\Omega}_{3/0}}{d\delta}\right)_0 \\ &= \vec{M}_0(\text{aero} \rightarrow \text{blade}) \cdot \vec{z}_1 \end{aligned} \qquad [3.25]$$

The moment in O caused by aerodynamic loads is characterized by:

$$\vec{M}_A(\text{aero} \rightarrow \text{blade}) \cdot \vec{z}_1 = M_{\text{aero}/\delta} = \int_{\text{blade}} \overrightarrow{AM} \wedge d\vec{F}_{\text{Aero}} \cdot \vec{z}_1 \qquad [3.26]$$

Figure 3.4 shows that:

$$M_{\text{aero}/\delta} = -\frac{\gamma I_p \Omega^2}{8}\left(\theta - \frac{\dot{\beta}}{\Omega}\right)\frac{\dot{\beta}}{\Omega} \qquad [3.27]$$

Because it was noticed that [3.17]:

$$M_{\text{aero}/\beta} = \frac{\gamma I_p \Omega^2}{8}\left(\theta - \frac{\dot{\beta}}{\Omega}\right)$$

Hence, we simplify in:

$$M_{\text{aero}/\delta} = -M_{\text{aero}/\beta}\frac{\dot{\beta}}{\Omega} \qquad [3.28]$$

and using the blade flapping equation [3.18]:

$$I_p\ \ddot{\beta} + \Omega^2\ \beta = M_{aero/\beta} \qquad [3.29]$$

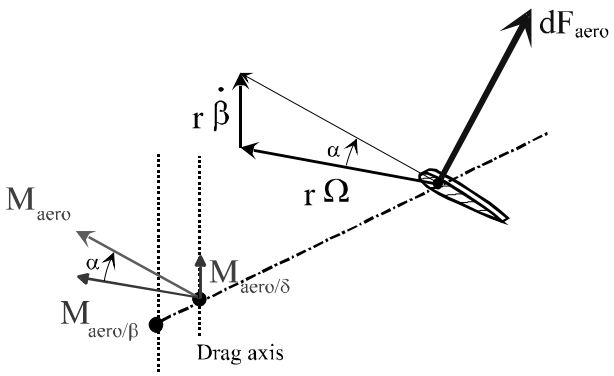

Figure 3.4. *Illustration of the relationship between drag and flapping moments*

We show that:

$$M_{aero/\delta} = -I_p(\ddot{\beta} + \Omega^2\ \beta)\frac{\dot{\beta}}{\Omega} \qquad [3.30]$$

The drag equation is thus given by:

$$\ddot{\delta} - 2\Omega\ \beta\ \dot{\beta} + \omega_\delta^2\ \delta = -(\ddot{\beta} + \Omega^2\ \beta)\frac{\dot{\beta}}{\Omega} \qquad [3.31]$$

if:

$$\ddot{\delta} + \omega_\delta^2\ \delta = \Omega\beta\dot{\beta} - \frac{1}{\Omega}\ddot{\beta}\dot{\beta} \qquad [3.32]$$

with:

$$\omega_\delta = \sqrt{\frac{K_\delta + e\ m_s\Omega^2}{I_p}} \qquad [3.33]$$

We notice here that the drag is excited by the blade flapping.

Let us analyze the behavior of the blade for the configuration of a straight line forward flight and a level flight; let:

$$\theta(t) = \theta_0 - \theta_{1c}\cos(\psi(t)) \qquad [3.34]$$

In these situations, we notice a longitudinal tilt of the rotor disk, since equation [3.22] shows that the flapping response is:

$$\beta(t) = \beta_0 - \beta_{1c}\ \cos(\psi(t)) \qquad [3.35]$$

The drag equation [3.31] can be written:

$$\ddot{\delta} + \omega_\delta^2\ \delta = -\beta_0\beta_{1c}\Omega^2\ \sin(\psi(t)) + \frac{\beta_{1c}^2}{4}\Omega^2\ \sin(2\psi(t)) \qquad [3.36]$$

The blade is thus subjected to loads during drag in 1Ω and 2Ω. Hence, the forced response has the following form:

$$\delta(t) = -\frac{\Omega^2}{\omega_\delta^2 - \Omega^2}\left(\beta_0\ \beta_{1c}\ \sin(\psi(t)) - \frac{\beta_{1c}^2}{4}\sin(2\psi(t))\right) \qquad [3.37]$$

Following the technology of rotors, it is possible to place the drag angular frequency ω_δ according to the speed of rotation Ω (Figure 3.5). We try to avoid the resonance in 1Ω and 2Ω for the drag, in order to avoid very high drag loads. We usually use a drag damper in order to obtain the desired damping and to position the resonant frequency of the first drag mode.

Thus, it can be said that, during flapping, the rotor works in resonance. This is possible thanks to the very strong aerodynamic damping during flapping (see Chapter 4).

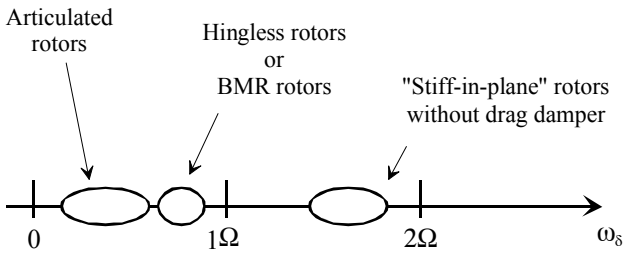

Figure 3.5. *Type of rotor according to the drag stiffness*

3.2.2.2. *Homokinetic rotor*

We intend to prove that the rotor behaves as if it were homokinetic. We will calculate the inertial effects generated by the blade in the plane of rotation.

For example:

$$\begin{aligned} m_p\ A_{G,blade/R_g} \cdot \vec{y}_1 &= m_p \left. \frac{d\vec{V}_{G,blade/R_g}}{dt} \right)_0 \cdot \vec{y}_1 \\ &= m_p \left(\frac{d(\vec{V}_{G,blade/R_g} \cdot \vec{y}_1)}{dt} + \vec{V}_{G,blade/R_g} \cdot \Omega\, \vec{x}_1 \right) \end{aligned} \quad [3.38]$$

The speed of the blade inertial center (see [3.3]) is given by:

$$\vec{V}_{G,blade/R_g} = e\,\Omega\,\vec{y}_1 + R\,(\dot{\delta}+\Omega)\,\cos(\beta)\,\vec{y}_2 - R\,\dot{\beta}\,\vec{z}_3 \quad [3.39]$$

thus preserving only the orders less than or equal to 2:

$$\begin{aligned} \vec{V}_{G,blade/R_g} \cdot \vec{y}_1 &= e\,\Omega + R(\dot{\delta}+\Omega)\,\cos(\beta)\,\cos(\delta) - R\,\dot{\beta}\sin(\beta)\,\sin(\delta) \\ &\approx (e+R)\,\Omega + R\,\dot{\delta} - R\,\Omega\,\frac{\beta^2}{2} \end{aligned} \quad [3.40]$$

and:

$$\begin{aligned} \vec{V}_{G,blade/R_g} \cdot \vec{x}_1 &= -R\,(\dot{\delta}+\Omega)\,\cos(\beta)\,\sin(\delta) - R\,\dot{\beta}\sin(\beta)\,\cos(\delta) \\ &\approx -R\Omega\delta - R\dot{\beta}\beta \end{aligned} \quad [3.41]$$

then:

$$m_p\ \vec{A}_{G,blade/R_g} \cdot \vec{y}_1 = m_p\ R\,(\ddot{\delta} - \Omega^2\delta - 2\Omega\beta\dot{\beta}) \quad [3.42]$$

Then, using only [3.37] and [3.35], equation [3.42] gives:

$$m_p \ \vec{A}_{G,blade/R_g}.\vec{y}_1 = 2(a-1)\, m_p \ R\, \Omega^2 \left[\beta_0 \ \beta_{1c} \ \sin(\psi(t)) - \frac{\beta_{1c}^2}{4} \sin(2\psi(t)) \right] \quad [3.43]$$

with:

$$a = \frac{\Omega^2}{\omega_\delta^2 - \Omega^2} \quad [3.44]$$

Two observations can be made:

– the excitation caused by inertial effects is in 1Ω and 2Ω [3.43]. In order to minimize the loads in the mechanical parts, the term a must be either closest to 1, or $\omega_\delta << \Omega$,

– the rotor mast is not loaded during torque by the inertial effects following the axis of rotation. Indeed, during torque, the contribution of inertial effects of the blades group is defined by:

$$\begin{aligned} \vec{M}_0 \ (\text{inertia} \rightarrow \text{hub}) &= \sum_{i=1}^{b} r\, \vec{x}_1 \wedge m_p \ \vec{A}_{G,\text{blade } i/R_g}.\vec{z}_1 \\ &= 2\, r(a-1)\, m_p \ R\, \Omega^2 \sum_{i=1}^{b} \left[\beta_0 \, \beta_{1c} \sin\left(\psi \ (t)\right) - \frac{\beta_{1c}^2}{4} \sin\left(2\psi \ (t)\right) \right] \\ &= 0 \end{aligned} \quad [3.45]$$

The rotor has a homokinetic behavior; see Chapter 5.

3.3. Rotor technologies

Rotors have evolved historically. Based on their design technology, they can be divided into three categories:

– articulated rotors,

– hingeless rotors,

– bearingless rotors.

3.3.1. *Articulated rotors*

There are two types of articulated rotors:

– the conventional rotor which equips Puma, SuperPuma MK1 or Gazelle helicopters,

– Starflex® and Spheriflex® rotors which equip the EC120: the Ecureuil family, the Dauphin family, SuperPuma MK2, EC725 and the NH90.

3.3.1.1. *Conventional articulated rotors*

The pitch hinges are assembled on bearings and require lubricant. This functioning principle requires flapping bearings which will not let the blade fall when stopping. They release the blade under the effect of the centrifugal force when the rotor is in rotation.

Drag dampers were initially hydraulic. Stiffness and damping are obtained through fluid throttling/flow restriction.

Due to reliability, maintenance and manufacturing costs, the rotor *design* is simplified. Hydraulic dampers, which require a constant supply of fluid, are replaced by viscoelastic dampers which use elastomer to dissipate energy and provide stiffness (see Figures 3.6 and 3.7).

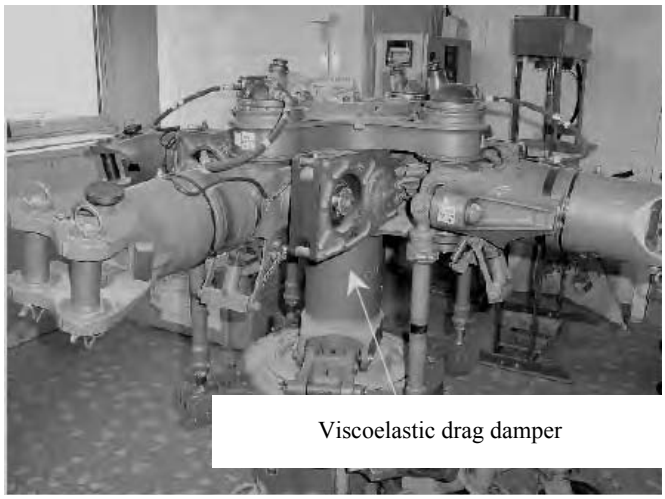

Figure 3.6. *Main rotor hub for SuperPuma 332MK1.*
Photo: Eurocopter

Figure 3.7. *Viscoelastic drag damper, rotor EC155.*
Photo: Eurocopter

3.3.1.2. *Starflex® and Spheriflex® rotors*

The Starflex® hub is an articulated hub which does not have hinge axes. It works thanks to the flexibility of the laminated composite star which flaps, to the viscoelastic damper linking the star ball to the blade for drag, and to the self-lubricated ball for the pitch motion. The laminated spherical bearing is meant to form the rotation center of the blade, and to transmit the coaxial loads to the longitudinal axis, from the blade to the rotor mast, relieving the arm of the Starflex® star.

Figure 3.8. *Starflex® hub for 365N3.*
Photo: Eurocopter

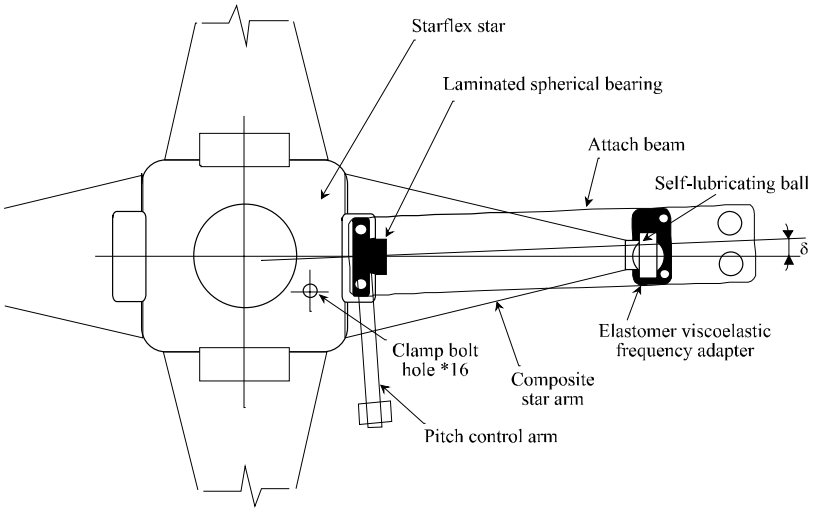

Figure 3.9. *Starflex® hub – schematic diagram seen from above*

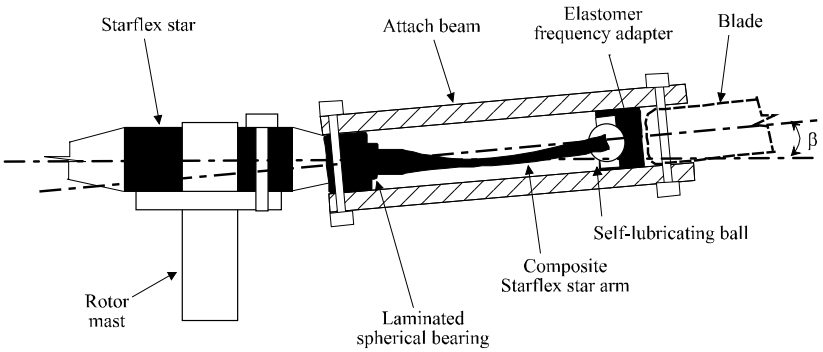

Figure 3.10. *Starflex® hub – schematic diagram: side view*

Figure 3.11. *Starflex® hub for EC120 – general implementation*

Another hub model is the Spheriflex® hub, developed by Eurocopter (see Figures 3.11 and 3.12).

3.3.2. *Hingeless rotors*

For certain types of rotors, flapping and drag hinges have been replaced by elastic elements.

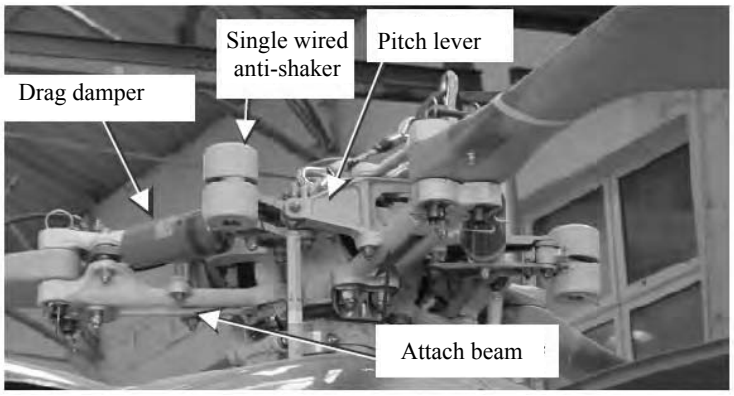

Figure 3.12. *Component parts of Spheriflex® hub for EC120. Photo: Eurocopter*

Hingeless rotors have a high flap eccentricity, which improves the controllability of the helicopter. On a Spheriflex® articulated rotor, the same effect can be obtained by placing the spherical bearing farther from the rotor center. Another consequence is the strong increase in the drag frequency (around 0.7Ω for the tiger helicopter as opposed to 0.3Ω for an articulated device).

A good example for this type of rotor is the Tiger main rotor (Figure 3.13). Drag and flap are possible due to the flexibility of the blade neck made of composites. Drag is damped by a hydraulic damper integrated in the root of the blade (Figure 3.14). The deformations related to the damper hard point on the blade provoke oil throttling and generate damping (Figure 3.14). Pitch control is obtained by a conventional swash plate and a pivot type elastomeric pitch hinge.

Figure 3.13. *Flexible blade neck (instrumented prototype Tiger helicopter). Photo: Eurocopter*

The pitch hinge enables the rotation of the blade around its longitudinal axis.

Figure 3.14. *Integration of the drag damper (instrumented prototype Tiger helicopter). Photo: Eurocopter*

3.3.3. *Hingeless rotor*

For this type of rotor, all hinges have been replaced by elastic elements. The main rotor of the EC135 is a good example of this type of technology (see Figures 3.15 and 3.16).

For this type of rotor, the flexible element plays the role of flapping, drag and pitch hinges. The drag damper is placed between the cuff and the flexible element in order to accentuate the deformation of the drag damper.

Figure 3.15. *Rotor hub for EC135.*
Photo: Eurocopter Deutschland

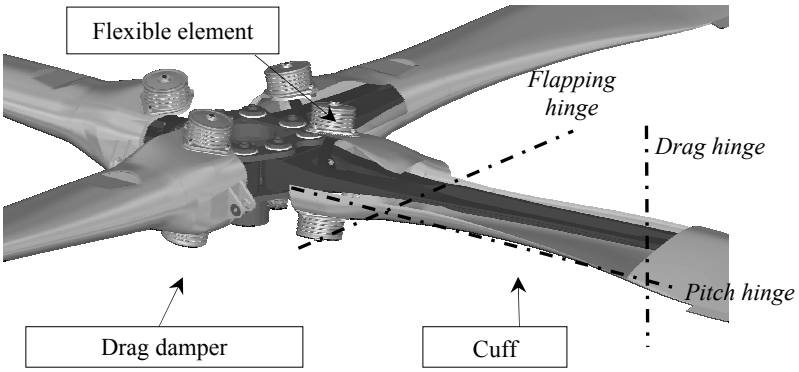

Figure 3.16. *Schematic diagram of rotor hub for EC135.*
Photo: Eurocopter Deutschland

3.4. Influence of alternate aerodynamic loads

We have seen previously that a blade undergoes alternate aerodynamic loads. Blades can transmit these loads to the rotor mast. This transmission is linked to the dynamic response of the blade with a risk of amplification. This risk is represented in the block diagram of Figure 3.17.

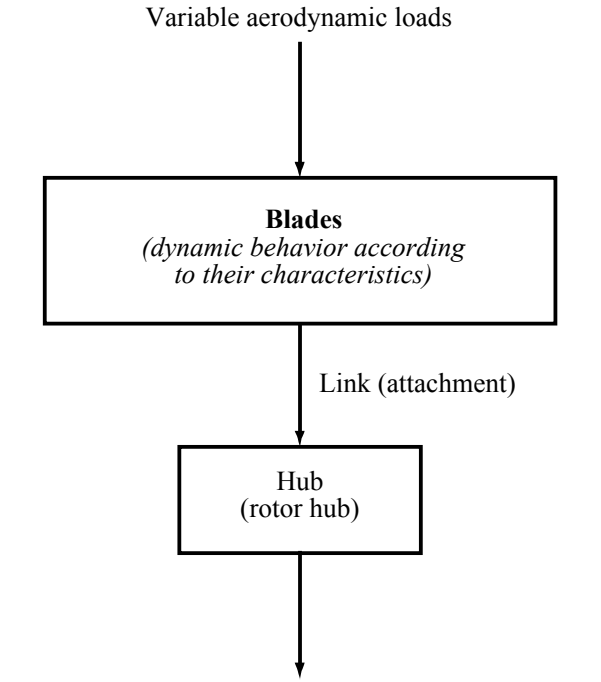

Figure 3.17. *Schematic diagram of load transmission to the fuselage*

This part presents the calculation of loads transmitted to the rotor hub in order to establish the means for technological actions which enable dynamic optimization of the rotor.

3.4.1. *Load characterization*

3.4.1.1. *Loads on a blade*

Each section of the blade undergoes alternate aerodynamic loads due to the variation in the blade speed following its azimuth angle. This phenomenon is linked to the functioning principle of the rotor.

Our goal is to analyze the consequences linked to lift loads.

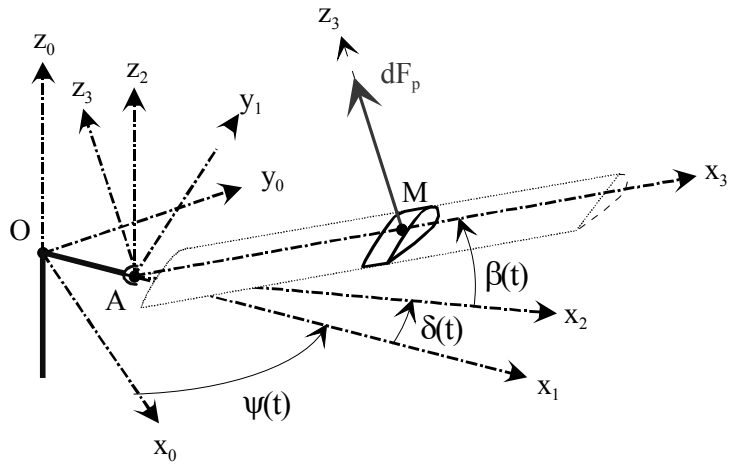

Figure 3.18. *Lift loads applied to a blade element*

The lift load is a function of the lift coefficient, which is variable:

$$\overrightarrow{dF}_{lift} \approx \frac{1}{2}\rho a\, C_p(M,t)\, \vec{V}^2_{air/blade}(M)\, dr\, \vec{z}_3 \qquad [3.46]$$

The lift coefficient C_p varies along the length of the blade. In fact, the angle of attack varies according to the blade twist and Mach number which varies because of the variation in relative speed (see Figure 3.19). This makes the calculation of the lift for the entire blade very difficult.

On the other hand, it is possible to show that each section of the blade undergoes alternate aerodynamic loads due to the functioning principle of the rotor.

In [3.11] it was shown that:

$$\vec{V}_{M,blade/air} = -r\,\dot{\beta}\,\vec{z}_1 + (e + r\cos(\beta))\,\Omega\,\vec{y}_1 + \vec{V}_{M,fuselage/air} \qquad [3.47]$$

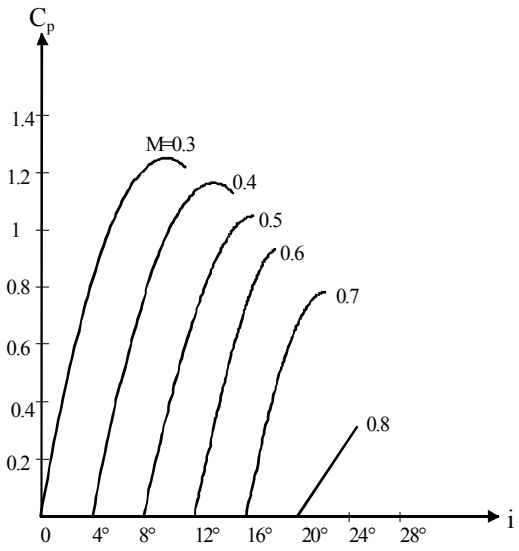

Figure 3.19. *Lift coefficient of an NACA0012 profile according to the angle of attack*

For the forward flight of the helicopter following the axis $-x_0$ we can define:

$$\vec{V}_{M,blade/air} = -r\,\dot{\beta}\,\vec{z}_1 + (e + r\cos(\beta))\,\Omega\,\vec{y}_1 - V_x\,\vec{x}_0 \qquad [3.48]$$

– for hover flight, $V_X = 0$. Each blade undergoes the same flow,

– for forward flight, we can project in the rotating coordinates:

$$\vec{V}_{M,blade/air} = -r\,\dot{\beta}\,\vec{z}_1 + (e + r\cos(\beta))\,\Omega\,\vec{y}_1 - V_X\,\cos(\psi_i)\,\vec{x}_1 + V_X\,\sin(\psi_i)\,\vec{y}_1 \qquad [3.49]$$

Hence, the speed component in the profile plane is:

$$\vec{V}_{M,blade/air} = -r\,\dot{\beta}\,\vec{z}_1 + \left[(e + r\cos(\beta))\Omega + V_X\sin(\psi_i)\right]\vec{y}_1 \qquad [3.50]$$

We saw that this speed will evolve following the position of the blade. If $0 \le \Psi \le \pi$, we are on the side of the advancing blade, if not, we are on the side of the retreating blade. Thus we can conclude that a blade receives loads of variable intensity during one turn (during forward flight), which are called alternate aerodynamic loads.

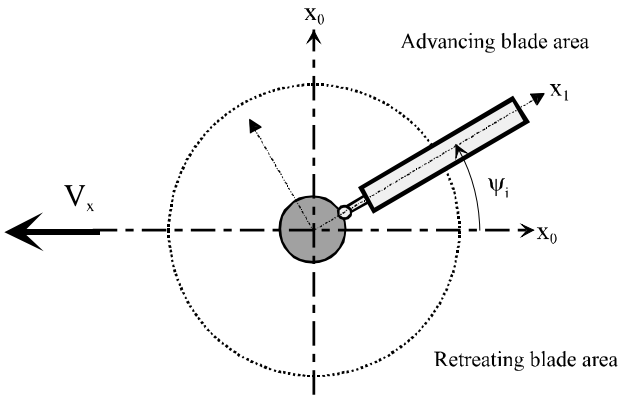

Figure 3.20. *Definition of the notions of advancing and retreating blades*

These loads can also be represented by a period function linked to the rotation speed Ω of the rotor. We suppose that e is small in comparison to r, and ignore the effect of the induced speed:

$$\overrightarrow{dF_{lift}} \approx \frac{1}{2}\rho\, a\, C_p\; i\; \left((r\,\Omega + V_X \sin(\psi_i))^2 + r^2\;\dot{\beta}^2\right) dr\, \vec{z}_3 \qquad [3.51]$$

with the incidence which can be defined by:

$$i \approx \theta - \frac{r\,\dot{\beta}}{r\,\Omega + V_x\;\sin(\psi_i)} \qquad [3.52]$$

then:

$$\begin{aligned}\overrightarrow{dF_{lift}} \approx \frac{1}{2}\rho a C_p \left((r\,\Omega + V_x\;\sin(\psi_i))^2\,\theta - \ldots\right.\\ \left.\ldots - r\,\dot{\beta}\,(r\,\Omega + V_x\;\sin(\psi_i))\right)\, dr\,\vec{z}_3\end{aligned} \qquad [3.53]$$

The blade pitch variation is represented as follows:

$$\begin{aligned}&\theta\;(\psi) = \theta_{control}(\psi) + \theta_{torsion}(\psi)\\ &\theta_{control}(\psi) = \theta_0 + \theta_{1c}\cos\psi + \theta_{1s}\sin\psi\\ &\theta_{torsion}(\psi) = \theta_0' + \sum_{i=1}^{k}\left(\theta_{ic}\;\cos(i\,\psi) + \theta_{1s}\sin(i\,\psi)\right)\end{aligned} \qquad [3.54]$$

with $\theta_{control}$, the conventional control of the rotor (Chapter 4), and $\theta_{torsion}$, the torsion dynamic deformation of the blade on all higher harmonics.

Supposing that the blade is non-deformable and ignoring the effects of the induced speed we see that, with the help of expression [3.53], the lift load has dynamic components in 1Ω, 2Ω and 3Ω.

Given that there is:

– a dynamic torsion of the blade for the higher harmonics (direct action on lift; see [3.54]),

– dynamic flapping for the higher harmonics because the blade is deformable,

– a variation in the field of the induced speed Vi (Vi is not constant), ignored in the demonstration.

Hence, there is a dynamic excitation on the blade for all harmonics [3.55]:

$$\overrightarrow{dF_{lift}} = \vec{f}(\text{static}, 1\Omega, 2\Omega, 3\Omega \ldots) \qquad [3.55]$$

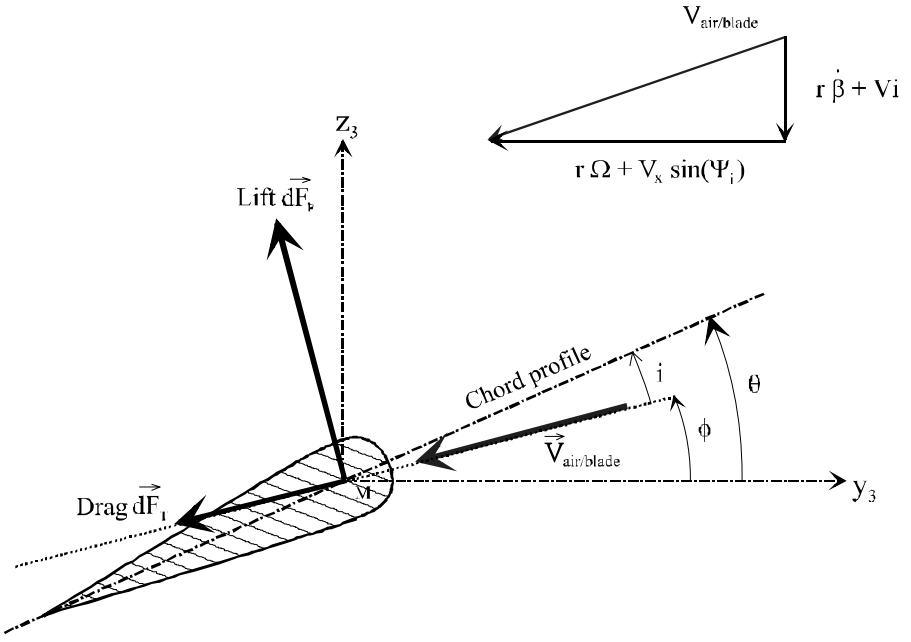

Figure 3.21. *Diagram of the angle of attack of the air with respect to the blade in forward flight*

3.4.1.2. *Dynamic response of a blade*

Considering the complexity presented in the previous section, we will break down the aerodynamic loads in the Fourier series through the expression:

$$dF_{aero} = \sum_{n=0}^{\infty} \left(A_{cn}(r)\ \cos(n\,\Omega\,t) + A_{sn}(r)\ \sin(n\,\Omega\,t) \right)\ dr\ \vec{z}_3 \qquad [3.56]$$

with: A_{cn} and A_{sc} as breakdown coefficients in the Fourier series.

It is interesting to analyze how the blade will react to these loads and what type of loads it will transmit to the hub, through the hard point.

For this type of analysis, the behavior of the blade can no longer be considered as non-deformable.

With the help of the deformable media theory, we can show that there is an infinity of natural bending modes. Hence, the blade will transmit the loads differently according to the excitation frequency, and that is what we will be analyzing.

Let y(r,t) be the motion of a blade point within a distance r from the axis of the rotor during a bending load. By using the generalized coordinates, we prove that it can be written as follows:

$$y(r,t) = \sum_{n=1}^{\infty} W_n(r)\ q_n(t) \qquad [3.57]$$

with q_n, generalized coordinate of the mode n and $W_n(r)$, as the deformation of the mode n.

We can define the following quantities:

$$\begin{cases} T = \sum_{n=1}^{\infty} \frac{1}{2}\ \mu_n\ \dot{q}_n^2 & \text{Galilean kinetic energy} \\ U = \frac{1}{2} \sum_{n=1}^{\infty} \mu_n\ \omega_n^2\ q_n^2 & \text{potential function due to elastic deformation} \\ D = \sum_{n=1}^{\infty} \mu_n\ \alpha_n\ \omega_n\ \dot{q}_n^2 & \text{dissipation function} \\ Q_{q_n} & \text{generalized stresses due to aerodynamic stresses for mode n} \end{cases}$$

with:

– ω_n: natural angular frequency associated with mode n,

– μ_n: generalized mass associated with mode n,

– α_n: reduced damping coefficient associated with mode n.

Then we write Lagrange equations for each of the generalized coordinates:

$$\frac{d}{dt}\left(\frac{\partial\, T\left(\Sigma/R_g\right)}{\partial \dot{q}_n}\right)-\frac{\partial\, T\left(\Sigma/R_g\right)}{\partial q_n}+\frac{\partial\, U}{\partial q_n}+\frac{\partial\, D}{\partial \dot{q}_n}=Q_{q_n} \qquad [3.58]$$

Thus we obtain an infinity of equations governing the infinity of assumed modes:

$$\mu_n\left(\ddot{q}_n+2\,\alpha_n\,\omega_n\,\dot{q}_n+\omega_n^2\,q_n\right)=Q_{q_n} \qquad [3.59]$$

Hence, equation [3.59] can be written:

$$\overline{q}_n=\frac{\overline{Q}_{q_n}}{\mu_n}\frac{1}{\left(\omega_n^2-\omega^2+2i\,\alpha_n\,\omega_n\,\omega\right)} \qquad [3.60]$$

3.4.1.3. *Loads transmitted by a mode i*

The load at the blade shank [TAY 88], for the n^{th} mode, is given by:

$$\left(\vec{F}_t\right)_n=\int_{\text{blade}} dF_n\,\vec{z}_3 \qquad [3.61]$$

The elementary load is given by:

$$\begin{aligned} dF_n &= \ddot{y}_n(r,t)\,dm \\ &= -\omega_n^2\,y_n(r,t)\,dm \end{aligned} \qquad [3.62]$$

with: $y_n(r,t)=w_n(r)\,q_n(t)$

Let:

$$\left(F_t\right)_n=\int_{\text{blade}} \omega_n^2\,w_n(r)\,q_n(t)\,dm \qquad [3.63]$$

Hence, the load transmitted for mode i for an excitation frequency ω is given by:

$$F_{ti} = \left(\int_{blade} w_i(r)\, dm \right) \omega_i^2\, q_i \qquad [3.64]$$

With equations [3.60] and [3.64] we have:

$$F_{ti} = \left(\int_{blade} w_i(r)\, dm \right) \frac{Q_{qi}}{\mu_i} \frac{\omega_i^2}{\omega^2} \sqrt{\frac{1}{\left(1 - \left(\frac{\omega_i}{\omega}\right)^2\right)^2 + \left(2\alpha_i \frac{\omega_i}{\omega}\right)^2}} \qquad [3.65]$$

The shape coefficient f_i can be defined as follows:

$$f_i = \left(\int_{blade} w_i(r)\, dm \right) \frac{Q_{q_i}}{\mu_i} \qquad [3.66]$$

It is difficult to calculate this coefficient (usage of numeric codes is required) because of the generalized load Q_{q_i}.

Transmissibility is defined by [TAY 88]:

$$T_{r_i}(\omega) = \frac{F_{ti}}{f_i} = \frac{\omega_i^2}{\omega^2} \frac{1}{\sqrt{\left(\left(\frac{\omega_i}{\omega}\right)^2 - 1\right)^2 + \left(2\,\alpha_i \frac{\omega_i}{\omega}\right)^2}} \qquad [3.67]$$

The calculated load was for mode i and the excitation frequency ω. To obtain the total load entailed by the vibrations, we have to take into account all modes.

For which we get the expression of total load:

$$F_{Total} = \left(\sum_{i=1}^{\infty} f_i\; T_{r_i}\; (\omega) \right) \qquad [3.68]$$

3.4.2. *Analysis of loads transmitted to the rotor hub*

The loads of blade number i at the level of the hinge can be broken down in the rotating coordinate R_1:

$$\vec{F}_i(\text{blade} \rightarrow \text{hub}) = F_{ci}\ \vec{x}_1 + F_{\delta i}\ \vec{y}_1 + F_{\beta i}\ \vec{z}_1$$

with:

– F_{ci}: radial component,

– $F_{\beta i}$: axial component,

– $F_{\delta i}$: tangential component.

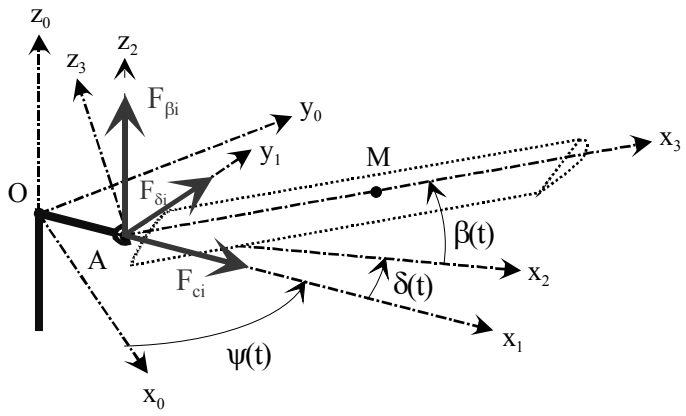

Figure 3.22. *Breakdown of blade loads on the rotor hub*

We suppose that the load components F_{ci}, $F_{\beta i}$ and $F_{\delta i}$ can be broken down in the Fourier series if:

$$\begin{aligned} F_{ci} &= \sum_n \left(F_{cc}\right)_n \cos(n\,\psi_i(t)) + \left(F_{cs}\right)_n \sin(n\,\psi_i(t)) \\ F_{\beta i} &= \sum_n \left(F_{\beta c}\right)_n \cos(n\,\psi_i(t)) + \left(F_{\beta s}\right)_n \sin(n\,\psi_i(t)) \\ F_{\delta i} &= \sum_n \left(F_{\delta c}\right)_n \cos(n\,\psi_i(t)) + \left(F_{\delta s}\right)_n \sin(n\,\psi_i(t)) \end{aligned} \qquad [3.69]$$

with $n - n^{th}$ excitation harmonics.

3.4.2.1. *Loads transmitted to the rotor*

If we express the moment in O, the torsion of the mechanical action of the rotor (group of blades) on the hub is defined by:

$$\begin{aligned}\vec{R}\ (\text{rotor} \rightarrow \text{hub}) &= \sum_{i=1}^{b} \vec{R}\ (\text{blade i} \rightarrow \text{hub}) \\ \vec{M}_O\ (\text{rotor} \rightarrow \text{hub}) &= \sum_{i=1}^{b} \vec{M}_O\ (\text{blade i} \rightarrow \text{hub})\end{aligned} \quad [3.70]$$

Using the definitions from Figure 3.22:

$$\begin{aligned}\vec{R}\ (\text{rotor} \rightarrow \text{hub}) &= \sum_{i=1}^{b} F_{ci}\ \vec{x}_{1i} + F_{\beta i}\ \vec{z}_1 + F_{\delta i}\ \vec{y}_{1i} \\ \vec{M}_O\ (\text{rotor} \rightarrow \text{hub}) &= \sum_{i=1}^{b} e\ F_{\delta i}\ \vec{z}_1 - e\ F_{\beta i}\ \vec{y}_{1i}\end{aligned} \quad [3.71]$$

These loads can be broken down in relation to the axis of rotation by:

$$\begin{aligned}\vec{R}\ (\text{rotor} \rightarrow \text{hub}) &= \vec{F}_{xy} + F_z\ \vec{z}_1 \\ \vec{M}_O\ (\text{rotor} \rightarrow \text{hub}) &= M_z\ \vec{z}_1 - \vec{M}_{xy}\end{aligned} \quad [3.72]$$

with:

– F_z: pumping load,

– F_{xy}: in-phase load in the plane perpendicular to the rotation axis,

– M_z: yawing moment,

– M_{xy}: pitch and roll moment.

3.4.2.1.1. Pumping load F_z

If we return to the definitions [3.72] and [3.68] we can define the component for n harmonics of the pumping load by:

$$\begin{aligned}F_{zn} &= \sum_{i=1}^{b} \left(F_{\beta i}\right)_n = \sum_{i=1}^{b} \left(F_{\beta c}\right)_n \cos(n\ \psi_i(t)) + \left(F_{\beta s}\right)_n \sin(n\ \psi_i(t)) \\ &= \left(F_{\beta c}\right)_n \sum_{i=1}^{b} \cos\left(n\left(\Omega\ t + \frac{2\pi}{b}(i-1)\right)\right) + \left(F_{\beta s}\right)_n \sum_{i=1}^{b} \sin\left(n\left(\Omega\ t + \frac{2\pi}{b}(i-1)\right)\right)\end{aligned} \quad [3.73]$$

or we can show that:

$$\sum_{i=1}^{b} \sin\left(n\left(\Omega t + \frac{2\pi}{b}(i-1)\right)\right) = \frac{e^{j\frac{2\pi}{b}n} - e^{j\left(\frac{2\pi}{b}n\right)(b+1)}}{1 - e^{j\frac{2\pi}{b}n}} \quad [3.74]$$

Hence, if n is not a multiple of b:

$$\sum_{i=1}^{b} \sin\left(n\left(\Omega t + 2\pi\frac{(i-1)}{b}\right)\right) = 0 \quad [3.75]$$

and if n is a multiple of b, with n = kb:

$$\sum_{i=1}^{b} \sin\left(n\left(\Omega t + (i-1)\frac{2\pi}{b}\right)\right) = b \sin(k\, b\Omega t) \quad [3.76]$$

By applying the same procedure for cosine terms, we can conclude that:

– if n is not a multiple of b:

$$F_{zn} = 0 \quad [3.77]$$

– if n is a multiple of b, with n = kb:

$$F_{zn} = \left(F_{\beta c}\right)_n \; b \cos(n\,\Omega\; t) + \left(F_{\beta s}\right)_n \; b \sin(n\,\Omega\; t) \quad [3.78]$$

The transmission of loads to the fuselage is done without a change in frequency. The vertical pumping loads are transmitted to the fuselage only if their frequency is a multiple of bΩ.

3.4.2.1.2. Excitations in the plane of the rotor hub F_{xy}

The load F_{xy} in the plane of the rotor hub is broken down in the fixed coordinate in two components, F_x and F_y, defined by:

$$\vec{F}_{xy} = \sum_{i=1}^{b} F_{\delta i}\; \vec{y}_{1i} + F_{ci}\; \vec{x}_{1i} = \sum_{i=1}^{b} F_{xi}\; \vec{x}_0 + F_{yi}\; \vec{y}_0 = F_x\; \vec{x}_0 + F_y\; \vec{y}_0 \quad [3.79]$$

The projection of each component makes it possible to obtain:

$$\begin{aligned} F_{xi} &= F_{ci}\ \cos(\psi_i) - F_{\delta i}\ \sin(\psi_i) \\ F_{yi} &= F_{ci}\ \sin(\psi_i) + F_{\delta i}\ \cos(\psi_i) \end{aligned} \qquad [3.80]$$

with:

$$\psi_i = \Omega\, t + \frac{2\,\pi}{b}(i-1) \qquad [3.81]$$

By developing with the help of equation [3.69], we obtain for the component following x_0:

$$\begin{aligned} F_{xi} = &\sum_n \left[\left(F_{cc}\right)_n \cos(n\ \psi_i(t)) + \left(F_{cs}\right)_n\ \sin(n\ \psi_i(t)) \right] \cos(\psi_i) \\ &- \sum_n \left[\left(F_{\delta c}\right)_n \cos(n\ \psi_i(t)) + \left(F_{\delta s}\right)_n\ \sin(n\ \psi_i(t)) \right] \sin(\psi_i) \end{aligned} \qquad [3.82]$$

To obtain the total load, it is enough to take into consideration all blades and all harmonics:

$$\begin{aligned} F_X &= \sum_{i=1}^{b} F_{xi} \\ &= \sum_{i=1}^{b} \sum_n \left[\left(F_{cc}\right)_n \cos\ (n\ \psi_i(t)) + \left(F_{cs}\right)_n\ \sin\ (n\ \psi_i(t)) \right] \cos(\psi_i) \\ &- \sum_{i=1}^{b} \sum_n \left[\left(F_{\delta c}\right)_n \cos\ (n\ \psi_i(t)) + \left(F_{\delta s}\right)_n\ \sin\ (n\ \psi_i(t)) \right] \sin(\psi_i) \end{aligned} \qquad [3.83]$$

Harmonics of order 0

Order 0 of the load (constant part) is defined by:

$$\left(F_X\right)_0 = \sum_{i=1}^{b} \left(F_{cc}\right)_0\ \cos(\psi_i) - \sum_{i=1}^{b} \left(F_{\delta c}\right)_0\ \sin(\psi_i) \qquad [3.84]$$

If the blades are properly balanced, $\left(F_{cc}\right)_0$ and $\left(F_{\delta c}\right)_0$ are the same for all the blades, and harmonics of order 0 cancel each other out.

Harmonics of order n

Order n of the load is defined by:

$$\begin{aligned}\left(F_X\right)_n = &\sum_{i=1}^{b}\left[\ \left(F_{cc}\right)_n\ \cos\left(n\ \psi_i(t)\right)+\left(F_{cs}\right)_n\ \sin\left(n\ \psi_i(t)\right)\right]\cos\ \left(\psi_i\right)\\ &-\sum_{i=1}^{b}\left[\ \left(F_{\delta c}\right)_n\ \cos(n\ \psi_i(t))+\left(F_{\delta s}\right)_n\ \sin\left(n\ \psi_i(t)\right)\right]\sin\ \left(\psi_i\right)\end{aligned} \qquad [3.85]$$

We show that:

$$\begin{aligned}\cos\left(n\ \psi_i(t)\right)\cos\left(\psi_i(t)\right) &= \frac{1}{2}\left[\cos\left((n+1)\ \psi_i(t)\right)+\cos\left((n-1)\ \psi_i(t)\right)\right]\\ \sin\left(n\ \psi_i(t)\right)\cos\left(\psi_i(t)\right) &= \frac{1}{2}\left[\sin\left((n+1)\ \psi_i(t)\right)+\sin\left((n-1)\ \psi_i(t)\right)\right]\\ \cos\left(n\ \psi_i(t)\right)\sin\left(\psi_i(t)\right) &= \frac{1}{2}\left[\sin\left((n+1)\ \psi_i(t)\right)-\sin\left((n-1)\ \psi_i(t)\right)\right]\\ \sin\left(n\ \psi_i(t)\right)\sin\left(\psi_i(t)\right) &= \frac{1}{2}\left[\cos\left((n-1)\ \psi_i(t)\right)-\cos\left((n+1)\ \psi_i(t)\right)\right]\end{aligned} \qquad [3.86]$$

Then:

$$\begin{aligned}\left(F_X\right)_n = &\frac{1}{2}\sum_{i=1}^{b}\left((F_{cc})_n+(F_{\delta s})_n\right)\left[\cos\left((n+1)\ \psi_i(t)\right)\right]\\ &+\frac{1}{2}\sum_{i=1}^{b}\left((F_{cc})_n-(F_{\delta s})_n\right)\left[\cos\left((n-1)\ \psi_i(t)\right)\right]\\ &+\frac{1}{2}\sum_{i=1}^{b}\left((F_{cs})_n-(F_{\delta c})_n\right)\left[\sin\left((n+1)\ \psi_i(t)\right)\right]\\ &+\frac{1}{2}\sum_{i=1}^{b}\left((F_{cs})_n+(F_{\delta c})_n\right)\left[\sin\left((n-1)\ \psi_i(t)\right)\right]\end{aligned}$$

or we can show that:

$$\sum_{i=1}^{b}\sin\left((n+1)\ \psi_i(t)\right) = \frac{e^{j\frac{2\pi}{b}(n+1)}-e^{j\left(\frac{2\pi}{b}(n+1)\right)(b+1)}}{1-e^{j\frac{2\pi}{b}(n+1)}} \qquad [3.87]$$

– if n is different from (k b + 1) or (k b – 1), k integer, then:

$$\sum_{i=1}^{b} \sin\left((n+1)\,\psi_i(t)\right) = 0 \qquad [3.88]$$

– if n is equal to $(k\,b+1)$ or $(k\,b-1)$, k integer, then:

$$\sum_{i=1}^{b} \sin\left((n+1)\,\psi_i(t)\right) = b\,\sin\left(k\,b\,\Omega\,t\right) \qquad [3.89]$$

We can have the same type of calculation for the other terms as well; then for F_Y we show that:

– if n is different from $(k\,b \pm 1)$:

$$F_{X_n} = 0 \text{ and } F_{Y_n} = 0 \qquad [3.90]$$

– if n is equal to $(k\,b \pm 1)$:

$$\begin{aligned}\left(F_X\right)_n = &\frac{1}{2}\left[\left(\left(F_{cc}\right)_{kb+1} - \left(F_{\delta s}\right)_{kb+1}\right) + \left(\left(F_{cc}\right)_{kb-1} - \left(F_{\delta s}\right)_{kb-1}\right)\right] b\cos\left(k\,b\,\Omega\right)\\ &+\frac{1}{2}\left[\left(\left(F_{cs}\right)_{kb+1} + \left(F_{\delta c}\right)_{kb+1}\right) + \left(\left(F_{cs}\right)_{kb-1} - \left(F_{\delta c}\right)_{kb-1}\right)\right] b\sin\left(k\,b\,\Omega\right)\end{aligned} \qquad [3.91]$$

and:

$$\begin{aligned}\left(F_Y\right)_n = &\frac{1}{2}\left[\left(\left(F_{cs}\right)_{kb+1} - \left(F_{\delta c}\right)_{kb+1}\right) + \left(-\left(F_{cs}\right)_{kb-1} + \left(F_{\delta c}\right)_{kb-1}\right)\right] b\cos\left(k\,b\,\Omega\right)\\ &+\frac{1}{2}\left[\left(-\left(F_{cc}\right)_{kb+1} + \left(F_{\delta s}\right)_{kb+1}\right) + \left(\left(F_{cc}\right)_{kb-1} + \left(F_{\delta s}\right)_{kb-1}\right)\right] b\sin\left(k\,b\,\Omega\right)\end{aligned} \qquad [3.92]$$

The fuselage loads in the plane of rotation have the frequency k b Ω. They are transmitted to the fuselage only if their frequency is $\left(k\,b \pm 1\right)\,\Omega$.

Table 3.1 reiterates what has been said earlier.

The same reasoning can be applied to the in-phase moments in $(M_x)_n$ and $(M_y)_n$.

Origin of blade/hub excitation in a rotating coordinate		**Hub/fuselage excitation in a fixed coordinate**	
Excitation	**Frequency**	**Excitation**	**Frequency**
F_β flapping	k b Ω	F_z: vertical pumping	k b Ω
	(k b ± 1) Ω	M_{xy}: in-phase bending moment	k b Ω
F_δ drag	k b Ω	M_z: torsion moment on the rotor mast	k b Ω
	(k b ± 1) Ω	F_{xy}: in-phase load	k b Ω

Table 3.1. *Different types of excitation according to the observation coordinate*

We can illustrate the periodicity of phenomena of the universal sets linked to the main rotor by the following reasoning.

In a steady flight, if we place an observer in a coordinate linked to the main rotor (for example, an observer placed on the blade), at a time t0, it will take at least one turn of the main rotor for it to be in the same place again. All dynamic phenomena within a rotating coordinate appear thus at the harmonics of rotor speed Ω.

For the periodicity of phenomena of the coordinates linked to the structure in steady flight, if we place an observer in a coordinate linked to the structure (for example an observer placed in the cabin), at a time t0, it will take it at least 1/b of a turn of rotation speed of the rotor to get to be in the same place again (provided the b blades are identical). All dynamic phenomena within a fixed coordinate thus appear at the harmonics b Ω.

Conclusion

The rotor is a filter that transmits loads whose frequency is an angular frequency harmonic (k b Ω) to the fuselage.

The vertical components within a fixed coordinate (F_z, M_z), whose frequency is a harmonic in $k\,b\,\Omega$, resulting from the loads of the rotating coordinate whose frequency is a harmonic in $(k\,b\,\Omega)$.

The components of in-phase loads at the rotor hub (f_x, f_y, m_x, m_y), whose frequency is also a harmonic in $k\,b\,\Omega$, resulting from the loads of the rotating coordinate whose frequency is a harmonic in $(k\,b \pm 1)\,\Omega$.

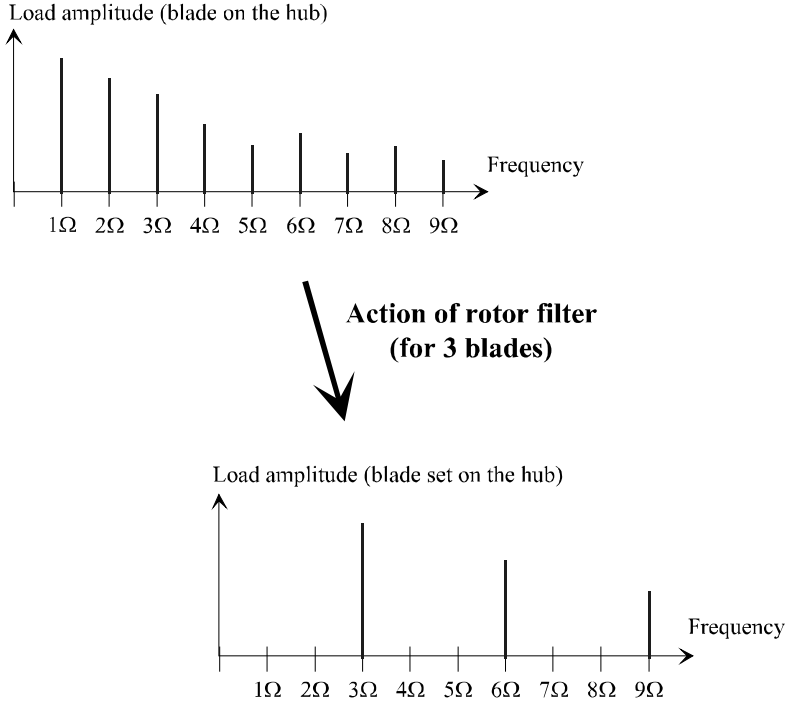

Figure 3.23. *Load graphs transmitted from the rotating loads to the fixed coordinates*

3.4.2.2. *Synthesis of rotor loads on the rotor mast*

For mode i we have:

– F_{ti}: shear load at the blade foot,

– N: the number of modes taken into account.

Often, for a four blade rotor, the second flapping mode represents around 70% of the in-phase moment at the rotor hub. The dynamic optimization of the second flapping mode is enough for the dynamic optimization of the rotor.

This is the reason why we are content with the study of this flapping mode.

Frequencies within the rotating coordinate		Nature	Load intensity – equations [3.63], [3.67]
Flapping	(k b-1) Ω	In-phase moments	$m_x = \sum_{i=1}^{N} e \frac{b\,Ft_i}{2\mu_i\,\omega_i^2} Tr_i\left((k\,b-1)\Omega\right)\,Q_{i,kb-1}^{flap}$
			$m_y = \sum_{i=1}^{N} e \frac{b\,Ft_i}{2\mu_i\,\omega_i^2} Tr_i\left((k\,b-1)\Omega\right)\,Q_{i,kb-1}^{flap}$
	k b Ω	Pumping	$f_z = \sum_{i=1}^{N} \frac{b\,Ft_i}{\mu_i\,\omega_i^2} Tr_i(k\,b\,\Omega)\,Q_{i,kb}^{flap}$
	(k b+1) Ω	In-phase moments	$m_x = \sum_{i=1}^{N} e \frac{b\,Ft_i}{2\mu_i\,\omega_i^2} Tr_i\left((k\,b+1)\Omega\right)\,Q_{i,kb+1}^{flap}$
			$m_y = \sum_{i=1}^{N} e \frac{b\,Ft_i}{2\mu_i\,\omega_i^2} Tr_i\left((k\,b+1)\Omega\right)\,Q_{i,kb+1}^{flap}$
Drag	(k b-1) Ω	In-phase loads	$f_x = \sum_{i=1}^{N} \frac{-b\,Ft_i}{2\mu_i\,\omega_i^2} Tr_i\left((k\,b-1)\Omega\right)\,Q_{i,kb-1}^{drag,x}$
			$f_y = \sum_{i=1}^{N} \frac{b\,Ft_i}{2\mu_i\,\omega_i^2} Tr_i\left((k\,b-1)\Omega\right)\,Q_{i,kb-1}^{drag,y}$
	k b Ω	Torsion of rotor mast (torque modulation)	$m_z = \sum_{i=1}^{N} e \frac{b\,Ft_i}{\mu_i\,\omega_i^2} Tr_i(k\,b\,\Omega)\,Q_{i,kb}^{drag,z}$
	(k b+1) Ω	In-phase loads	$f_x = \sum_{i=1}^{N} \frac{b\,Ft_i}{2\mu_i\,\omega_i^2} Tr_i\left((k\,b+1)\Omega\right)\,Q_{i,kb+1}^{drag,x}$
			$f_y = \sum_{i=1}^{N} \frac{b\,Ft_i}{2\mu_i\,\omega_i^2} Tr_i\left((k\,b+1)\Omega\right)\,Q_{i,kb+1}^{drag,y}$

Table 3.2. *Excitations at the rotor hub due to blade movement*

3.4.3. *Dynamic optimization of a blade*

3.4.3.1. *Introduction*

According to the previous expressions, reducing loads at the rotor hub leads to the optimization of the following parameters:

– increase in the generalized mass μ_i,

– decrease in the shear load at the hinge Ft_i,

– an eccentricity as low as possible,

– optimization of parameter $Tr_i(\omega)$, which implies:

- the correct positioning of the natural frequencies,

- the study of the influence of the number of blades,

– decrease in the generalized excitation load. For a rotor, aerodynamic excitation decreases along with the increase in the harmonics rate.

3.4.3.2. *Study of the example of an optimized blade*

During the pre-design phase, while making the architectural choices for the blades, it is very important to take into account the fundamental role of the dynamic rotor hub loads which generate vibrations and alternate loads in different mechanical parts. A method of dynamic optimization is illustrated in the example of a helicopter having a four blade rotor.

It is important to bear in mind that the vibratory level in the cabin depends on the following factors:

– aerodynamic loads on the blades (profiles, twist, camber, balance, tabs, tip shape),

– dynamic response of the blades,

– transfer of excitations from the rotor hub to the fuselage (in order to decrease the loads applied to the structure, suspensions are often used),

– dynamic response of the structure.

The following example deals with the first two factors.

The intensity of a modal load generated by a blade can have the form given by equation [3.65]. We try to reduce the generalized force Q_{qi} by shifting the aerodynamic load towards the places where $w_i(r)$ is less important, that is, towards the lower radius. The blade must be tapered by increasing the chord on the lower radius in order to preserve the same lift level.

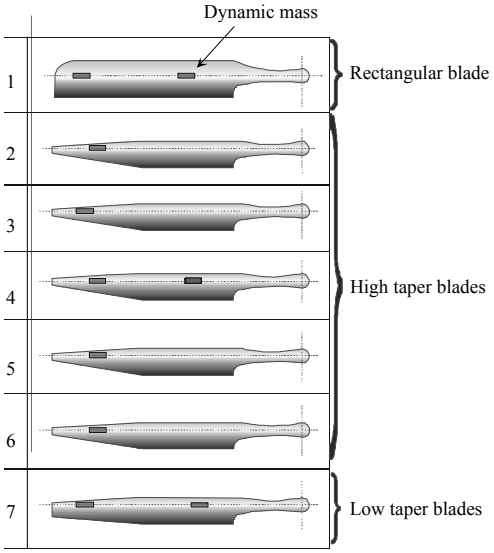

Figure 3.24. *Types of blades.*
Photo: G. Guarnieri (Eurocopter)

We propose seven types of blades which were recalculated so as to have the same aerodynamic characteristics.

The definition of the different blades is given in Table 3.3.

Blade number	Dynamic mass 1	Dynamic mass 2	Mass per unit length (kg/m)	Flapping stiffness (Nm^2)
1 reference	4 kg at 0.45R	1.4 kg at 0.95R	4.45	5,885
2	Absent	2 kg at 0.8R	5.94	11,775
3	Absent	1.6 kg at 0.92R	5.94	11,775
4	4 kg at 0.55R	2 kg at 0.8R	5.94	11,775
5	Absent	2 kg at 0.8R	5.94	16,847
6	Absent	2 kg at 0.8R	5.94	5,674
7	3.15 kg at 0.4R	2 kg at 0.92R	5.09	6,941

Table 3.3. *Blade characteristics*

Table 3.4 provides the values of natural frequencies, generalized masses and shear loads for flapping and drag.

	Type of blade						
	1	**2**	**3**	**4**	**5**	**6**	**7**
2nd flapping mode							
Nat. frequency/omega	2.44	2.6	2.53	2.37	2.64	2.55	2.42
Generalized mass (m^2kg)	8.02	2.16	3.84	4.52	2.26	2.12	6.1
Shear load (N)	66,730	36,030	46,880	47,640	38,110	33,500	55,560
3rd flapping mode							
Nat. frequency/omega	4.62	3.78	4.1	3.94	3.89	3.67	3.94
Generalized mass (m^2kg)	6.3	6.3	1.52	2.6	0.85	1.02	12.5
Shear load (N)	129,200	28,080	41,050	24,300	28,700	28,680	36,270
2nd drag mode							
Nat. frequency/omega	6.61	5.61	4.49	4.21	4.69	5.4	4.29
Generalized mass (m^2kg)	8.3	2	6.41	2.09	5.06	2.09	3.2
Shear load (N)	294,700	98,100	74,960	47,700	35,940	109,300	69,790

Table 3.4. *Dynamic characteristics of blades*

Two effects can already be observed:

– a decrease in the generalized mass. The generalized mass μ_I decreases for the tapered blade because on the current part the mass of the tapered blade is higher than the mass of the rectangular blade, but the modal deformation is much lower,

– a decrease in the shear load: see equation [3.63]. The mass distribution enables a clear decrease in the shear load.

Thus, we note that blade taper and the obtained mass distribution led to:

– a decrease in the in-phase load at the blade shank, which is a good point for the reduction of the transmitted load,

– a very significant decrease in the generalized mass, which increases the transmitted load.

What remains to be analyzed is whether the variation of the generalized load and the transmissibility can compensate for the decrease in the generalized mass. The next calculations address the second flapping mode and then we will verify whether the conclusions drawn from this mode are to our satisfaction.

Second flapping mode

Calculations have been made for $\Omega = 40$ rad/s.

No.	ω_p/Ω	Generalized mass	Tr (3Ω)	In-phase load	Generalized load	M2B (analytical)
1	2.44	8.02	1.95	66,730	273	177
2	2.6	2.16	3.02	36,030	180.6	319
3	2.53	3.84	2.46	46,880	177.7	200
4	2.37	4.52	1.66	47,640	251	186
5	2.64	2.26	3.43	38,110	148	292
6	2.55	2.12	2.6	33,500	210	316
7	2.42	6.1	1.86	55,560	211	145

Table 3.5. *Analytical calculations of in-phase rotor hub moment (SI units)*

We have:

– M2B: coplanar moment at rotor hub in 3Ω of second flapping mode,

– Tr(3Ω): transmissibility in 3Ω,

– ω_p/Ω reduced angular frequency of the second flapping mode.

Note: generalized loads are calculated using a numeric code.

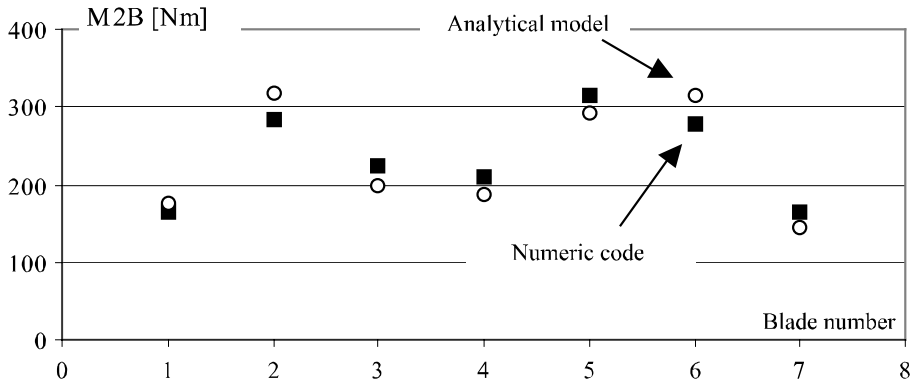

Figure 3.25. *Coplanar moment at rotor hub in 3Ω coming from the second flapping mode*

The code of numeric calculation used in the study and enabling the validation of numeric calculation is described in [ALL 89].

Consequence of taper ratio on the generalized mass

The taper ratio effect leads to a significant decrease in the generalized load; however, the table above indicates that the reference blade behaves better than the highly tapered blade. The explanation of this phenomenon is based on the significant decrease in the generalized mass of the second flapping mode, which cannot be compensated either by the decrease in the modal load at the hinge or by the decrease in aerodynamic excitation.

Effects of additional masses and local stiffness

Influence of additional masses

The technique of additional masses was applied in order to shift the frequency of the flapping modes. In solution 4, this method is limited and can result in only moderate improvements for two reasons:

– the decrease in the flapping natural frequency (decrease in transmissibility) is accompanied by a slight increase in the modal shear load in the hinge,

– the shape of the second flapping mode is changed (important displacement of the node of the mode), which leads to a significant increase in the generalized load.

Effects of the local stiffness

One of the opportunities to adjust the dynamic properties of the blade is to alternate the local stiffness. This parameter was modified for the tapered blade in the case of solution 5 (stiffness increased by 45% in comparison to blade number 2) and solution 6 (stiffness decreased by 52% in comparison to blade number 2).

It is proved that the natural frequency, the generalized mass and the shear load at the hinge for the second flapping mode are affected very little by this variation in the local stiffness.

Conclusion on taper ratio

The analysis of these results leads to the conclusion that, in order to have the lowest rotor hub excitation in-phase moment, we have to associate the dynamic features of a rectangular blade with the aerodynamics of the tapered blade (low generalized load).

This result led to a compromise solution: a blade with a lower taper ratio (solution 7). This solution makes it possible to increase the generalized mass without over-affecting the aerodynamic excitation.

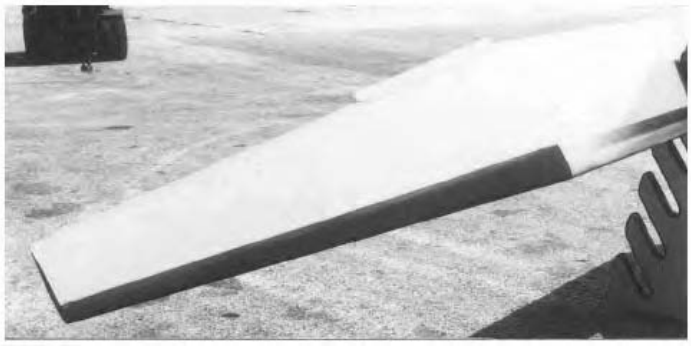

Figure 3.26. *Example of a tapered blade.*
Photo: Eurocopter

3.4.3.3. *Contribution of the second flapping mode*

In this section we will analyze the contribution of the second flapping mode $\left(M_{2B}(3\Omega)\right)$ with respect to the resulting in-phase moment (Mtotal). In the case of blades number 1 and 2, Table 3.6 shows the calculation of the total contribution of other modes (with numerical software).

No.	$M_{2B}(3\Omega)$ [Nm]	Mtotal [Nm]	Contribution of 2B [%]
1	165	206	80
2	293	380	77
3	200	342	59
4	186	317	59
5	292	444	66
6	316	370	85
7	145	245	59

Table 3.6. *Contribution of the second flapping mode for the coplanar moment in 3Ω (at the center of rotor hub within the rotating axis)*

In both cases we see that the moment of the second flapping mode is clearly greater than the moments corresponding to other modes.

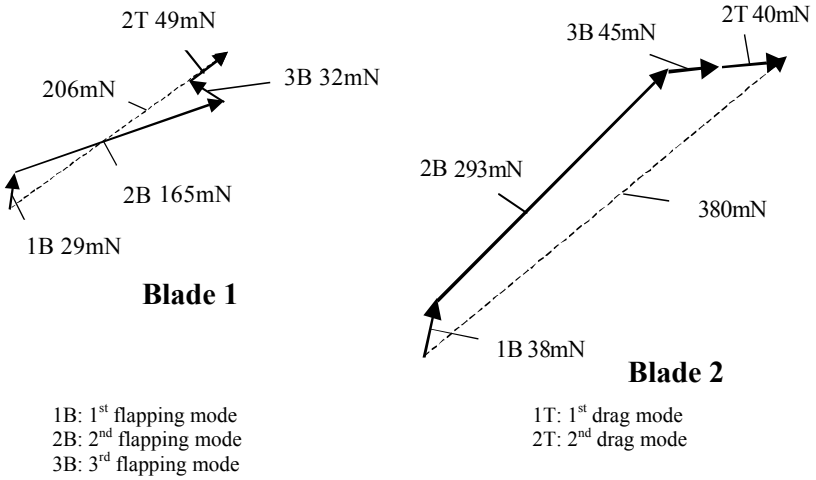

Figure 3.27. *Contribution of different modes in the in-phase moment in 3 Ω for blades number 1 and 2 (at the center of rotor hub within the rotating axis)*

Observation regarding the aerodynamic excitation

In the generalized load, the aerodynamic excitation in $k\Omega$ greatly decreases when k increases, which explains the low intensity of modes other than 2B, as they are excited by higher excitation frequencies.

To conclude:

– $M_{2B}(3\,\Omega)$ represents more than 70% of the resulting in-phase moment at the rotor hub,

– $M_{2B}(3\,\Omega)$ is paramount with respect to the moments corresponding to other modes; hence if $M_{2B}(3\,\Omega)$ is optimized, this will reduce a significant part of the loads at the rotor hub.

Therefore, amongst all these solutions, compromised optimization must be found. The number of blades and the eccentricity of the rotor during the pre-design phase are not chosen according to the vibration criterion. The method can be applied even if there are not four blades. For certain configurations, the study must deal with other flapping modes apart from the second one.

Chapter 4

Rotor Control

4.1. Introduction

For the majority of applications, vibrations are considered a negative element, being detrimental to comfort and health or generating alternating loads that might damage mechanical parts.

In certain applications, vibrations are used to control a process. This is the situation for vibratory drilling. Vibrating motions can be used in controlling helicopters. In this case, in order to direct the motion of the structure in space, the dynamics of the blade are used.

We will show how a helicopter is controlled by using the vibrating motion of the blades.

Lift and piloting of a helicopter are ensured by the main rotor. The main rotor consists of a central hub connected to a rotating shaft driven by an engine. The blades are attached to the hub by the equivalent of a ball link or an elastic element enabling the blade to move. The rotor is driven by an engine set at a constant speed irrespective of the type of flight (forward flight, hover flight, descending flight, etc.).

The aerodynamic actions of each blade contribute to the lift loads of the rotor. By modifying the angle of each blade, it is possible to modify the lift in both direction and amplitude, and thus control the helicopter.

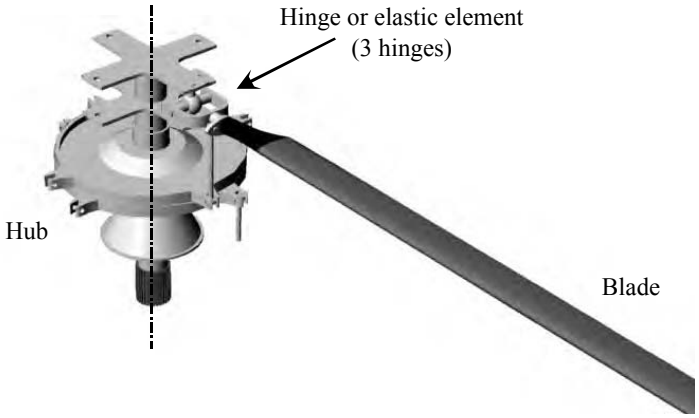

Figure 4.1. *Definition of a hub*

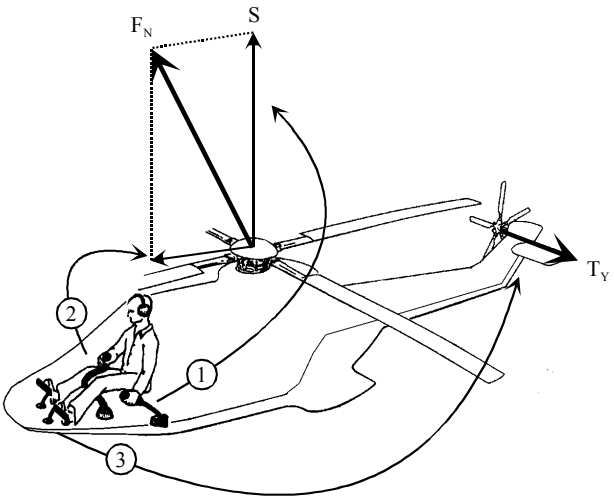

Figure 4.2. *Control through blade angle*

The pilot has three ways of controlling a helicopter:

– the collective pitch lever (1) which controls the F_N module,

– the cyclic stick (2) which produces the orientation in space of the lift load through the tilt of the rotor disk,

– the pedals (3) which control the T_y thrust of the tail rotor.

The collective pitch lever (1) ensures the simultaneous angle variation of all blades.

The variation in the orientation of the vector F_N is ensured by causing an unbalanced variation of the blade angle on a rotor turn. This is called cyclic pitch. This function is technically obtained either by a swashplate (conventional rotors) or by a flap system placed on the blades (rotors with flaps) [FUL 97, GAL 00, ORM 91, ORM 98, ORM 01].

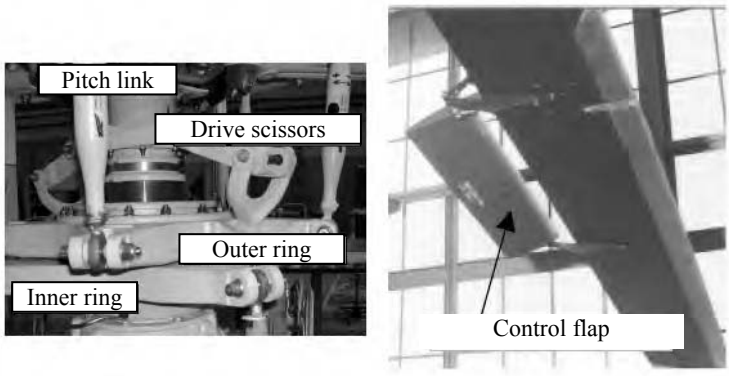

Figure 4.3. *Control through rings or flaps.*
Photos: Eurocopter and Kaman Aerospace Corporation

4.2. Blade motions

4.2.1. *Flapping equation – general case*

In order to understand the control of a blade, it is necessary to use the equations given in the previous chapter. It is used for symmetric and non-symmetric profile helicopters with different aerodynamic properties. The essential geometric characteristics are the chord a (see Figure 4.4) and the lift and drag coefficients.

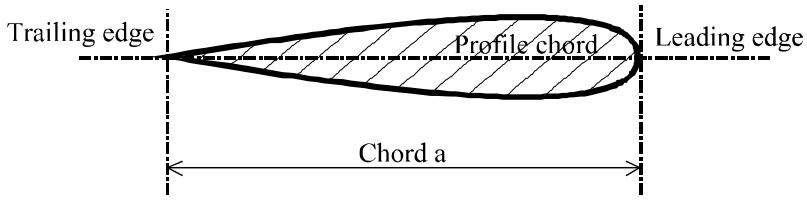

Figure 4.4. *Aerodynamic profile (air foils)*

Aerodynamic loads are generally modeled (see Figure 4.5) by a quasi-static model:

$$\begin{cases} dF_p = \frac{1}{2}\rho\, C_p \vec{V}^2_{air/blade}\, dS & \text{lift} \\ dF_T = \frac{1}{2}\rho\, C_t\, \vec{V}^2_{air/blade}\, dS & \text{drag} \end{cases} \quad [4.1]$$

with:

– C_p: lift coefficient,

– C_t: drag coefficient,

– ρ: air density,

– dS: surface element.

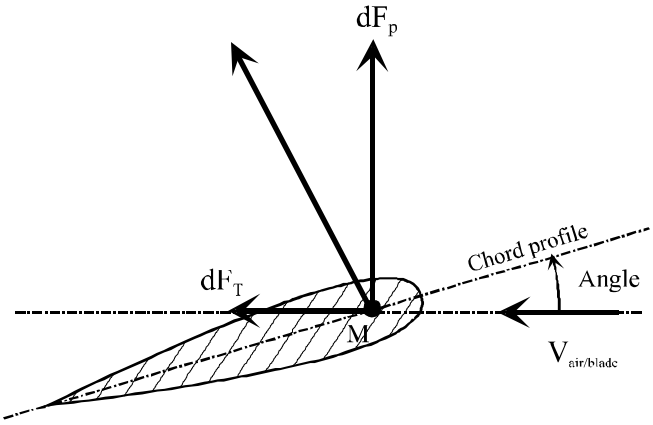

Figure 4.5. *Modeling of aerodynamic loads*

Equation [3.18] from Chapter 3 gives:

$$\ddot{\beta} + \frac{\gamma\,\Omega}{8}\dot{\beta} + \left(\left(1 + \frac{e\, m_s}{I_p}\right)\Omega^2 + \frac{K_\beta}{I_p}\right)\beta = \frac{\gamma\,\Omega^2}{8}\theta \quad [4.2]$$

with:

– β: blade flapping,

– θ: blade pitch.

The equation can be transformed:

$$\ddot{\beta} + 2\,\lambda\,\omega_p\,\dot{\beta} + \omega_p^2\,\beta = -\frac{\gamma\,\Omega^2}{8}\theta \qquad [4.3]$$

by saying:

$$\begin{cases} \omega_p = \Omega\sqrt{\left(1+\dfrac{e\,m_s}{I_p}\right)+\dfrac{K_\beta}{I_p\,\Omega^2}} & \text{(flapping natural angular frequency)} \\ \lambda = \dfrac{\gamma}{16}\sqrt{\left(\dfrac{I_p}{\left(I_p + e\,ms\right)+\dfrac{K_\beta}{\Omega^2}}\right)} & \text{(flapping damping ratio)} \end{cases}$$

Equation [4.3] represents the behavior of the blade under aerodynamic loads which will be controlled through the pitch θ.

4.2.2. *The case of a rotor without eccentricity and flapping stiffness*

For a rotor without eccentricity (e = 0) and without flapping stiffness ($K_\beta = 0$) the following simplification can be made:

$$\begin{cases} \omega_p = \Omega \\ \lambda = \dfrac{\gamma}{16} \end{cases} \qquad [4.4]$$

Lock's number (see Chapter 3) varies from 6 to 12 according to the size of the helicopter. The variation range of damping ratio λ then increases from 50 to 75%. We notice that the flapping is in any case greatly damped.

For harmonic excitation, we can show that the amplitude of the flapping response β_0, and of the phase difference φ with respect to the excitation, is given by:

$$\begin{cases} \beta_0 = \dfrac{\gamma\,\Omega^2}{8}\dfrac{1}{\sqrt{\left(\omega_p^2-\omega^2\right)^2+\left(2\,\lambda\,\omega_p\,\omega\right)^2}}\theta_0 \\ \varphi = \operatorname{atan}\left(\dfrac{2\,\lambda\,\omega_p\,\omega}{\left(\omega_p^2-\omega^2\right)}\right) \end{cases} \quad [4.5]$$

The resonant angular frequency (β_0 maximum) is given by:

$$\omega_\beta = \Omega\sqrt{1-\lambda^2} = \Omega\sqrt{1-\left(\frac{\gamma}{16}\right)^2} \quad [4.6]$$

The analysis of amplitude β_0 and of phase difference φ according to ω (with Lock's number set at 10 and a speed of rotation of 27 rad/s (see Figures 4.6 and 4.7) leads to the following conclusions.

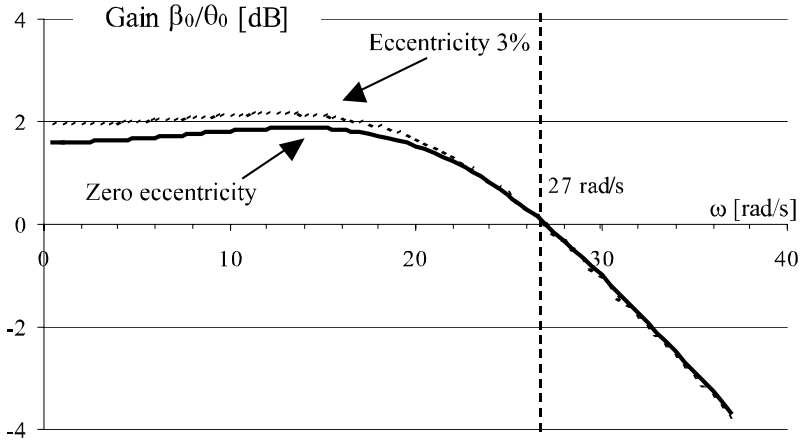

Figure 4.6. *Transfer function of flapping – gain*

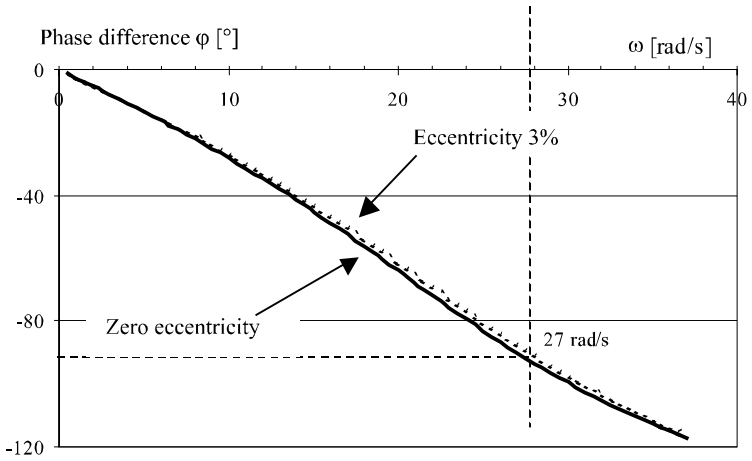

Figure 4.7. *Transfer function of flapping – phase difference*

The blade responds to the order in $\theta(t)$ like a 2nd order system.

Flight control imposes varying of the pitch at the rotation frequency. In fact the blade is excited at its natural frequency. The amplitude of the response is limited by the high damping given by aerodynamic loads. In the case of an articulated rotor, the response has a phase difference of 90º with respect to the pitch excitation. The rotor behaves like a gyroscope [RIC 92]. A gyroscope reacts in such a way that it tends to align the vector of the dynamic moment to that of the applied moment.

An example of gyroscopic effect is the gyro spinner. The dynamic moment of the gyroscope is oriented following the axis Z. The moment M has the value $m\,g\,l\sin(\alpha)$ because of the weight of the gyro spinner (Figure 4.8). The gyroscopic effect tends to align the dynamic moment $I\Omega$ (following Z_t) with the moment M of external load, which leads to the motion of the gyro spinner following the trajectory c at the angular speed ω.

$$\omega = \frac{m\,g\,l}{I\,\Omega} \qquad [4.7]$$

with:

– I: inertia of gyro spinner around its axis of rotation Z_t,

– M: mass of gyro spinner,

– l: distance OG,

– Ω: speed of rotation of the gyro spinner around its own axis Z_t.

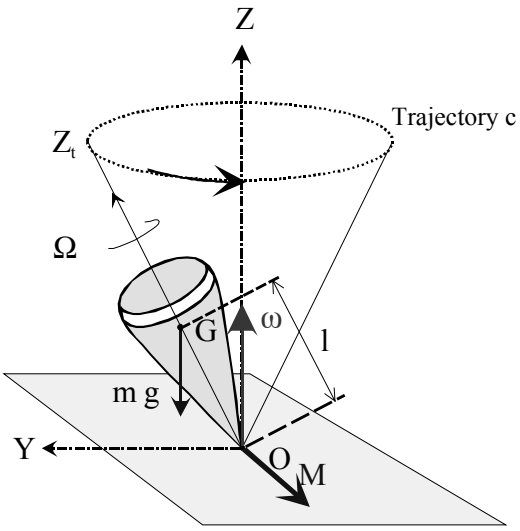

Figure 4.8. *Illustration of the gyroscopic effects by the gyro spinner*

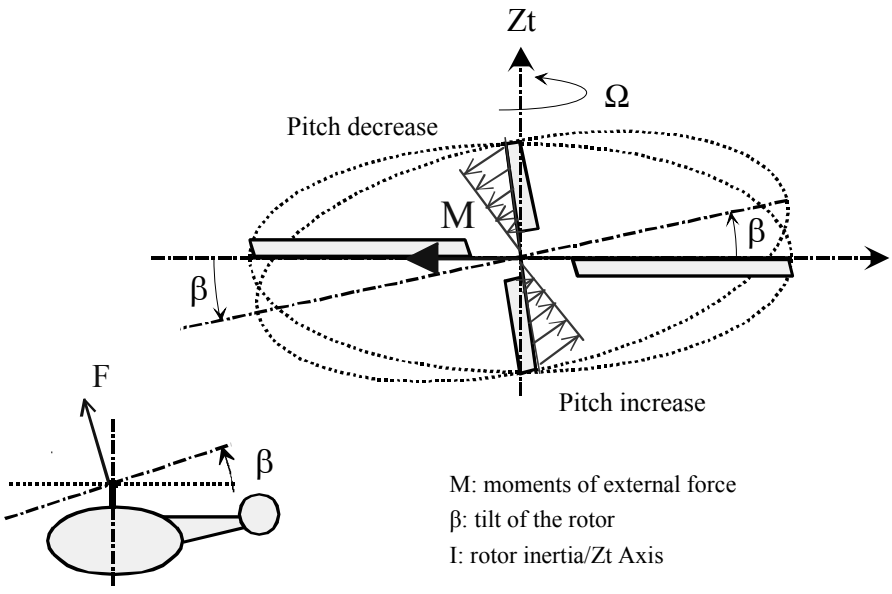

Figure 4.9. *Gyroscopic effects on a helicopter rotor*

The behavior of the rotor can be compared to the functioning of the gyroscope.

The decrease of the incidence on the advancing blade and the pitch increase on the retreating blade provoke a moment of external loads M (caused by aerodynamic effects). The dynamic moment IΩ tends to become aligned with the moment of external loads M, which leads to the tilt of the rotor β, with I as the rotor inertia and Ω the rotation speed of the rotor.

For certain types of rotors, the blade is connected to the hub through a flexible element. For this type of rotor, the flapping natural angular frequency is higher than 1Ω and often close to 1.1Ω, which gives a phase difference of less than 90º. In order to ensure proper control, the phase difference is often corrected by the flying controls system.

The principle of dynamic response of the 2nd order system excited at the resonant frequency is used, in the case of a helicopter, to ensure the function of space orientation of the aircraft.

This function is represented by two systems:

– the control system through a cyclic swashplate,

– the control system through a flap.

4.3. Control through cyclic and collective swashplates

In the case of swashplate control (see Figure 4.11), the behavior of the blade is reflected on the behavior of the entire rotor.

The cyclic swashplate leads, in the rotating reference system, to the motion of the blade which consists of static motion and dynamic motion θ_{1c} and θ_{1s} in 1Ω

The pitch angle θ(t) falls under the law:

$$\theta_i(t) = \theta_0(t) + \theta_{1c}(t)\ \cos(\Omega t + \Psi_i) + \theta_{1s}(t)\ \sin(\Omega t + \Psi_i) \qquad [4.8]$$

– θ_0: collective pitch managed by the collective lever,

– θ_{1c}: longitudinal pitch and θ_{1s} lateral pitch, both managed by the cyclic stick.

In order to see the contribution of each of these terms on the blades' movement, we change the following variable. For each blade labeled i, the equation of motion is written with i varying from 1 to 4 for a four blade rotor:

$$\ddot{\beta}_i + \frac{\gamma\,\Omega}{8}\dot{\beta}_i + \Omega^2\ \beta_i = \frac{\gamma\,\Omega^2}{8}\theta_i \qquad [4.9]$$

We then say:

$$\beta_i(t) = \beta_0(t) + \beta_{Ic}(t)\ \cos(\Omega\,t + \Psi_i) + \beta_{Is}(t)\ \sin(\Omega\,t + \Psi_i) \qquad [4.10]$$

with:

$$\beta_{Ic} = \frac{1}{2}\sum_{i=1}^{4}\beta_i\ \cos(\Omega\,t + \Psi_i),\ \beta_{Is} = \frac{1}{2}\sum_{i=1}^{4}\beta_i\ \sin(\Omega t + \Psi_i),\ \beta_0 = \frac{1}{4}\sum_{i=1}^{4}\beta_i \qquad [4.11]$$

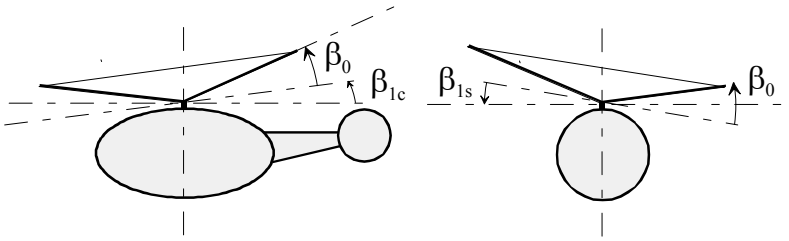

Figure 4.10. *Definition of the 1st harmonics parameters*

With equations [4.9] and [4.10] we show that:

$$\begin{cases} \ddot{\beta}_0 + \dfrac{\gamma\,\Omega}{8}\dot{\beta}_0 + \Omega^2\ \beta_0 = \dfrac{\gamma\,\Omega^2}{8}\theta_0 \\ \left(\ddot{\beta}_{1c} + 2\,\Omega\ \beta_{1s} - \Omega^2\ \beta_{1c}\right) + \dfrac{\gamma\,\Omega}{8}\left(\dot{\beta}_{1c} + \Omega\,\beta_{1s}\right) + \Omega^2\ \beta_{1c} = \dfrac{\gamma\,\Omega^2}{8}\theta_{1c} \\ \left(\ddot{\beta}_{1s} - 2\,\Omega\ \beta_{1s} - \Omega^2\ \beta_{1c}\right) + \dfrac{\gamma\,\Omega}{8}\left(\dot{\beta}_{1c} - \Omega\,\beta_{1c}\right) + \Omega^2\ \beta_{1s} = \dfrac{\gamma\,\Omega^2}{8}\theta_{1s} \end{cases} \qquad [4.12]$$

The last two equations can be written in the form of the following matrix:

$$\begin{bmatrix}\ddot{\beta}_{1c}\\ \ddot{\beta}_{1s}\end{bmatrix}+\begin{bmatrix}\frac{\gamma\,\Omega}{8} & 2\,\Omega\\ -2\,\Omega & \frac{\gamma\,\Omega}{8}\end{bmatrix}\begin{bmatrix}\dot{\beta}_{1c}\\ \dot{\beta}_{1s}\end{bmatrix}+\begin{bmatrix}0 & \frac{\gamma\,\Omega^2}{8}\\ -\frac{\gamma\,\Omega^2}{8} & 0\end{bmatrix}\cdot\begin{bmatrix}\beta_{1c}\\ \beta_{1c}\end{bmatrix}=\frac{\gamma\,\Omega^2}{8}\begin{bmatrix}\theta_{1c}\\ \theta_{1s}\end{bmatrix} \quad [4.13]$$

If we consider only the static case, we will arrive at the following two equations:

$$\begin{cases}\frac{\gamma\,\Omega^2}{8}\beta_{1s} = \frac{\gamma\,\Omega^2}{8}\theta_{1c}\\ -\frac{\gamma\,\Omega^2}{8}\beta_{1c} = \frac{\gamma\,\Omega^2}{8}\theta_{1s}\end{cases} \quad [4.14]$$

Hence:

$$\begin{cases}+\beta_{1s} = \theta_{1c}\\ -\beta_{1c} = \theta_{1s}\end{cases} \quad [4.15]$$

Note that a lateral blade tilt corresponds to a variation of longitudinal pitch and vice versa. Thus, there is a 90º phase difference between excitation and response. The functioning principle of the cyclic swashplate is shown in Figure 4.11.

4.4. Control through flaps

4.4.1. *Description*

On each blade, the flap is controlled by control rods that transmit the conventional controls of the pilot.

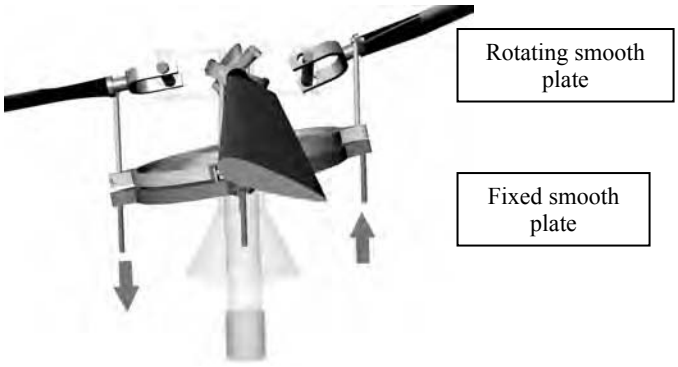

Figure 4.11. *Illustration of a cyclic swashplate*

The motion of the flap causes the rotation of the blade around its pitch axis. The forces necessary to pivot the flap are low in comparison to those necessary to directly pivot the entire blade, as in a control system through a cyclic swashplate. The flap control loads are low because the principle of dynamic amplification is used.

Figure 4.12. *Implementation of the flap on a blade.*
Photo: Kaman Aerospace Corporation

It is interesting to analyze the vibratory behavior of the blade and flap system in order to show that it can be used to control a helicopter.

4.4.2. *Modeling*

It is desirable to suggest a model that makes it possible to put forward the usage of the blade movement for rotor control.

The model used consists of a rigid blade with two degrees of freedom (flapping β and torsion angle θ).

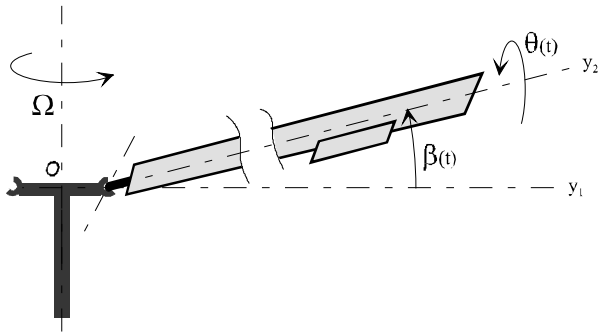

Figure 4.13. *Parametric transformation of a blade motion*

Moreover, the modeling is based on the following hypotheses:

– the entire blade is profiled,

– the blade is not twisted,

– the blade chord is constant,

– the center of inertia of the flap is situated on the flap/blade hinge axis,

– the speed of the wind is zero.

4.4.2.1. *Flapping equation*

In order to obtain the flapping equation of a blade, we can use the equation from the previous section to which we must add the action of the flap.

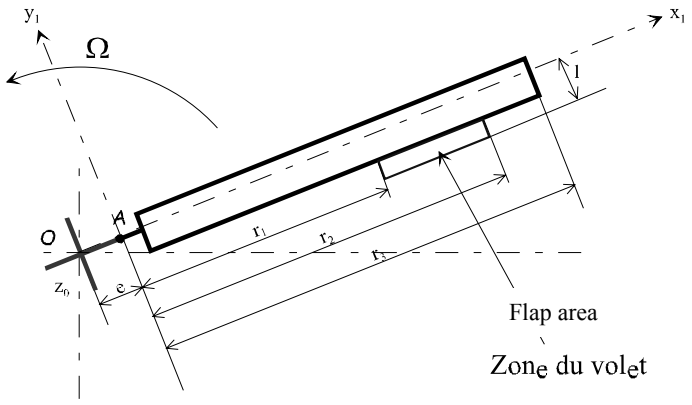

Figure 4.14. *Blade and flap definition*

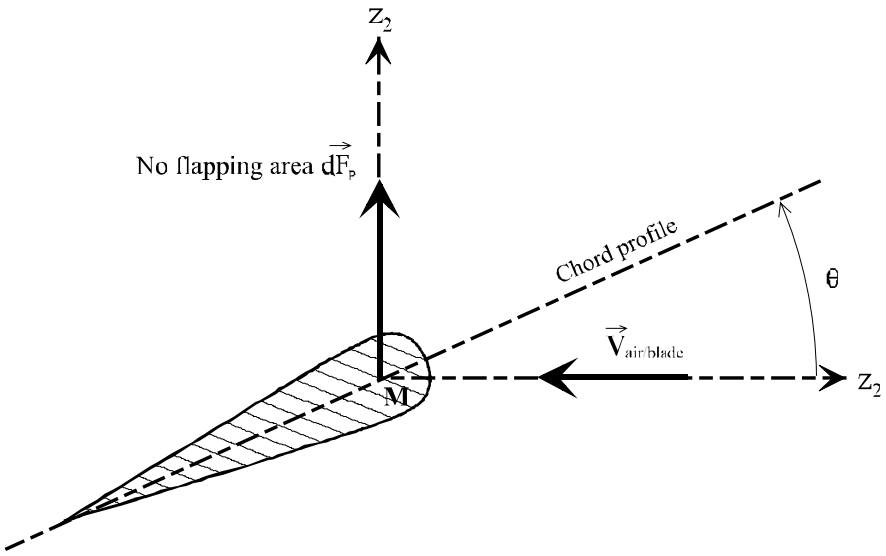

Figure 4.15. *Aerodynamic loads on the blade*

We suppose that the flap does not affect the aerodynamic moment caused by the blade. For the flap, the aerodynamic moment is expressed by:

$$\begin{aligned}\overrightarrow{M}_A(\text{Aero} \rightarrow \text{flap}) \cdot \vec{y}_1 &= \left(\int_{\text{surfaceflap}} \overrightarrow{AN} \wedge d\vec{F}_{\text{aero}} \right) \cdot \vec{y}_1 \\ &= -\int_{r_1}^{r_2} \frac{1}{2} \rho \, a_v C_p^v(i) \, r(r\Omega)^2 \, dr \\ &= -\rho \, a_v \left(\frac{\partial C_p^v}{\partial \delta} \delta \right) \Omega^2 \, \frac{r_2^4 - r_1^4}{4} \\ &= -\frac{\gamma \, I_\beta \, \Omega^2}{8} \hat{a} \, A_4 \, C_{\delta p} \, \delta\end{aligned} \qquad [4.16]$$

where $C_p^v(i)$ is the lift coefficient of the flap, and with:

$$\begin{cases} C_{\delta p} = \left(\dfrac{\partial C_p^v}{\partial \delta} \Big/ \dfrac{\partial C_p}{\partial \alpha} \right) \\ \gamma = \dfrac{\rho \, a}{I_\beta} \dfrac{\partial C_p}{\partial \alpha} R^4 \\ A_4 = \dfrac{r_2^4 - r_1^4}{R^4} \\ \hat{a} = \dfrac{a_v}{a} \end{cases} \qquad [4.17]$$

with:

– a: blade chord,

– a_v: flap chord.

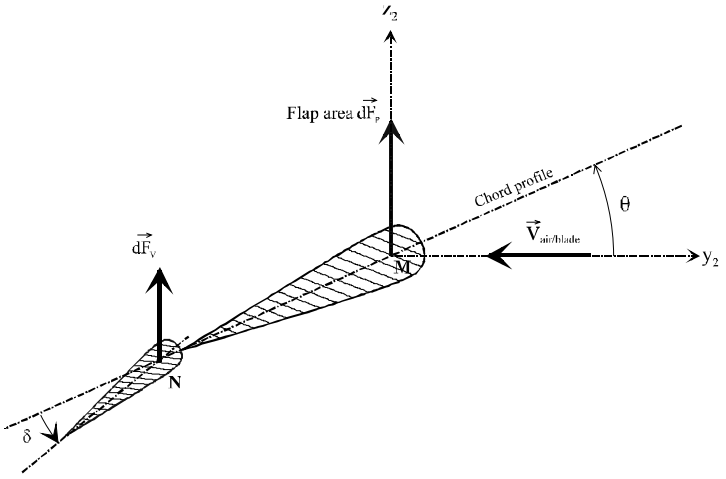

Figure 4.16. *Aerodynamic loads on the blade and on the flap*

Hence, the flapping equation of the blade gives:

$$\ddot{\beta} + \frac{\gamma\,\Omega}{8}\dot{\beta} + \left(\left(1 + \frac{e\,m_s}{I_\beta}\right)\Omega^2 + \frac{K_\beta}{I_\beta}\right)\beta = \frac{\gamma\,\Omega^2}{8}\theta + \frac{\gamma\,\Omega^2}{8}\hat{a}\,A_4\,C_{\delta p}\,\delta \qquad [4.18]$$

conventional control

direct load of the flap

4.4.2.2. *Torsion equation*

The center of inertia and the thrust center of aerodynamic loads of a blade element are situated on the longitudinal axis (M, x_2) (see Figure 4.16). The center of inertia and the thrust center of aerodynamic loads of a flap element are situated on the longitudinal axis (N, x_2).

If we isolate the set consisting of the blade and the flap:

$$\vec{\delta}_A\left(\Sigma/R_g\right)\cdot\vec{x}_2 = [\overrightarrow{M}_A\left(\text{aero} \to \Sigma\right) + \overrightarrow{M}_A(\text{link} \to \Sigma)]\cdot\vec{x}_2 \qquad [4.19]$$

For the flap:

$$\vec{\delta}_A(\text{flap}/R_g)\cdot\vec{x}_2 = \vec{\delta}_N(\text{flap}/R_g)\cdot\vec{x}_2 + \left(\overrightarrow{AN} \wedge m\,\vec{A}_{N,\text{flap}/R_g}\right)\cdot\vec{x}_2 \qquad [4.20]$$

with m as the mass of the flap.

Let:

$$\vec{\delta}_A\left(\text{flap}/R_g\right)\cdot\vec{x}_2 = \vec{\delta}_N(\text{flap}/R_g)\cdot\vec{x}_2 + m\,l^2\left(\ddot{\theta}+\Omega^2\,\cos(\theta)\,\sin(\theta)\right) \qquad [4.21]$$

For the blade:

$$\begin{aligned}\vec{\delta}_A(\text{blade}/R_g)\cdot\vec{x}_2 &= \vec{\delta}_M(\text{blade}/R_g)\cdot\vec{x}_2 + \left(\overrightarrow{AM}\wedge M\,\vec{A}_{M,\text{blade}/R_g}\right)\cdot\vec{x}_2 \\ &\approx I_\theta\,\ddot{\theta} + I_\theta\,\Omega^2\,\theta\end{aligned} \qquad [4.22]$$

with I_θ as the blade inertia around the axis (A, x_2).

Then, supposing that the inertial loads of the flap are negligible in comparison to those of the blade:

$$\vec{\delta}_A(\Sigma/R_g)\cdot\vec{x}_2 \approx I_\theta\,\ddot{\theta} + I_\theta\,\Omega^2\,\theta \qquad [4.23]$$

The moment of aerodynamic loads on the flap in A is given by:

$$\begin{aligned}\overrightarrow{M}_A(\text{Aero}\rightarrow\text{flap})\cdot\vec{x}_2 &= \left(\overrightarrow{OA}\wedge\int_{\text{surface}}d\vec{F}_{\text{aero}}\right)\cdot\vec{x}_2 \\ &= -\int_{r_1}^{r_2}\frac{1}{2}\,\rho\,a_v^2\;C_m^v(\delta)\;\left(r\,\Omega\right)^2\;dr\end{aligned} \qquad [4.24]$$

with $C_m^v(i)$, as the coefficient of the moment associated with the flap. Then:

$$\left|\overrightarrow{M}_A(\text{Aero}\rightarrow\text{flap})\cdot\vec{x}_2\right| = \frac{1}{2}\rho\,a_v^2\,\frac{\partial C_m^v}{\partial\delta}\,\delta\left(\frac{r_2^3-r_1^3}{3}\right)\Omega^2 \qquad [4.25]$$

The same goes for the aerodynamic loads on the blade:

$$\begin{aligned}\left|\overrightarrow{M}_A(\text{Aero}\rightarrow\text{blade})\cdot\vec{x}_2\right| &= \frac{1}{2}\rho\,a^2\,\frac{\partial C_m}{\partial\delta}\;\frac{a\,\dot{\theta}}{R\,\Omega}\;\frac{R^3}{3}\Omega^2 \\ &= C\,I_\theta\,\dot{\theta}\end{aligned} \qquad [4.26]$$

with:

$$C = \frac{\gamma}{6}\frac{I_\beta}{I_\theta}\frac{\partial C_m/\partial\delta}{\partial C_p/\partial\alpha}\left(\frac{a}{R}\right)^2 \Omega \qquad [4.27]$$

The torsion equation is written as follows:

$$I_\theta\ \ddot{\theta} + I_\theta\ \Omega^2\ \theta + K_\theta\ \theta = -\frac{1}{2}\rho\ a_v^2\frac{\partial C_m^v}{\partial\delta}\left(\frac{r_2^3 - r_1^3}{3}\right)\Omega^2\ \delta - C\ I_\theta\ \dot{\theta} \qquad [4.28]$$

with K_θ as the angular stiffness at the torsion blade root.

4.4.3. *Ways to control the blade*

The flap has two types of actions:

– a direct effect through lift variation (see equation [4.18]),

– an indirect effect (*servo-effect*) through the angle variation due to the blade torsion (see equation [4.28]).

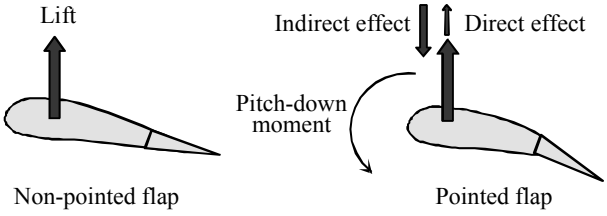

Figure 4.17. *Direct and indirect effects of the flap*

The two effects have opposite directions of variation but, in the case studied, the effect due to the torsion dominates. We set out the following notations:

$$\begin{cases} C_{\delta m} = \dfrac{\partial C_m^v/\partial\delta}{\partial C_p/\partial\delta} & \hat{a} = \dfrac{a_v}{a} \\ \overline{I}_\theta = \dfrac{I_\theta}{I_\beta} & A_3 = \dfrac{r_2^3 - r_1^3}{R^3} \end{cases}$$

Thus, equations [4.28] and [4.29] become:

$$\ddot{\theta} + C\,\dot{\theta} + \left(\Omega^2 + \frac{K_\theta}{I_\theta}\right)\theta = -\frac{\gamma}{6}\frac{1}{\bar{I}_\theta}\frac{\hat{a}}{R} C_{\delta m}\ A_3\ \Omega^2\ \delta \qquad [4.29]$$

$$\ddot{\beta} + \frac{\gamma\,\Omega}{8}\dot{\beta} + \left(\left(1 + \frac{e\ m_s}{I_\beta}\right)\Omega^2 + \frac{K_\beta}{I_\beta}\right)\beta - \frac{\gamma\,\Omega^2}{8}\theta = \frac{\gamma\,\Omega^2}{8}\hat{a}\ A_4\ C_{\delta p}\ \delta \qquad [4.30]$$

The system can be written in the form of a matrix:

$$\begin{bmatrix}\ddot{\theta}\\ \ddot{\beta}\end{bmatrix} + \begin{bmatrix}2\,\lambda_\theta\ \omega_\theta & 0\\ 0 & 2\,\lambda_\beta\ \omega_\beta\end{bmatrix}\begin{bmatrix}\dot{\theta}\\ \dot{\beta}\end{bmatrix} + \begin{bmatrix}\omega_\theta^2 & 0\\ -2\,\lambda_\beta\ \omega_\beta\,\Omega & \omega_\beta^2\end{bmatrix}\begin{bmatrix}\theta\\ \beta\end{bmatrix} = \begin{bmatrix}H_1\\ H_2\end{bmatrix}\delta \qquad [4.31]$$

with the following notations:

$$\omega_\beta^2 = \left(\left(1 + \frac{e\ m_s}{I_\beta}\right)\Omega^2 + \frac{K_\beta}{I_\beta}\right) \quad \text{and} \quad \omega_\theta^2 = \left(\Omega^2 + \frac{K_\theta}{I_\theta}\right) \qquad [4.32]$$

$$2\,\lambda_\beta\ \omega_\beta = \frac{\gamma\,\Omega}{8} \quad \text{and} \quad 2\,\lambda_\theta\ \omega_\theta = C \qquad [4.33]$$

$$H_1 = -\frac{\gamma}{6}\frac{1}{\bar{I}_\theta}\hat{a}\ C_{\delta m}\ A_3\ \Omega^2 \quad \text{and} \quad H_2 = \frac{\gamma\,\Omega^2}{8}\hat{a}\ A_4\ C_{\delta p} \qquad [4.34]$$

Based on the system [4.31], we can define the torsion complex response of the blade:

$$\bar{\theta} = \frac{H_1}{\left(\omega_\theta^2 - \omega^2 + 2\,i\,\lambda_\theta\ \omega_\theta\ \omega\right)}\bar{\delta} \qquad [4.35]$$

and equally the flapping response of the blade:

$$\bar{\beta} = \frac{H_2}{\left(\omega_\beta^2 - \omega^2 + 2\,i\,\lambda_\beta\ \omega_\beta\ \omega\right)}\left(1 + 2\,\lambda_\beta\,\omega_\beta\ \Omega\frac{H_1}{\left(\omega_\theta^2 - \omega^2 + 2\,i\,\lambda_\theta\ \omega_\theta\ \omega\right)}\right)\bar{\delta} \qquad [4.36]$$

The flapping response $\overline{\beta}$ depends on the flap control $\overline{\delta}$. The transfer from $\overline{\delta}$ to $\overline{\beta}$ is achieved through two transfer functions:

– between $\overline{\delta}$ and $\overline{\theta}$, the flap motion and the blade pitch,

– between $\overline{\theta}$ and $\overline{\beta}$, the pitch motion of the blade and the rotor flapping.

In order to improve the control efficiency, the principle of dynamic amplification is used. For instance, we define the blade root in order to get close to the first torsion frequency of the blade, from 1Ω to 1.5Ω. The motion effect of the flap is increased by the proximity of the excitation frequency (1Ω for the cyclic control and the static for the lift) of the torsion frequency of the blade. The torsion response of the blade which acts directly on the aerodynamic angle causes the rotor flapping by the mechanism which has already been explained in the case of control through a cyclic swashplate. The principle of dynamic amplification makes it possible to decrease the control loads and to remove the hydraulic servo-controls which are necessary for control through the cyclic swashplate. This benefit is measured against a loss of profile aerodynamic efficiency entailed by flap installation.

The numeric application was carried out for a 6 ton class helicopter; the torsion frequency of the blade was set at 1.5Ω.

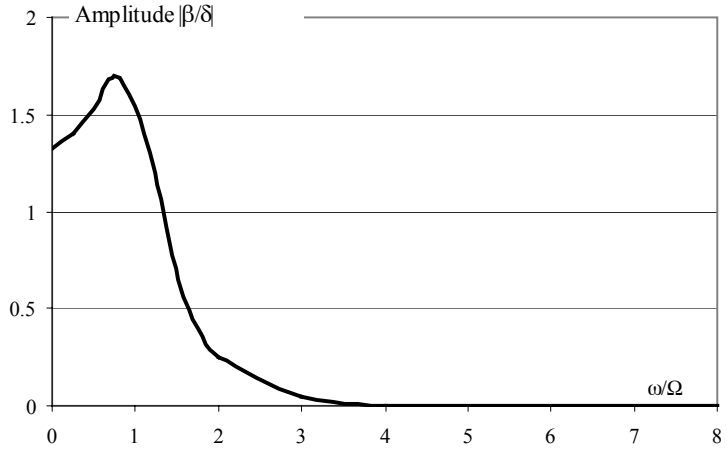

Figure 4.18. *Flapping transfer function β according to the flap pitch δ for the frequency of low torsion mode (1.5Ω)*

Two points of the curve are rather interesting: the value $\omega = 0$, corresponding to the collective pitch, and the value $\omega = \Omega$, corresponding to the cyclic pitch. The gains of these two frequencies must be high in order for a reasonable flap

displacement to be enough to reach the extreme pitch values so as to ensure the control of the device. These gains depend on the aerodynamic characteristics of the flap, its position with respect to the span and chord of the blade and, obviously, the torsion frequency setting of the blade.

The following observations can be made:

– the gain of 1.45 and 1.80 between the flap motion and the rotor flapping: static (0 frequency) and dynamic (1Ω frequency) (see Figure 4.18),

– the flapping response with respect to the flap motion has a 90º phase difference. This is due to the fact that the frequency of the torsion mode is higher than 1Ω and the phase difference between blade torsion and flap motion is close to zero at the rotor control frequency (1Ω) (see Chapter 2). Between the torsion motion of the blade (pitch) and the flapping we find the conventional 90º phase difference. We obtain a configuration which is very similar to the control through cyclic swashplate (see section 4.2.2).

In Figure 4.19, we see the rotor response for a high torsion natural frequency. We note that the system efficiency is very low.

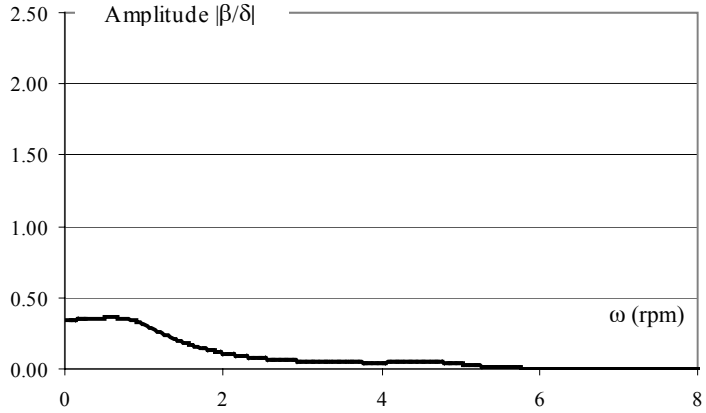

Figure 4.19. *Flapping transfer function β according to the flap pitch δ for the high torsion mode frequency (4.5Ω)*

For this type of control, the torsion mode of the blade must be positioned very closely to the excitation frequency in order to benefit from the dynamic amplification, as shown in Figure 4.18.

Chapter 5

Non-Homokinetic Couplings

5.1. Introduction

The first Cardan joint application dates back to the 16th century when G. Gardano invented the system that isolated the marine compasses from the ships' motions [KER 68, TEC 97].

Figure 5.1. *Cardan joint – link of two non-coaxial axes: 2 CV. Photo: F. Combes*

The Cardan joint is also called *Hooke's joint*. This name comes from the name of an English inventor, R. Hooke, who filed a patent on the transmission of movement between two joint shafts. The problem raised by R. Hooke is still fundamental for rotating systems: "How do you link two shafts whose rotation axes are not coaxial?".

Due to the way it operates, this type of link is an important source of vibrations for rotating systems. This chapter will deal with the practical problems that occur during the dimensioning of such systems.

5.2. Analysis of operation

In order to understand the operation of the Cardan joint (Figure 5.1), it is important to analyze how the rotation speed of the driven shaft depends on the rotation speed of the drive shaft. The first 2 CV had a front wheel Cardan joint which, for curves and slopes, would lead to vibrations felt by the driver. Double Cardan joints solved this problem. The principle of the link through the Cardan joint is shown in Figure 5.2. The rotation speed of the drive shaft is considered constant. The Cardan joint consists of an input shaft and an output shaft linked together by a spider.

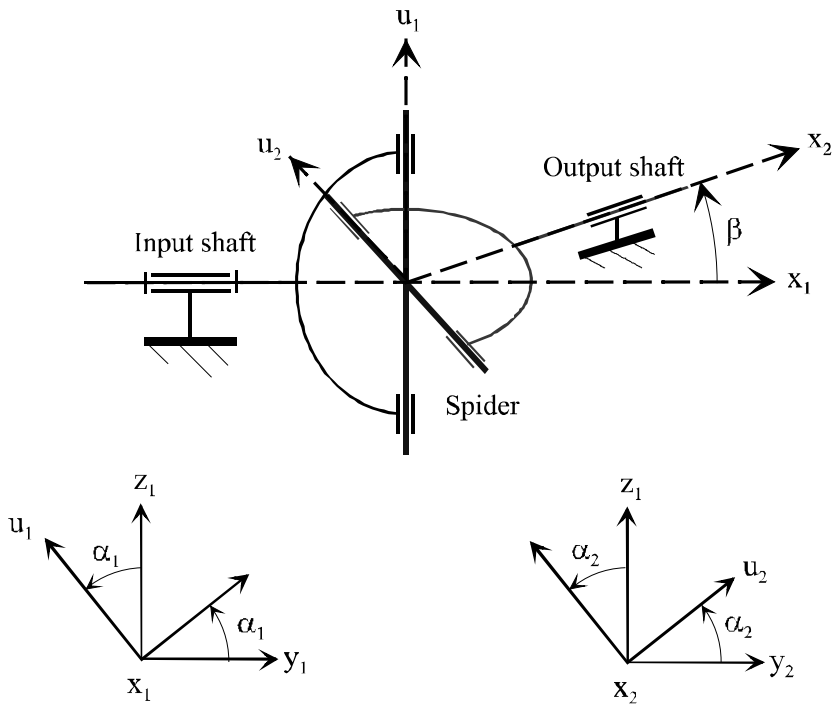

Figure 5.2. *Cardan joint – kinematic diagram*

5.2.1. *Parametric transformation*

We note by β the angle between the two shafts. This angle is constant. When the drive shaft turns at an angle α_1, the rotation angle of the output shaft is α_2.

The relationship between $\alpha_2(t)$ and $\alpha_1(t)$, which defines the input/output law, is obtained by expressing the perpendicularity of the axes of the coupling pins. Hence, it is shown that:

$$\begin{aligned}\vec{u}_2 \cdot \vec{u}_1 &= \left(\cos(\alpha_2)\,\vec{y}_2 + \sin(\alpha_2)\,\vec{z}_1\right)\cdot \vec{u}_1 \\ &= \cos(\alpha_2)\,\left(\cos(\beta)\,\vec{y}_1 - \sin(\beta)\,\vec{x}_1\right)\cdot \vec{u}_1 + \sin(\alpha_2)\cos(\alpha_1) \\ &= -\cos(\alpha_2)\cos(\beta)\,\sin(\alpha_1) + \sin(\alpha_2)\cos(\alpha_1)\end{aligned} \qquad [5.1]$$

The perpendicularity makes it possible to define the relationship linking the parameters:

$$\vec{u}_2 \cdot \vec{u}_1 = 0 \quad \Rightarrow \quad \tan(\alpha_2) = \cos(\beta)\,\tan(\alpha_1) \qquad [5.2]$$

The derivative of this relationship leads to:

$$\left[1+\tan^2(\alpha_2)\right]\dot{\alpha}_2 = \cos(\beta)\,\left[1+\tan^2(\alpha_1)\right]\dot{\alpha}_1 \qquad [5.3]$$

Let:

$$\frac{\dot{\alpha}_2}{\dot{\alpha}_1} = \frac{1+\tan^2(\alpha_1)}{1+\tan^2(\alpha_2)}\cos(\beta) = \frac{\cos(\beta)}{1-\sin^2(\beta)\sin^2(\alpha_1)} \qquad [5.4]$$

The transmission ratio between the input speed and the output speed is not constant. It depends on the position of the input shaft. Thus, we show that this type of transmission does not verify the homokinetic property.

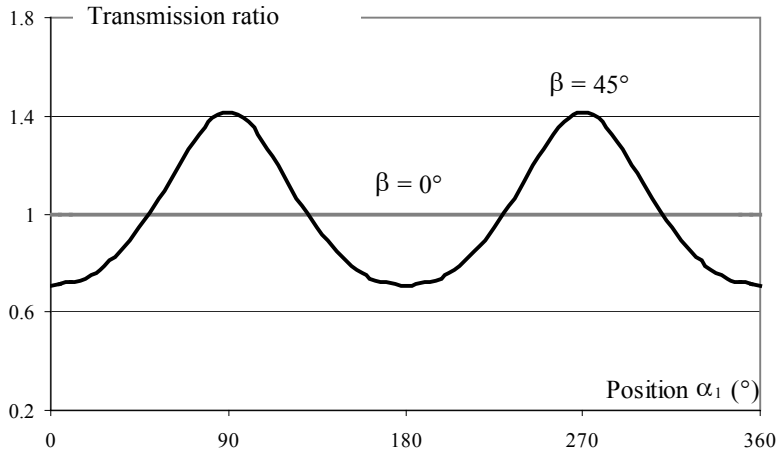

Figure 5.3. *Transmission ratio of a Cardan joint*

This kinematic feature can have consequences on the kinematic performances of the system. In certain cases, these are the dynamic concerns which cause the bad functioning of this type of non-homokinetic link.

5.2.2. *Effects of non-homokinetics: modulation of acceleration*

We suggest analyzing the accelerations to which the receiver is subjected in this type of transmission. These are representative of dynamic excitations.

We note:

$$\begin{cases} \alpha_2(t) = \Omega\, t + \theta_2(t) \\ \alpha_1(t) = \Omega\, t + \theta_1(t) \end{cases} \qquad [5.5]$$

with:

– Ω: speed of rotation (constant) of the drive shaft,

– θ_1: dynamic perturbations of the drive shaft,

– θ_2: dynamic perturbations of the driven shaft.

This variable change leads to:

$$\frac{\dot{\alpha}_2}{\dot{\alpha}_1} = \frac{\Omega + \dot{\theta}_2}{\Omega + \dot{\theta}_1} = \frac{\cos(\beta)}{1 - \sin^2(\beta)\ \sin^2(\Omega t)} \qquad [5.6]$$

Since the angle β is generally small, we can make the following approximation:

$$\frac{\Omega + \dot{\theta}_2}{\Omega + \dot{\theta}_1} \approx \cos(\beta)\left(1 + \sin^2(\beta)\sin^2(\Omega t)\right)$$

if:

$$\Omega + \dot{\theta}_2 \approx \left(\cos(\beta)\ \left(1 + \sin^2(\beta)\ \sin^2(\Omega\, t)\right)\right)\ \left(\Omega + \dot{\theta}_1\right) \qquad [5.7]$$

Equation [5.7] is derived with respect to time:

$$\ddot{\theta}_2 = \cos(\beta)\ \left[\left(\Omega \sin^2(\beta)\ \sin(2\,\Omega\, t)\right)\ \left(\Omega + \dot{\theta}_1\right) + \left(1 + \sin^2(\beta)\ \sin^2(\Omega\, t)\right)\ \ddot{\theta}_1\right] \qquad [5.8]$$

Taking into account the order of magnitude of the different terms, we show that:

$$\ddot{\theta}_2 \approx \cos(\beta)\ \left[\Omega^2\ \sin^2\ (\beta)\ \sin(2\,\Omega\ t) + \ddot{\theta}_1\right] \qquad [5.9]$$

In the case of a Cardan joint and for a constant speed of the drive shaft, we obtain a modulation of acceleration of the operated shaft in 2Ω.

This modulation of acceleration, depending on β and Ω^2 is expressed by:

$$\ddot{\theta}_2 \approx \cos(\beta)\ \Omega^2\ \sin^2(\beta)\ \sin(2\,\Omega\,\tau) \qquad [5.10]$$

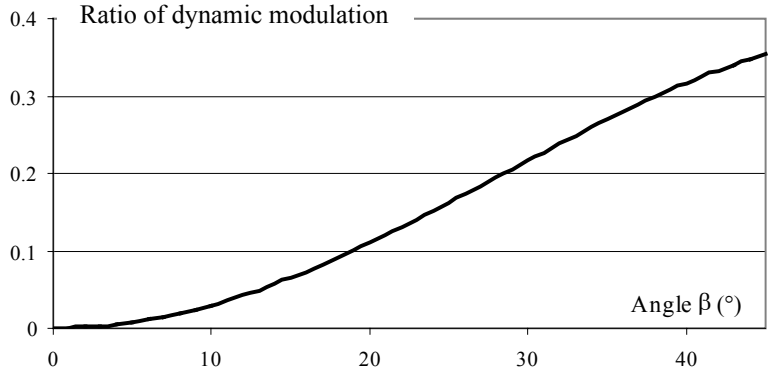

Figure 5.4. *Evolution of the modulation of acceleration according to position β of the axes*

$\frac{\ddot{\theta}_2}{\Omega^2}$: ratio of dynamic modulation

If we consider that a mechanism is operated by a Cardan joint, we prove that the mechanism entails oscillations of angular frequency double the speed of rotation Ω.

5.2.3. *Effects of non-homokinetics: variation of the motor torque*

Experience shows that it is interesting to see the influence of this type of joint when the drive shaft is highly deformable. The modeling used is illustrated in Figure 5.6.

Figure 5.5. *Illustration of a mechanism operated by dynamic Cardan joints. Illustration: C. Guarnieri (Eurocopter)*

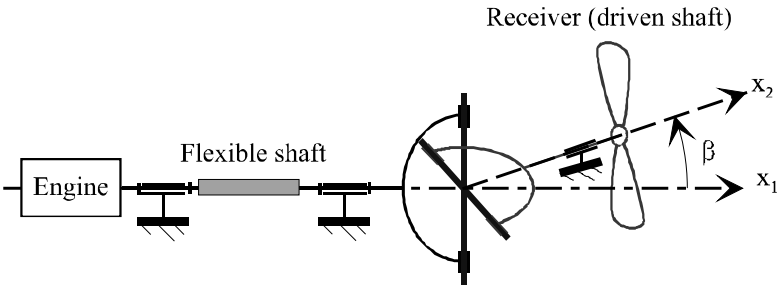

Figure 5.6. *Cardan joint coupled to a flexible shaft*

We have:

– J_R: inertia of the receiver (driven shaft),

– $C_{joint/constant}$: constant part of the torque transmitted through the Cardan joint,

– ΔC_{joint}: dynamic part of the torque transmitted through the Cardan joint.

We apply the dynamic moment theorem to the receiver (driven shaft) [BIE 92]:

$$J_R\ \ddot{\theta}_2 = C_{joint\to 2} - C_{ext\to 2} = \left[C_{joint} \right)_{constant} + \Delta C_{joint\to 2} \Big] - C_{resistant\to 2} \quad [5.11]$$

While in the static position, the constant resistant torque is:

$$C_{joint} \Big)_{constant} = C_{resistant\to 2} = \text{constant}$$

thus, the dynamic part of equation [5.11] becomes:

$$J_R\ \ddot{\theta}_2 = C_{joint\to 2} \quad [5.12]$$

We assume that the behavior of the Cardan joint is perfect (no energy loss) and that the variation of the kinetic energy of the Cardan components (coupling pins) is negligible. The preservation of force with respect to the Cardan joint gives:

$$P\left(\text{input shaft} \to \text{joint}/R_g\right) + P\left(2 \to \text{joint}/R_g\right) = 0 \quad [5.13]$$

If we introduce the kinematic law [5.4] and if we take into account only the variable part, then we obtain:

$$C_{\text{drive shaft}\rightarrow\text{joint}} = -\frac{1}{\cos(\beta)}\Delta C_{2\rightarrow\text{joint}} \qquad [5.14]$$

The mechanical action of the flexible shaft on the Cardan joint is modeled by an action of linear stiffness; let:

$$C_{\text{driveshaft}\rightarrow\text{joint}} = -K\,\theta_1 \qquad [5.15]$$

Thus, the behavior equation [5.12] of the 2nd shaft can be written:

$$J_R\,\ddot{\theta}_2 + (K\,\theta_1)\,\cos(\beta) = 0 \qquad [5.16]$$

or, by introducing the kinematic relationship (equation [5.10]) due to the Cardan joint, let:

$$\ddot{\theta}_2 \approx \cos(\beta)\,\left(\ddot{\theta}_1 + \Omega^2\,\sin^2(\beta)\,\sin(2\,\Omega\,t)\right) \qquad [5.17]$$

We obtain:

$$J_R\,\ddot{\theta}_1 + K\,\theta_1 = -J_R\,\Omega^2\,\sin^2(\beta)\,\sin(2\,\Omega\,t) \qquad [5.18]$$

an equation that can be written:

$$\ddot{\theta}_1 + \omega_t^2\,\theta_1 = -\,\Omega^2\,\sin^2(\beta)\,\sin(2\,\Omega\,t) \qquad [5.19]$$

with: $\omega_t^2 = \dfrac{K}{J_R}$

Differential equation [5.19] makes it possible to obtain the value $\theta_1(t)$ for forced speed:

$$\theta_1(t) = -\frac{\Omega^2\sin^2(\beta)}{\omega_t^2 - 4\Omega^2}\sin(2\Omega t) \qquad [5.20]$$

Then we can also express, through equation [5.15], the torque experienced by the engine:

$$C_{\text{engine}\rightarrow\text{joint}} = K\frac{\Omega^2 \sin^2(\beta)}{4\Omega^2 - \omega_t^2}\sin(2\Omega t) \qquad [5.21]$$

This shows that a Cardan type joint causes a dynamic moment in 2Ω in the rotor mast, whose amplitude depends on the angle between the shafts (β) as well as on the adaptation of the cinematic chain (position of natural angular frequency ω_t with respect to Ω).

This disturbing engine torque, defined by equation [5.21] in the shaft, has two negative consequences:

– the set of alternate torsion *loads* which can be a nuisance if the torsion modes of the cinematic chain are close to 2Ω,

– the set of *vibrations* due to the introduction of the dynamic moment in 2Ω, which can cause discomfort to the passengers of a vehicle having a Cardan joint.

It can be proved that higher and multiple harmonics of 2Ω are also present, but with much lower amplitudes. We have ignored them.

In the case of a double joint (see Figure 5.7), the dynamic motion appears only on the intermediate shaft. In practice, this shaft is very rigid and light in order to avoid considerable dynamic effects.

It is important to analyze the methods which make it possible to suppress the oscillations in 2Ω caused by the Cardan joint. We mean by a homokinetic joint a system that makes it possible to transmit a rotational movement from a drive shaft to a driven shaft, with no angular difference, irrespective of the kink angle between these two shafts and irrespective of its variation. We say that the Cardan joint is not homokinetic.

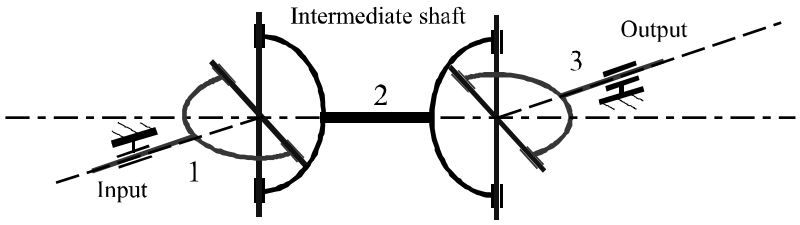

Figure 5.7. *Double Cardan joint*

5.3. Solutions to make the link homokinetic

5.3.1. *Double Cardan*

A solution to obtain a homokinetic link consists of linking two Cardan joints in series, as illustrated in Figure 5.8. Hence, we have a double Cardan joint. This type of link is homokinetic, provided the kink angle between the drive shaft and the driven shaft is equally distributed on the two Cardans.

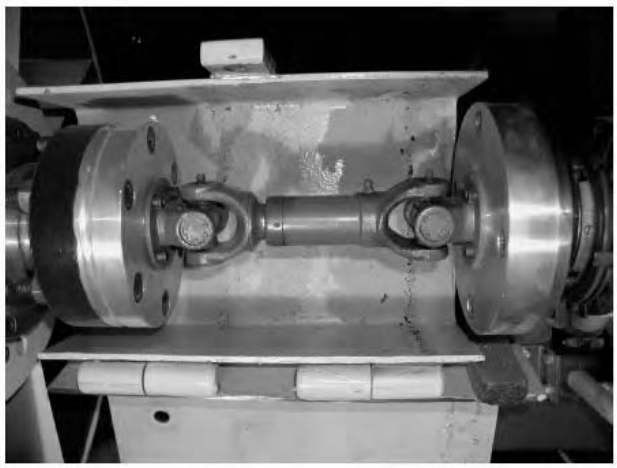

Figure 5.8. *Cardan joint for a transmission. Photo: J. Szabela*

An example of a homokinetic joint application is found on a front wheel drive car. The functions of drive and direction are concentrated on the front wheels.

When the front wheels are straight, the application of the Cardan joint is obvious because, for the angle $\beta = 0$, the speed of the driven shaft and that of the drive shaft are the same, as long as the wheels are blocked ($\beta = 0$). The non-homokinetic character of the Cardan joint entails cyclic acceleration and deceleration of the wheel at a frequency of two times per turn (in 2Ω). The car will thus undergo unacceptable vibrations and alternate constraints. For this type of application the homokinetic joint is essential.

Another conventional application of the double joint is the test stand used for the endurance analysis of power transfer systems. It involves subjecting the transmission unit with a very low power feed to a large torque.

The kinematic chain is a closed chain and the engine has the role of only compensating the losses. A hydraulic system enables the introduction of the torsion torque within the transmission chain. The geometry of elements supposes complex kinematics with high speeds of rotation. The double Cardan joint makes it possible to close the kinematic chain by preserving the homokinetic properties.

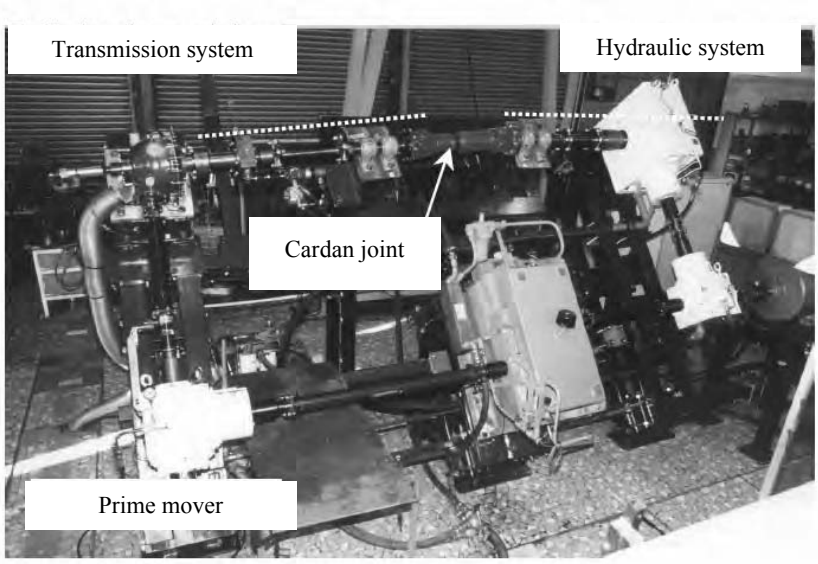

Figure 5.9. *Cardan joint for the test stand of transmission units. Photo: Eurocopter*

5.3.2. *Introduction of high flexibility*

The principle of this solution consists of introducing torsion flexibility which makes it possible to have a very small torsion angular frequency compared to 2Ω (see Figure 5.10).

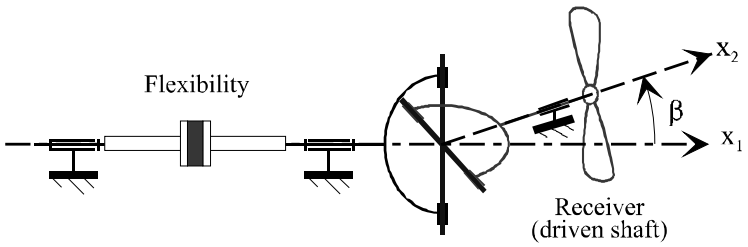

Figure 5.10. *Artificial flexibility associated with a Cardan joint*

This solution is often limited by the strength of the elastic element introduced in the line shafting. The elastic element breaks under the effect of the static torque.

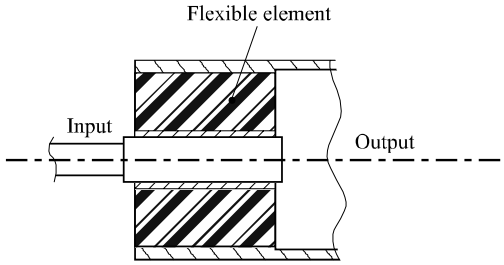

Figure 5.11. *Flexibility introduced in a line shafting*

We can also imagine greatly increasing the stiffness of the shaft so that the torsion natural angular frequency is higher than 2Ω. This solution is very difficult to apply because it consists of increasing, at the same time, the inertias of the line shafting.

5.3.3. *Homokinetic drive system of a tilt rotor*

We will analyze the link used for the rotor drive of a tilt rotor (see Figure 5.12).

A tilt rotor is the intermediate between a helicopter and a plane. Thus, thanks to its ability to tilt the rotors on the wing tips, it can take off vertically and then fly horizontally like a plane.

Figure 5.12. *Rotor of a V22 tilt rotor.*
Photo: Eurocopter

The following analysis deals with the rotor of a tilt rotor. Figure 5.13 shows the hub of this rotor. The transmission of the engine torque, from the rotor mast to the star, is ensured by three interconnecting links.

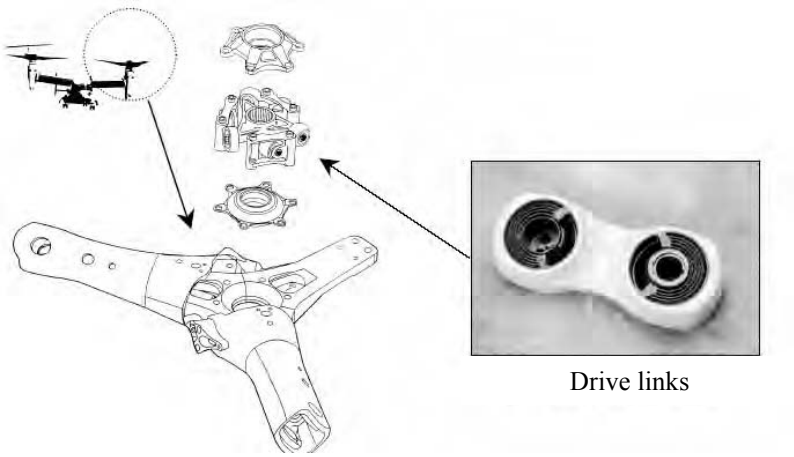

Figure 5.13. *Rotor of a V22 tilt rotor and drive links. Photo: LORD Corporation*

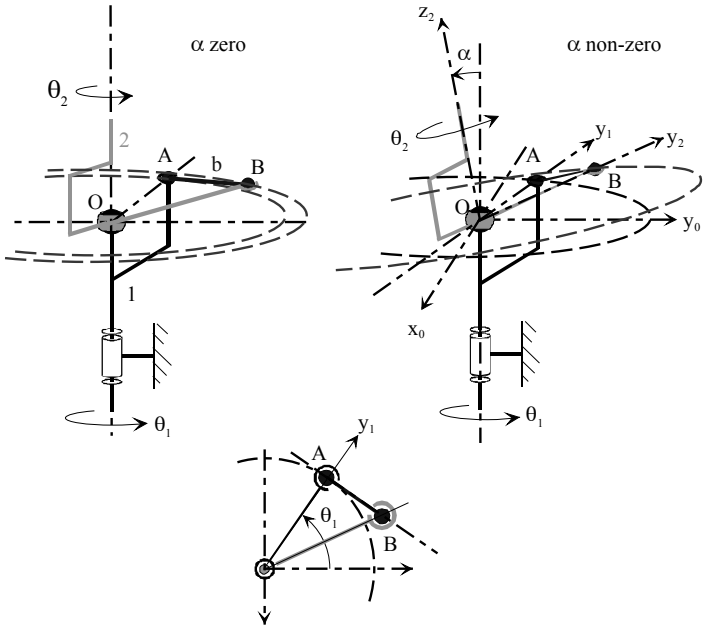

Figure 5.14. *Kinematic diagram of a link*

A link works in the following way: point A follows the rotational movement in the plane that is perpendicular to the rotor mast; point B follows the rotational movement in an inclined plane (angle measured by α).

We suggest analyzing the behavior of this type of rotor and the influence of such a link on the drive. Each one of the analyzed elements is non-deformable.

Let the parametric transformation be:

$$\overrightarrow{OA} = r\,\vec{y}_1$$
$$\overrightarrow{OB} = d\,\vec{y}_2$$
$$\overrightarrow{AB} = L\,\vec{u}$$

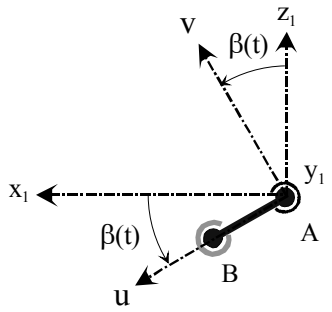

Figure 5.15. *Kinematic diagram of a link*

We are interested in the speed of point B:

$$\vec{V}_{B,2/R_g} = \left.\frac{d\overrightarrow{OB}}{dt}\right)_{R_g} = \left.\frac{dr\,\vec{y}_1}{dt}\right)_{R_g} + \left.\frac{dL\,\vec{u}}{dt}\right)_{R_g} \qquad [5.22]$$
$$= -r\,\Omega\,\vec{x}_1 - L\,\Omega\cos(\beta)\,\vec{y}_1 + L\,\dot{\beta}\,\vec{v}$$

Hence, the resulting Galilean acceleration following x_1 is:

$$\vec{A}_{B,2/R_g}\cdot\vec{x}_1 = \frac{d\left(\vec{V}_{B,2/R_g}\cdot\vec{x}_1\right)}{dt} - \vec{V}_{B,2/R_g}\cdot\Omega\vec{y}_1 \qquad [5.23]$$

If we use equation [5.22] we obtain:

$$\begin{aligned}\vec{A}_{B,2/R_g} \cdot \vec{x}_1 &= \frac{d\left(\vec{V}_{B,2/R_g} \cdot \vec{x}_1\right)}{dt} - \vec{V}_{B,2/R_g} \cdot \Omega\, \vec{y}_1 \\ &= L\left(\ddot{\beta}\, \sin(\beta) + \dot{\beta}^2\, \cos(\beta)\right) + L\, \Omega^2\, \cos(\beta)\end{aligned} \quad [5.24]$$

The motion of B is in an inclined plane α; we can say that β has the following form:

$$\beta(t) = \beta_0 + \beta_c \cos(\Omega t) \quad [5.25]$$

Moreover, if β is small, equation [5.24] is written:

$$\begin{aligned}\vec{A}_{B,2/R_g} \cdot \vec{x}_1 &\approx L\left(\ddot{\beta}\, \beta + \dot{\beta}^2\right) + L\, \Omega^2 \\ &= L\, \Omega^2 \left(1 - \left(\beta_0\, \beta_c\, \cos(\Omega t) + \beta_c^2\, \cos(2\, \Omega t)\right)\right)\end{aligned} \quad [5.26]$$

For the type of rotor used:

– $\beta_0 \cong 0$ (static deformation only of the rotor disk),

– $\beta_0 \cong$ star inclination.

Hence:

$$\vec{A}_{B,2/R_g} \cdot \vec{x}_1 \approx L\, \Omega^2\, \left(1 - \beta_c^2\, \sin(2\, \Omega t)\right) \quad [5.27]$$

The in-plane acceleration of the link which drives the solid 2 is not constant. We find here the conventional problem of 2Ω, similar to the Cardan joints, if we take into account only one drive link. In this case, the rotor has a non-homokinetic behavior, which leads us to the same conclusions as those reached in the previous chapter.

In order to solve this problem, we can use a multiple link drive. Since the system is hyperstatic, flexibility is introduced in the transmission links.

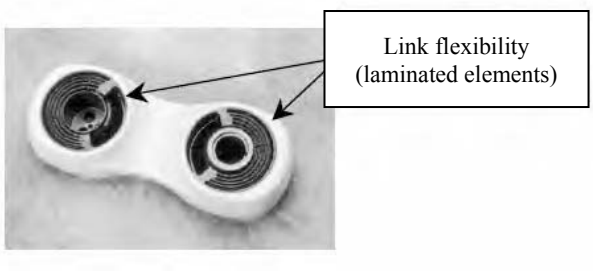

Figure 5.16. *Transmission link: introduction of flexibility. Photo: LORD Corporation*

In this case, the motor torque link will be:

$$\begin{aligned}\vec{M}_O(\text{links} \to 2) &= \sum_{i=1}^{3} \overrightarrow{OB_i} \wedge \vec{R}\ (\text{links} \to 2) \\ &= \sum_{i=1}^{3} \overrightarrow{OB_i} \wedge R\ \vec{u}_i \\ &= \sum_{i=1}^{3} \left(r\ \vec{x}_{1i} + L\ \vec{u}\right) \wedge R\ \vec{u}_i \\ &= -\sum_{i=1}^{3} \left(r\ R \sin(\beta)\ \vec{x}_{1i}\right) - \sum_{i-1}^{3} \left(r\ R \cos(\beta)\right) \vec{z}_1\end{aligned} \qquad [5.28]$$

If we introduce the inclination of the rotor, which implies for the parameter $\beta(t)$ a law of the following type:

$$\beta_i(t) = \beta_c\ \cos\left(\Omega\ t + 2\ \pi \frac{(i-1)}{3}\right) \qquad [5.29]$$

with the help of [5.28], we show that:

$$\begin{aligned}\vec{M}_O(\text{links} \to 2) &\approx -\sum_{i=1}^{3} \left(r\ R\ \beta\ \vec{x}_{1i}\right) - \sum_{i-1}^{3} \left(r\ R\right) \vec{z}_1 \\ &= -3\ r\ R\ \vec{z}_1\end{aligned} \qquad [5.30]$$

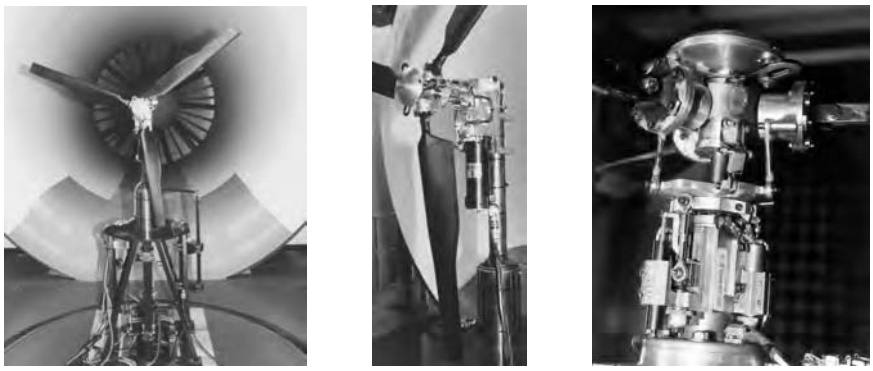

Figure 5.17. *Mock-up of a tilt rotor. Photos: ENSAM, Aix-en-Provence*

The coplanar drive torque is constant in this instance. It is thus shown that the behavior is similar, during flapping, to a homokinetic rotor. The rotor does not oscillate in 2Ω.

The flexible elements, shown in Figure 5.16, are those "receiving" the excitations in 2Ω. Their stiffness must be sufficiently high so that they do not become deformed under the effect of the static torque. However, this stiffness must be sufficiently low in order to have acceptable dynamic loads in 2Ω, because the system operates dynamically during the imposed movement.

Another example of such a link is the rotor of a rotor model made by the students of the National School of Arts and Professions in Aix-en-Provence. This model (Figure 5.17) was made in accordance with Froude's similarity for a dynamic study of stability in a wind tunnel.

The elastic elements consisted of channel-shaped elements, as shown in Figure 5.17.

Chapter 6

Aerodynamic Excitations

6.1. Introduction

In certain flight conditions, airplanes and helicopters are subject to aerodynamic excitation generated by the interaction of the flow around the front part of the aircraft with the rear surfaces. Figure 6.1 illustrates a wind tunnel simulation with a helicopter model. On a helicopter, this phenomenon is referred to as *tail-shake*. This term perfectly describes the phenomenon, because basically the excitation is at the same frequency as a flexion mode of the tail boom.

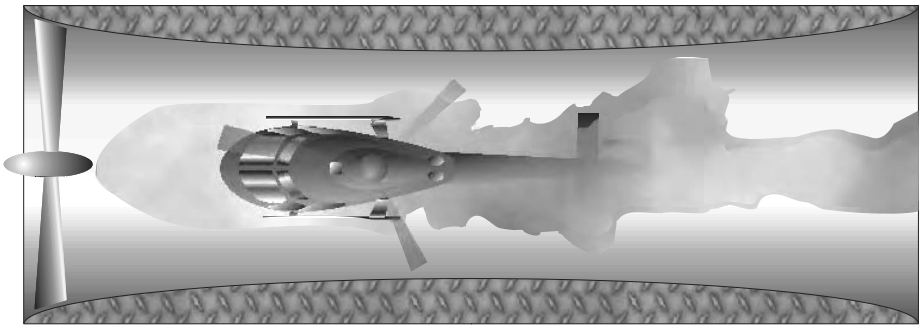

Figure 6.1. *Wind tunnel simulation of tail-shake.*
Photo: Eurocopter

The tail-shake phenomenon has several causes: the Karman vortices created by the rotor fairing and the vortices created by the main rotor.

6.2. Excitations caused by the Karman vortices – fuselage effects

This phenomenon is due to the separation of the boundary layer on a surface, which creates alternate vortices – usually called Karman vortices.

This phenomenon is illustrated by the behavior of the flow around a circular cylinder at different speeds or at different Reynolds numbers R_e [BLE 77]. This number, which is a characteristic of the flow, is defined by:

$$R_e = \frac{U\,D}{\nu} \qquad [6.1]$$

where U is the flow speed, D is the reference diameter of the cylinder and v is the fluid cinematic viscosity.

The flow regimes can be defined as follows:

– if $R_e < 1$, the flow is viscous and laminar without boundary layer separation,

– if $1 < R_e < 40$, symmetric laminar separation occurs,

– if $40 < R_e < 3.10^5$, the speed is subcritical, and there is boundary layer separation and alternate Karman vortices,

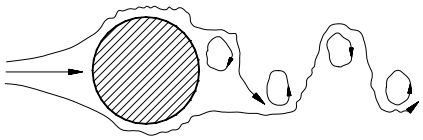

Figure 6.2. *Regular Karman vortices*

– if $3.10^5 < R_e < 6.10^6$, the speed is transient with boundary layer separation and the formation of irregular vortices,

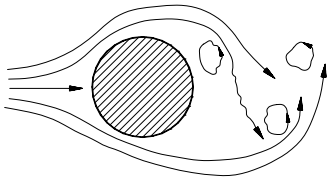

Figure 6.3. *Irregular vortices*

– if $R_e > 6.10^6$, the speed is supercritical and turbulent separation occurs. The boundary layer separation zone becomes narrower.

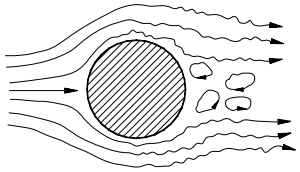

Figure 6.4. *Turbulent flow*

The alternate vortices create dynamic loads that stimulate the surfaces on which the flow arrives. There is a range of Reynolds numbers (see Figure 6.4) in which the excitation is wideband, the excitation frequency varying randomly within an interval [BLE 77, SIM 96].

This multitude of excitations is illustrated by the Strouhal number S:

$$S = \frac{Fs\ D}{U} \qquad [6.2]$$

where:

– Fs is the frequency of vortex shedding,

– D is the reference diameter,

– U is the flow speed.

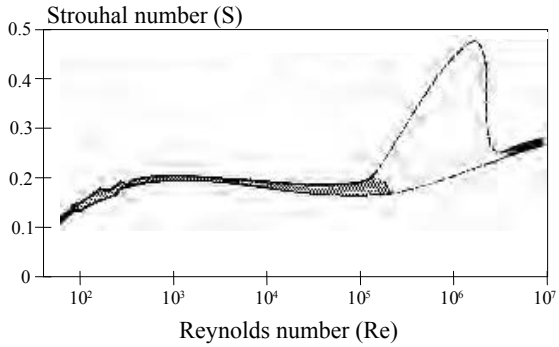

Figure 6.5. *Strouhal number versus Reynolds number*

In the Reynolds No. range from 40 to 3.10^5, the Strouhal number is constant and close to 0.2. In these conditions, the excitation frequency is directly proportional to the flow speed.

For a helicopter, vortices are generated by the slipstream of the rotor head and the engine covers, as illustrated in Figure 6.6.

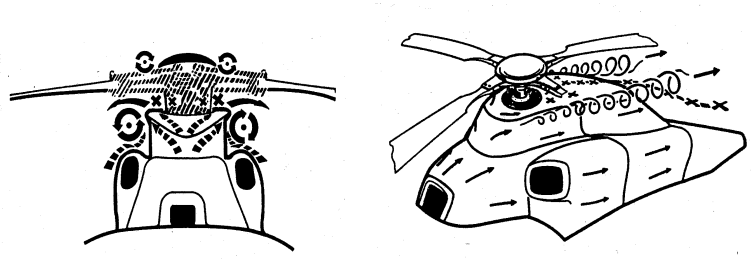

Figure 6.6. *Helicopter rotor and its fairing*

The vibrations that occur can be amplified if the natural frequency of the system is close to the excitation frequency. As the speed of the helicopter increases, the shedding frequency of these vortices increases until it reaches the natural frequency of the structural mode. The interaction zone, referred to as *lock-in*, is relatively large due to the multitude of excitation frequencies (see Figure 6.7).

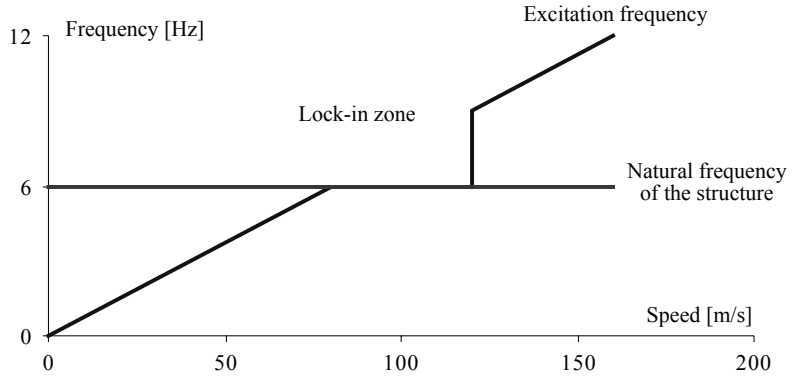

Figure 6.7. *Interaction of aerodynamic loads/resonant structure*

The *lock-in* phenomenon was illustrated in the wind tunnel during a test conducted on a circular cylinder.

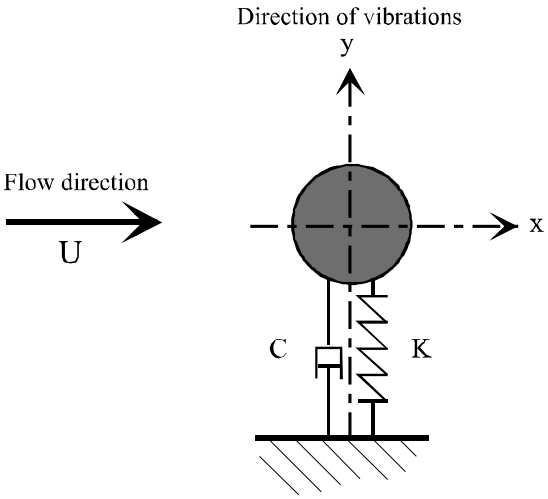

Figure 6.8. *Wind tunnel test model (cylinder)*

We have:

– D: cylinder diameter,

– M: cylinder mass,

– K: link stiffness,

– C: link damper,

– A_y: amplitude of y-axis vibrations.

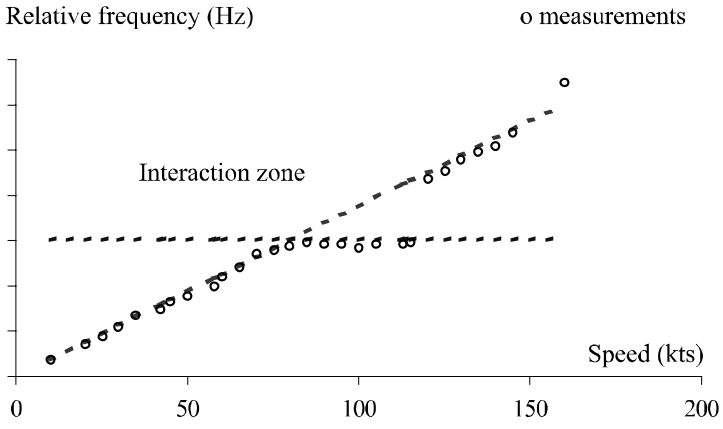

Figure 6.9. *Frequencies versus model flow speed*

The flow conditions are taken such that the frequency of appearance of the phenomenon corresponds to 6 Hz.

Figure 6.10 shows that in the speed range between 90 and 130 kts, the vibrations increase.

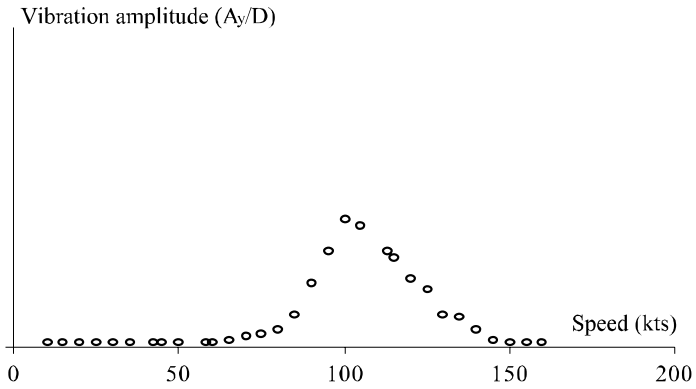

Figure 6.10. *Lock-in phenomenon – tests with the model*

6.3. Aerodynamic excitations generated by the main rotor of a helicopter

Apart from the vortices caused by the rotor head, there are also multiple excitations from the rotor harmonics. During forward flight, the airflow around the rotor shaft assembly, blade shanks and blade tip creates a stationary vortex behind the rotor head. This horizontally aligned vortex is stimulated by the motion of the blades at the frequency $b\Omega$; where b is the number of blades and Ω the rotor rotational speed.

The second harmonics ($2b\Omega$) have a significant effect, but the wind tunnel study shows that these vortices also have other harmonics, in particular at 1Ω and 2Ω. These harmonics can only be generated by rotary parts turning at 1Ω and 2Ω and feeding energy to the vortex.

This is the case, for example, for the drive scissors (see Figure 6.11), which are double and generate excitation at 2Ω

The harmonic excitations of Ω can create differences between the blades, for example, airfoil dispersion.

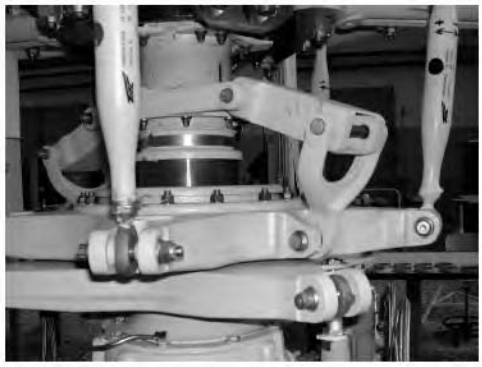

Figure 6.11. *Drive scissors of a helicopter – a source of aerodynamic interference. Photo: Eurocopter*

Another source of tail-shake is the deviation of the rotor slipstream due to the Magnus effect. The rotation of the rotor creates a higher pressure in the advancing blade zone (see Figure 6.12), which causes the airflow to deflect to the right side of the aircraft (the side – left or right – depends on the direction of rotation chosen for the rotor).

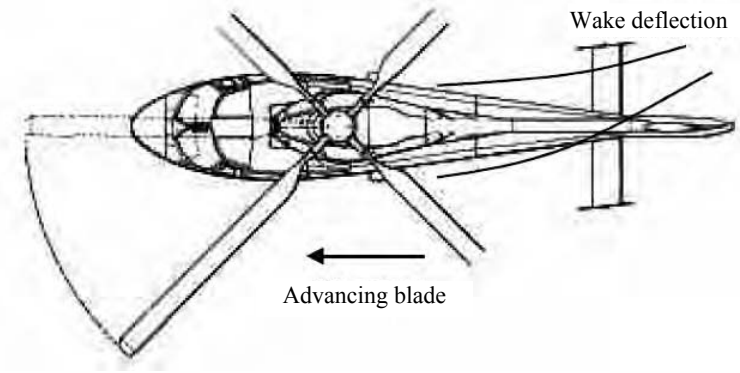

Figure 6.12. *Wake deflection caused by the Magnus effect*

This hypothesis is confirmed by the speed maps (Figure 6.15) carried out in a wind tunnel on a small sized model.

In these tests, different speed components were measured by the lazer velocimetry technique on a virtual grid positioned slightly upstream of the vertical stabilizer leading edge (Figure 6.13).

Figure 6.13. *Wind tunnel model during lazer velocimetry tests. Photo: Eurocopter*

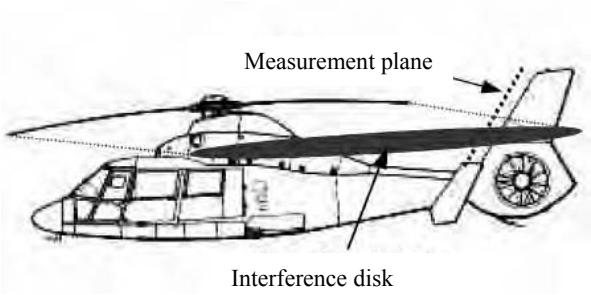

Figure 6.14. *Visualization of the "interference disk"*

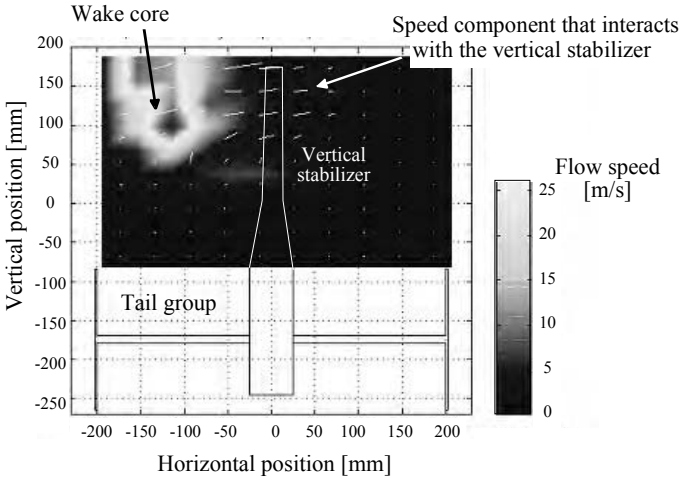

Figure 6.15. *Interference cores at the second harmonic frequency of the rotor – wind tunnel tests*

The main interferences are located on the left side of the visualizations, which corresponds to a deflection towards the right side of the aircraft.

The slipstream seems to be organized in “cores”. The values obtained in these speed maps are interference amplitudes so the vectors shown in these figures indicate a privileged interference direction and not a flow direction.

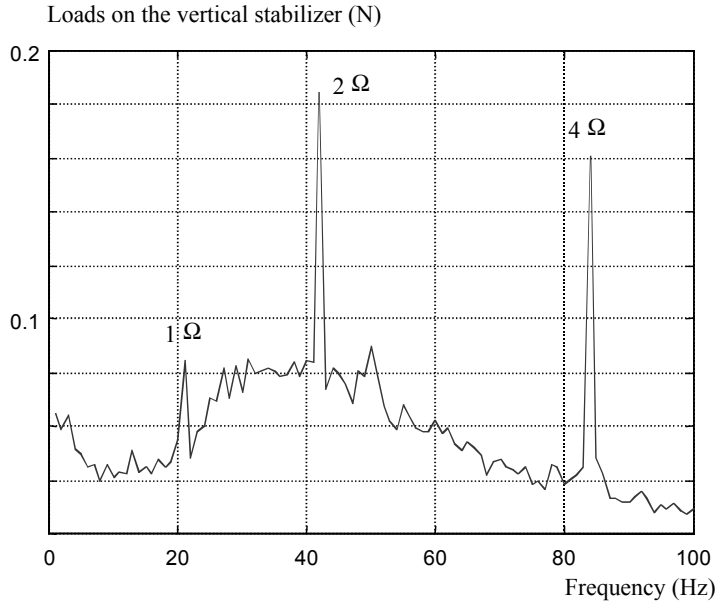

Figure 6.16. *Loads on the vertical stabilizer of a wind tunnel model*

We see the influence of the Magnus effect on the positioning of the “cores”. Only the lateral speed interferences reach the vertical stabilizer. Aerodynamic effects have been calculated by integrating the measured pressures on the vertical stabilizer of the model (see Figure 6.16).

The rotor harmonics are seen to dominate. The presence of an arbitrary excitation in the 30-50 Hz range is also noted.

The large number of harmonic vortices is not a problem as long as the frequency of the airframe vibration mode is different from kΩ (k integer); however, the vortices are very problematic when the helicopter’s own vibration mode is close to a harmonic.

6.4. Practical solutions for tail-shake

In practice, there are two techniques to alleviate the slipstream phenomenon: installing a fairing around the rotor mast and a fairing around the hub (Figure 6.17). These techniques are applied to the wake coming from the rotor and fuselage.

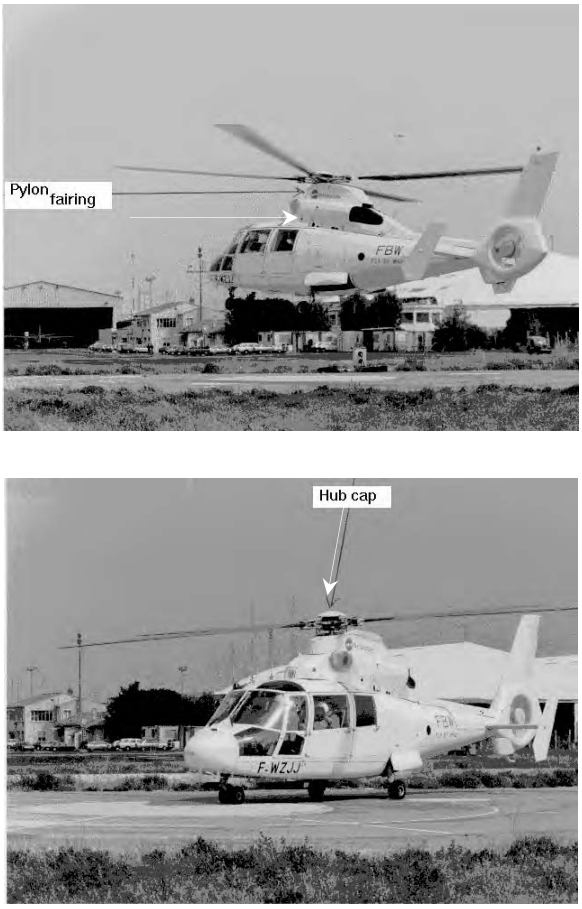

Figure 6.17. *Fairings designed to optimize the aerodynamic flow*

The measurements carried out on a real helicopter structure confirm the occurrence of the phenomenon and show the influence of the fairing (see Figure 6.18).

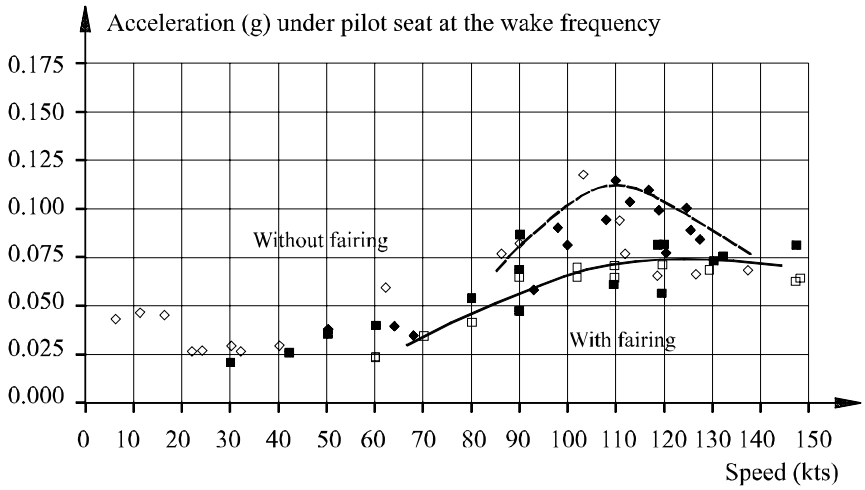

Figure 6.18. *Example of lock-in phenomenon on a helicopter*

PART II

Vibration Monitoring Systems

Introduction

The most natural method to reduce the vibratory level is to act at the level of vibration sources.

Hence, for a helicopter rotor, the dynamic optimization of blades is based on an appropriate choice of aerodynamic and mechanical features, such as mass and stiffness distribution. For a piston engine, the torque excitation can be optimized by controlling the fuel injection in the chamber. A careful balancing of rotating shafts is an example of minimization of excitations at the source.

Nevertheless, at times, it is necessary to make use of anti-vibration systems that enable the minimization of the vibratory level as much as possible. Since the required comfort level of installations is bigger and bigger, it cannot be reached without these systems. In addition, the installation of anti-vibration systems makes it possible to decrease the dynamic stresses in the structure holding the dynamic sets and thus to increase the reliability of the installed components.

From an industrial point of view, it is proved that, in order to be viable, these mechanical systems must meet the following requirements:

– performance in decreasing the vibratory level,

– low cost (development, manufacture, maintenance),

– light mass of the system (all architecture changes necessary for the installation of the system must be considered),

– possibility to follow-up the industrial evolution of the product

It is important to list the different anti-vibration systems that are available and to outline their applications. A classification will always make it possible to choose the best anti-vibration system for a particular problem.

Therefore, anti-vibration systems were divided, based on experience, according to:

– their mode of action: passive, active or semi-active,

– the strategy of their implementation place on the structure.

The main differences of anti-vibration systems, in terms of efficiency and complexity, are described below, according to their mode of action.

Passive systems, which adjust the structure on the basis of their characteristics (mass, stiffness, damping) have the particularity of not completely adjusting to the excitation changes caused by modifications of the machine functioning conditions, of the machine mass or its configuration.

Semi-active systems work by the same principle as passive systems, but they have the capacity to adjust the setting so that they adapt to modifications either of the amplitude or frequency excitation stresses or of the dynamic parameters of the structure to control (mass, stiffness or damping).

The principle of *active systems* is based on the injection of supplementary dynamic stresses at the level of the excitation source, at the level of the interface between the excitation source and the mechanical structure, or in the place where vibrations need to be controlled (a helicopter fuselage, public works vehicle, etc.).

It is important to choose the systems according to the place of their implementation on the structure, and also according to the function of the system.

As such we differentiate between:

– systems that act at the interface of two structures; the function of the system is to isolate one from the other;

– systems that act inside the structure and control vibrations exactly in the place where comfort is required. The cushions of a car seat are a good example of this type of system;

– systems that act near the source in order to minimize the dynamic stresses which are the origin of vibrations.

These different principles can be summarized in the following table, which corresponds to different chapters.

	Passive	**Semi-active**	**Active**
On the interface	Suspensions (Chapter 7)	Self-tuning suspensions (Chapter 8)	Active suspensions (Chapter 9)
Inside the structure	Absorbers (Chapter 10)	Self-adjusting absorbers (Chapter 11)	Active absorbers (Chapter 12)
Near the source	Resonators (Chapter 13)	Self-adapting resonators (Chapter 14)	Active systems (Chapter 15)

Table 1. *Summary of anti-vibration systems*

Chapter 7

Suspensions

7.1. Introduction

The link between two structures can be designed in order to isolate one of the structures from the other. This concept of structural isolation is achieved by canceling the variable loads transmitted to the support structure.

The task of the engineer is to determine the characteristics of the link by analyzing the dynamic behavior and vibrations, without modifying its main function, i.e. its static characteristics.

In practice, the link characteristics can be modified by varying its stiffness (appropriate positioning of the system natural frequencies) or its damping (energy transfer). Another technique consists of introducing a flapping mass whose inertial effects will neutralize the excitation inputs. We will analyze the implementation of these techniques.

7.2. Filtering effects of the interface link

7.2.1. *Stiffness modification for an excitation in force*

7.2.1.1. *Modeling*

For better understanding, we will consider two rigid structures with unidirectional motion. The link between the two structures is modeled by stiffness and damping. The mass of the parts in the link can usually be neglected.

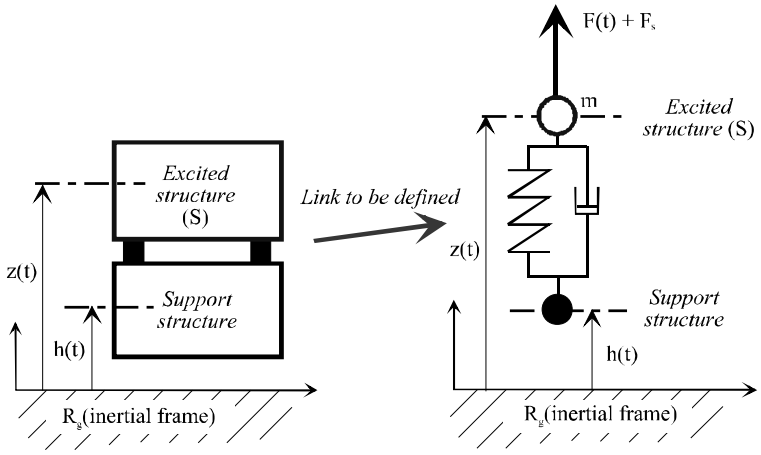

Figure 7.1. *Model of a suspension*

The equation of motion of the excited structure (denoted by S) is derived by applying the fundamental principle of dynamics to the structure:

$$m(s)\,\vec{A}_{M\in S/R_g} = \vec{R}_{spring\to S} + \vec{R}_{damper\to S} + \vec{R}_{gravity\to S} + \vec{R}_{excitation\to S} \qquad [7.1]$$

Let the chosen parametric transformation be:

$$m\,\ddot{z} = -k\,(z - h - l_0) - c\,(\dot{z} - \dot{h}) - m\,g + F(t) + F_s \qquad [7.2]$$

where:

– m is mass of the excited structure (s),

– k is the spring stiffness,

– l_0 is the no-load length of the spring,

– c is the damping coefficient,

– g is the acceleration due to gravity,

– F(t) is the dynamic component of the external load,

– F_s is the static component of the external load.

We assume that the parametric transformation is such that h(t) has no static component. The position of equilibrium is defined by:

$$0 = -k\,(z_e - l_0) - m\,g = F_s \qquad [7.3]$$

Application of the variable transformation $z(t) = z_e + \varepsilon(t)$ yields the following equation of small motion:

$$m\,\ddot{\varepsilon} + c\,\dot{\varepsilon} + k\,z = F(t) + c\,\dot{h} + k\,h \qquad [7.4]$$

7.2.1.2. *Response to a harmonic excitation*

We will now study the case without excitation for an imposed displacement and with harmonic excitation; thus:

$$\begin{cases} h(t) = 0 \\ F(t) = F_0 \cos(\omega t) \end{cases} \qquad [7.5]$$

Equation of small motion [7.4] reduces to:

$$m\,\ddot{\varepsilon} + c\,\dot{\varepsilon} + k\,\varepsilon = F_0 \cos(\omega t) \qquad [7.6]$$

The response of the structure has the form:

$$\varepsilon(t) = E_0(\omega)\cos\left(\omega t + \varphi(\omega)\right) \qquad [7.7]$$

where:

$$\begin{cases} E_0(\omega) = \dfrac{F_0}{\sqrt{\left(k - m\omega^2\right)^2 + (c\omega)^2}} \\ \tan\left(\varphi(\omega)\right) = \dfrac{-c\omega}{k - m\omega^2} \end{cases} \qquad [7.8]$$

7.2.1.2.1. Study of transmissibility

The force transmitted to the foundation is defined as being the dynamic part of the load acting through the link. In this case:

$$F_T(t) = c\dot{\varepsilon} + k\varepsilon \qquad [7.9]$$

Transmissibility is defined as the ratio of the amplitude of the transmitted dynamic force to the excitation force.

Let:

$$T = \frac{|F_T|}{F_0} = \frac{\sqrt{k^2 + c^2\omega^2}}{\sqrt{\left(k - m\omega^2\right)^2 + \left(c\omega\right)^2}} \qquad [7.10]$$

This equation is usually written in terms of modal characteristics as follows:

$$T = \frac{\sqrt{1 + \left(2\lambda\frac{\omega}{\omega_p}\right)^2}}{\sqrt{\left(1 - \left(\frac{\omega}{\omega_p}\right)^2\right)^2 + \left(2\lambda\frac{\omega}{\omega_p}\right)^2}} \qquad [7.11]$$

where:

$\omega_p = \sqrt{\frac{k}{m}}$ *is the natural angular frequency or* $f_p = \frac{\omega_p}{2\pi}$ *natural frequency*

$\lambda = \frac{c}{2\sqrt{km}}$ *is the damping ratio*

7.2.1.2.2. Study of the case with no damping

In this case, the damping ratio is zero and the transmissibility factor can be simplified to:

$$T = \frac{1}{\left|1 - \left(\frac{\omega}{\omega_p}\right)^2\right|} \qquad [7.12]$$

A plot of transmissibility versus reduced angular frequency $u = \omega/\omega_p$ is shown in Figure 7.2.

The curve shows load amplification for $\omega < \omega_p$, theoretically infinite resonance at $(\omega = \omega_p)$, followed by attenuation.

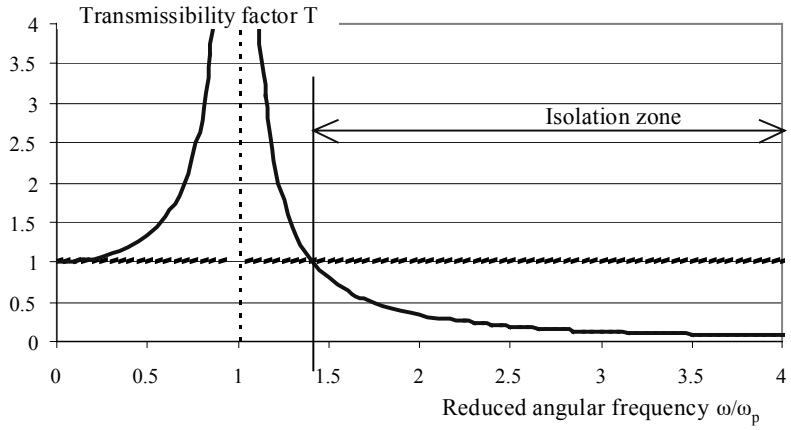

Figure 7.2. *Transmissibility curve with no damping*

Mechanical filtering is performed by means of stiffness. This solution is worth using only if the disturbing frequency is higher than the cut-off frequency f_p. For many applications this requires low stiffness and very flexible suspension.

In certain cases, this solution may not be suitable because of the static loads. The spring deformation is given by:

$$z_e - l_0 = \frac{(-mg + F_0)}{k} \qquad [7.13]$$

The deformation is inversely proportional to stiffness. The static design of the link for minimum deformation requires a very high stiffness, which is not compatible with the dynamic criterion.

Consider a structure with a mass of 500 kg, subject to load of 105 N at a frequency of 1,000 Hz. If a 10% transmissibility factor is desired, the necessary stiffness of the link will be 45 daN/mm.

We can then calculate that the displacement of the structure due to its own weight will be 11.1 mm, which may be incompatible with its correct operation.

7.2.1.2.3. Analysis of damping effect

The main constraint for a fixed installation is that the natural frequency of the suspension must be chosen outside the range of the machine's vibrations, otherwise mechanical damage could be caused at resonance.

In certain cases, a suspension may also be excited by displacement-generated forces. If they are random, they will have a broad spectrum, which means there is always some energy at the suspension's natural frequency, and if the links are purely elastic, the amplitude may become too high at this frequency.

This effect can be reduced by adding damping to the support's elasticity. The transmissibility of a Newtonian viscous material is expressed as:

$$T = \frac{\sqrt{1+\left(2\lambda\frac{\omega}{\omega_p}\right)^2}}{\sqrt{\left[1-\left(\frac{\omega}{\omega_p}\right)^2\right]^2+\left[2\lambda\frac{\omega}{\omega_p}\right]^2}} \qquad [7.14]$$

When $\omega = \omega_p$, the transmissibility is no longer infinite and its value, which depends on the damping, is given by:

$$T = \sqrt{1+\frac{1}{4\lambda^2}} \qquad [7.15]$$

There is a specific frequency ω_c such that:

$$T = 1, \text{ where } \omega_c = \omega_p\sqrt{2}$$

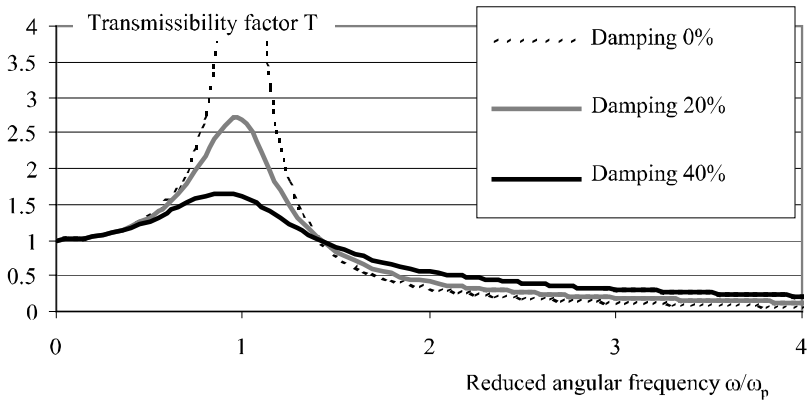

Figure 7.3. *Transmissibility curve with damping*

It should be noted that, at excitation frequencies higher than ω_c, the transmissibility increases with the damping value (see Figure 7.3).

Another mechanical filter was therefore designed by adding a viscous material. Compared to the previous filter, the new filter has the advantage that its resonance can be lower but has the disadvantage that, in the attenuation zone, it reduces the transmitted level more slowly versus ω.

7.2.1.3. *Response to an unbalanced excitation*

We will now study the case where there is no displacement excitation imposed by the supporting structure but only harmonic excitation whose amplitude is proportional to the square of the excitation angular frequency. In the case of unbalance, the amplitude is also proportional to the mass M of the rotating part and to the eccentricity e (see Chapter 1). This type of excitation therefore corresponds to the excitations caused by the unbalance:

$$\begin{cases} h(t) = 0 \\ F(t) = F_0\omega^2 \cos(\omega t) \end{cases} \quad [7.16]$$

The dynamic response of the structure is given by:

$$\varepsilon(t) = E_0 \cos(\omega t + \varphi) \quad [7.17]$$

where:

$$\begin{cases} E_0(\omega) = \dfrac{F_0\omega^2}{\sqrt{\left(k - m\omega^2\right)^2 + (c\omega)^2}} \\ \tan(\varphi) = \dfrac{c\omega}{k - m\omega^2} \end{cases} \quad [7.18]$$

The transmissibility takes the following form:

$$T = \frac{|F_T|}{F_0} = \frac{\omega^2\sqrt{\left(k^2 + c^2\omega^2\right)}}{\sqrt{\left(k - m\omega^2\right)^2 + (c\omega)^2}} \quad [7.19]$$

or, in terms of modal characteristics:

$$T = \frac{\left(\frac{\omega}{\omega_p}\right)^2 \sqrt{1+\left(2\lambda\frac{\omega}{\omega_p}\right)^2}}{\sqrt{\left(1-\left(\frac{\omega}{\omega_p}\right)^2\right)^2+\left(2\lambda\frac{\omega}{\omega_p}\right)^2}} \qquad [7.20]$$

At very high frequencies $(\omega_p << \omega)$, the transmissibility is given by:

$$T \approx \sqrt{1+\left(2\lambda\frac{\omega}{\omega_p}\right)^2} \qquad [7.21]$$

With viscous damping the value of λ is independent of ω, and the transmitted load keeps increasing with ω. However, with viscoelastic damping, our experience has shown that the resistance depends on the dynamic displacement ε and on the frequency of the motion. This behavior is modeled by:

$$R_{damping \rightarrow mass} = -(K' + i\, K'')\, \varepsilon \qquad [7.22]$$

where by definition:

$$K'' = c\, \omega \qquad [7.23]$$

Using the definition of the damping ratio yields:

$$\lambda = \frac{c}{2\sqrt{k\, m}} = \frac{c}{2\omega_p\, m} = \frac{c\omega_p}{2K'} \qquad [7.24]$$

where:

$$K' = \omega_p^2\, m \qquad [7.25]$$

Hence, the damping ratio is expressed by:

$$\lambda = \frac{1}{2}\frac{\omega_p}{\omega}\frac{K''}{K'} = \frac{1}{2}\frac{\omega_p}{\omega}\tan(\phi) \qquad [7.26]$$

where ϕ is the loss angle.

Therefore, at very high frequencies, the transmissibility is given by:

$$T \approx \sqrt{1+\tan^2(\phi)} \qquad [7.27]$$

Figure 7.4 compares the influence of the type of damping on the transmissibility.

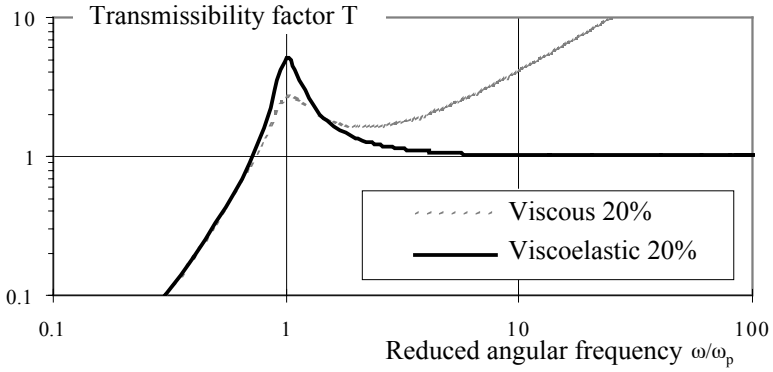

Figure 7.4. *Transmissibility curve for unbalance type excitation*

It should be noted that, for a viscoelastic material, the transmissibility is limited to its value at resonance and that there is no increase in transmissibility at high frequencies.

It is therefore better to use a viscoelastic suspension for structures excited by unbalance.

7.2.2. *Stiffness modification for displacement excitation*

The link between two structures can be designed to reduce the movement of the excited structure, the excitation being generated by the motion of the other structure.

In this case, the transmissibility factor is defined in the same way as the displacement ratio. This situation applies to the movement of the body of a surface vehicle, when excited by road roughness. The excitation can be random or undulating. We will study the latter here.

7.2.2.1. *Modeling*

In the proposed model, the chassis and tire deformations are neglected. The suspension is modeled by a spring and a damper in parallel.

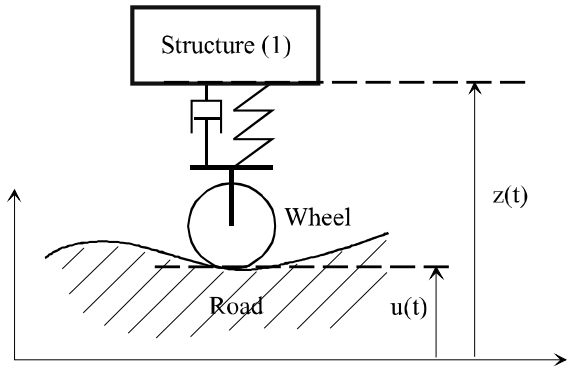

Figure 7.5. *Model of a vehicle suspension*

The resultant theorem of the dynamic equation of motion yields:

$$m\,\vec{A}_{G,1/R_g} = \vec{F}_{spring\to 1} + \vec{F}_{damper\to 1} + \vec{F}_{gravity\to 1} \qquad [7.28]$$

Hence, by projecting on to the vertical axis:

$$m\,\ddot{z} = -k\,\left(z - u(t) - l_0\right) - c\,\left(\dot{z} - \dot{u}(t)\right) - m\,g \qquad [7.29]$$

The static position z_0 is given by the relation:

$$z_0 = l_0 - \frac{m\,g}{k} \qquad [7.30]$$

where l_0 is the no-load length of the spring.

Using the same method as in the previous sections and by changing the variable:

$$z(t) = z_0 + \varepsilon(t) \qquad [7.31]$$

we obtain the equation:

$$m\,\ddot{\varepsilon} + c\,\dot{\varepsilon} + k\,\varepsilon = k\,u(t) + c\,\dot{u}(t) \qquad [7.32]$$

The response of the structure to a harmonic excitation is then:

$$u(t) = U_0 \cos(\omega\, t) \quad \rightarrow \quad \varepsilon(t) = E_0 \cos(\omega t + \varphi) \qquad [7.33]$$

where:

$$\begin{cases} E_0 = \dfrac{k\,U_0}{\sqrt{\left(k - m\,\omega^2\right)^2 + (c\,\omega)^2}} \\ \tan(\varphi) = \dfrac{c\,\omega}{k - m\,\omega^2} \end{cases} \qquad [7.34]$$

For displacement excitation, the transmissibility equation can be written:

$$T = \frac{E_0}{U_0} = \frac{1}{\sqrt{\left(1 - \left(\dfrac{\omega}{\omega_p}\right)^2\right)^2 + \left(2\lambda\dfrac{\omega}{\omega_p}\right)^2}} \qquad [7.35]$$

7.2.2.2. *Analysis of the results*

We suggest looking at the transmissibility in terms of the excitation frequency ω.

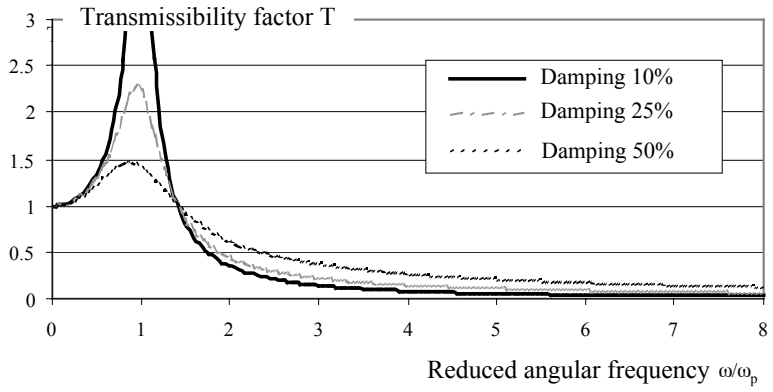

Figure 7.6. *Frequency response of the excited structure*

The analysis of the curves shows that in this case there are two possible types of links:

– the link is very rigid (e.g. a bolted assembly), and it is assumed that the resonance is much higher than the disturbing frequencies. Note that, in this case, damping has very little influence on the behavior of the structure,

– the link is flexible, and it is assumed that the resonance is lower than the disturbing frequencies. In this case, damping does not play an important role. On the other hand, it is worthwhile reducing the resonance peak by using damping.

There can be other suspension design criteria: climbing ability and comfort for the suspension of a vehicle, crash resistance for the suspension of a helicopter, etc.

7.2.2.3. *Example: vehicle suspension*

We assume that the speed of the vehicle is close to 80 km/h. We show that the vertical displacement felt by the wheel has the form:

$$u(t) = U_0 \cos\left(\frac{\pi V}{L} t\right) \qquad [7.36]$$

where:

– V = 80 km/h, the speed of the vehicle,

– L = 1 m, road defect length,

– U_0 = 3 cm, the amplitude of road defects.

The suspension stiffness was set to produce a 10 cm compression under the effect of its own weight. The stiffness is given by:

$$k = \frac{m\ g}{l_0} \qquad [7.37]$$

The natural angular frequency of the system is:

$$\omega_0 = \sqrt{\frac{k}{m}} = \sqrt{\frac{g}{l_0}} = \sqrt{\frac{9.81}{10 \times 10^{-2}}} = 9.9 \text{ rad/s} \qquad [7.38]$$

which yields natural frequency of 1.58 Hz.

The excitation frequency is calculated to be equal to this natural frequency at a speed of 11.34 km/h:

$$V = \frac{L\ \omega_0}{\pi} = 3.15 \text{ m/s} = 11.34 \text{ km/h} \qquad [7.39]$$

For a vehicle whose speed is 80km/h the excitation angular frequency is:

$$\omega_{exc} = \frac{\pi\ V}{L} = 69.81 \text{ rad/s} \qquad [7.40]$$

Hence, an excitation frequency of 11.12 Hz.

Table 7.1 compares the values of the responses with different damping ratios, i.e. the response at resonance (speed of 11.34 km/h) and the response at 80 km/h.

λ_r **(reduced damping)**	**0%**	**15%**	**50%**
V = 11.34 km/h	infinite	104.4 mm	42.43 mm
V = 80 km/h	0.62 mm	1.44 mm	4.34 mm

Table 7.1. *Structure response versus vehicle speed and damping ratio*

It is seen that an efficient damper at resonance (ω = 50%) provides very inefficient filtering at a higher frequency.

To obtain good results, the damping must be matched to the application in question.

Therefore, if the excitation frequencies are above the resonance frequency, the lowest possible damping should be selected.

For lower excitation frequencies, high damping should be chosen so that the amplitude of vibrations is lower around resonance.

In the case of an excitation with a broad spectrum, a compromise must be reached.

7.2.3. *Damping modification*

7.2.3.1. *Principle*

We have already noted that a viscous damper which is efficient at resonance filters very badly at higher frequencies. The ideal solution would be to apply damping only in the resonance area, for which a fluid should be used. The block diagram of a system used in the automotive industry is represented in Figure 7.7.

The elastic element made of very resilient rubber is cone-shaped. A rigid plate delineates a closed chamber under the cone. A second chamber is delineated on the other side of the plate by a very flexible bellows. An orifice through the plate, called a "column", enables communication between the chambers. The interior part of the support is filled with antifreeze agent (fluid).

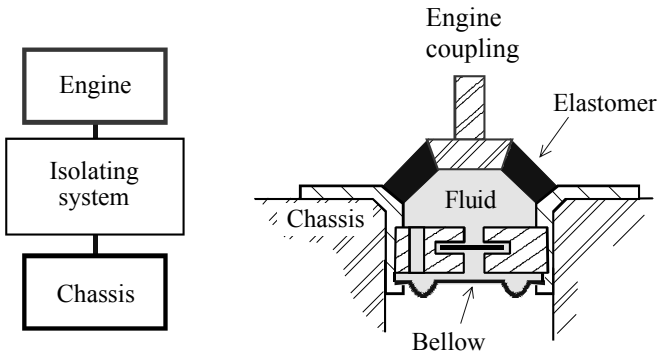

Figure 7.7. *Technology of high damping supports*

Elastic energy is generated by the chamber wall deformations and kinetic energy by the fluid movement in the column.

The system's natural resonance can be designed to coincide with the vertical excitation frequency produced by the engine. With the help of this system, it is possible to generate efficient damping because the column transfers a great deal of energy.

A supplementary device, called a decoupling flap, is often used to reduce transmissibility at high frequency. It provides a direct connection between the chambers for the low amplitude vibrations that must be filtered. For high amplitude vibrations that must be damped, the flap is blocked by its end stops and the fluid must flow through the column. This guarantees high damping.

7.2.3.2. *Modeling*

To simplify modeling, we have shown that the mass in the chambers can be ignored so that only the mass in the column is taken into account.

Let H be the fluid height in the chambers and h the fluid height in the column. Let S be the fluid cross-sectional area of the chambers and s the fluid cross-sectional area of the column.

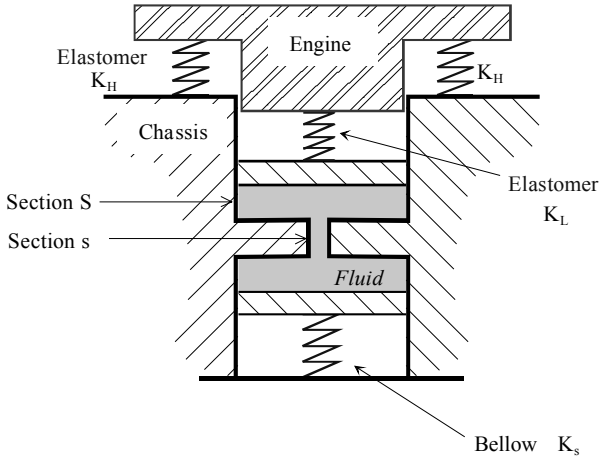

Figure 7.8. *Diagram of the support*

The kinetic energy of the fluid in the two compartments is written as follows:

$$\begin{cases} T(\text{fluid of the column/R}) = \frac{1}{2}\rho_{fl}\ s\ h\ V^2_{\text{fluid in column}} \\ T(\text{fluid of the chambers/R}) = \frac{1}{2}\rho_{fl}\ S\ H\ V^2_{\text{fluid in chamber}} \end{cases} \quad [7.41]$$

The conservation of the flow rate leads to the following relation:

$$Q = s\, V_{\text{fluid in column}} = S\, V_{\text{fluid in chamber}} \qquad [7.42]$$

The ratio of the kinetic energies depends on the ratio of the surfaces and heights:

$$\frac{T(\text{fluid of the column/R})}{T(\text{fluid of the chambers /R})} = \frac{h\, S}{H\, s} \qquad [7.43]$$

For h/H = 0.25 and S/s = 100, which are typical values for this system, we obtain:

$$\frac{T(\text{fluid of the column/R})}{T(\text{fluid of the chambers /R})} = 25 \qquad [7.44]$$

The column has more kinetic energy than the fluid in the chambers. In the model used, the effects of the fluid mass in the column are ignored. The fluid is considered to be incompressible.

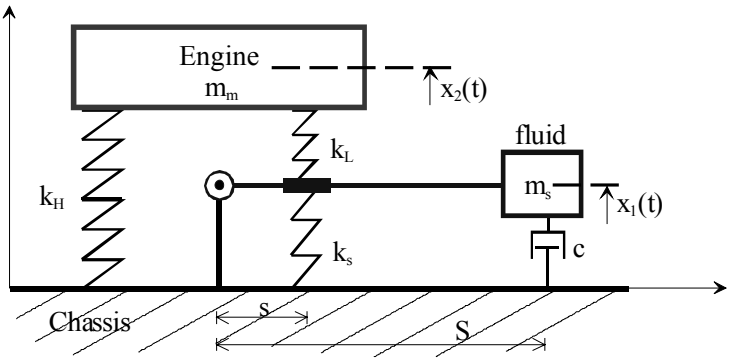

where:

– m_m is the engine mass,

– m_s is the fluid mass in the column,

– k_H is the stiffness of the elastomer between the engine and the chassis,

– k_L is the stiffness of the elastomer in contact with the fluid,

– k_S is the bellows stiffness.

Figure 7.9. *Modeling of system behavior*

The energy dissipation at the column inlet and outlet and the friction in the column are modeled by Newtonian viscous fluid damping.

The equations of motion are derived by isolating the engine and by applying the projection resultant theorem following the vertical axis, and then isolating the fluid and the bellows by using the dynamic moment theorem. The displacements $x_1(t)$ and $x_2(t)$ are defined as respectively relative to the static equilibrium positions of the fluid and engine.

This yields:

$$\begin{bmatrix} m_s & 0 \\ 0 & m_m \end{bmatrix} \begin{bmatrix} \ddot{x}_1 \\ \ddot{x}_2 \end{bmatrix} + \begin{bmatrix} c & 0 \\ 0 & 0 \end{bmatrix} \begin{bmatrix} \ddot{x}_1 \\ \ddot{x}_2 \end{bmatrix} + \begin{bmatrix} \frac{s}{S}(k_s + k_L) & -\frac{s}{S}k_L \\ -k_L & k_L + k_H \end{bmatrix} \begin{bmatrix} x_1 \\ x_2 \end{bmatrix} = \begin{bmatrix} 0 \\ F \end{bmatrix} \quad [7.45]$$

We will assume that the excitation is harmonic, which gives:

$$\begin{aligned} F &\rightarrow \bar{F}_0 e^{i\omega t} \\ x_1(t) &\rightarrow \bar{X}_{10} e^{i\omega t} \\ x_2(t) &\rightarrow \bar{X}_{20} e^{i\omega t} \end{aligned} \quad [7.46]$$

where:

- $\bar{F}_0$ is the complex excitation amplitude,
- $\bar{X}_{10}$: the complex amplitude of the fluid motion,
- $\bar{X}_{20}$: the complex amplitude of the engine motion.

The complex dynamic stiffness is defined by:

$$\bar{K} = \frac{\bar{F}_0}{\bar{X}_{20}} \quad [7.47]$$

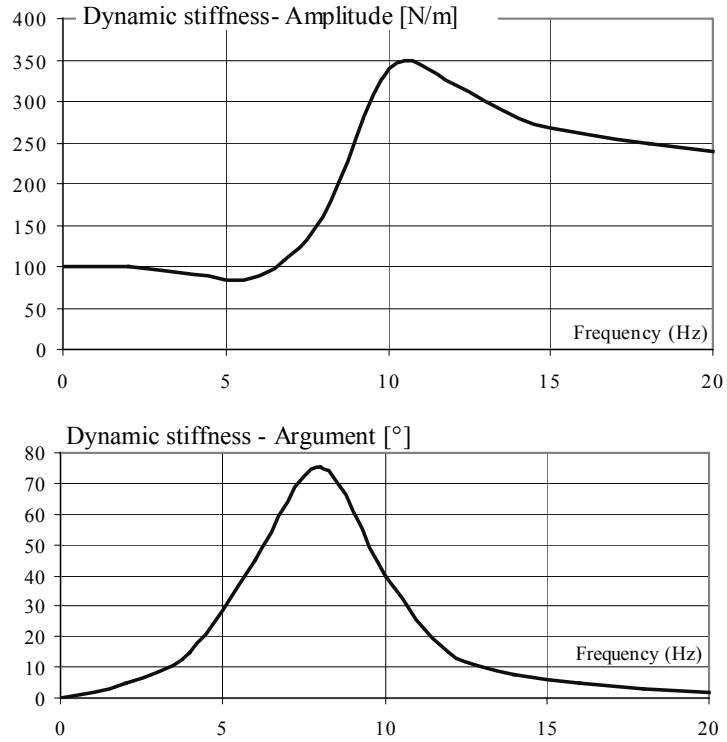

Figure 7.10. *Dynamic stiffness of a mounting*

Based on equation [7.45] it is shown that:

$$K = \frac{\left(s\left(k_s + k_L\right) - Sm_s\omega^2\right)\left(k_L + k_H - m_m\omega^2\right) - sk_L^2 + iS\omega c\left(k_L + k_H + m_m\omega^2\right)}{\left(s\left(k_s + k_L\right) - Sm_s\omega^2\right) + iS\omega c} \quad [7.48]$$

The dynamic stiffness, which is the ratio between the excitation and the engine displacement, is dependent on the excitation angular frequency.

The system's behavior is non-linear. Figure 7.10 shows the dynamic stiffness of a variable hydraulic support versus the frequency of motion. On the phase curve, the damping is restricted to a narrow frequency range, which corresponds to the natural frequency of the suspension. There is thus very high damping at the system's natural frequency. At high frequencies, the damping is very low because the fluid flows through the flaps. There is no dissipation in the fluid column.

There are thus distinct modes of operation at high and low frequencies, which produce excellent filtering at both the resonance frequency and higher frequencies. This system compensates for the negative effects of the viscous systems described in the last chapter.

7.2.4. *Complex case of the rotor/fuselage link of a helicopter*

A complex example of the link problem between two structures is the link between the main transmission unit and the fuselage of a helicopter.

This link has two objectives. It must be capable of transmitting the static loads necessary to lift the fuselage during all flight phases. In addition, it must filter out the dynamic loads generated by the rotor to ensure adequate comfort in flight.

The link is represented in Figure 7.11.

At the rotor head, where the blades are attached, the load set of the mechanical effects of the rotor is:

$$\{\text{rotor} \rightarrow \text{mast}\}: \begin{Bmatrix} R_x & M_x \\ R_y & M_y \\ R_z & M_z \end{Bmatrix}_{(H,x,y,z)} \qquad [7.49]$$

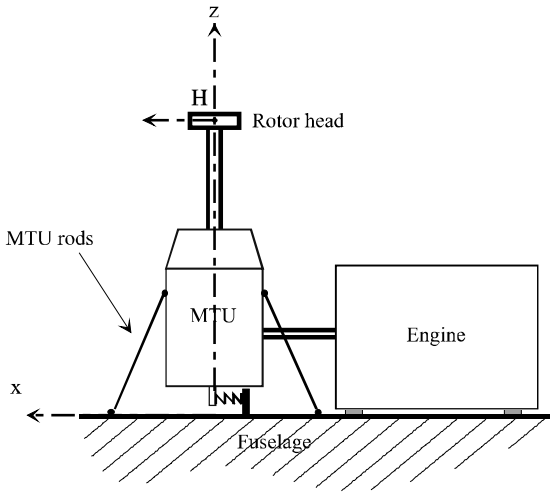

Figure 7.11. *The link between the main transmission unit (MTU) and the fuselage*

The rotor hub loads have a static component generated by the flight loads and a dynamic component induced by the dynamic excitations of the rotor on the fuselage (see Chapter 3).

This combination of static and dynamic components makes the use of an entirely flexible suspension impossible. We will now analyze why this is so, using the complex example of a helicopter.

For a 4-bladed helicopter with a mass of about 10 tons, the excitation frequency created by the blades is about 17 Hz. According to industrial specifications, in order to obtain good filtering, the stiffness of the link must be designed so that the system's natural frequency is below 12 Hz.

The required stiffness is thus:

$$k = \omega_0^2 \frac{m\ M}{M+m} = (12)^2 \frac{1,500 \times 8,500}{10,000} \approx 184 \text{ daN/mm} \qquad [7.50]$$

With such stiffness, under the dead weight of the machine, the static deformation would be 46 mm. For a 60° turn in flight, the lift is doubled because of centrifugal effects. The deformation would then be close to 92 mm.

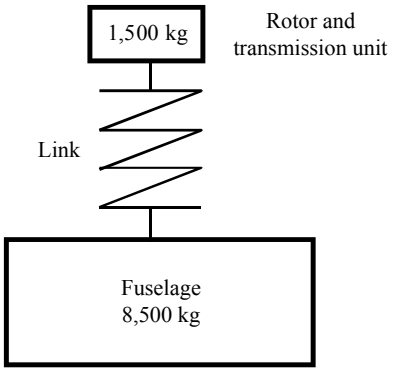

Figure 7.12. *Weight distribution for modeling the fuselage/rotor link of a helicopter*

These static deformations are incompatible with the angular movements imposed on the engines.

A specific link has been developed, called a "barbecue"[1] link; it is capable of filtering the pitch and roll loads (see Figure 7.17), while remaining rigid with respect to the lift load and the yawing.

This link was introduced for the first time in 1965 on the Puma helicopter. It injects vibrations into part of the helicopter – the transmission unit – in order to cancel out the vibrations in the fuselage, where there are occupants.

At the bottom of the gearbox, a flexible element allows the main transmission unit to pivot about its pitch point, while transmitting the engine torque. The four rods suspend the fuselage rigidly from the rotor. The transmission unit/main rotor assembly is attached to the structure at two locations:

– to the mast, by three or four rods that transmit the lift from the rotor to the structure,

– to the lower part of the transmission unit, via a flexible suspension.

Under dynamic excitation on the rotor head, the suspension rods allow the transmission unit to rotate about the joining point of the rods, which is also called the focal point. The flexible suspension makes this angular motion possible. The dynamic loads introduced in the structure at the bottom of the transmission unit are strongly reduced. The loads input at the bottom of the transmission unit are filtered by setting the natural frequency of the pendular system to be well below the excitation frequency of the rotor.

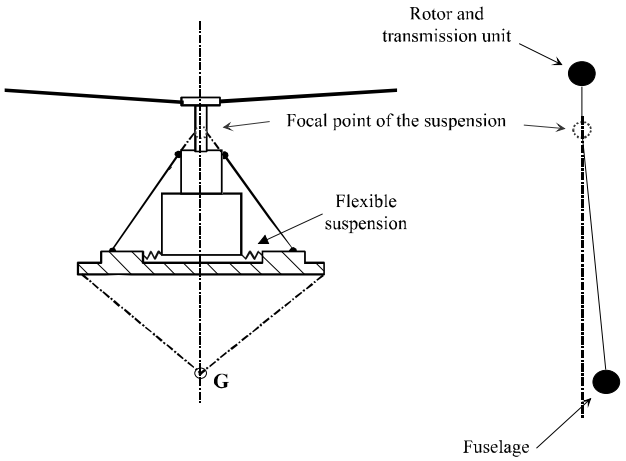

Figure 7.13. *Modeling of the behavior of the "barbecue" suspension*

1 The name "barbecue" was chosen because of the shape of the suspension, which resembles a barbecue grill.

The main problem in the design of the "barbecue" system is defining the system of the flexible element at the bottom of the transmission unit. This link must ensure:

– very high stiffness under the main rotor torque,

– stiffness for linear displacements and angular movements that should be sufficiently small to ensure filtering, and sufficiently large to transmit the flight static loads with acceptable displacements (see Figure 7.14).

The filter function is ensured by a cylindrical laminated stop consisting of joined stacks of small rubber and Dural disks.

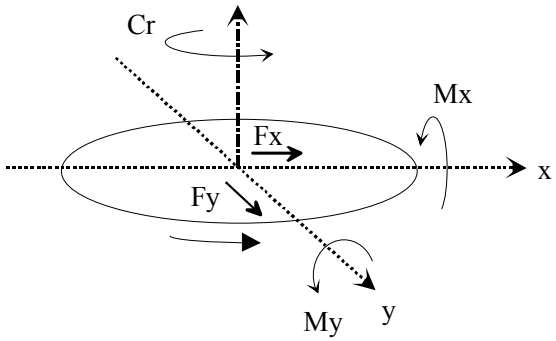

F_y: lateral load
F_x: longitudinal load
M_y: roll load
M_x: pitch load
Cr: rotor torque

Figure 7.14. *"Barbecue" suspension. Loads on the structure interface with the transmission unit*

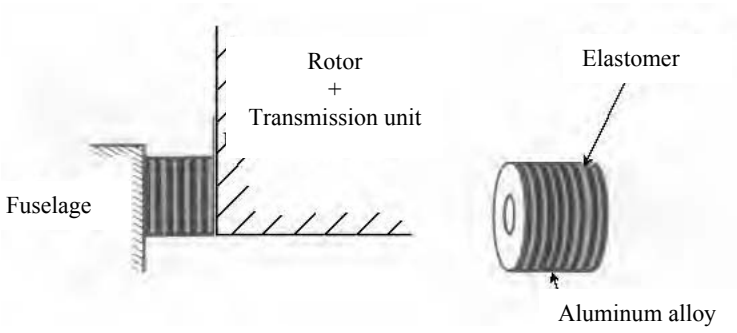

Figure 7.15. *Laminated stops of the "barbecue" suspension*

Flexibility is obtained in the radial direction of the elements, which are deformed by shear loading. The stiffness of these elements is high in compression, which makes it possible to have very high torsional stiffness.

These laminated elements are located at the bottom of the transmission unit by a component, called the "dog bone" because of its shape (see Figure 7.16). The reaction torque of the rotor is transferred in compression by four laminated elements. At the same time, during linear movements, the laminated elements are subjected to shearing loads, which make the existence of low stiffness and load filtering possible.

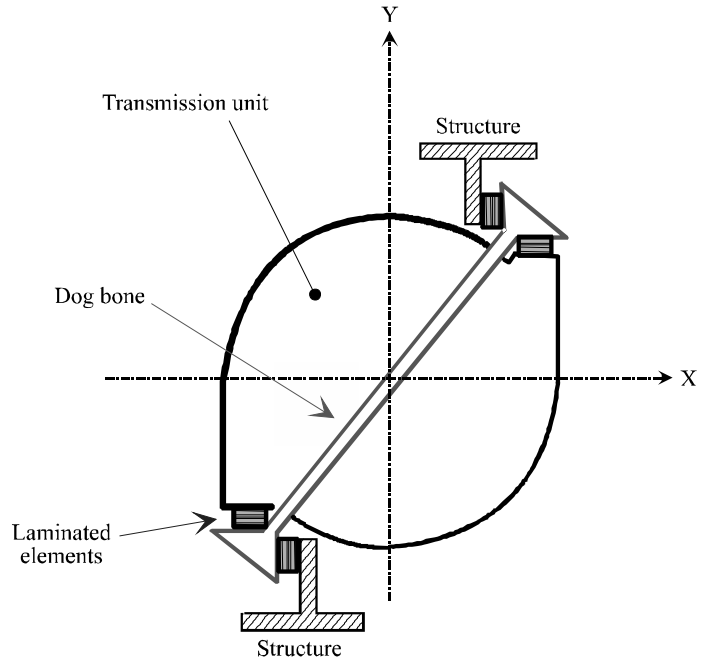

Figure 7.16. *Installation of the "barbecue" suspension at the bottom of the transmission unit*

The suspension described above is bidirectional.

Another possible technology is to insert a flexible plate at the bottom of the transmission unit (see Figure 7.17). In this case, the suspension is unidirectional only.

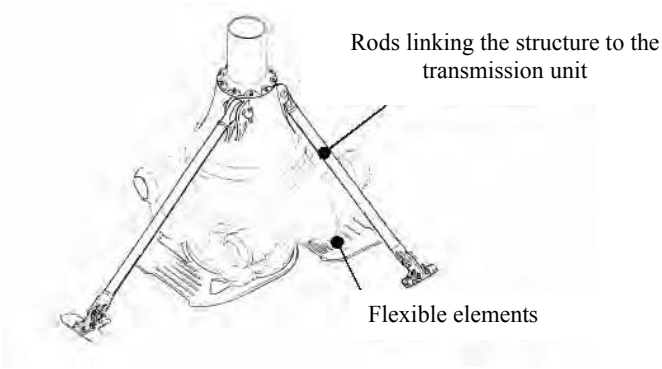

Figure 7.17. *"Barbecue" system with a flexible plate*

A simplified and 2D modeling of the system will highlight some of the operating principles.

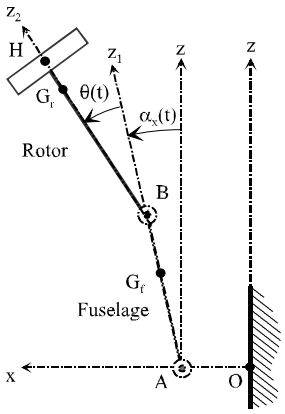

Figure 7.18. *Modeling of the pitch behavior for the rotor-fuselage link*

Low amplitude pitch and roll movements will be studied separately. The example below cover the case of pitch: the fuselage rotates about the center of pitch (point A) and the rotor section (the main transmission unit and rotor mast) rotates about its pitch point (point B).

Let:

$$\overrightarrow{OA} = x(t)\vec{x} \qquad \overrightarrow{AB} = L\ \vec{z}_1 \qquad \overrightarrow{BH} = 1\ \vec{z}_1$$
$$\overrightarrow{AG_f} = H\ \vec{z}_1 \qquad \overrightarrow{BG_r} = h\ \vec{z}_1 \qquad [7.51]$$

where:

– I_f and M_f are the pitch inertia and fuselage mass,

– I_r and m_r are the inertia and mass of the rotor,

– k is the equivalent angular stiffness of the rotor with respect to the fuselage,

– G_f and G_r are the center of inertia of the fuselage and of the rotor.

The kinematic parameters are θ(t), the rotation of the rotor with respect to the fuselage, $\alpha_x(t)$ the pitch of the fuselage, and x(t) the shaking of the fuselage.

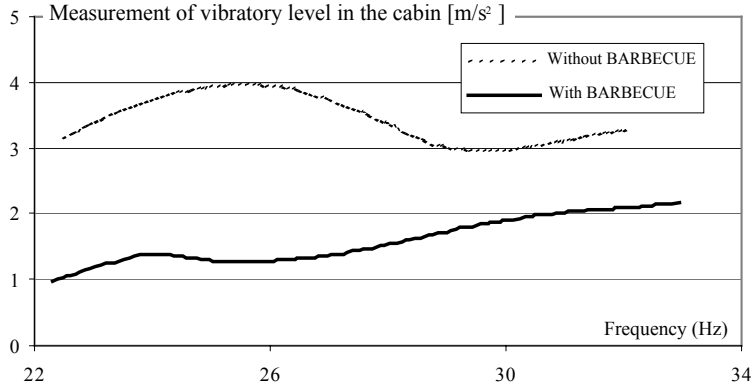

Figure 7.19. *"Barbecue" suspension effect; vibration test (shake test)*

The equations of motion of the system can be written in a matrix form:

$$M\ddot{X} + KY = F \qquad [7.52]$$

with the position vector:

$$X = \begin{bmatrix} x(t) \\ \alpha_x(t) \\ \theta(t) \end{bmatrix} \qquad [7.53]$$

and mass and stiffness matrices:

$$M = \begin{bmatrix} M_f + m_r & -m_r(L+h) - M_{fus}H & -m_r h \\ -m_r(L+h) - M_{fus}H & I_f + M_f H^2 + I_r + m_r(L+h)^2 & I_r m_r h \\ -m_r h & I_r m_r h & I_r + m_r h^2 \end{bmatrix} \qquad [7.54]$$

$$K = \begin{bmatrix} 0 & 0 & 0 \\ 0 & k & -k \\ 0 & -k & k \end{bmatrix} \quad [7.55]$$

The excitation vector is defined by:

$$F = \begin{bmatrix} F_x \\ M_y \\ 0 \end{bmatrix} \quad [7.56]$$

Figure 7.19 shows the effect of the suspension, when subjected to a constant amplitude excitation M_y of 500 Nm at the rotor head (pitch moment) at different frequencies.

In the scanned frequency range, the "barbecue" suspension is seen to produce gains 35 to 70%.

7.3. Acting on the interface through kinematic coupling

7.3.1. *The example of the DAVI system*

7.3.1.1. *Principle*

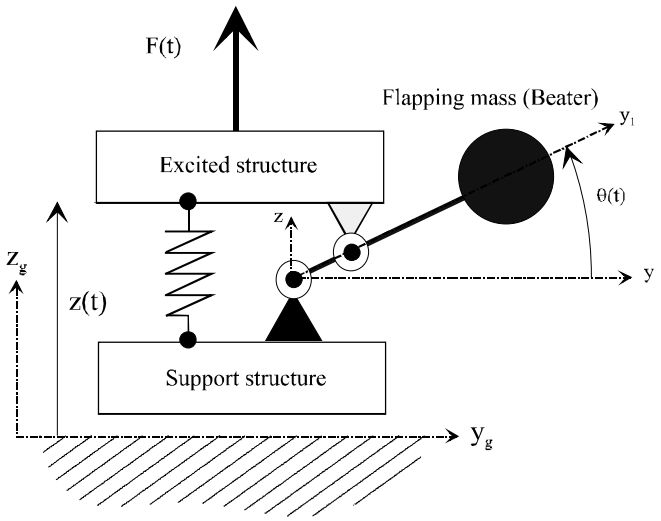

Figure 7.20. *Suspension with DAVI kinematic coupling*

To achieve proper filtering characteristics while preserving low static deformations, another system was designed, known as DAVI (Dynamic Antiresonant Vibration Isolator) [DES 76, DES 78, FLA 66, RIT 76]. In this system, a flapping mass (beater) is added near each point. The flapping mass is kinematically attached to the excited and support structures. It is designed to generate inertial effects on the support structure at a given frequency, in contrast to the action of the flexible link.

7.3.1.2. *Formulation of the equations*

For small motions, the model below is used to formulate the equations of the system. The motion of the transmission unit, except for the vertical units, are ignored.

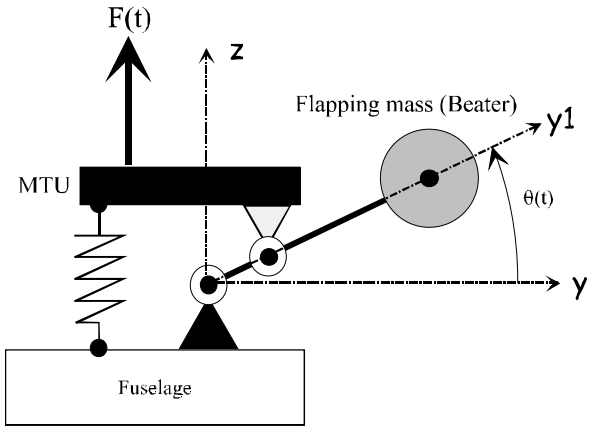

Figure 7.21. *DAVI modeling*

The resultant of the link actions on the fuselage is expressed as:

$$\vec{R} = \vec{R}_{spring \rightarrow fuselage} + \vec{R}_{pivot \rightarrow fuselage} \qquad [7.57]$$

If we isolate the flapping mass, the theorem of moments yields:

$$\left(I_b + m_b l^2\right) \ddot{\theta} = -a\, R_{Rod \rightarrow Beater} \qquad [7.58]$$

where a is the distance between the connection points of the flapping mass with the fuselage and the main transmission unit rod.

If we isolate the main transmission unit rod and designate its vertical displacement by z(t) , the resultant theorem shows that:

$$m_{MTU}\ddot{z} = -k\ z(t) + R_{Beater \rightarrow Rod} + F(t) \qquad [7.59]$$

However, for small motions the kinematic coupling requires that:

$$\dot{z} = a\ \dot{\theta} \qquad [7.60]$$

The equation of motion is then:

$$m_{eq}\ddot{z} + k\ z = F(t) \qquad [7.61]$$

where:

$$m_{eq} = \frac{I_b + m_b l^2}{a^2} + m_{MTU} \qquad [7.62]$$

Thus, the response amplitude to harmonic excitation is:

$$Z_0(\omega) = \frac{F_0}{\left| k - \omega^2 \left(\frac{I_b + m_b l^2}{a^2} + m_{MTU} \right) \right|} \qquad [7.63]$$

It is reasonable to assume that the inertial effects I_b of the flapping mass are negligible compared to the effects of m_b. We can therefore write:

$$\lambda = \frac{1}{a} \qquad [7.64]$$

then:

$$Z_0(\omega) = \frac{F_0}{\left| k - \omega^2 \left(m_b\ \lambda^2 + m_{MTU} \right) \right|} \qquad [7.65]$$

If now we isolate the "main transmission unit rods and flapping mass" system and apply the resultant theorem on the vertical axis, the equation of motion is:

$$\left(m_b\ \lambda + m_{MTU}\right)\ \ddot{z} = R_{Spring \rightarrow Rod} + R_{Fuselage \rightarrow Flapping\ mass} + F(t) \qquad [7.66]$$

Then, considering the harmonic response:

$$R = R_{Spring \rightarrow Rod} + R_{Fuselage \rightarrow Flapping\ mass} = \left(m_b\ \lambda + m_{MTU}\right)\ \ddot{z} - F(t) \quad [7.67]$$

which yields the amplitude:

$$R = -\left[\frac{m_b\ \lambda\ \omega^2\ +\ k\ -\ m_b\ \lambda^2\ \omega^2}{\left(k-\omega^2\left(m_b\ \lambda^2\ +\ m_{MTU}\right)\right)}\right] F_0 \qquad [7.68]$$

Note that for a fixed angular frequency ω, there is a combination of λ and m_b, which cancels the mechanical action R, regardless of the amplitude F_0 and the mass value m_{MTU}. The value of the corresponding stiffness k is defined by:

$$k = \left(\lambda - 1\right)\lambda\omega^2 m_b \qquad [7.69]$$

The transmissibility factor can be expressed in terms of the excitation angular frequency ω:

$$T = \frac{|R|}{F_0} = \left|\frac{m_b\ \lambda\ \omega^2\ + k - \omega^2 m_b \lambda^2}{k - \omega^2\left(m_b\lambda^2 + m_{MTU}\right)}\right| \qquad [7.70]$$

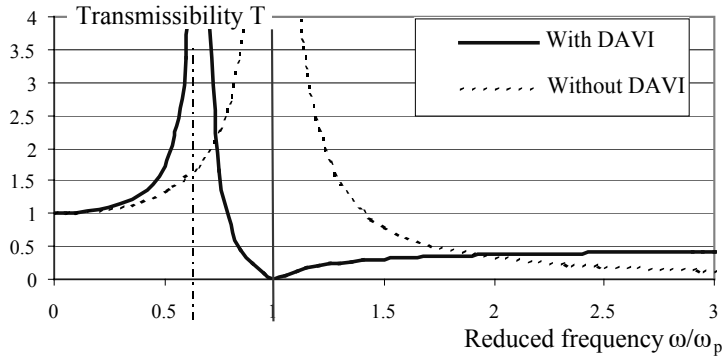

Figure 7.22. *Transmissibility factor with and without DAVI*

7.3.1.3. *Implementation*

There are several technologies for the DAVI system and we will examine a few examples below.

In the case of a helicopter, four flapping masses are positioned close to each suspension rod in a system called Sarib® (suspension with a resonator secured on the rod) [HEG 83, SEI 92]. An example of this suspension is shown in Figure 7.23.

Figure 7.23. *Implementation of Sarib® flapping masses*

In the case of this system, the stiffness of the link is guaranteed by a bending tab.

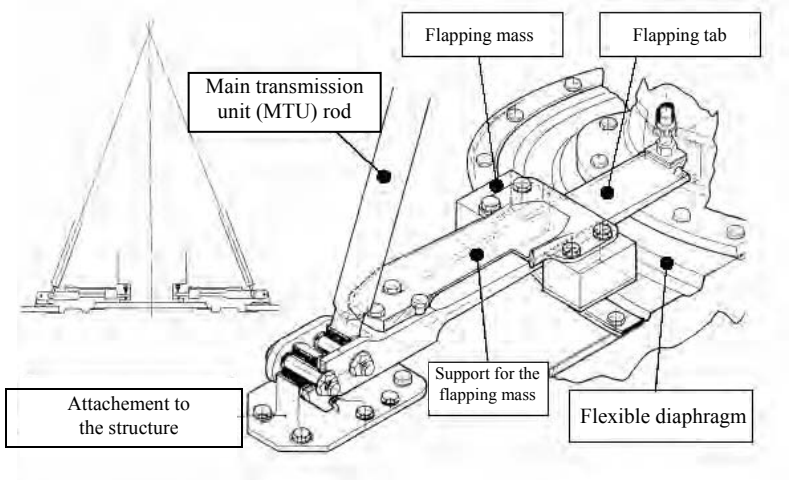

Figure 7.24. *Sarib® technology*

The modeling of a flapping mass is represented in Figure 7.25.

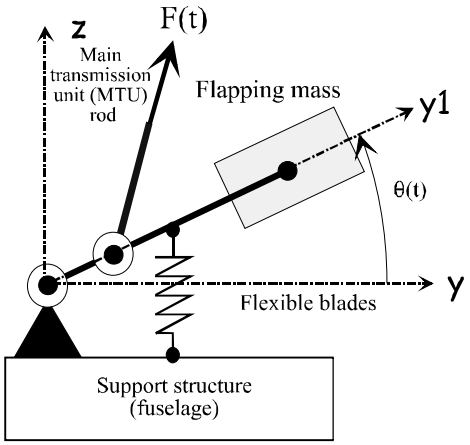

Figure 7.25. *Modeling of a Sarib® flapping mass*

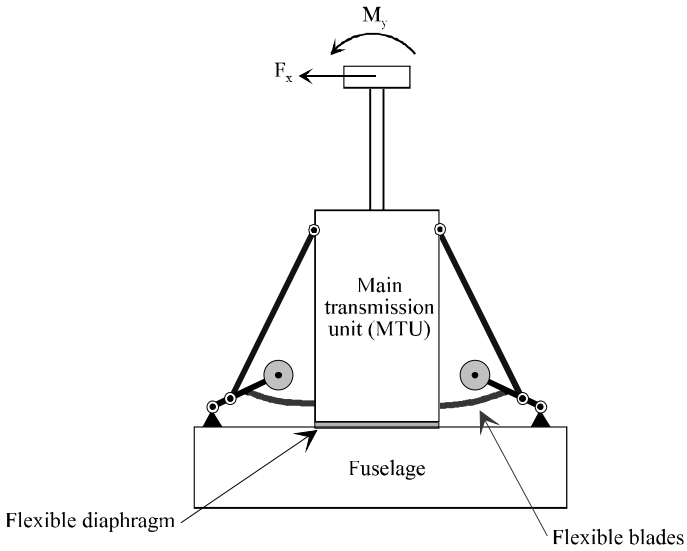

Figure 7.26. *Modeling of Sarib® implementation*

7.3.1.4. *Experimental analysis*

An important phase in tuning anti-vibration systems is the experimental analysis on the structure. It is necessary to analyze whether the model is sufficient for this

study and especially to determine what the real role of damping is in the system's behavior.

To do this, the system can be tested on a specific model or directly on the structure (a helicopter in the example presented).

7.3.1.4.1. Tests conducted on a model

The results of the tests show a strong correlation between simulations and calculations. The structural damping has a negligible role for this type of behavior.

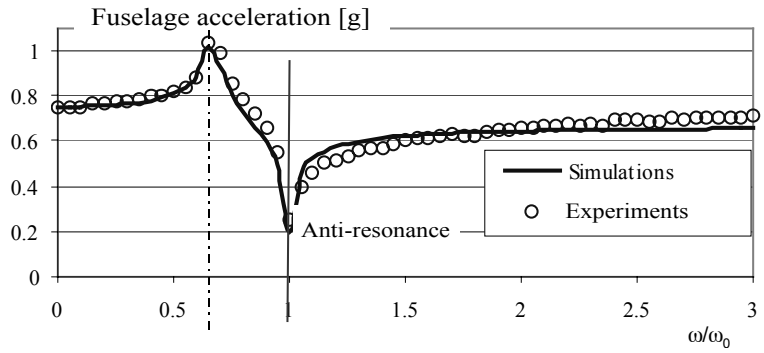

where ω_0 is the setting frequency of the suspension

Figure 7.27. *Comparison tests/calculations for the Sarib® system*

7.3.1.4.2. Tests conducted on a prototype

In tests conducted on a prototype, it is useful to analyze the system's behavior to loads other than vertical "pumping" (dynamic vertical loads).

We have therefore analyzed the behavior with excitation by a moment, for example, the pitch moment M_y [SEI 92].

The vibratory level in the pilot cabin was therefore measured with a rotor head excitation of 1,000 Nm pitching moment. Note that the Sarib® suspension guarantees anti-resonance (zero vibration) at the excitation frequency bΩ.

Figure 7.28. *Sarib® system mounted on a device for behavior tests. Photo: Eurocopter*

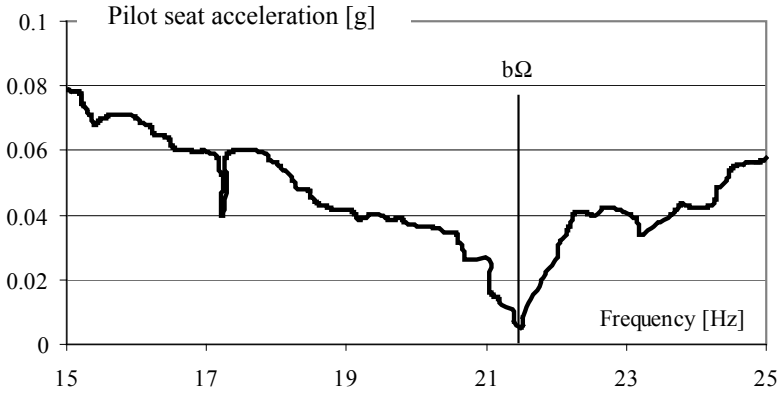

Figure 7.29. *Results of laboratory tests for a helicopter with Sarib® suspension*

7.3.2. *Example of the Aris system*

7.3.2.1. *Mechanical system*

Figure 7.30 illustrates the Aris concept along with a schematic view of the mechanical isolator [BRA 80, BRA 82a, BRA 82b].

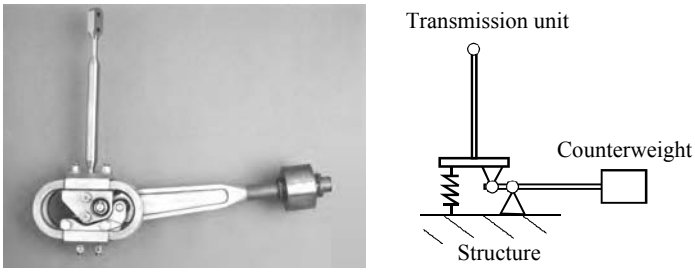

Figure 7.30. *Principle of Aris mechanical system. Photo: Eurocopter Deutschland*

Two parallel annular blades are used as springs. To connect the pendulum arm to the fittings situated on the sides of the fuselage and the transmission unit, the system uses elastomer bearings. The following requirements must be met:

– very high radial rigidity of the bearing,

– low twist rigidity of the bearing,

– very low loss factor in the elastomer material to avoid damping.

7.3.2.2. *Hydraulic system*

The isolator design can be based of a hydraulic system, as shown in Figure 7.31.

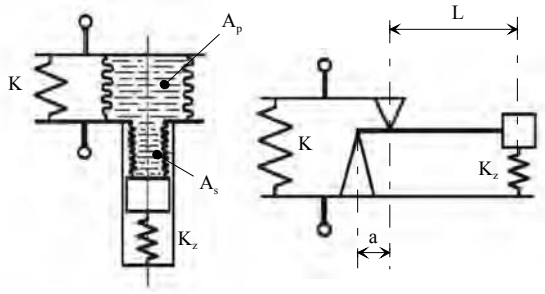

Figure 7.31. *Modeling of a passive anti-resonance system with a hydraulic force generator*

Assuming K_Z is small in comparison to K and using equation [7.69]:

$$m_b = \frac{K}{\omega^2 \frac{A_p}{A_s}\left(\frac{A_p}{A_s} - 1\right)} \qquad m_b = \frac{K}{\omega^2 \frac{L}{a}\left(\frac{L}{a} - 1\right)} \qquad [7.71]$$

Fundamentally, this type of isolator consists of a spring and a pendulum with a hydraulic transmission that are connected in parallel. The hydraulic force generator has two metallic bellows and a supplementary spring. The bellows system is an independent model completely filled with a low-viscosity hydraulic liquid. To minimize friction losses, sharp edges must be avoided in the bellows system. The pendulum counterweight, which is attached to the free end of the smaller of the two bellows (the secondary bellows), is supported by appropriate linear bearings. For accurate setting, this counterweight has several disks.

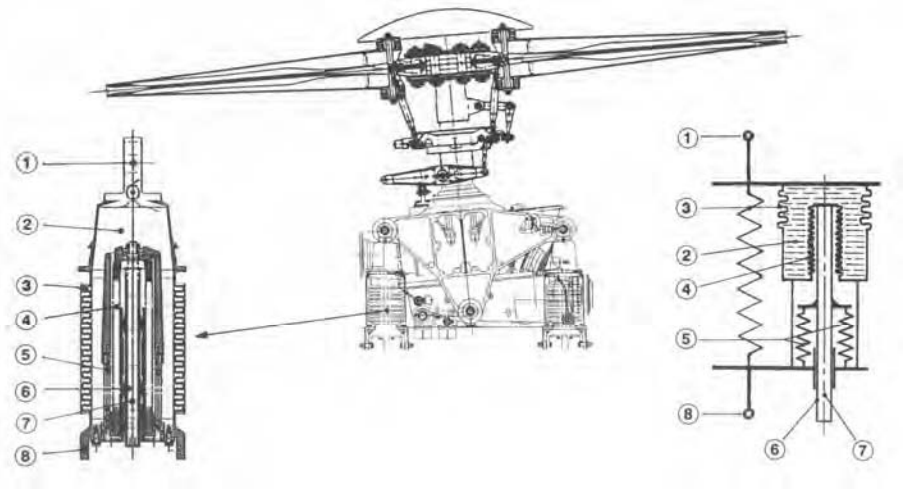

1. Attachment to the transmission unit
2. Hydraulic fluid of low viscosity
3. Primary spring and bellows
4. Bellows
5. Preload spring
6. Guide pin
7. Active mass
8. Attachment to the fuselage

Figure 7.32. *Integration of Aris system in the architecture of a helicopter*

The operating method can be described as follows. The stroke of the main or primary bellows, which is displaced by the periodical motion of the transmission unit with respect to the fuselage, amplifies the stroke of the secondary bellows and of the pendulum counterweight. The motion is amplified by varying the cross-sections A_p and A_s and because the fluid is incompressible.

The resultant inertia force produces a pressure variation in the hydraulic fluid that acts like a dynamic force on the isolator fitting points on the sides of the fuselage and transmission unit. For frequency tuning, these dynamic forces are in opposite phase to the spring forces of the isolator.

Figure 7.32 illustrates a model of an isolator with hydraulic force generator integrated on a helicopter.

Figure 7.33. *Aris system elements.*
Photo: Eurocopter Deutschland

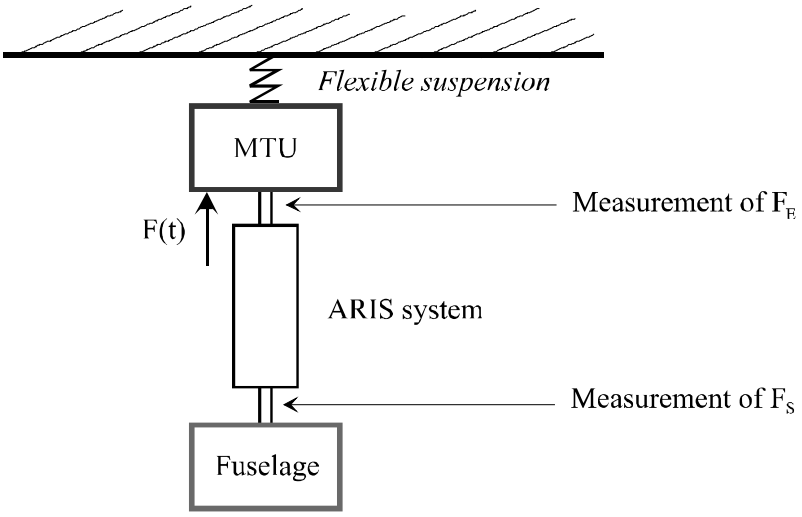

Figure 7.34. *Modeling of the Aris system test bench*

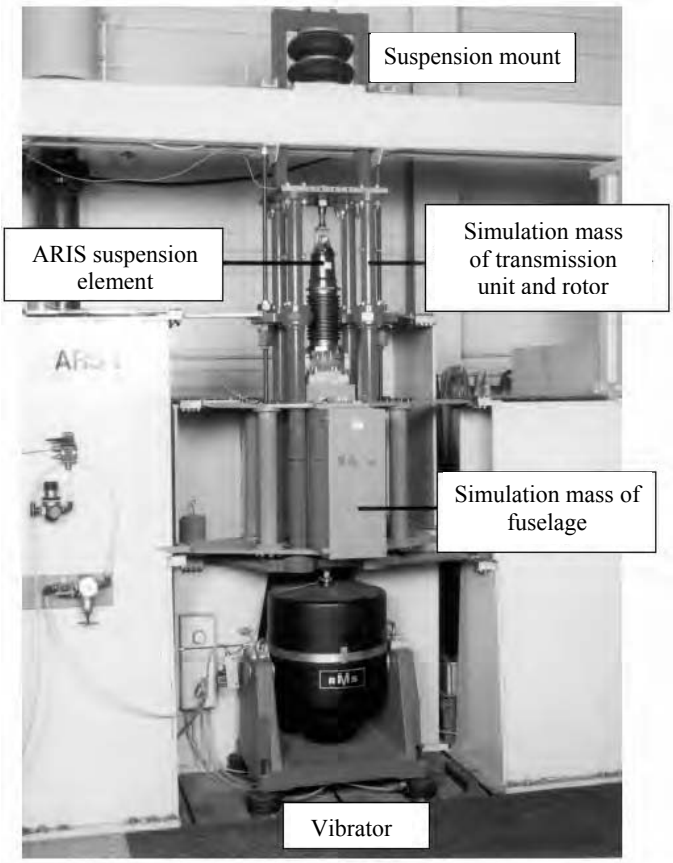

Figure 7.35. *Test bench for suspension characterization. Photo: Eurocopter Deutschland*

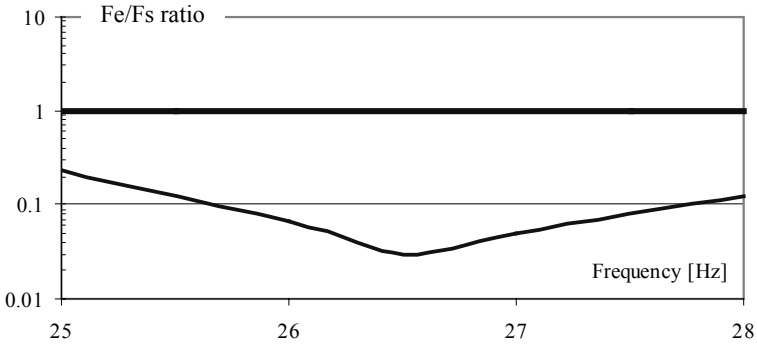

Figure 7.36. *Experimental transmissibility of ARIS hydraulic system*

7.3.3. *Example of a fluid inertia resonator*

7.3.3.1. *Principle*

In this system, a resonator is placed between two mobile masses, one of which is excited by an input load (see Figure 7.37) [HAL 80, HAL 81, SMI 99]. The resonator has two chambers filled with fluid that are separated by a piston. A running line enables the fluid to flow from one chamber to the other. The rod connecting the two masses is attached to the piston; a spring is mounted coaxially on the rod on each side of the piston.

The transfer function of such a system will produce an anti-resonance effect that can be used to reduce the transmitted load at its frequency. This anti-resonance depends only on the characteristics of the resonator, which makes it possible to choose it by correctly designing the system.

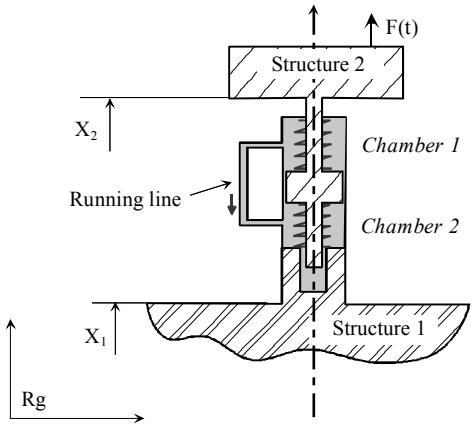

Figure 7.37. *Schematic diagram of the principle of the fluid inertia resonator*

The running line has a section S_c and a length L. Its function is to disperse energy. This loss is characterized by λ, representing the friction loss coefficient.

The piston has a cross-section S_v. P1 is the pressure in chamber 1 and P2 in chamber 2. The density of the fluid used is denoted by ρ.

7.3.3.2. *Formation of the equations*

The fundamental principle of dynamics applied to structure 1 gives:

$$M(1)\,\vec{A}_{G\in 2/R_g} = \vec{F}_{fluid\to 1} + \vec{F}_{spring\to 1} \qquad [7.72]$$

Integrating the characteristics of the spring and the geometric dimensions of the piston, we obtain:

$$M_1\ddot{X}_1 = S_v(P_1 - P_2) - K(X_1 - X_2) \qquad [7.73]$$

where:

– M_1 is the mass of structure 1,

– K is the stiffness of the springs,

– A_{fluid} is the fluid acceleration.

We assume that the fluid is incompressible and that the side walls do not deform. We initially ignore the regular and local friction losses. If we isolate the mass in the running line, we obtain the following equation:

$$L\,\rho\,A_{fluid} = (P_1 - P_2) \qquad [7.74]$$

By conservation of flow rate, we obtain the following complementary relation:

$$S_c\ A_{fluid} = -S_v(\ddot{X}_1 - \ddot{X}_2) \qquad [7.75]$$

Based on equations [7.74] and [7.75]:

$$\begin{aligned}(P_1 - P_2) &= -L\,\rho\frac{S_v}{S_c}(\ddot{X}_1 - \ddot{X}_2)\\ &= -L\,\rho\,\lambda\,(\ddot{X}_1 - \ddot{X}_2)\end{aligned} \qquad [7.76]$$

where λ is the cross-sectional ratio S_v/S_c.

By using equation [7.73], it is seen that:

$$M_1\ \ddot{X}_1 = -\rho\,S_c\ L\,\lambda^2(\ddot{X}_1 - \ddot{X}_2) - K(X_1 - X_2) \qquad [7.77]$$

We define the fluid inertia by:

$$M_a = \rho S_c\ L\lambda^2 \qquad [7.78]$$

In the case of harmonic motion, the isochronic transfer function is given by:

$$H(\omega) = \frac{X_1}{X_2} \qquad [7.79]$$

which yields:

$$K\ X_1 - \omega^2 (M_1 + M_a) X_1 = K\ X_2 - \omega^2\ M_a\ X_2 \qquad [7.80]$$

hence:

$$H(\omega) = \frac{K - M_a \omega^2}{K - (M_1 + M_a)\omega^2} \qquad [7.81]$$

This produces an anti-resonance frequency and a zero displacement of structure 1, for which the transmitted acceleration is almost zero.

It is important to remember that this frequency depends only on the fluid inertia (M_a) and not on the system's mobile masses. The anti-resonance frequency is given by:

$$f_{anti-r} = \frac{1}{2\pi}\sqrt{\frac{K}{M_a}} \qquad [7.82]$$

The resonance frequency is given by:

$$f_r = \frac{1}{2\pi}\sqrt{\frac{K}{M_s + M_a}} \qquad [7.83]$$

7.3.3.3. *Example of application: integration of the system on a helicopter*

In the proposed example, a fluid actuator is placed on the connection rods between the fuselage and the main transmission unit of the helicopter (see Figure 7.38).

The objective of the system is to reduce the vibrations in bΩ induced by the rotor. The data used are outlined in Table 1.2.

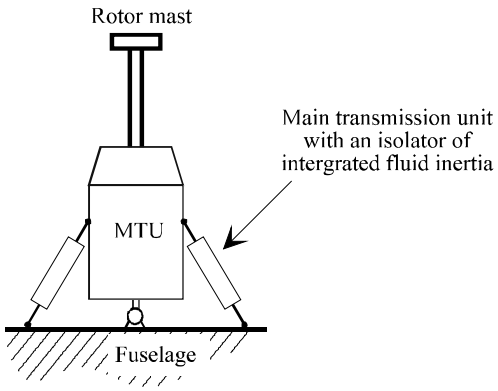

Figure 7.38. *Fluid inertia system in a main transmission unit rod*

b	**Number of blades**	5	**M_2**	**Mass of the main transmission unit**	150 kg
Ω	**Speed of rotation**	36.5 rad/s	**K**	**Rod stiffness**	3.7 10^7 N/m
M_1	**Fuselage mass**	875 kg			

Table 7.2. *Data used for a helicopter*

The excitation frequency is thus 29 Hz. To have an anti-resonance frequency of 29 Hz, the fluid inertia must be:

$$M_a = \frac{K}{(2\pi f_c)^2} = 1,054\text{Kg} \qquad [7.84]$$

The actuator is then designed (length of running line and sections for a given fluid) using the relation:

$$M_a = \frac{S_v^2}{S_c} L\rho \qquad [7.85]$$

The transfer function is plotted in Figure 7.39. The resonance phenomenon occurs at 21.4 Hz and the anti-resonance phenomenon at 29 Hz.

For the modeling previously presented, the friction losses, which are typical for all hydraulic circuits, were ignored. Damping is especially due to the laminar and local friction losses.

These friction losses reduce the efficiency of the system. The system must therefore be designed to ensure that the damping does not degrade the anti-resonance efficiency.

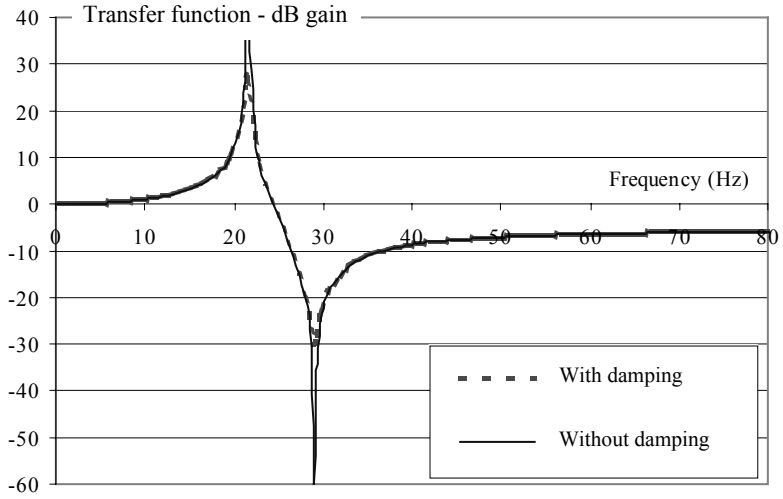

Figure 7.39. *Transfer function of a fluid inertia resonator*

Chapter 8

Self-Tuning Systems

8.1. Introduction

In Chapter 7, we saw that it was possible to isolate two structures using different methods to modify the loads at the interface between the structures. For example, it is possible:

– to change the stiffness of the link,

– to add moving masses so that their inertial effects counteract the effects of the addition of excitation.

These systems are designed to target a range of excitation frequencies. For certain applications, the dynamic parameters can vary with time. The driving function, as well as the frequencies of the structure, can then be changed by adjusting the stiffness or mass characteristics of the system.

The mass of systems like cars, airplanes and helicopters, decreases as they consume fuel. In addition, distinct flight conditions (level flight, maneuvers, or landing) produce different types of excitation.

Two cases are possible:

– the effect of the fluctuations is not sufficient to require the development of a more complex system. A passive system is sufficient, and it is designed to obtain a good trade-off for all the operating configurations of the structure,

– the initial characteristics of the solution no longer meet the requirements of the system's working conditions. The system characteristics are therefore adapted to match the variation in the different parameters of the excitation or of the system itself.

The methods used in self-tuning systems involve slow variations of the system characteristics. For example, this relative concept involves analyzing the system's vibration frequency and its timewise variation. Tuning is usually performed by an actuator. After the system status is measured, the tuning system will modify one feature of the system, e.g. stiffness, position of a mass, etc. Note that the suspension is still valid in the passive mode.

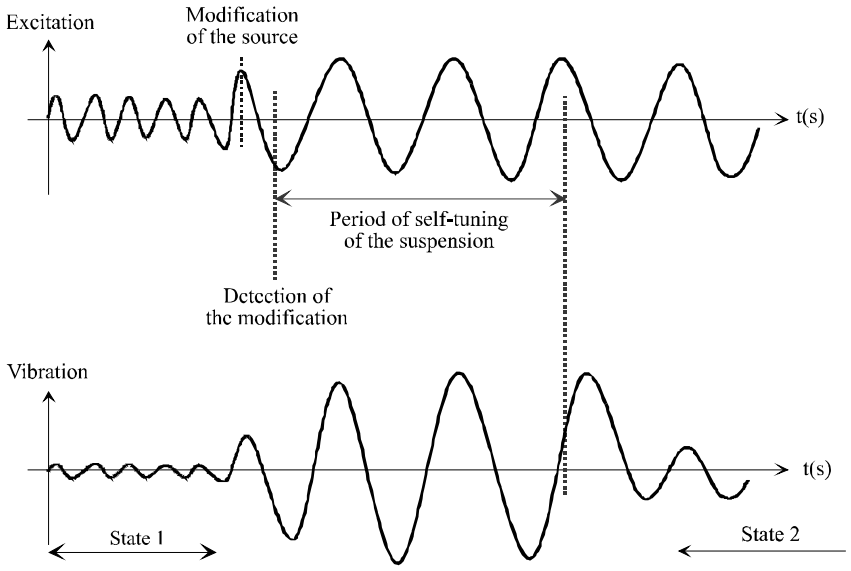

Figure 8.1. *Operating modes of a self-tuning system*

A self-tuning system is tuned by a control algorithm, which must be defined. This definition phase is based on theoretical simulations, mainly to identify the setting parameters of the algorithm and to verify the reliability of the system during parametric studies. Subsequently, the model must be validated by experimental tests on a model or real structure.

8.2. Modification of link characteristics (stiffness or damping)

For certain applications, the suspension has to be adapted for the various operating configurations. A case in point is a car suspension, which can have several configurations depending on the type of driving or the desired comfort. To do this, we propose modifying, using various techniques, either the stiffness of the suspension or its damping (see Figure 8.2).

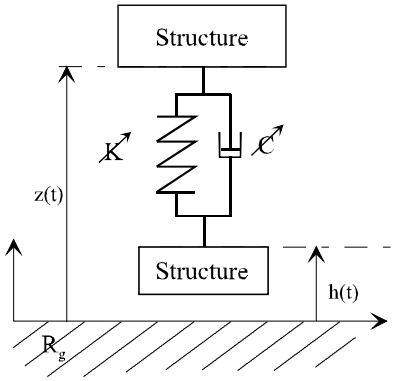

Figure 8.2. *Self-adapting control of a suspension*

8.3. Modification of the kinematic coupling: example of self-tuning Sarib®

The aim of this section is to present, through the example of the Sarib® suspension outlined in the previous chapter, the possibility of making a suspension become self-tuning by means of a kinematic coupling [KRY 98]. From a technological point of view, we suggest modifying the inertial effects of mobile masses by controlling their position $l_i(t)$.

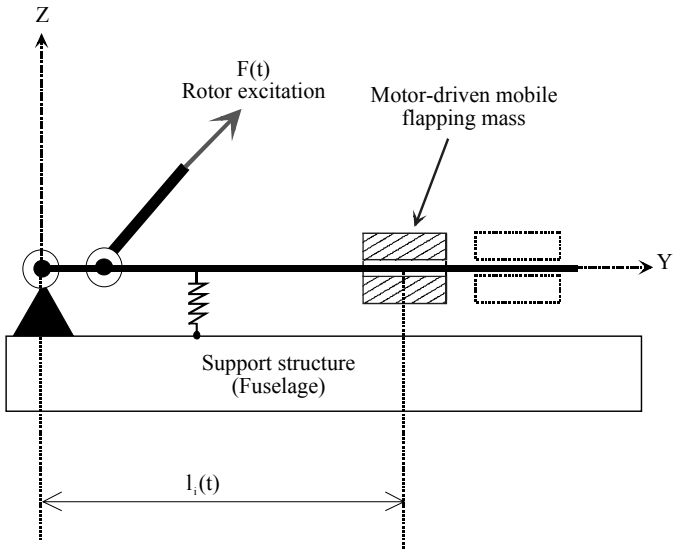

Figure 8.3. *Modeling of a Sarib® actuator of the self-tuning system*

The flapping mass center of gravity is moved by a motor mounted on the fixed tab (see Figure 8.4).

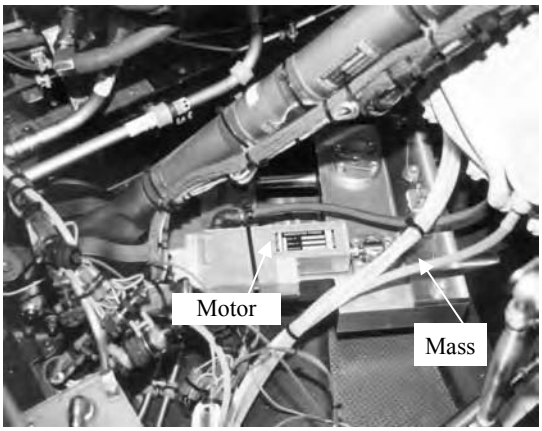

Figure 8.4. *Mass supports, example of integration on a helicopter (10 T)*

8.3.1. *Modeling of the suspension behavior*

To tune a self-tuning system requires a higher performance model than that described in the previous chapter. The excitation of the proposed suspension is spatial. In Chapters 3 and 7 we saw that the rotor excitation could consist of vertical "pumping" forces or in-plane moments.

In addition, the movements of the structure are coupled, consisting of both rotational and horizontal displacements.

The goal is to organize the group of masses in such a way as to eliminate the vibrations induced by the vertical "pumping", longitudinal and transversal in-plane loads, and the roll and pitch moments. In this case, the solutions provided by the unidirectional systems presented in section 8.2 are not directly applicable.

8.3.1.1. *Degrees of freedom of the system*

The dynamic behavior of the Sarib® suspension is modeled by a system having 12 degrees of freedom. Figure 8.5 shows the small mock-up used to validate the model.

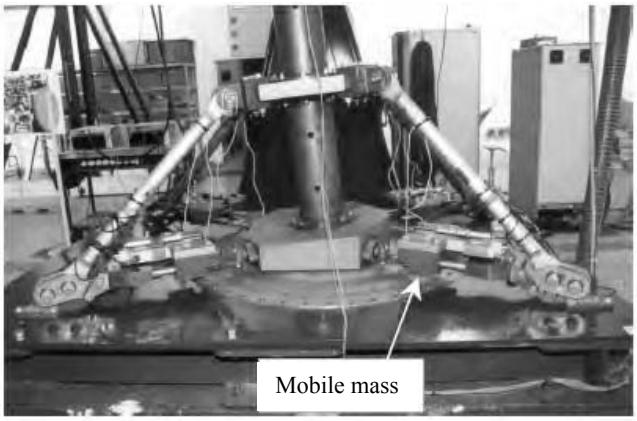

Figure 8.5. *Model of Sarib® self-tuning suspension*

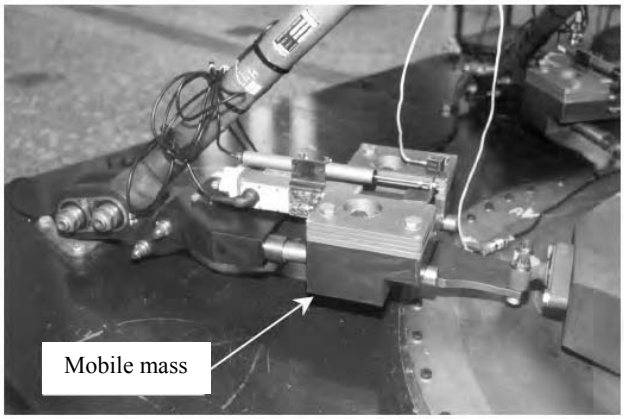

Figure 8.6. *Flapping masses of Sarib® self-tuning suspension*

The degrees of freedom (DOF) include the DOFs of the fuselage, transmission unit and flapping masses.

The fuselage is assumed to be a rigid body. The longitudinal and transversal displacements (in-plane) are denoted by X_F and Y_F, the vertical displacement (pumping) by Z_F and the transverse rotations (roll and pitch) by α_x and α_y.

The vertical movement (pumping) of the main transmission unit (MTU) relative to the fuselage is denoted by Z_{MTU}, and its rotation (roll and pitch) relative to the fuselage by θ_x and θ_y. The vertical movement of each flapping mass indicated by the subscript i is indicated by the arrow fq_i (see Figure 8.7).

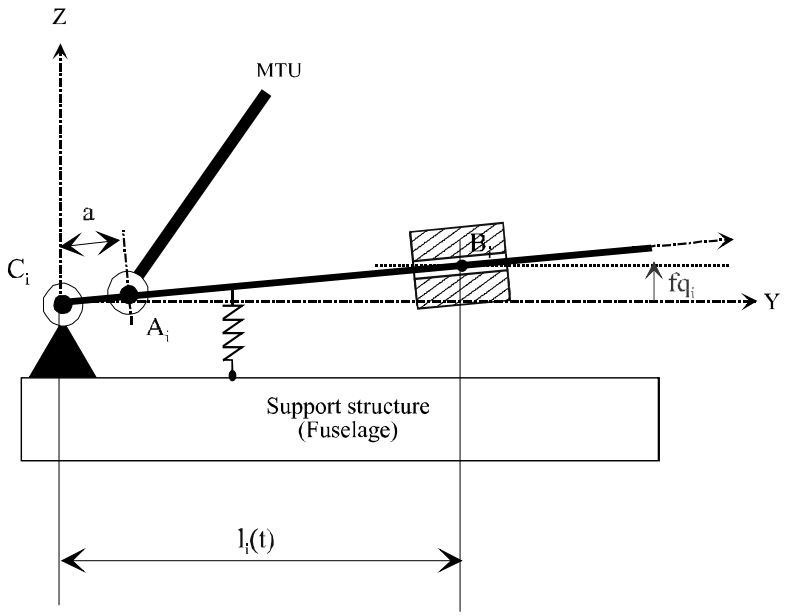

Figure 8.7. *Modeling of the behavior of flapping masses*

The flapping mass number i is located relative to point C_i. The power ratio λ_i is defined by the following equation:

$$\lambda_i = \frac{l_i}{a} \qquad [8.1]$$

8.3.1.2. *Formulation of the equations*

The system position vector is given by:

$$X = \left\{ X_F \;\; Y_F \;\; \alpha_x \;\; \alpha_y \;\; \theta_x \;\; \theta_y \;\; Z_F \;\; Z_{MTU} \;\; fq_1 \;\; fq_2 \;\; fq_3 \;\; fq_4 \right\}^T \qquad [8.2]$$

and the excitation vector defined at the top of the transmission unit by:

$$F = \{Fy \quad Fx \quad Fz \quad My \quad Mx\}^T \qquad [8.3]$$

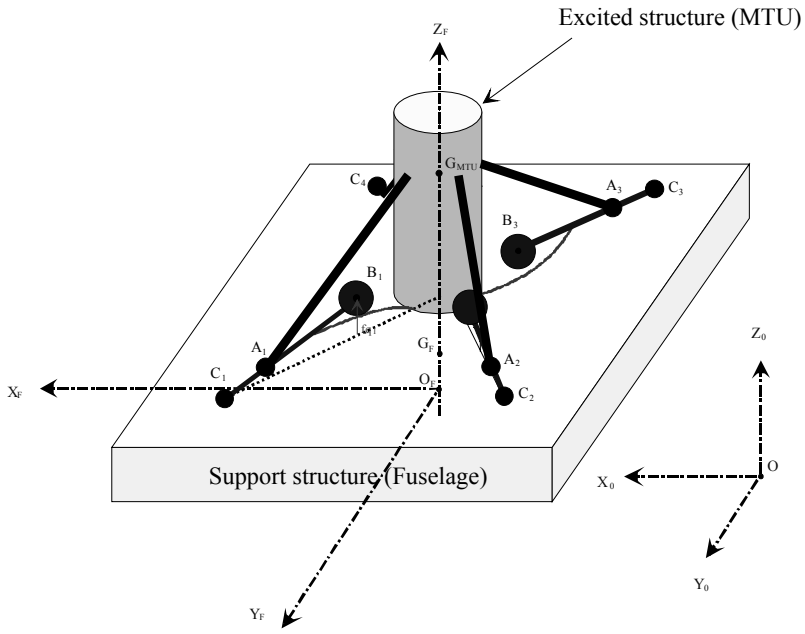

Figure 8.8. *Degrees of freedom for the adaptive Sarib®*

With the help of Lagrange's equations, the small motion equations can be written in the following form:

$$M\ddot{X} + C\dot{X} + K\,X = L\,F \qquad [8.4]$$

Matrices M, C, K are the mass, damping and stiffness matrices. Matrix F contains the five components of the excitation load set. Matrix L represents the influence of external mechanical actions on each of the selected degrees of freedom.

8.3.1.3 *Analysis of the general behavior of the suspension*

It is worth analyzing whether the setting of the masses can respond at the same time to the filtering of different excitations, pumping, in-plane loads or roll and pitch moments.

In order to do this, we will define a new overall vibratory level (OVL) based on the measurements of the six accelerations as follows:

$$\text{OVL} = \sqrt{\frac{A_1^2 + A_2^2 + A_3^2 + A_4^2 + A_5^2 + A_6^2}{6}} \qquad [8.5]$$

where:

– A1, A2, A3 and A4 are vertical accelerations on Z_F,

– A5 is the transversal acceleration on Y_F,

– A6 is the longitudinal acceleration on X_F.

The acceleration measurement points on the support structure are defined in Figure 8.9.

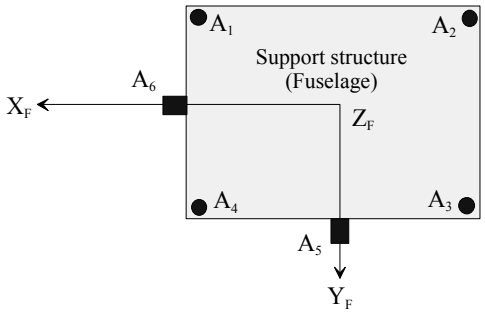

Figure 8.9. *Theoretical position of accelerometers*

For each type of excitation, the positions of the flapping masses vary simultaneously with the same increment of 0.5 mm (see Figure 8.10).

The optimum positions of the flapping masses for minimum vibration vary with the type of excitation.

Type of excitation	**Pumping**	**Roll**		**Pitch**	
	Fz 1,000 N	Fy 1,000 N	Mx 1,000 Nm	Fx 1,000 N	My 1,000 Nm
Positions (l_i) I = 1 … 4	1.473 m	0.480 m	0.498 m	0.479 m	0.487 m

Table 8.1. *Optimal positions versus type of excitation*

On a helicopter, the excitation load set at the rotor head is a combination of five types of excitation and also depends on the forward flight speed. According to the flight configurations, it is not possible to optimize the setting of the suspension without control of the flapping masses.

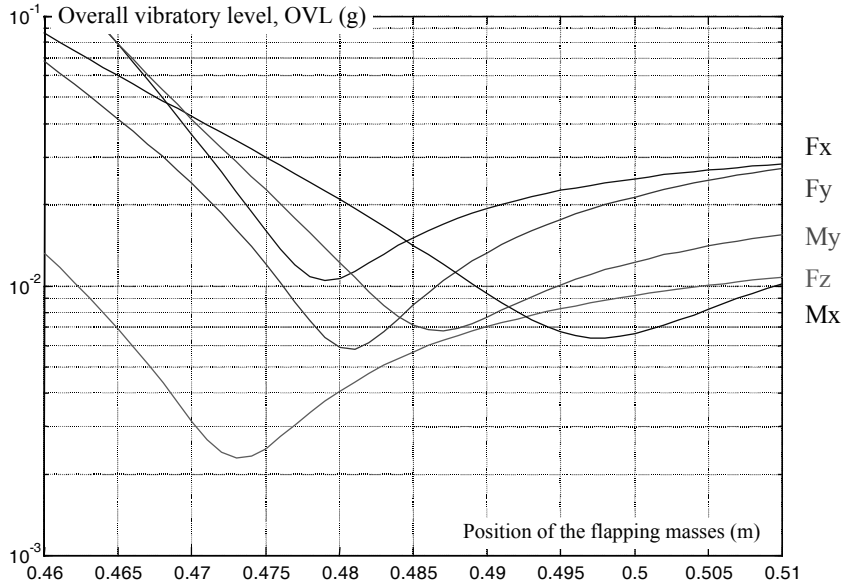

Figure 8.10. *Variation of vibratory level with the position of the masses*

8.3.1.4. *Conclusion*

With the analytic model, it is possible to:

– simulate the dynamic behavior of the Sarib® suspension,

– validate the activation concept of the Sarib® suspension. According to the flight configurations, the optimal setting of the suspension is dependent on the position of the flapping masses.

A control algorithm must be developed in order to minimize the vibratory level based on the excitation at the rotor head. The choice and functioning of the algorithm require special attention.

8.3.2. *Presentation of the control algorithm*

The control algorithm must manage the motion of flapping masses based on:

– variations of the rotor head load set (modification of flight configurations),

– variations of the structure (variation of the fuel and load masses),

– change of objectives (comfort, aiming, firing, etc.).

Problem formulation

If n accelerometers are placed on the structure, the minimization criterion or the overall vibratory level (root mean square) is defined as follows:

$$\text{CRITERION} = \text{OVL} = \sqrt{\frac{\gamma_1^2 + \cdots + \gamma_i^2 + \cdots + \gamma_n^2}{n}} \qquad [8.6]$$

where γ_i is the acceleration module of accelerometer No. i at the frequency bΩ.

The accelerations γ_i are dependent on the positions of the four flapping masses. The OVL criterion is therefore a non-linear function, noted by f, of four parameters having the position l_i of the flapping masses:

$$\text{OVL} = f(l_1, l_2, l_3, l_4) \qquad [8.7]$$

The objective is to minimize function f by finding a combination of parameters (l_1, l_2, l_3, l_4) so that $f(l_1, l_2, l_3, l_4)$ is minimal.

This minimization takes place under the constraint that the movement of flapping masses, for reasons of size, is limited to a bound domain.

In addition, the algorithm must satisfy the following specifications:

– minimize the OVL criterion, irrespective of the excitation at the rotor head,

– adapt to different flight configurations (speed, objectives, etc.),

– adapt to variations in the rotation speed,

– be easily implemented experimentally.

The control is not linear because the shift of the flapping masses modifies the matrices M, K, C and consequently the natural frequencies of the system. The lack

of a model of constant coefficients does not support the usage of conventional linear algorithms.

In addition, this problem differs from a classical vibratory control system in which the forces to inject are necessary in order to minimize a vibratory criterion. We have to deal here with a problem of parametric control where the system's internal parameters - in our case the flapping masses - are necessary to minimize a criterion, the OVL. This criterion is not cannot be differentiated, in the sense that a simple formulation of partial derivatives of the criterion with respect to the parameters of positions l_i is not possible.

This supplementary constraint eliminates the various algorithms (Newton, LMS, etc.) whose operation requires knowledge of the partial derivatives of the criterion with respect to parameters l_i.

Among all the possible methods, we have chosen an algorithm whose formulation is based on the constant step gradient method.

Let dl_i be a variation of the position of the masses; the development of the function f around a position in a first order Taylor series yields:

$$f(l_i + dl_i) = f(l_i) + \sum_{i=1}^{4} \left[\frac{\partial f}{\partial l_i} \right] dl_i \qquad [8.8]$$

where $\left[\frac{\partial f}{\partial l_i} \right]$ is the gradient of the criterion.

In this expression, the four parameters vary simultaneously.

For the variation of a single parameter, for example, parameter 1, expression [8.8] is written as:

$$f(l_1 + dl_1,\ l_2,\ l_3,\ l_4) - f(l_1,\ l_2,\ l_3,\ l_4) = \left[\frac{\partial f}{\partial l_1} \right]_{l_2, l_3, l_4} dl_1 \qquad [8.9]$$

The complexity of function f makes it difficult to explain the gradient analytically. Consequently, it is evaluated through calculations for simulations, or by measuring the value of function f on the structure at the points $x_1 = (l_1 + dl_1, l_2, l_3, l_4)$ and $x_2 = (l_1, l_2, l_3, l_4)$.

An iteration k is completed once the four flapping masses have moved. The position of the masses at the iteration k will be marked $l_1^k, l_2^k, l_3^k, l_4^k$.

The motion step of the masses is identical and is defined as $dl_i = dl$. Based on iteration k, the mass positions at iteration k + 1 are obtained in the following way.

The first mass moves from d1. Expression [8.9] is written:

$$f(l_1^k + d1, l_2^k, l_3^k, l_4^k) - f(l_1^k, l_2^k, l_3^k, l_4^k) = \left[\frac{\partial f}{\partial l_1^k}\right]_{l_2^k, l_3^k, l_4^k} d1 \qquad [8.10]$$

The position of the first mass at iteration k + 1 is written:

$$l_1^{k+1} = l_1^k - d1 \text{ sign} \left(\left[\frac{\partial f}{\partial l_1^k}\right]_{l_2^k, l_3^k, l_4^k} d1 \right) \qquad [8.11]$$

The first mass is l_1^{k+1}, while the second mass is moved from d1. Equation [8.10] becomes:

$$f(l_1^{k+1}, l_2^k + d1, l_3^k, l_4^k) - f(l_1^{k+1}, l_2^k, l_3^k, l_4^k) = \left[\frac{\partial f}{\partial l_2^k}\right]_{l_1^{k+1}, l_3^k, l_4^k} d1 \qquad [8.12]$$

The position of the second mass at iteration k + 1 is written:

$$l_2^{k+1} = l_2^k - d1 \text{ sign} \left(\left[\frac{\partial f}{\partial l_2^k}\right]_{l_1^{k+1}, l_3^k, l_4^k} d1 \right) \qquad [8.13]$$

The first mass is in l_1^{k+1}, the second in l_2^{k+1}, and the third moved from d1. Equation [8.12] is written:

$$f(l_1^{k+1}, l_2^{k+1}, l_3^k + d1, l_4^k) - f(l_1^{k+1}, l_2^{k+1}, l_3^k, l_4^k) = \left[\frac{\partial f}{\partial l_3^k}\right]_{l_1^{k+1}, l_2^{k+1}, l_4^k} d1 \qquad [8.14]$$

The position of the third mass at iteration k + 1 is written:

$$l_3^{k+1} = l_3^k - d1 \ \text{sign} \left(\left[\frac{\partial f}{\partial l_3^k} \right]_{l_1^{k+1}, l_2^{k+1}, l_4^k} d1 \right) \qquad [8.15]$$

The position of the fourth mass, at iteration k + 1, is obtained in a similar way.

Taking into account a noise level on the measurements requires the study of the $\text{sign} \left[\frac{\partial f}{\partial l_i} \right] d1$ and its value with respect to the sign of the noise level.

However, the range of variation of the flapping masses is limited. This constraint implies continuous testing of the positions of the masses with respect to stops. If a mass reaches the limit stop, the direction of its movement is changed for the following iteration.

8.3.3. *Performances*

We will now compare the performances and contribution of such a system with a conventional passive system, by simulations and tests conducted on models and prototypes.

8.3.3.1. *Simulation and behavior analysis*

8.3.3.1.1. Decoupled excitations

Let Fx be the component of excitation hub loads generating pitch excitation. The performances of the algorithm are analyzed based on the movements of the flapping masses and the variation of the criteria.

The control algorithm is seen to optimize the overall vibratory level (see Figure 8.11). Once the minimum is obtained, the flapping masses oscillate, without diverging, around the optimal positions (see Figure 8.12). In addition, these positions correspond to those determined during the parametric study.

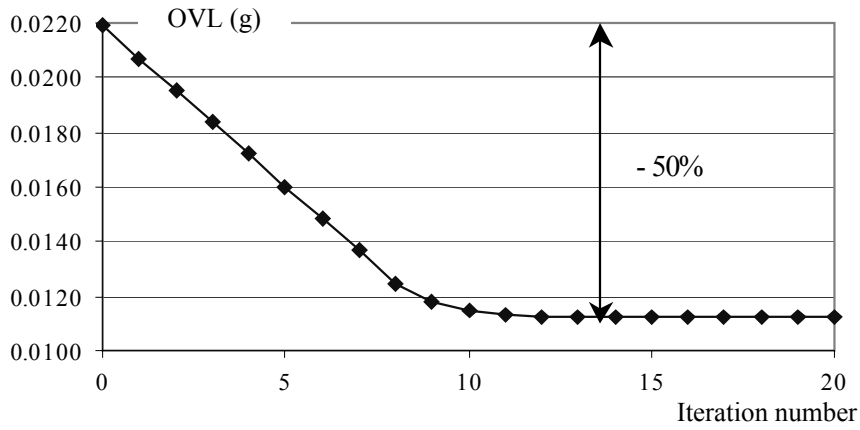

Figure 8.11. *Variation of OVL criterion with number of iterations for a 1,000 N Fx excitation*

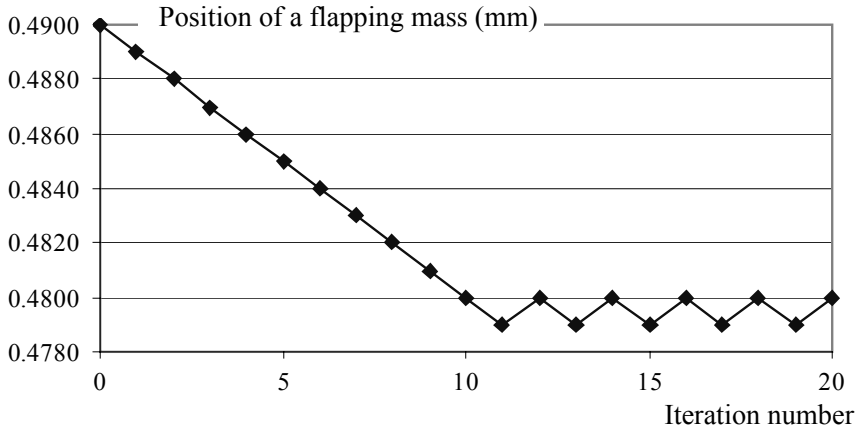

Figure 8.12. *Positions of the flapping masses versus number of iterations for a 1,000 N Fx excitation*

The gains in vibration level compared to a suspension without control are appreciable: in the order of 50% over the OVL.

This type of simulation can be carried out for different types of decoupled excitations. Compared to a suspension system without control, the gains can be high (see Table 8.2 below). Note that the performances are different and depend on the type of excitation.

Excitation	Gain
Fx = 1,000 N	50%
My = 1,000 Nm	13%
Fy = 1,000 N	62%
Mx = 1,000 Nm	27%
Fz = 1,000 N	64%

Table 8.2. *Algorithm performance for decoupled excitations*

In practice, the rotor hub loads are a combination of five basic excitations, and the performance study for combined excitations is necessary.

8.3.3.1.2. Combined excitations

The components of the rotor hub loads are defined as follows:

Fx = 900 N Fy = 1,200 N Fz = 900 N
Mx = 2,100 Nm My = 1,800 Nm

These values correspond to a high speed flight configuration for a four bladed helicopter weighing 8-10 tons. In order to simplify matters, the phase differences between excitations are ignored.

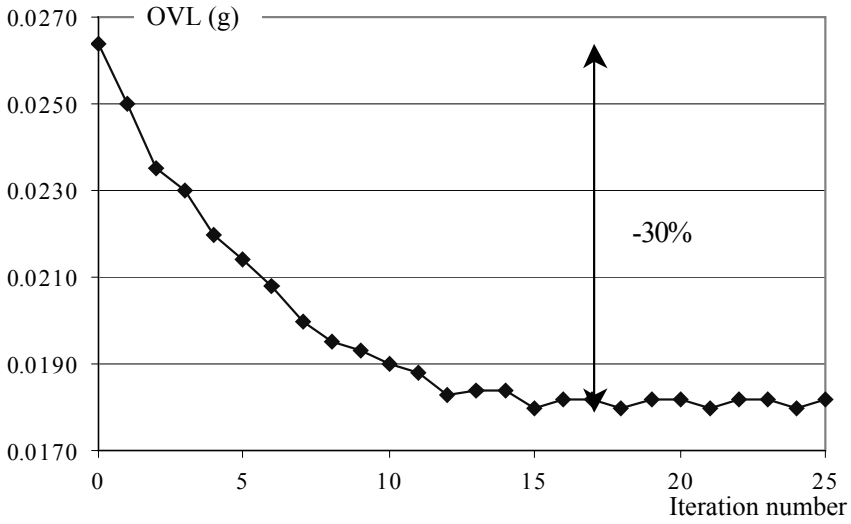

Figure 8.13. *Control algorithm performance for combined excitations*

Compared to a conventional suspension, flapping mass position control decreases the vibratory level by 30%. We have shown above how the algorithm works through simulations, and the order of theoretical magnitude that can be expected from such a system.

8.3.3.2. *Tests conducted on a model*

The tests conducted on a model generally make it possible to verify if the analytical model is valid and how robust the control algorithms area against external changes. The model and the measuring points have been presented in Figures 8.6 and 8.9.

8.3.3.2.1. Change of excitation frequency

Among these tests, we included the suspension's self-tuning capability to adapt to a variation in the excitation frequency, i.e. by varying the rotation speed. The excitation frequency was thus set at 17.1 Hz for t < 180 s and at 16 Hz for t > 180 s.

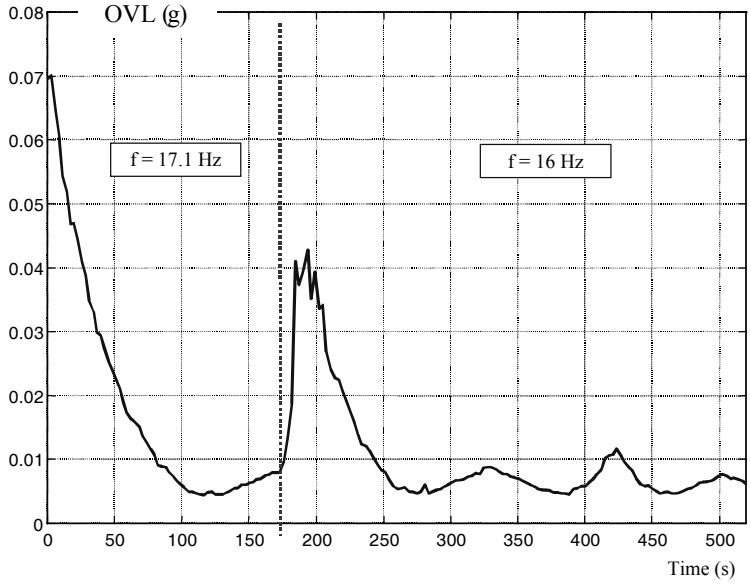

Figure 8.14. *Adaptation to a change in excitation frequency*

This test reveals the suspension's self-tuning capability to adapt to a variation in excitation frequency.

Excitation frequency	17.1 Hz	16 Hz
Gain (%)	92%	89%

Table 8.3. *Algorithm performance*

8.3.3.2.2. Actuating cylinder failure

The control algorithm must be able to adapt to one or more actuating cylinder failures.

Several configurations were simulated:

– the four actuators operational,

– one actuator failed,

– two actuators failed.

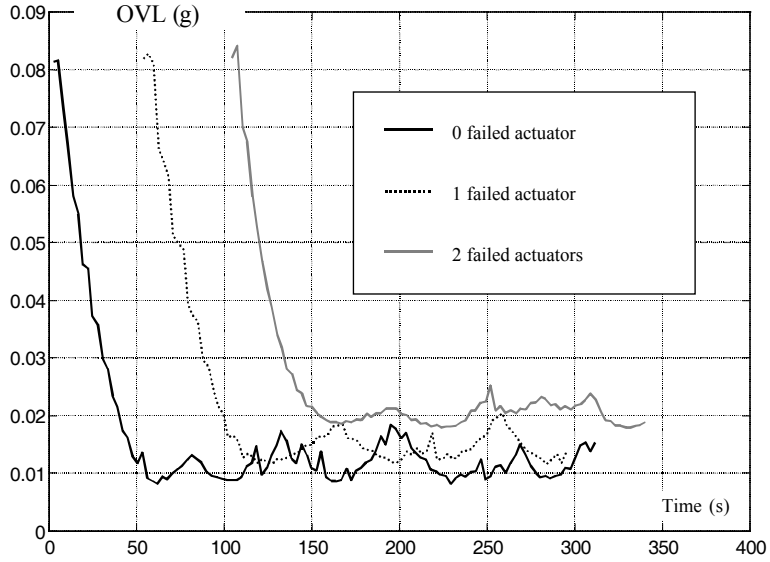

Figure 8.15. *Robustness in case of actuator failure*

The failure of one or more actuators partially limits the decrease of the global vibratory level.

Number of the configuration	Number of failed actuators	Decrease of OVL (%)
1	0	90
2	1	85
3	2	78

Table 8.4. *Summary of the effect of actuator failure on the performance criterion*

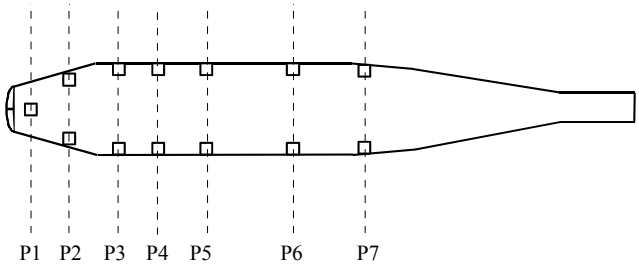

Figure 8.16. *Location of the acceleration sensors*

Location		Location	
P1	**Nose**	**P5**	**Right front cabin**
	Accelerometers in Y, Z		Accelerometer in Z
P2	**Pilot feet**		**Left front cabin**
	Accelerometer in Z		Accelerometer in Z
	Copilot feet	**P6**	**Left rear cabin**
	Accelerometer in Z		Accelerometer in Z
P3	**Pilot seat**		**Right rear cabin**
	Accelerometers in X, Y, Z		Accelerometer in Z
	Copilot seat	**P7**	**Left rear cabin**
	Accelerometers in X, Y, Z		Accelerometer in Z
P4	**Right front cabin**		**Right rear cabin**
	Accelerometer in Z		Accelerometer in Z
	Left front cabin		
	Accelerometer in Z		

Table 8.5. *Distribution of accelerometers on the structure*

8.3.3.3. *Flight tests on a real structure*

The measurements on the aircraft used were made with 20 accelerometers evenly distributed around the cabin (see Figure 8.16 and Table 8.5).

8.3.3.3.1. Algorithm convergence

The tests on the real structure make it possible to validate the modeling carried out in order to perfect the control algorithm. This makes it possible to ensure that the hypotheses made about the behaviors (linearity, recognition of certain phenomena, etc.) do not question the working principle and in particular that the performance of the system is sufficient.

The algorithm performances in Figure 8.17 are for a speed of 140 Kts. The helicopter is in level flight at constant speed, and at an altitude of 2,000 ft.

The suggested configuration generates a 33% decrease in the criterion.

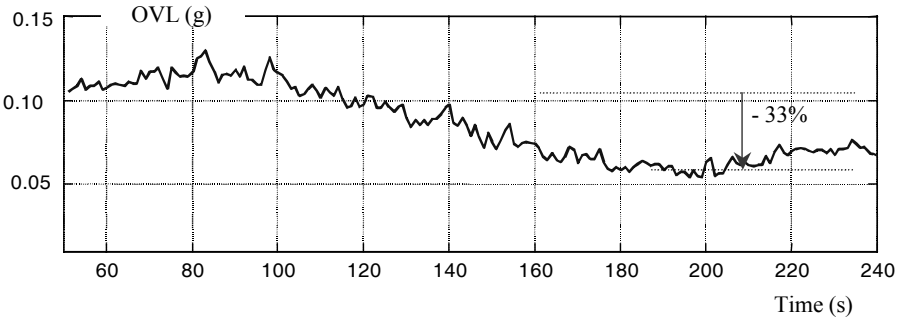

Figure 8.17. *Algorithm performance at 140 Kts*

8.3.3.3.2. System reliability during variations of forward flight speed

The performance levels at different speeds are compared below with and without a self-tuning system.

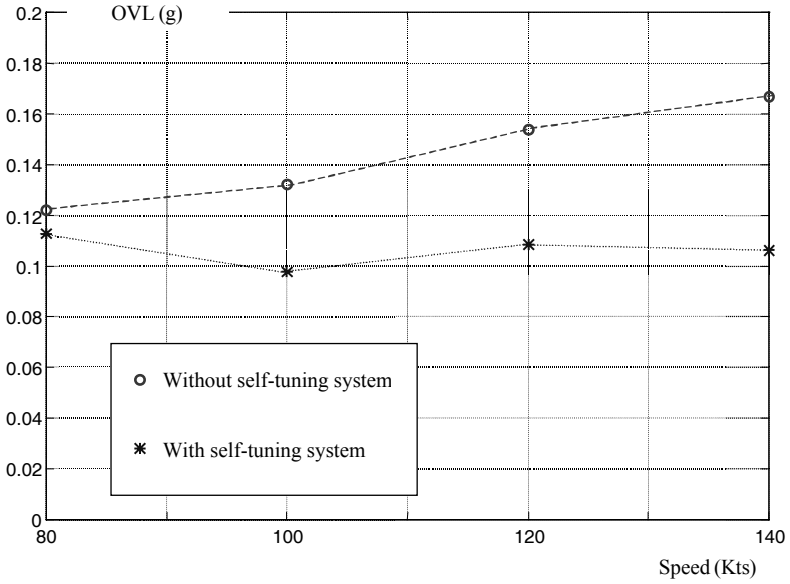

Figure 8.18. *Influence of the speed on the performance criterion*

Irrespective of the speed, the decrease is seen to be homogenous. The results are summarized in Table 8.6.

Speed (Kts)	80	100	120	140
Gain	7%	26.5%	30%	33%

Table 8.6. *Performance obtained according to the forward flight speeds of the aircraft*

The tests validate the building principle of the algorithm and demonstrate its performance. The objectives set during the definition of this type of suspension were attained and the decrease of the vibratory level in the structure is significant.

Chapter 9

Active Suspensions

9.1. Principle

Several active principles are used to isolate one structure from another. In this chapter, we will present an active system that ensures the isolation function by distribution of the internal loads.

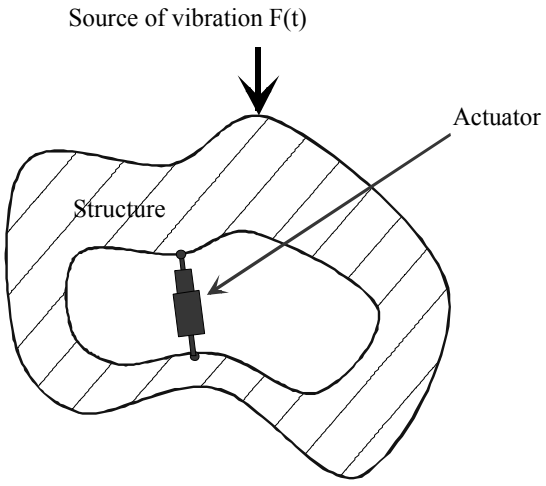

Figure 9.1. *Actuators used for the control of internal loads in a structure*

The principle of the internal load control system is to inject a set of dynamic loads into the structure in order to minimize its vibratory response. The loads depend on the vibratory condition of the structure (a condition that is identified with the help of a set of accelerometers or strain gauges). The loads are injected via hydraulic or electro-dynamic actuators suitably located on the structure itself.

An example of hydraulic technology is shown in Figure 9.2.

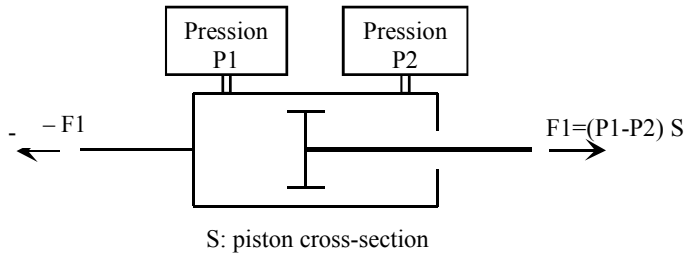

Figure 9.2. *Principle of introduction of internal loads in a structure – example of a hydraulic system*

Each actuator introduces two control forces in the structure, F1 and –F1, which are of opposite sign. The excitation load set of a actuator is therefore zero and we have an internal load. The principle of the system is to modify the distribution of internal loads in the structure. The role of the actuators is no longer to disperse the vibratory energy of the structure (a dispersing control would increase the reduced damping of different modes), but to modify the distribution of vibratory energy for the different modes to minimize the vibrations of the structure.

9.2. Formulation of system equations and analysis of the system

In this case study on the dynamic behavior of a deformable structure, we will use a finite element method-based numerical approach. The need for a numerical approach is due to the complexity of the geometries and conditions at specific limits, which are difficult to model using an analytical approach.

Thus, the overall structure is modeled by a system of n degrees of freedom, using for example a finite element code. The behavior equation is given by:

$$M\ddot{X} + C\dot{X} + KX = F \qquad [9.1]$$

where:

– X is the vector response,

– M, C, K are respectively the mass, damping and stiffness matrices,

– F is the excitation vector.

The excitation consists of external excitations denoted by U and control excitations by V. Then:

$$F = T\,U + S\,V \qquad [9.2]$$

where:

– T is the localization matrix of external loads,

– S is the localization matrix of controls.

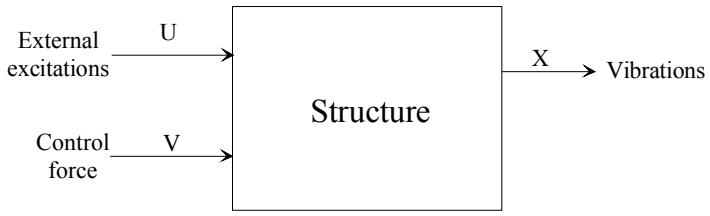

Figure 9.3. *Block diagram of the system*

For a harmonic excitation, we define the isochronous transfer function of the structure as follows:

$$X = H(\omega)\ F \qquad [9.3]$$

where:

$$H(\omega) = (K - M\,\omega^2 + i\,C\,\omega)^{-1} \qquad [9.4]$$

and:

– H(ω) is the transfer matrix,

– H_{ij} is the ratio between the response x_i at point i and excitation F_j at point j.

It is interesting to express this magnitude in terms of the modal characteristics in the case when the damping matrix C can be diagnosed in the modal basis of the conservative system.

Let:

$$q = \Phi^T X \qquad [9.5]$$

This yields:

$$\Phi^T M \Phi = \begin{bmatrix} \ddots & 0 & 0 \\ 0 & \mu_i & 0 \\ 0 & 0 & \ddots \end{bmatrix} \qquad \Phi^T K \Phi = \begin{bmatrix} \ddots & 0 & 0 \\ 0 & \gamma_i & 0 \\ 0 & 0 & \ddots \end{bmatrix}$$
$$\Phi^T C \Phi = \begin{bmatrix} \ddots & 0 & 0 \\ 0 & \beta_i & 0 \\ 0 & 0 & \ddots \end{bmatrix} \qquad [9.6]$$

Hence:

$$q_i = \frac{\sum_{k=1}^{n} \Phi_{k,i} F_k}{\gamma_i - \mu_i \omega^2 + i \beta_i \omega} \qquad [9.7]$$

We can write:

$$\begin{cases} \omega_{pi}^2 = \dfrac{\gamma_i}{\mu_i} \\ 2 \lambda_i \omega_{pi} = \dfrac{\beta_i}{\mu_i} \end{cases}$$

where:

– ω_{pi} is the natural angular frequency of mode i,

– λ_i is the damping ratio of mode i.

Hence, H_{ij} – the transfer function between the degree of freedom no. i and component no. j of the excitation vector – is given by:

$$H_{ij}(\omega) = \sum_{k=1}^{n} \frac{\Phi_{ik}\Phi_{jk}}{\mu_k(\omega_{pk}^2 - \omega^2 + 2i\lambda_k\omega_{pk}\omega)} \quad [9.8]$$

The control depends on the choice of performance criterion: in our case, the acceleration. Let the functional J be the weighted sum of the measured accelerations:

$$J = X_m^T \; W \; X_m \quad [9.9]$$

where:

– X_m is the vector of acceleration measurements,

– W is the weighting matrix.

We will assume that the system is linear. The overlapping method can be used. The measurement vector can be broken down into the sum of the measurements without the control X_{m0} and those with the control, as follows:

$$X_m = X_{m0} + B_m \; V \quad [9.10]$$

where B_m, is the matrix of control influence on the vibratory levels.

Hence, the functional J can be expressed as:

$$J = (X_{m0} + B_m \; V)^T \;\; W \; (X_{m0} + B_m \; V) \quad [9.11]$$

or after differentiation:

$$\frac{dJ}{dV} = B_m^T W(X_{m0} + B_m \; V) + (X_{m0} + B_m \; V)^T W \; B_m \quad [9.12]$$

Functional J is a minimum for:

$$V = -(B_m^T \; W \; B_m)^{-1} \; B_m^T \; W \; X_{m0} \qquad [9.13]$$

Several conclusions can be drawn from equation [9.13].

The optimal control is a linear function of the non-controlled X_{m0} vibratory level, which is in its turn a linear function of the generalized loads ($\Phi^T F$). The control is thus a linear function of the result of external loads introduced in structure F and of the modal deformations at the introduction point Φ_i of the loads.

Thus, the equation of optimal control [9.13] shows that the higher the modal deformations at the control forces' introduction point, the weaker the amplitude V of the controls.

For rigid body modes, the modal components of the control forces are zero, which makes these modes non-controllable. The control force must sense the deformations occurring when the loads are introduced, which is not the case for a rigid body. Therefore, it is better to place the controls (or to modify the structure) in order to maximize the deformations of the modes to be controlled when these loads are introduced. The control forces must sense a relative modal stiffness (of the modes to be controlled), which should be as low as possible. For a rigid body mode, the modal stiffness between two control points is, by definition, infinite. The control amplitude is not affected by the fact that the control frequency is a natural frequency of the structure.

Control amplitude is also independent of the value of the structure's natural frequencies.

9.3. Technological application

A set of dynamic loads are injected into the structure to minimize its vibratory response. The loads are based on the vibratory condition of the structure, which is identified by accelerometers or strain gauges. The loads are injected via hydraulic or electro-dynamic actuators suitably located on the respective structure.

Each actuator introduces two control forces in the structure, F1 and –F1, which are of opposite sign.

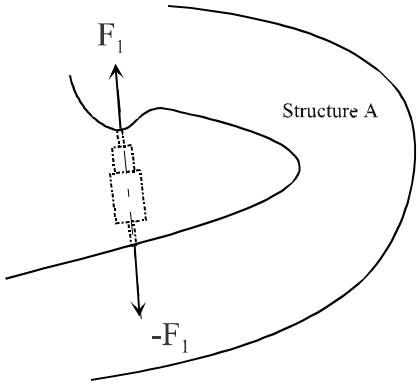

Figure 9.4. *Actions of the actuators on the structure*

The role of the actuators is not to disperse the vibratory energy of the structure, but to modify the distribution of vibratory energy for the different modes in order to minimize the vibrations of the structure.

The control forces must sense a relative modal stiffness (of the modes to be controlled), which should be as low as possible. The actuators cannot be placed between the vibration nodes of a structure, because the control would not be efficient. This is the reason why it is often necessary to introduce a supplementary flexibility in parallel with the actuator. This additional flexibility enables the local flexibility of the structure to be reduced, with the aim of decreasing the control force.

An example of a hydraulic actuator together with the flexibility is shown in Figures 9.5 and 9.6.

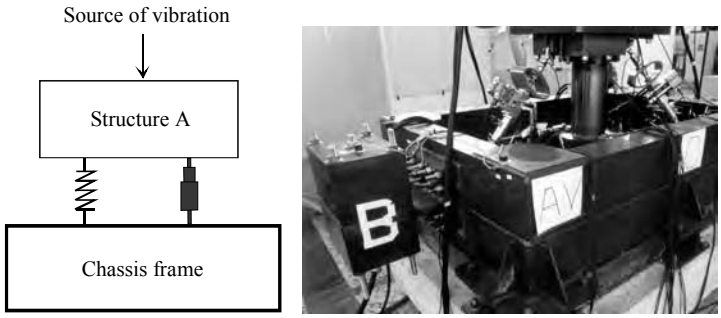

Figure 9.5. *A structure with a hydraulic actuator and flexibility. Photo: Eurocopter*

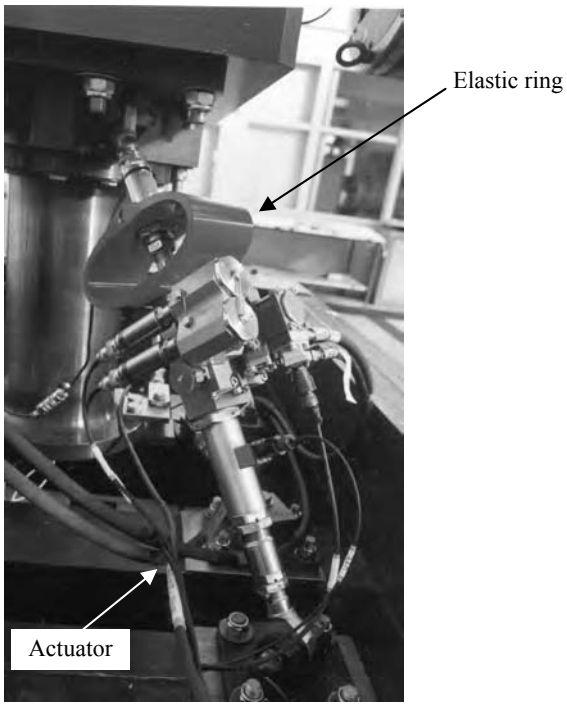

Figure 9.6. *Test model.*
Photo: Eurocopter

The control system of internal loads consists of three main elements: force-actuator, computer and sensors. The actuators retrieve the value of the force output by the computer, which uses the data provided by the sensors. The sensors measure the level of vibrations (stresses or loads) and send the signal directly to the computer.

There are two important types of algorithms associated with this output: the frequency algorithm, which focuses on a finite number of harmonics, and the time domain algorithm, often based on the recursive least squares algorithm at a filtered reference (X filtered Least Mean Squares (LMS)). The latter type is widely used in the active control of noise and vibrations, when there is a reference signal correlated to the noise or vibrations to eliminate.

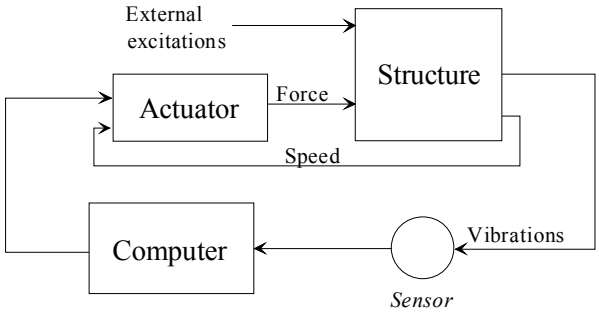

Figure 9.7. *Block diagram of the control*

We will now consider the system in Figure 9.8, where the problem is to determine the filter coefficients W that minimize the error e. Because of the scalar and discrete signals, $W(w_0, w_1 \ldots w_{N-1})$ can be sought in the form of a finite impulse response (FIR) filter of time N. Thus, the output $U(u_0, u_1 \ldots u_{N-1})$ of the filter at an instant k is written as a convolution integral:

$$u_K = \sum_{i=0}^{N-1} w_i x_{k-i} \qquad [9.14]$$

We can also consider H_s as an FIR filter of M time, providing the output X_s of the filter at the instant k, as a convolution product:

$$x_k^s = \sum_{i=0}^{M-1} h_i^s u_{k-i} \qquad [9.15]$$

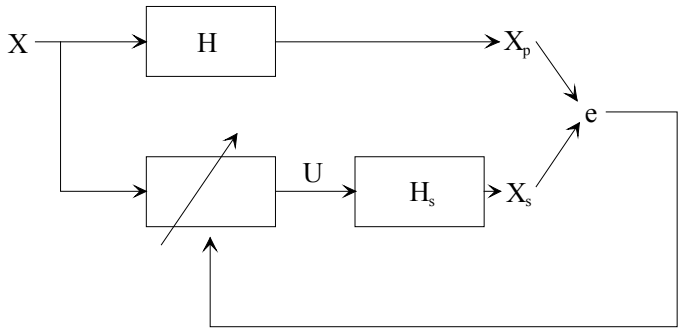

Figure 9.8. *Minimization by an LMS method*

Hence:

$$e_k = x_k^s + \sum_{i=0}^{M-1} h_i^s \sum_{j=0}^{N-1} w_j \, x_{k-i-j} = x_k^s + \sum_{j=0}^{N-1} w_j \sum_{i=0}^{M-1} h_i^s \, x_{k-i-j} \quad [9.16]$$

We can now define the filtered reference (from which the name of the algorithm is derived):

$$r_k = \sum_{i=0}^{M-1} h_i^s x_{k-i} \quad [9.17]$$

The problem is to adapt as well as possible the filter coefficients. We will use the cost function defined by:

$$J = \sum_k e_k^2 \quad [9.18]$$

where J, the function cost, is the square-law function of the coefficients.

More often, and under the filtered reference signal R, the function *J* presents a unique overall minimum. A simple gradient algorithm can thus converge towards this overall minimum.

Such an adaptive algorithm is written:

$$w_{i(k+1)} = w_{i(k)} - \mu \frac{\partial J}{\partial w_{i(k)}} \quad [9.19]$$

where:

– μ is the convergence coefficient,

– $w_{i(k)}$ is the FIR filter coefficient at a sampling time k.

We obtain:

$$w_{i(k+1)} = w_{i(k)} - 2\mu e_k \frac{\partial e_k}{\partial w_{i(k)}} \quad [9.20]$$

Based on equation [9.16], the error derivative e_k , with respect to the coefficient $w_{i(k)}$, is written:

$$\frac{\partial e_k}{\partial w_{i(k)}} = r_k$$

if:

$$w_{i(k+1)} = w_{i(k)} - 2\mu e_k \sum_{j=0}^{M-1} h_j^s x_{k-i-j} \qquad [9.21]$$

The calculation of a given coefficient of the FIR filter simply requires the product of the value of the filtered reference signal, associated with this coefficient, and of a signal proportional to the error. This product is then added up to the current value of the coefficient, to form the new coefficient. This process is repeated continuously until a stable coefficient value is obtained, corresponding to a minimum error. By suitable choosing the convergence coefficient μ, we will optimize the number of iterations necessary for algorithm convergence for the set of filter coefficients.

The convergence coefficient is often normalized by the reference in order to always obtain a relatively low coefficient:

$$\mu = \frac{\rho}{|X|^2} \qquad [9.22]$$

where ρ is a positive constant.

An experimental bench (see Figures 9.5 and 9.6) was used to validate this concept.

Figure 9.9 illustrates the vibratory performance with a 28 Hz bench excitation. The simulation was performed using the modal basis of a finite element code for the structure.

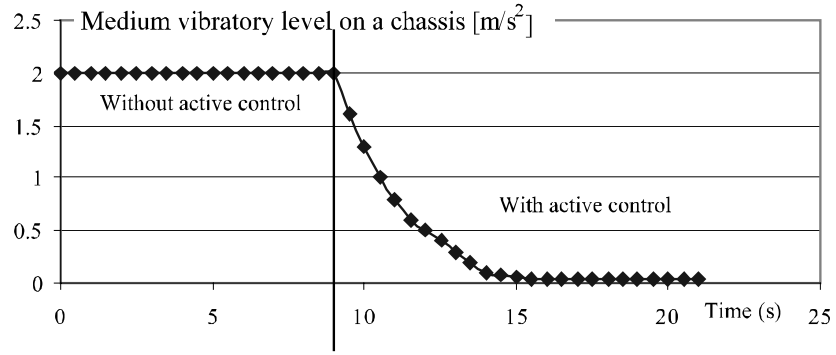

Figure 9.9. *Measurements of the vibratory level on the chassis with a 28 Hz excitation of structure A*

The analytical formulation of the algorithm presented earlier can be applied to determine the dynamic loads and the displacements of the actuator required for the control (see Figures 9.10 and 9.12). This method can be used for the complete specification of the required actuator.

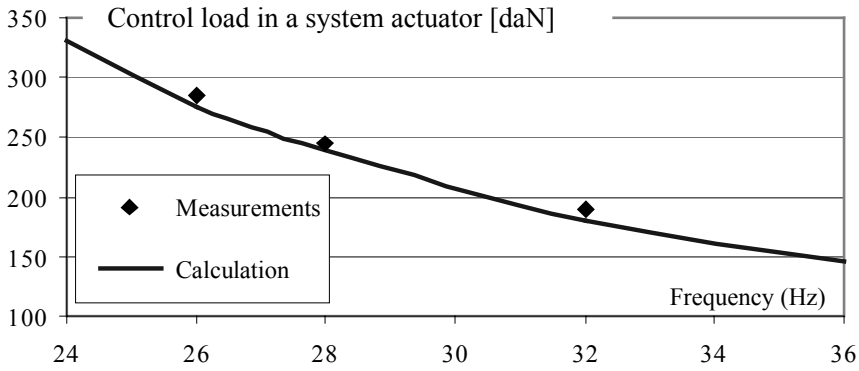

Figure 9.10. *Measurements of control loads based on the excitation frequency of structure A*

One of the first industrial applications of active systems was the anti-vibration system (Active Control of Structural Response) used on an EH101 helicopter of Augusta-Westland [STA 89, STA 90]. The dynamic loads are introduced in the structure by using four hydraulic actuators in the rods that connect the transmission unit to the fuselage of the helicopter.

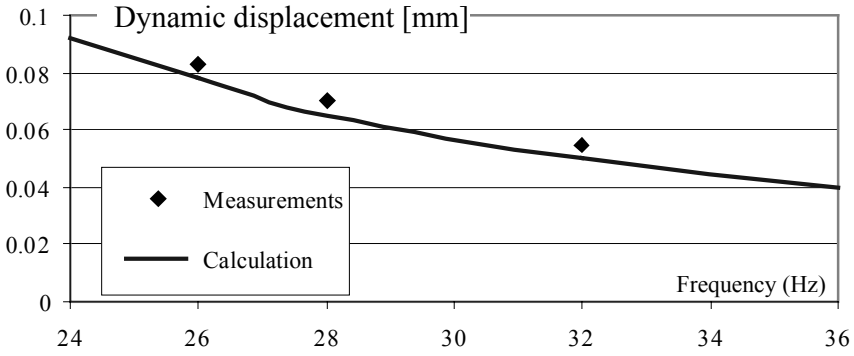

Figure 9.11. *Measurements of control displacements based on the excitation frequency of structure A*

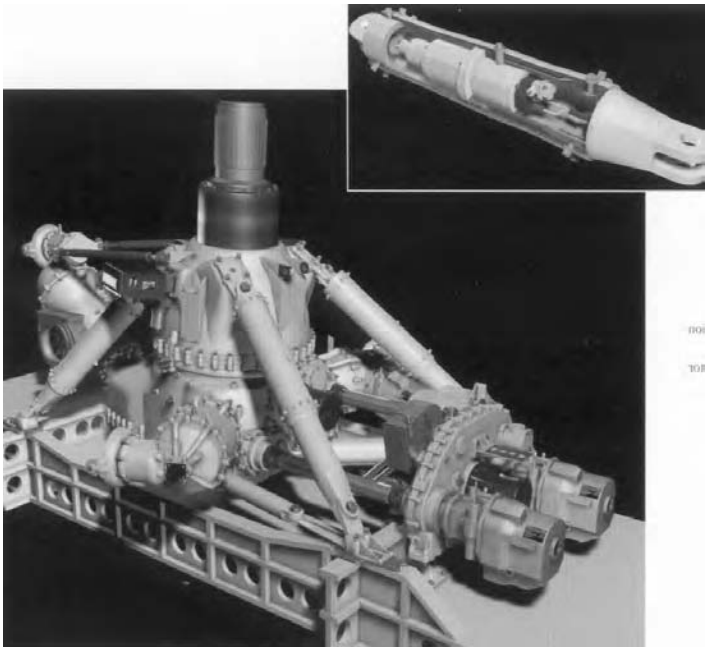

Figure 9.12. *Active anti-vibration system installed on an EH101 helicopter. Photo: Augusta-Westland*

Figure 9.12 shows the ACSR system on an EH101.

Chapter 10

Absorbers

10.1. Introduction

In the previous chapters, we have seen that it is possible to decrease the vibratory level by suitably designing the link between two structures. In the case of certain applications, it is better to act directly at the level of the structure.

In order to do this, among the passive solutions, there are two approaches:

– the optimization of the structure,

– the incorporation of a mechanism (dynamic absorber), whose role is to locally generate the variable loads that will prevent the disturbing vibrations.

10.2. Optimization of the structure

It is important to keep in mind that the structure can be modified to reduce the vibratory level at certain points of the structure. To achieve this, it is advisable to act on the mass distribution or its stiffness by modifying its geometry. The objective can be to modify the value of its natural angular frequencies or its mode shapes.

This can be the case of a machine tool where we often try to rigidify the chassis of the machine, so that the low frequency vibrations do not influence its performance. We can also optimize the structure so that the vibration nodes will be situated in strategic places (link joints, active part of the machine tool, etc.) at disturbing frequencies,

10.3. Dynamic absorbers

Certain structures are excited at a specific frequency, i.e. structures subject to unbalances, which are excited at a rotation frequency (see Chapter 1) or complex rotor structures, such as helicopters, subjected to multiple frequency excitations, depending on rotation frequency and number of blades (see Chapter 3). For this type of excitation, it is better to use a dynamic absorber which can reduce the vibrations. The system will be efficient for a given frequency.

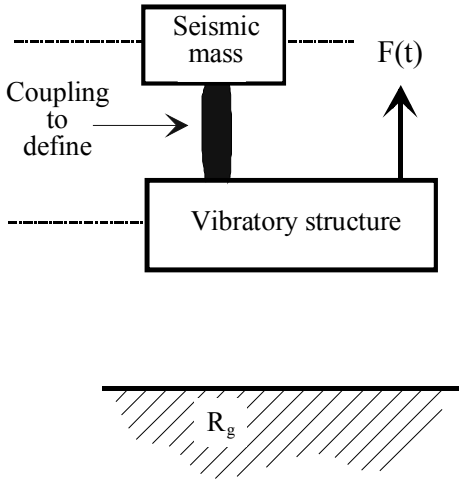

Figure 10.1. *The principle of dynamic absorbers*

The principle of dynamic absorbers is to add a mass to the system. The movement of the mass must be correlated to the movement of the structure in order to neutralize, by its inertial effects, the excitation.

Figure 10.2. *Record player arm with dynamic absorber. Illustration: C. Guarnieri*

There are several types of coupling: stiffness, damping and kinematics. This type of resonator can deal with translational or rotational motion. For a high-quality record player, it is possible to use an absorber in order to eliminate the effects of the first bending mode of the arm, which is excited by the record (see Figure 10.2). This frequency, which is close to 20 Hz, is at the limit of the audibility range.

10.3.1. *Coupling with preponderant stiffness*

10.3.1.1. *Translation system*

10.3.1.1.1. Principle

For this type of application, the vibration to be reduced is mono-directional (equivalent to translation). This is often the case for vertical "pumping" motions and it affects structures such as road vehicles, aircraft, engines and machines. In these systems, a supplementary mass is added to the system. The mass is coupled with a flexible link whose stiffness effects are predominant in comparison to the damping effects. Hence, damping is ignored.

We have adopted the modeling shown in Figure 10.3, where:

– m is mass of the structure,

– m_a is the mass of the additional element, very small in comparison to mass m,

– k_a is the stiffness of the link structure/additional element,

– k is the stiffness of the elastic suspension of the structure.

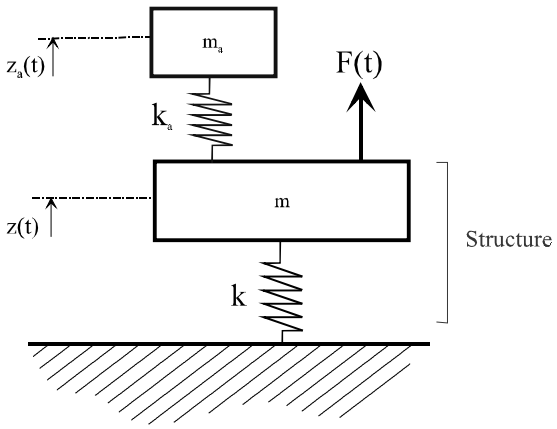

Figure 10.3. *Modeling of the dynamic absorber*

10.3.1.1.2. Formulation of the equations

The differential system obtained by applying the fundamental principle of dynamics to the motion of two masses with respect to their positions of static equilibrium is written:

$$\begin{cases} m\ z + (k + k_a)\ z\text{-}k_a z_a = F(t) \\ m_a\ z_a + k_a (z_a - z) = 0 \end{cases} \quad [10.1]$$

The system is written as a matrix:

$$\begin{bmatrix} m & 0 \\ 0 & m_a \end{bmatrix} \begin{bmatrix} \ddot{z} \\ \ddot{z}_a \end{bmatrix} + \begin{bmatrix} k + k_a & -k_a \\ -k_a & k_a \end{bmatrix} \begin{bmatrix} z \\ z_a \end{bmatrix} = \begin{bmatrix} F(t) \\ 0 \end{bmatrix} \quad [10.2]$$

In a steady state, for a harmonic excitation of ω frequency and F_0 amplitude, the harmonic response of the structure is given by:

$$\begin{cases} z(t) = Z_0 \cos(\omega t + \varphi) \\ z_a(t) = Z_{a0} \cos(\omega t + \varphi_a) \end{cases} \quad [10.3]$$

with the vibration modulus determined by the relations:

$$Z_0 = \left| \frac{\left(k_a - m_a \omega^2\right)}{\left[\left(k_a - m_a \omega^2\right)\ \left(k + k_a - m\omega^2\right) - k_a^2\right]} \right| F_0 \quad [10.4]$$

and:

$$Z_{a0} = \left| \frac{k_a}{\left[\left(k_a - m_a \omega^2\right)\ \left(k\text{-}k_a - m\ \omega^2\right) - k_a^2\right]} \right| F_0 \quad [10.5]$$

Note that there is a specific case of excitation angular frequency, ω_{ar}, called anti-resonance, when the motion Z_0 of the structure is zero. This angular frequency is defined by:

$$\omega_{ar} = \sqrt{\frac{k_a}{m_a}} \qquad [10.6]$$

In the case of anti-resonance, we then have:

$$\begin{cases} Z_0(\omega_{ar}) = 0 \\ Z_{a0}(\omega_{ar}) = \dfrac{F_0}{k_a} \end{cases} \qquad [10.7]$$

The frequency response curve (see Figure 10.4) shows that the additional mass not only generated an anti-resonance for the structure, but also generated two other possible resonances.

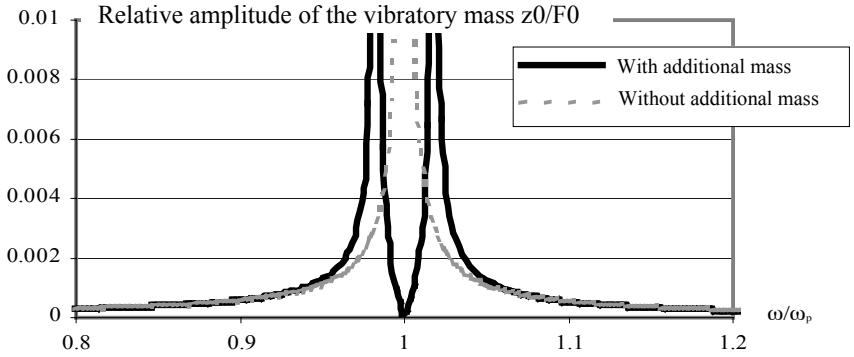

Figure 10.4. *Harmonic response of the motion of the structure without damping*

For an excitation angular frequency ω_e, corresponding to a natural angular frequency of the structure alone, the design criterion for the resonator is as follows:

$$\omega_{ar} = \omega_e \qquad [10.8]$$

The dynamic absorber is used when the structure alone is excited at its natural angular frequency, i.e. if:

$$\omega_e = \omega_p = \sqrt{\frac{k}{m}} \qquad [10.9]$$

Thus, the criterion for designing the resonator (choice of mass and stiffness) is:

$$\sqrt{\frac{k_a}{m_a}} = \omega_e = \sqrt{\frac{k}{m}} \qquad [10.10]$$

Figure 10.4 shows that small variations of the excitation angular frequency around the anti-resonance point considerably amplify the movement of mass m, due to the proximity of two resonance angular frequencies of the system, ω_1 and ω_2.

The resonance angular frequencies ω_1 and ω_2 are obtained by solving the equation:

$$\left(k_a - m_a\ \omega^2\right)\left(\left(k + k_a\right) - m\ \omega^2\right) - k_a^2 = 0 \qquad [10.11]$$

which reduces to:

$$\omega^4 - \frac{k_a}{m_a}\left(1 + \frac{m_a}{m}\left(1 + \frac{k}{k_a}\right)\right)\omega^2 + \frac{k_a}{m_a}\frac{k}{m} = 0 \qquad [10.12]$$

When:

$$\begin{cases} \omega_p^2 = \dfrac{k_a}{m_a} = \dfrac{k}{m} \\ \mu = \dfrac{m_a}{m} \end{cases} \qquad [10.13]$$

equation [10.12] becomes:

$$\omega^4 - 2\omega_p^2\left(1 + \frac{\mu}{2}\right)\omega^2 + \omega_p^4 = 0 \qquad [10.14]$$

The solutions of equation [10.14] are given by:

$$\omega^2 = \frac{1}{2}\omega_p^2\left(\left(1+\frac{\mu}{2}\right) \pm 2\sqrt{\left(1+\frac{\mu}{2}\right)^2 - 1}\right) \qquad [10.15]$$

It is seen that the higher the mass ratio μ, the longer the distance between the two resonance frequencies (see Figure 10.5). Therefore, we need to find a vibration absorber whose resonances are as far apart as possible, and we have to keep in mind that the farther apart they are, the higher the mass m_a becomes (for fixed m). Therefore, a compromise must be found to produce a minimal mass m_a.

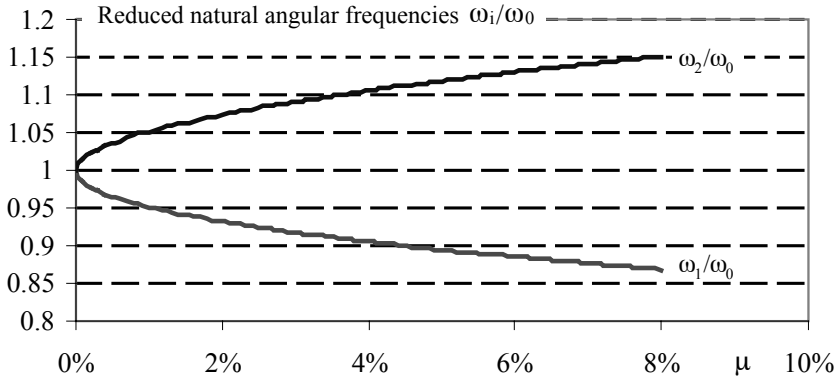

Figure 10.5. *Variation of resonance angular frequency versus mass ratio*

10.3.1.1.3. Example of a turbine blade

A turbine blade is excited by the fluid surrounding it, which can generate excitation at one of its natural frequencies. This is often the case for its first bending frequency. One solution is to insert a dynamic absorber with a vibratory mass to prevent resonance at this frequency.

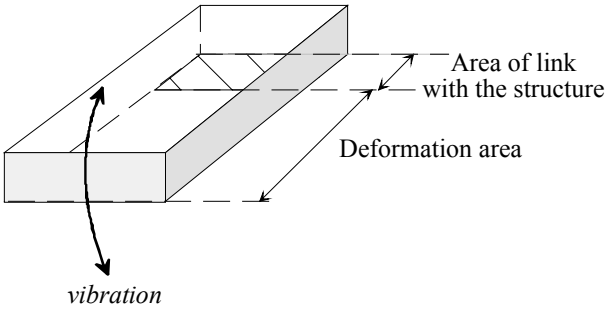

Figure 10.6. *Dynamic absorber of a turbine blade*

Figure 10.7. *Implementation of a dynamic absorber on a turbine blade. Illustration: C. Guarnieri*

10.3.1.1.4. Example of a helicopter cabin resonator

On a helicopter, the pilot and copilot can sense vibrations at the frequency bΩ, which can be disturbing. In order to decrease the vibratory level, a resonator was introduced in the structure (see Figure 10.8).

Figure 10.8. *Positioning of a passive cabin resonator on a helicopter. Photo: Eurocopter*

The stiffness of the resonator is obtained with a bending blade. To analyze the method for setting the system, we have used the model in Figure 10.9.

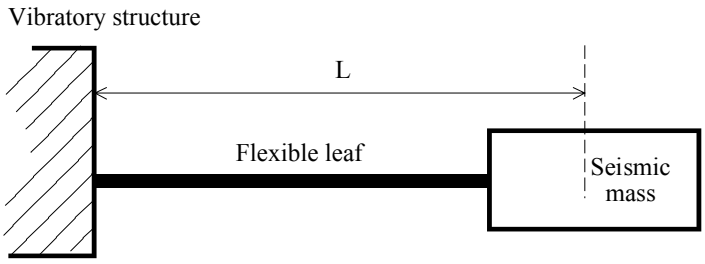

Figure 10.9. *Principle of a blade resonator*

The system is designed so that the flexible leaf and mass vibrate in the system's first bending mode although, to define the blade geometry, the stiffness is determined via its static deformation.

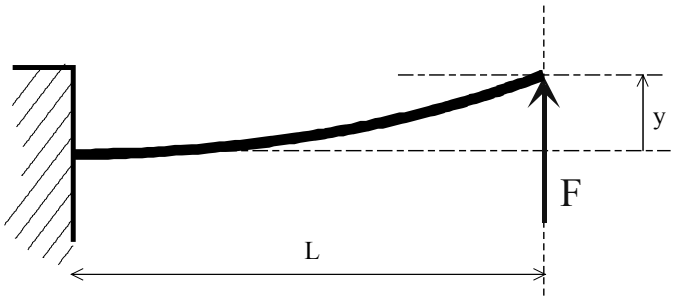

Figure 10.10. *Static deformation of the blade resonator*

The theory of beams shows that the deformation y is given by:

$$y = \frac{F\,L^3}{3\,EI} \qquad [10.16]$$

where:

– E is the Young's modulus of the beam material,

– I is the inertial moment of the beam section,

– L is the slenderness ratio of the beam.

The stiffness of the system is then defined by:

$$k_a = \frac{3\,EI}{L^3} \qquad [10.17]$$

Knowing the excitation angular frequency, the value of the mass and the features of the blade can be defined. The criterion for designing the resonator for an excitation angular frequency ω_e is such that:

$$\frac{k_a}{m_a} = \frac{3\,EI}{L^3\,m_a} = \omega_e^2 \qquad [10.18]$$

Equation [10.18] is used to design the resonator. Once manufactured, the system needs to be "tuned". It is possible to work on the value of the mass or on the stiffness using the intermediary of the mass position.

We propose exciting the structure at the disturbing frequency and measuring the motion of the mass. The system will be tuned via the flapping mass at resonance (see Figure 10.11).

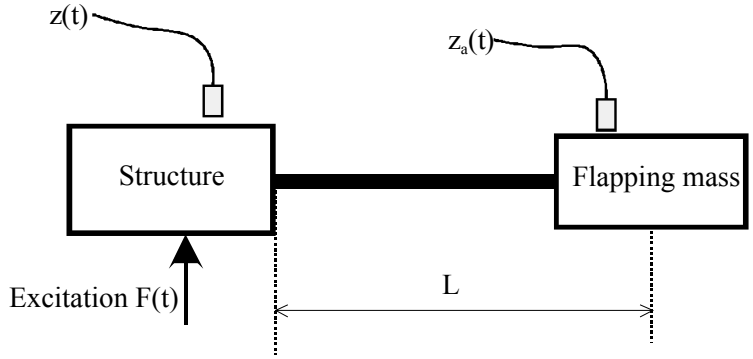

Figure 10.11. *Measuring procedure for the fine adjustment of the position of the flapping mass*

In order to see experimentally if there is excitation at anti-resonance, the following criterion is used. With the help of the equations of the motions of masses [10.2] and considering damping, we have:

$$\begin{bmatrix} m & 0 \\ 0 & m_a \end{bmatrix} \begin{bmatrix} \ddot{z} \\ \ddot{z}_a \end{bmatrix} + \begin{bmatrix} c+c_a & -c_a \\ -c_a & c_a \end{bmatrix} \begin{bmatrix} \dot{z} \\ \dot{z}_a \end{bmatrix} + \begin{bmatrix} k+k_a & -k_a \\ -k_a & k_a \end{bmatrix} \begin{bmatrix} z \\ z_a \end{bmatrix} = \begin{bmatrix} F(t) \\ 0 \end{bmatrix} \qquad [10.19]$$

For a harmonic excitation and using the complex amplitude, we show that:

$$\begin{bmatrix} (k+k_a) - m\,\omega^2 + i(c+c_a)\,\omega & -(k_a + ic_a\,\omega) \\ (-k_a + ic_a\,\omega) & k_a - m_a\,\omega^2 + ic_a\,\omega \end{bmatrix} \begin{bmatrix} \overline{z}_0 \\ \overline{z}_{a0} \end{bmatrix} = \begin{bmatrix} \overline{F}_0 \\ 0 \end{bmatrix} \qquad [10.20]$$

Hence, we can show that the ratio of complex amplitudes of motion is written:

$$\frac{\overline{z}_{a0}}{\overline{z}_0} = \frac{k_a + ic_a\,\omega}{k_a - m_a\,\omega^2 + ic_a\,\omega} \qquad [10.21]$$

Since the damping ratio linked to the natural damping is low, we note that at anti-resonance there is a phase difference close to $\pi/2$ between the two movements:

$$\left(\frac{\overline{z}_{a0}}{\overline{z}_0}\right)_{\omega=\omega_{ar}} \approx -i\frac{k_a}{c_a\ \omega_{ar}} \approx -i\frac{1}{2\ \lambda_a} \qquad [10.22]$$

Thus, it is sufficient to excite the structure at the disturbing frequency and position the flapping mass in such a way that the displacement measurements of the two masses are in phase quadrature.

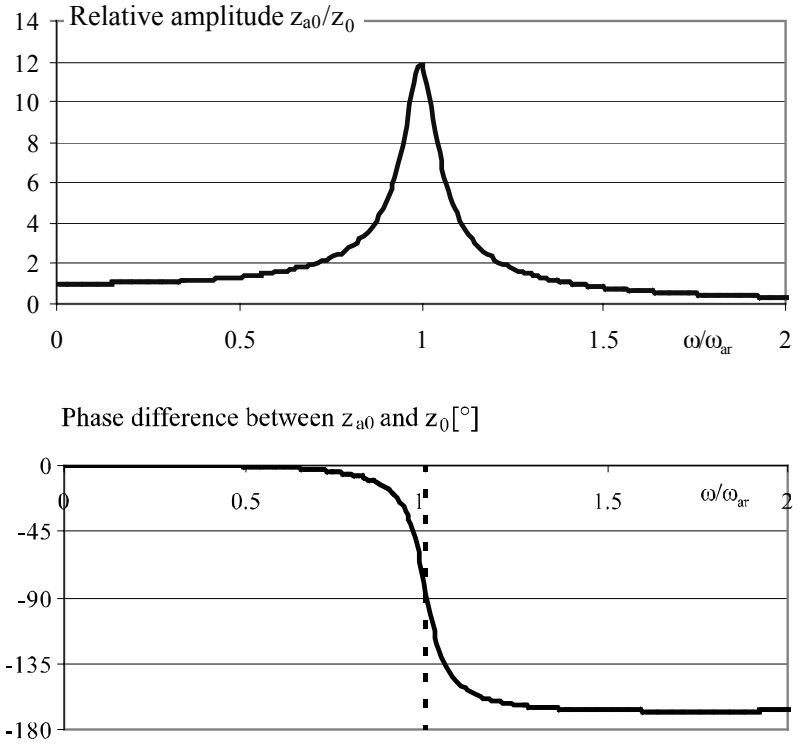

Figure 10.12. *Harmonic response of the structure's motions*

10.3.1.2. *Rotating system: torsion resonator*

The resonator can also be used for torsion vibrations. Frequently used in industry, it is used to reduce the vibratory level of a drive train system excited in torsion by an engine or a receiver.

We will take as an example the kinematic drive train described in Chapter 2. We saw then that, in order to prevent the excitation angular frequency of the engine coinciding with the torsion natural angular frequencies, it was possible to modify the inertia of a pulley.

It would have been possible to integrate a torsion dynamic absorber into the kinematic drive train. The absorber is integrated in the place where we want to modify the amplitude of torsion vibrations (see Figure 10.13).

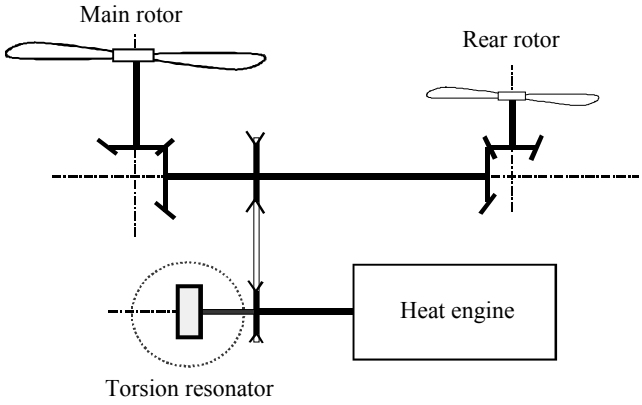

Figure 10.13. *Location of the torsion resonator in a drive train system*

Figure 10.14 shows the technology used for this type of resonator: a flywheel that will play the role of the flapping mass. The stiffness of the link between the additional element and the structure (drive shaft) depends on the geometry of the shaft.

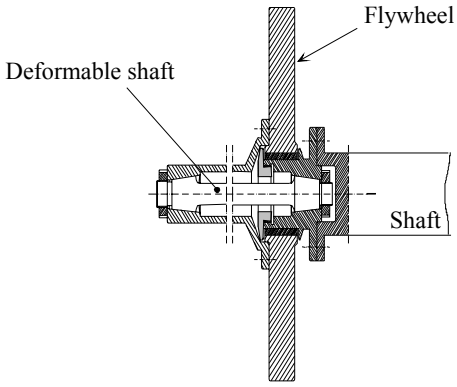

Figure 10.14. *Technology of a torsion resonator*

For an excitation ω_e, the tuning criterion is:

$$\sqrt{\frac{k_\theta}{I}} = \omega_e \qquad [10.23]$$

where:

– k_θ is the torsion stiffness of the link shaft,

– I is the inertia of the flywheel.

Figure 10.15 shows the influence that the resonator could have on the third torsion mode. This influence can be analyzed using the modulation ratio of the torque which represents the ratio of amplitudes of the dynamic and static torque.

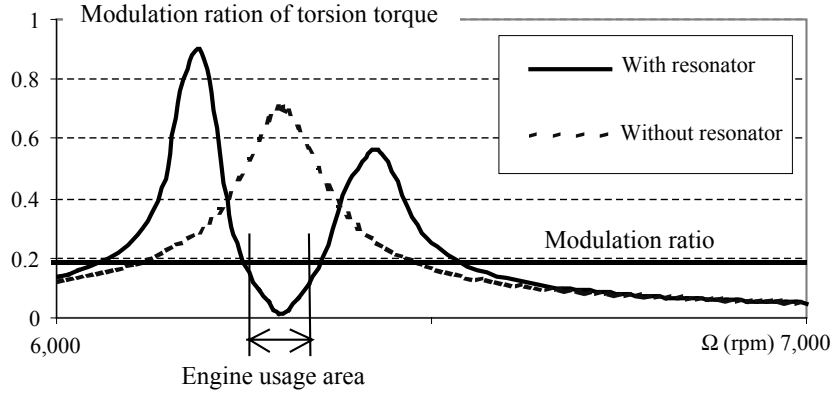

Figure 10.15. *Influence of the resonator on the torsion torque*

10.3.2. *Coupling using damping and stiffness*

We dealt with the characteristics of a resonator whose stiffness effect was predominant compared to the damping effect. We will now analyze the case where the damping effects are more important.

10.3.2.1. *Operation of the equations*

Modeling takes into account the damping of the structure link with the dynamic absorber, but also the damping of the structure mode. The system is thus modeled by a mass spring damping system outlined in Figure 10.16.

The differential system describing the motion of the two masses is:

$$\begin{cases} m\,\ddot{z} + (c + c_a)\,\dot{z} - c_a\,\dot{z}_a + (k + k_a)\,z - k_a\,z_a = F(t) \\ m_a\,\ddot{z}_a + c_a\,\dot{z}_a - c_a\,\dot{z} + k_a\,z_a - k_a\,z = 0 \end{cases} \qquad [10.24]$$

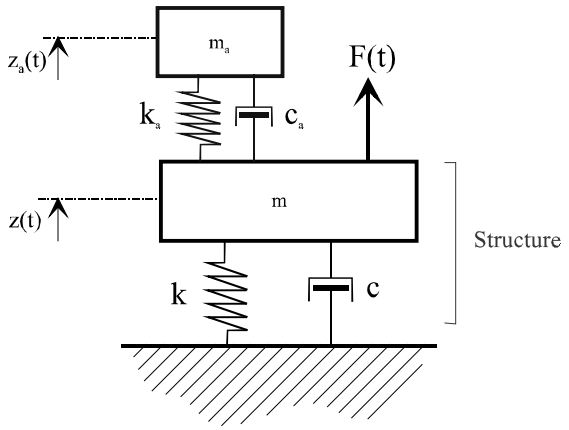

Figure 10.16. *Modeling of a dynamic absorber with damping*

The system can be written as a matrix:

$$\begin{bmatrix} m & 0 \\ 0 & m_a \end{bmatrix} \begin{bmatrix} \ddot{z} \\ \ddot{z}_a \end{bmatrix} + \begin{bmatrix} c + c_a & -c_a \\ -c_a & c_a \end{bmatrix} \begin{bmatrix} \dot{z} \\ \dot{z}_a \end{bmatrix} + \begin{bmatrix} k + k_a & -k_a \\ -k_a & k_a \end{bmatrix} \begin{bmatrix} z \\ z_a \end{bmatrix} = \begin{bmatrix} F(t) \\ 0 \end{bmatrix} \qquad [10.25]$$

Assuming the excitation is given by:

$$F(t) = F_0 \cos(\omega t) \qquad [10.26]$$

and:

$$\begin{cases} \omega_p^2 = \dfrac{k}{m} \\ \lambda = \dfrac{c}{2m\,\omega_p} \end{cases} \qquad \begin{cases} \omega_a^2 = \dfrac{k_a}{m_a} \\ \lambda_a = \dfrac{c_a}{2m_a\omega_a} \end{cases} \qquad \begin{cases} \mu = \dfrac{m_a}{m} \\ \alpha = \dfrac{\omega_p}{\omega_a} \\ \beta = \dfrac{\lambda}{\lambda_a} \end{cases} \qquad [10.27]$$

The system of equations [10.25] can be written:

$$M\ddot{Z} + C\dot{Z} + K\,Z = F \qquad [10.28]$$

where:

$$M = \begin{bmatrix} 1 & 0 \\ 0 & 1 \end{bmatrix} \qquad C = 2\lambda_a\omega_a \begin{bmatrix} \alpha\beta+\mu & -\mu \\ -1 & 1 \end{bmatrix}$$
$$K = \omega_a^2 \begin{bmatrix} \alpha^2+\mu & -\mu \\ -1 & 1 \end{bmatrix} \qquad F = \begin{bmatrix} \mu\dfrac{F(t)}{m_a} \\ 0 \end{bmatrix} \qquad [10.29]$$
$$Z = \begin{bmatrix} z \\ z_a \end{bmatrix}$$

We will analyze the frequency response of the structure to different stiffness and damping configurations.

We show that with harmonic excitation:

$$\begin{bmatrix} \left(\alpha^2+\mu-\bar{\omega}^2\right)+2i\,\lambda_a\bar{\omega}(\alpha\beta+\mu) & -\mu\left(1+2i\,\lambda_a\bar{\omega}\right) \\ -\left(1+2i\,\lambda_a\bar{\omega}\right) & \left(1-\bar{\omega}^2+2i\,\lambda_a\bar{\omega}\right) \end{bmatrix} \begin{bmatrix} \bar{z} \\ \bar{z}_a \end{bmatrix} = \begin{bmatrix} \dfrac{\mu}{k_a}\bar{F}_0 \\ 0 \end{bmatrix} \qquad [10.30]$$

where $\bar{\omega} = \omega/\omega_a$

Thus:

$$\bar{z} = \frac{\bar{F}_0}{k_a} \frac{\mu\left(1-\bar{\omega}^2+2i\lambda_a\,\bar{\omega}\right)}{\left[\left(1-\bar{\omega}^2+2i\lambda_a\,\bar{\omega}\right)\left(\alpha^2+\mu-\bar{\omega}^2+2i\lambda_a\,\bar{\omega}(\alpha\beta+\mu)\right)-\mu\left(1+2i\lambda_a\,\bar{\omega}\right)^2\right]} \qquad [10.31]$$

The ratio of the vibration and of the static displacement modulus is given by:

$$\left|\frac{\bar{z}}{\bar{F}_0/k_a}\right| = \frac{\mu\sqrt{\left(1-\bar{\omega}^2\right)^2+\left(2\lambda_a\bar{\omega}\right)^2}}{\sqrt{A^2+B^2}} \qquad [10.32]$$

where

$$A = \left(\left(1-\bar{\omega}^2\right)\left(\alpha^2-\bar{\omega}^2\right)-\mu\,\bar{\omega}^2-4\alpha\lambda\lambda_a\bar{\omega}^2\right)$$
$$B = \left(2\lambda_a\bar{\omega}\left[\alpha^2-(1+\mu)\bar{\omega}^2\right]+2\lambda\alpha\bar{\omega}\left(1-\bar{\omega}^2\right)\right)$$

We will analyze the influence of damping with the application of the resonator tuning technique developed in the previous chapter. Thus, we assume that:

$$\sqrt{\frac{k}{m}} = \sqrt{\frac{k_a}{m_a}} \qquad \text{where } \alpha = 1 \qquad [10.33]$$

Figure 10.17 shows that in the case of low damping values, it is possible to reduce the displacement of the structure, but there will be resonances.

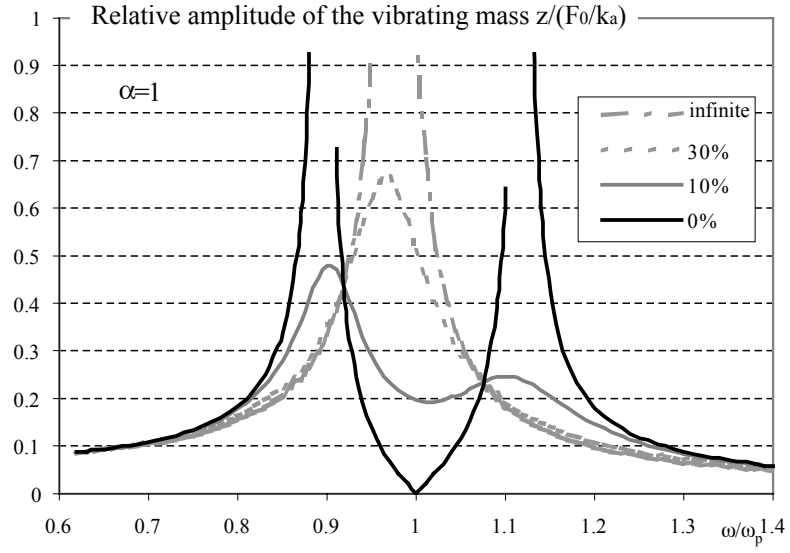

Figure 10.17. *Influence of damping on the relative amplitude of vibrations $\alpha = 1$*

It is seen that, if the damping is too high, resonances reappear. For an absorber with a high damping, we will not have an optimal tuning if we preserve the tuning assumption $\alpha = 1$.

10.3.2.2. *Tuning method*

The art of efficient tuning is to find an effective tradeoff between the attenuation at anti-resonance and the resonance peaks that appear. The objective in this case will be to obtain a sufficient attenuation over a wide range of frequencies.

The choice of characteristics, mass and stiffness, is performed in such a way that the admissible stresses in the link between the additional element and the structure are respected.

The tuning method consists of:

– choosing a ratio μ with the help of mass m_a,

– choosing a ratio α with the help of stiffness k_a,

– choosing damping in order to reach a compromise between resonance and anti-resonance.

We notice that all curves pass through two points, marked A and B, irrespective of the damping value. By ignoring the damping of the structure $(\lambda = 0)$ and considering two damping values, for instance $\lambda_a = 0$ and $\lambda_a = \infty$, we can calculate the abscissas of these points.

$$\left(\frac{\overline{z}}{\overline{F}_0 / k_a}\right)_{\lambda_a = 0} = \frac{\mu\left(1-\overline{\omega}^2\right)}{\left(1-\overline{\omega}^2\right)\left(\alpha^2-\overline{\omega}^2\right)-\mu\overline{\omega}^2} \qquad [10.34]$$

$$\left(\frac{\overline{z}}{\overline{F}_0 / k_a}\right)_{\lambda_a = \infty} = \frac{\mu}{\left[\alpha^2-(1+\mu)\overline{\omega}^2\right]} \qquad [10.35]$$

The abscissas of points A and B are defined by the identity of [10.34] and [10.35]:

$$\left|\frac{\left(1-\overline{\omega}^2\right)}{\left(1-\overline{\omega}^2\right)\left(\alpha^2-\overline{\omega}^2\right)-\mu\overline{\omega}^2}\right| = \left|\frac{1}{\alpha^2-(1+\mu)\overline{\omega}^2}\right| \qquad [10.36]$$

If we exclude the equation that gives the zero result $(\bar{\omega} = 0)$, then:

$$\bar{\omega}^4 - 2\frac{\left(1+\alpha^2+\mu\right)}{\left(2+\mu\right)}\bar{\omega}^2 + \frac{2\alpha^2}{\left(2+\mu\right)} = 0 \qquad [10.37]$$

The results of equation [10.37] are noted $\bar{\omega}_A$ and $\bar{\omega}_B$. The vibration amplitude for this excitation is given by:

$$\left(\frac{\bar{z}}{\bar{F}_0 / k_a}\left(\omega_A\right)\right)_{\lambda_a=\infty} = \frac{\mu}{\left[\alpha^2 - \left(1+\mu\right)\bar{\omega}_A^2\right]} \qquad [10.38]$$

$$\left(\frac{\bar{z}}{\bar{F}_0 / k_a}\left(\omega_B\right)\right)_{\lambda_a=\infty} = \frac{\mu}{\left[\alpha^2 - (1+\mu)\bar{\omega}_B^2\right]} \qquad [10.39]$$

In order to have equal amplitude for these points:

$$\left|\alpha^2 - \left(1+\mu\right)\bar{\omega}_B{}^2\right| = \left|\alpha^2 - \left(1+\mu\right)\bar{\omega}_A{}^2\right| \qquad [10.40]$$

which, excluding the zero result, yields:

$$-\alpha^2 + \left(1+\mu\right)\bar{\omega}_B{}^2 = \alpha^2 - \left(1+\mu\right)\bar{\omega}_A{}^2 \qquad [10.41]$$

An equation that gives the tuning criterion:

$$\bar{\omega}_B{}^2 + \bar{\omega}_A{}^2 = \frac{2\alpha^2}{1+\mu} \qquad [10.42]$$

Equation [10.37] leads to:

$$\bar{\omega}_B{}^2 + \bar{\omega}_A{}^2 = \frac{2\alpha^2}{\left(1+\mu\right)} = 2\frac{\left(1+\alpha^2+\mu\right)}{\left(2+\mu\right)} \qquad [10.43]$$

By solving equation [10.43], it is possible to establish the ratio criterion α in order to make the amplitudes equal:

$$\alpha = (1+\mu) \qquad [10.44]$$

It is possible to find the solution for minimizing the resonance amplitudes via the damping scanning while still minimizing the vibrations at anti-resonance (see Figure 10.18).

10.3.2.3. *Industrial application: resonator used on a helicopter for the tail boom vibrations*

A resonator can be used to decrease the "broadband" vibrations in the tail of the helicopter (see Figure 10.19).

The excitation frequency is a function of the trim of the helicopter. Irrespective of the helicopter's position, it is important for the efficiency of the resonator to be the same, and no resonance should appear. That is why we chose a high damping resonator. The measurement of the vibrations presented in Figure 10.20 demonstrates the efficiency of such a system.

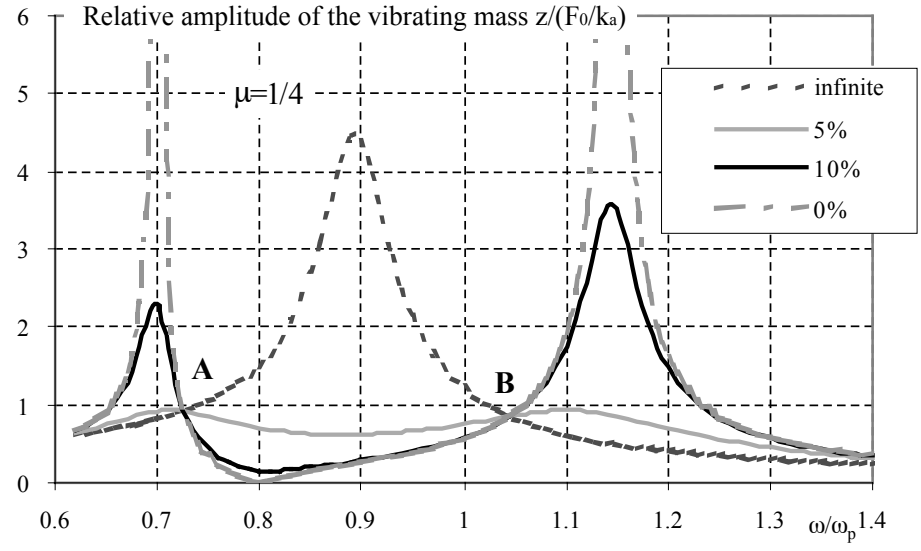

Figure 10.18. *Transfer function of the system versus damping* λ_a

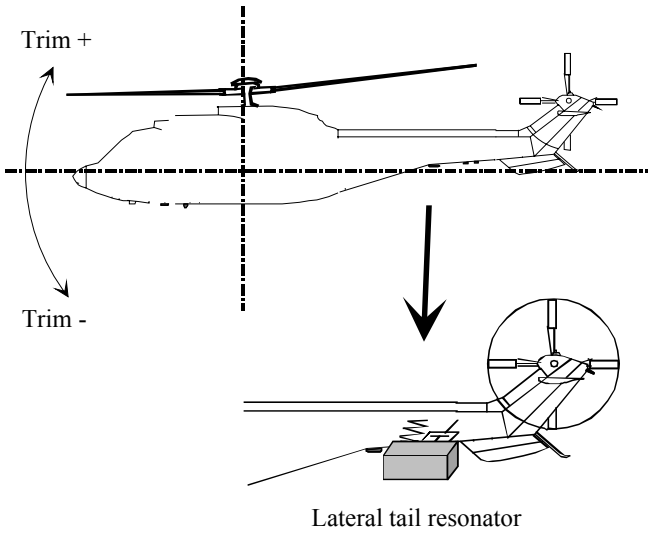

Figure 10.19. *Diagram of the implementation of a resonator on a helicopter*

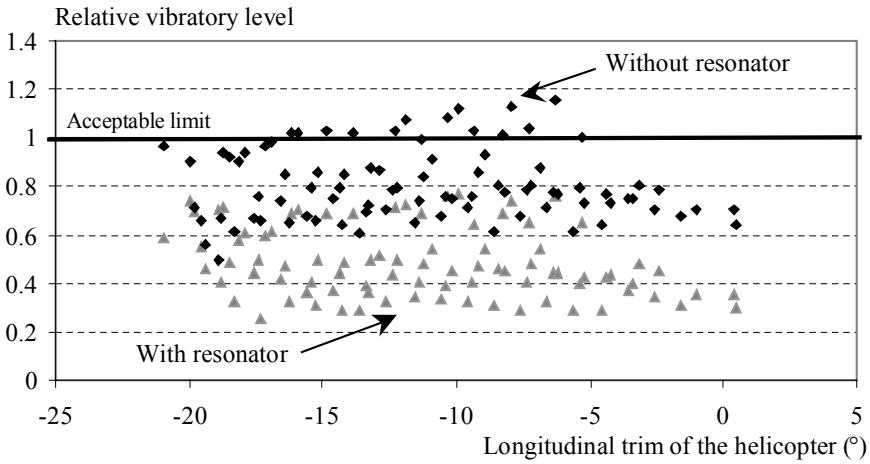

Figure 10.20. *Measurements of the cabin vibratory level versus the trim of the helicopter*

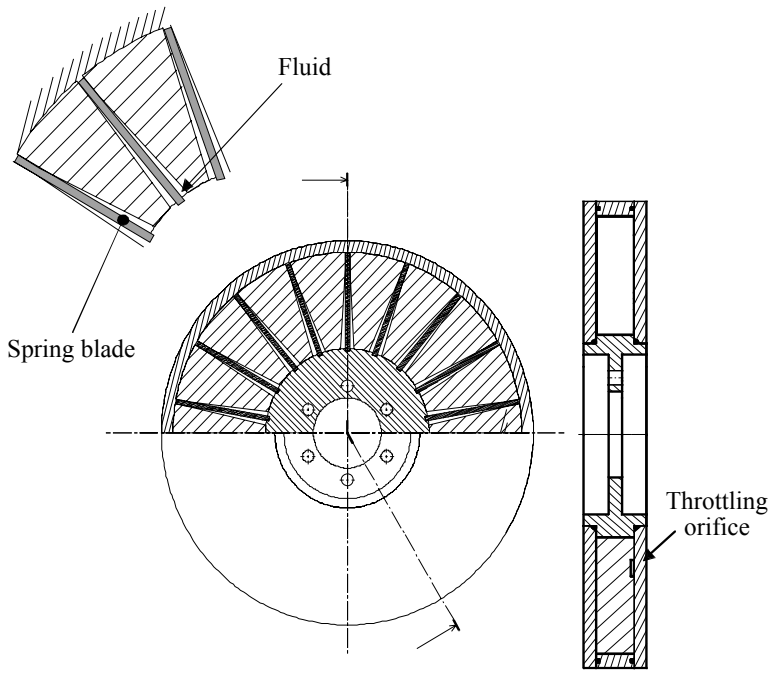

Figure 10.21. *Diagram of a torsion resonator with high damping*

10.3.2.4. *Industrial application: resonator for torsion movements*

In the case of rotating systems, it may be necessary to decrease the torsion vibrations in the drive train system, which is the case for vibrations induced by combustion engines. The torsion resonators combine stiffness and damping so that they can be used over a wide range of frequencies, whilst considerably decreasing the vibrations.

A diagram of such a resonator is presented in Figure 10.21. Stiffness is obtained using springs, and damping is obtained using fluid throttling and can be modified by the setting of the flaps.

10.3.3. *Coupling with preponderant damping*

For reasons of cost, it is often easier to integrate systems that do not have stiffness but only damping. The system is modeled by a mass damping system suggested in Figure 10.16.

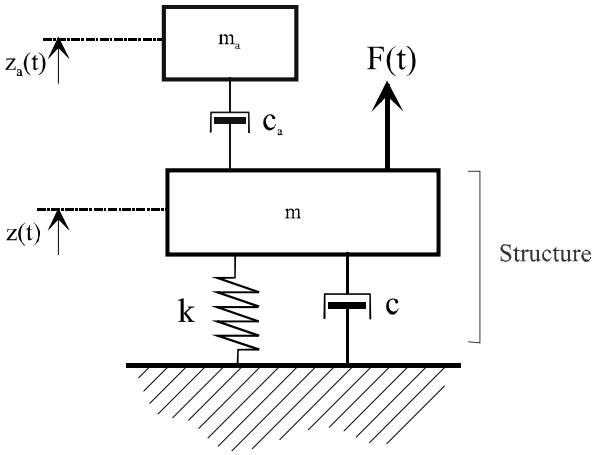

Figure 10.22. *Modeling of the dynamic absorber with damping coupling*

The differential system describing the motion of the masses is:

$$\begin{cases} m\,\ddot{z} + (c + c_a)\,\dot{z} - c_a \dot{z}_a + k\,z = F(t) \\ m_a\,\ddot{z}_a + c_a \dot{z}_a - c_a\,\dot{z} = 0 \end{cases} \qquad [10.45]$$

which in matrix form becomes:

$$\begin{bmatrix} m & 0 \\ 0 & m_a \end{bmatrix} \begin{bmatrix} \ddot{z} \\ \ddot{z}_a \end{bmatrix} + \begin{bmatrix} c + c_a & -c_a \\ -c_a & c_a \end{bmatrix} \begin{bmatrix} \dot{z} \\ \dot{z}_a \end{bmatrix} + \begin{bmatrix} k & 0 \\ 0 & 0 \end{bmatrix} \begin{bmatrix} z \\ z_a \end{bmatrix} = \begin{bmatrix} F(t) \\ 0 \end{bmatrix} \qquad [10.46]$$

We assume the excitation is of the form:

$$F(t) = F_0 \cos(\omega t) \qquad [10.47]$$

We will analyze the frequency response of the structure for different damping configurations. For harmonic excitation:

$$\begin{bmatrix} k - m\omega^2 + i(c + c_a)\omega & -ic_a\omega \\ -ic_a\omega & -m_a\omega^2 + ic_a\omega \end{bmatrix} \begin{bmatrix} z \\ z_a \end{bmatrix} = \begin{bmatrix} F_0 \\ 0 \end{bmatrix} \qquad [10.48]$$

If:

$$\left|\frac{\bar{z}}{\bar{F}_0}\right| = \frac{\sqrt{(m_a\omega)^2 + {c_a}^2}}{\sqrt{\left(m_a\left(k - m\omega^2\right) - \left(c + 2c_a\right)c_a\right)^2\omega^4 + \left(c_a\omega\left(k - m\omega^2\right) - \left(c + c_a\right)m_a\omega^3\right)^2}} \qquad [10.49]$$

Let:

$$\begin{cases} \omega_p^2 = \dfrac{k}{m} \\ \lambda = \dfrac{c}{2m\ \omega_p} \\ \lambda_a = \dfrac{c_a}{2m_a\ \omega_p} \end{cases} \qquad \begin{cases} \bar{\omega} = \dfrac{\omega}{\omega_p} \\ \mu = \dfrac{m_a}{m} \end{cases} \qquad [10.50]$$

then:

$$\left|\frac{\bar{z}}{\bar{F}_0 / k}\right| = \frac{\sqrt{\bar{\omega}^2 + 4\lambda_a^2}}{\sqrt{\left(1 - \bar{\omega}^2 + 4\lambda_a\lambda\right)^2\bar{\omega}^2 + 4\left(\lambda_a\left[1 - (1+\mu)\omega^2\right] - \lambda\bar{\omega}^2\right)^2}} \qquad [10.51]$$

The objective is to choose the damping value to yield the minimum amplitude of the ratio defined by equation [10.51]. We then show that there is an optimal damping value that minimizes the vibration amplitude.

Figure 10.24 shows a possible industrial application for this type of resonator, used for a drive train system.

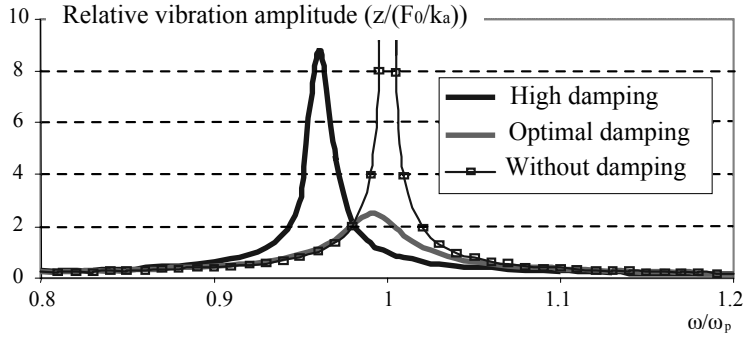

Figure 10.23. *Frequency response of a dynamic absorber with predominant damping*

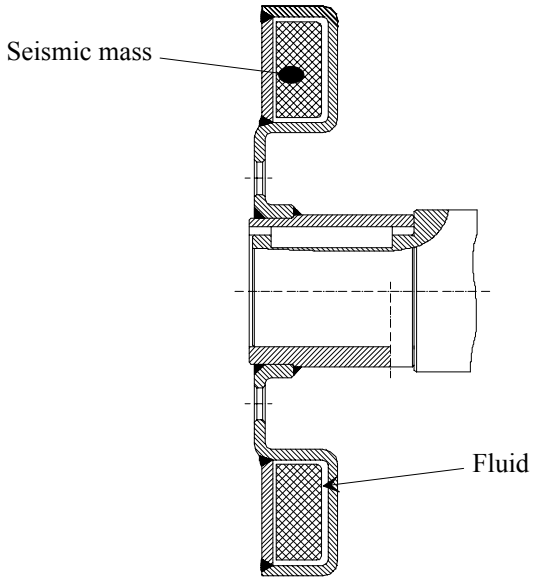

Figure 10.24. *Resonator with preponderant damping*

Damping is produced by throttling fluid between the seismic mass and the absorber's body. The aim of the tuning is to obtain the best damping. Figure 10.23 shows that if the damping is too high, the mass is blocked, the natural frequency of the assembly decreases and the absorption effect is lost.

Chapter 11

Self-Adjusting Absorbers

11.1. Introduction

In order to control certain vibration sources, we used the mechanical resonator (mass-spring system) (see Chapter 10). The system is placed where we want to reduce the vibrations. On a helicopter, for example, this will be under the pilot's cabin.

We saw that, in operation, the resonance frequency of the mass-spring system is adjusted with the excitation frequency. The mass vibrates and thus the vibratory level is decreased.

For certain structures, the excitation frequency can evolve with time. These changes take place over a long period, compared to the excitation frequency.

As a result, it was necessary to create a system whose resonance frequency would adjust automatically to the variations of the excitation frequency. This variation takes place between 1 and 3 seconds for an excitation frequency of around 20 Hz. This is the case for self-adjusting absorbers.

11.2. Implementation

The example we are going to analyze is the self-adjusting resonator used for a helicopter cabin. It works according to the principle described in the previous chapter, but can adjust its natural frequency to the variations in rotor speed. The resonator frequency will therefore always be adjusted to the excitation frequency.

The resonator used consists of a seismic mass and a flexible leaf, which acts as a spring (see Figure 11.1)

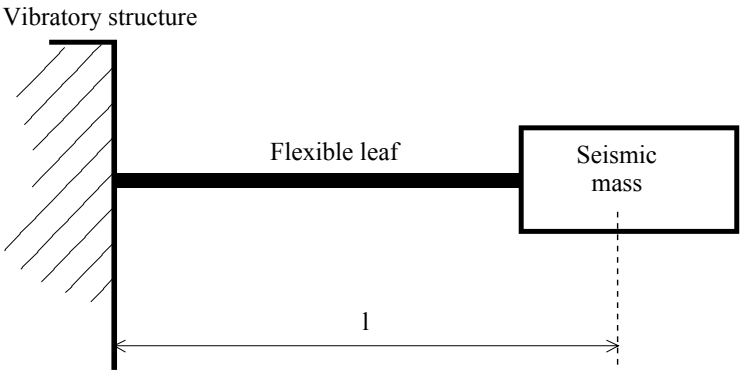

Figure 11.1. *Principle of a blade resonator*

An additional mobile mass modifies the resonance frequency of the assembly, and always maintains a 90º phase difference (resonance phase) between the accelerations measured on the structure and those measured on the flapping mass (see Figure 11.2).

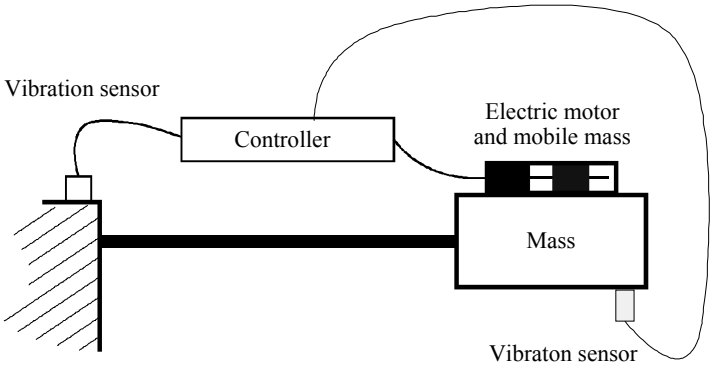

Figure 11.2. *Self-adjusting system*

For this type of system, the blade stiffness is varied by changing the center of gravity position.

11.3. System coupling

11.3.1. *Analog algorithm*

We can use an analog algorithm to control the displacement of the mass. This has the advantage of being easy to implement, which is a plus for its industrial integration. However, its efficiency is limited.

Figure 11.3 outlines the principle of the algorithm developed for this self-adjusting resonator: the vibratory behavior is analyzed and then a motion designed to minimize the vibration is applied to the mass.

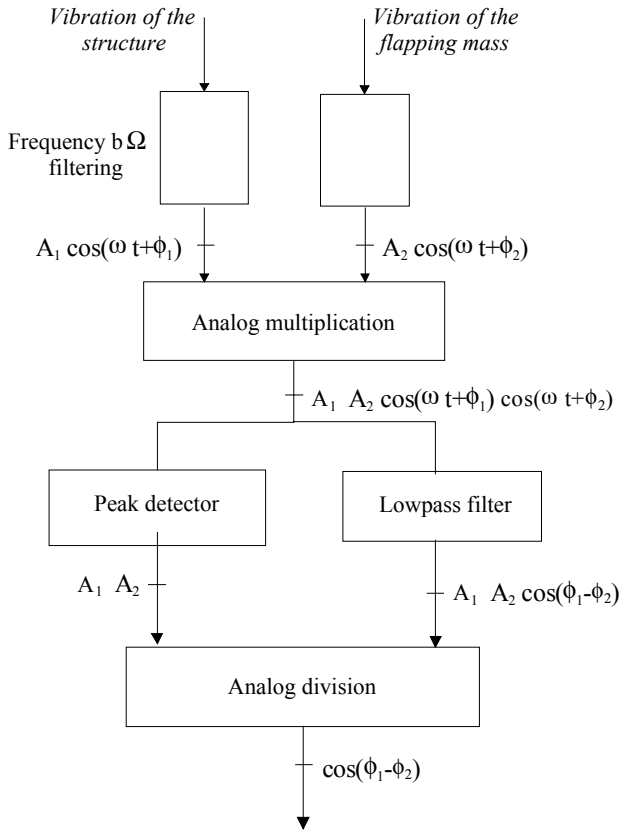

Figure 11.3. *Analog algorithm for the control of the position of the flapping mass*

11.3.2. *Digital algorithm*

There is one digital algorithm, based on an iterative method, which has been perfected. It adjusts the phase difference of the flapping mass with respect to the measured vibration. Thus, the natural frequency of the resonator must be at the excitation frequency, which is detected using signals from two sensors (accelerometers): one is fixed to the vibratory structure at the point of attachment of the resonator, and the other is at the extremity of the flapping mass.

The advantage of this algorithm is that it ensures convergence but its disadvantage is that it takes too long to calculate convergence. This would make it impossible to properly follow up the evolution of the vibrations induced by the variations of the excitation frequency.

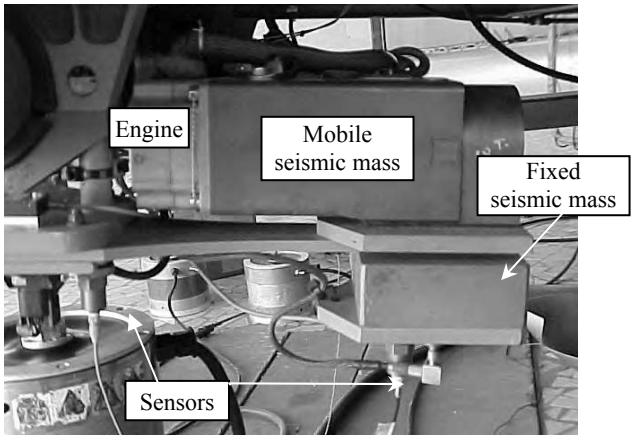

Figure 11.4. *Model of the self-adjusting resonator system*

Let:

– M be the fixed seismic mass,

– m be the mobile seismic mass

To overcome the problem of excessively long computing time, a second algorithm was used, ensuring a higher convergence speed. The principle is to calculate the position of the mobile mass after estimating the rotor speed.

The objective of this algorithm is to define the displacement of the resonator's mobile mass to establish as quickly as possible a –90º phase difference between the flapping mass and the structure.

In view of the curves in Figure 11.6, a constant step algorithm was out of the question; this kind of algorithm cannot be adjusted to phases far from –90º (high step preferred) and close to –90º (low step preferred).

Therefore, a predefined variable step algorithm was chosen, based on the principle of dichotomy: the step is halved when the direction of displacement of the mass changes.

For the area close to –90º, a gradient method was chosen. In this area, the curve can be approximated by a straight line. The following definition was finally considered (a mass M of 5 kg and m of 1.2 kg):

$-20^o < \Phi < 0$ to $-180^o < \Phi < -160^o$ dichotomy (big step)

$-50^o < \Phi < -20^o$ to $-160^o < \Phi < -130^o$ dichotomy (medium step)

$-85^o < \Phi < -50^o$ to $-130^o < \Phi < -95^o$ gradient (very small step)

Convergence is theoretically reached for $\Phi = -90^\circ \pm 5^\circ$.

The 10º difference that we fixed corresponds to the displacement of the mobile mass in order to calculate the curve slope when the gradient method is applied.

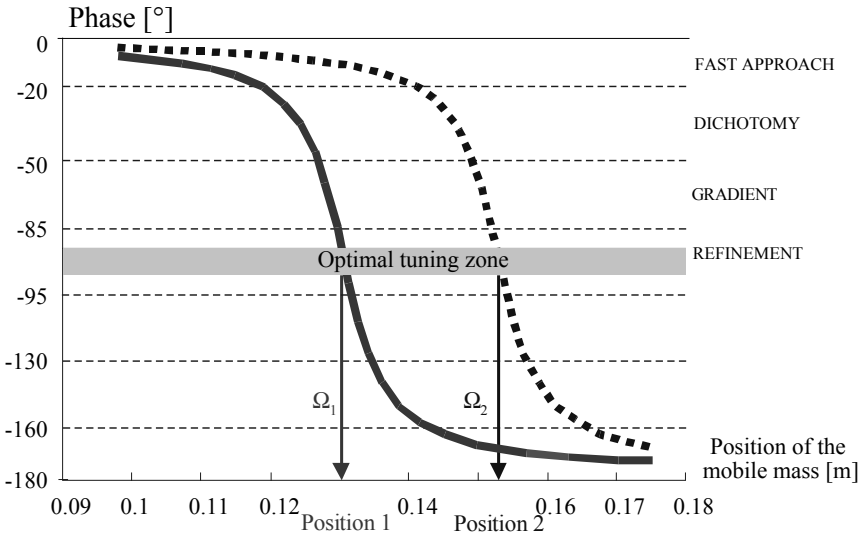

Figure 11.5. *Diagram of optimal tuning*

where Ω_1 and Ω_2 are the excitation angular frequencies.

Ground tests were conducted to validate the performance of the algorithm and to test its reliability with respect to damping variations.

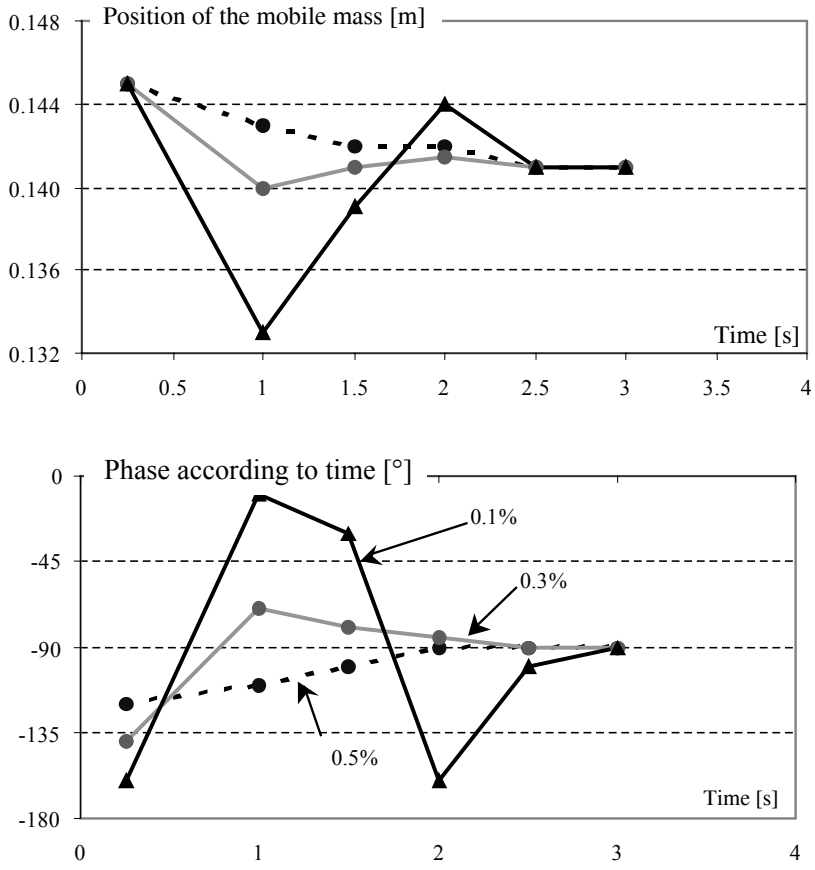

Figure 11.6. *Convergence of control algorithms of the self-adjusting resonator*

These curves show the convergence study with a damping, successively, equal to 0.5, 0.3 and 0.1% in identical initial conditions. They highlight the influence of damping on the convergence time and a few other important aspects:

– the convergence is obtained for any damping value higher than 0.1%,

– the optimization of convergence time during the tests was obtained with a medium damping value of 0.3%.

This algorithm works well, it ensures convergence, but it requires too much time before convergence. Because of these problems incurred with the first algorithm, a second algorithm was developed, based on the measurement of the excitation frequency (linked to the rotor speed).

In order to define the frequency, the method uses the signals output by the accelerometers, counting the zeros.

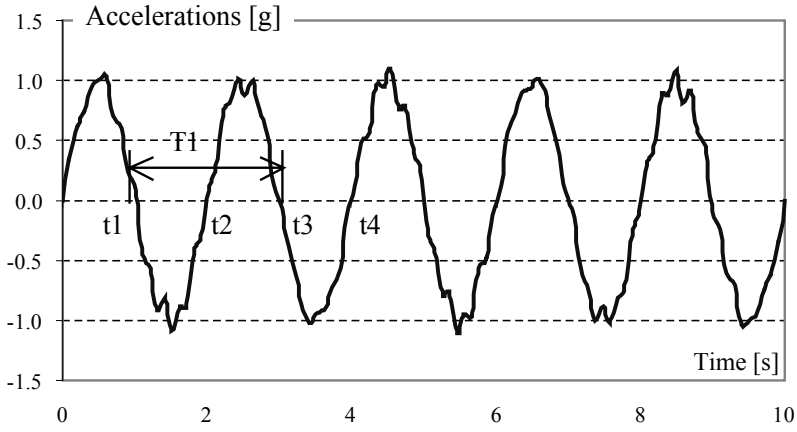

Figure 11.7. *Identification of frequency by the method of counting zeros*

The signal from the accelerometer is re-centered, then the frequency is estimated by:

$$f = \frac{1}{N}\sum_{i=1}^{N}\frac{1}{T_i} \qquad [11.1]$$

where:

$$T_i = t_{i+2} - t_i \qquad [11.2]$$

Once this frequency is estimated, we will try to generate the resonance frequency of the resonator.

To generate this frequency, we must know the law that links the position of the mobile mass to the resonance frequency of the resonator. This law was estimated

experimentally, by measuring the resonance frequency of the resonator for different positions of the mobile mass.

The law obtained was approximated using the following second order polynomial:

$$X_2(\Omega) = A\Omega^2 + B\Omega + C \qquad [11.3]$$

where:

– X_2 is the position of the mobile mass,

– Ω is the rotor speed,

– A, B, C are experimental constants.

These constants were calculated during many tests and then averaged for the best coverage of the range of resonator frequencies.

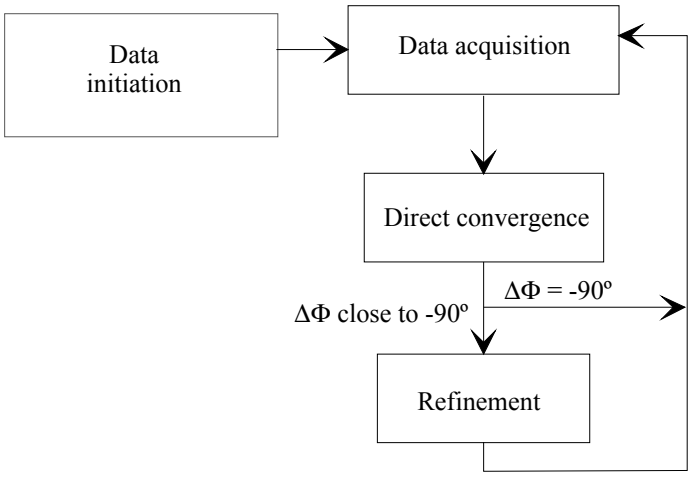

Figure 11.8. *Control algorithm*

When the phase difference is –90º, the algorithm returns to data acquisition.

When the phase difference is different from –90º during several consecutive loops, the C coefficient of the polynomial is adjusted to ensure a –90º phase difference. Then the algorithm starts the data acquisition.

Figure 11.9 presents the ratio of the flapping mass acceleration and the fuselage acceleration versus the forward speed of the helicopter.

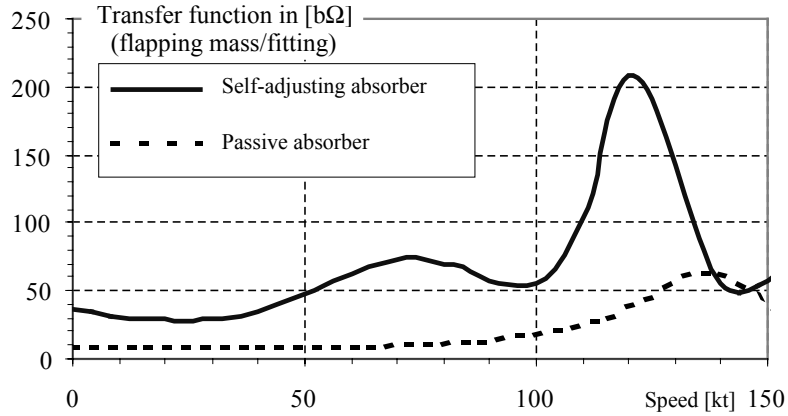

Figure 11.9. *Comparison of the transfer function with self-adjusting absorber and passive absorber*

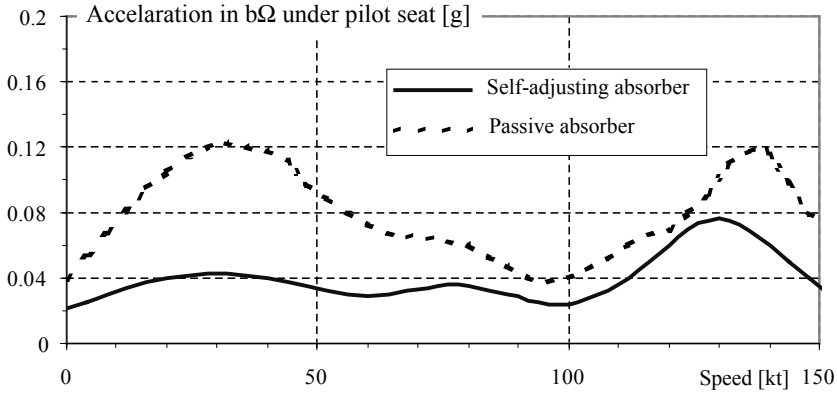

Figure 11.10. *Influence of a self-adjusting system on the cabin vibrations*

Note in Figure 11.10 that the active system improves the vibratory level compared to the passive system.

Chapter 12

Active Absorbers

12.1. Introduction

The self-adjusting systems presented in Chapter 11 are not always sufficient: either because the source characteristics vary too fast for the algorithms involved, or because the required level of performance is too high.

In these cases, active methods can be used to decrease the vibrations. The aim of this chapter is to present existing methods that can be used when we want to act locally on a structure. The decrease in vibrations is obtained by introducing dynamic loads in the structure. The dynamic loads are controlled by a computer in order to minimize the vibratory levels, as shown in Chapter 9. The technology of generating loads is fundamental in the control strategy. There are several technologies for generating loads. These dynamic loads can be generated by:

– resonant systems,

– specific loads or already-existing load generators.

12.2. Active control with a resonator

The principle of an active resonator consists of displacing a mass with an actuator.

Different types of actuator technologies – hydraulic, electromagnetic or piezoelectric actuators – can be used to match the fields of application in terms of forces and frequency.

The resonator uses the dynamic amplification of the mass to generate high loads using minimal energy.

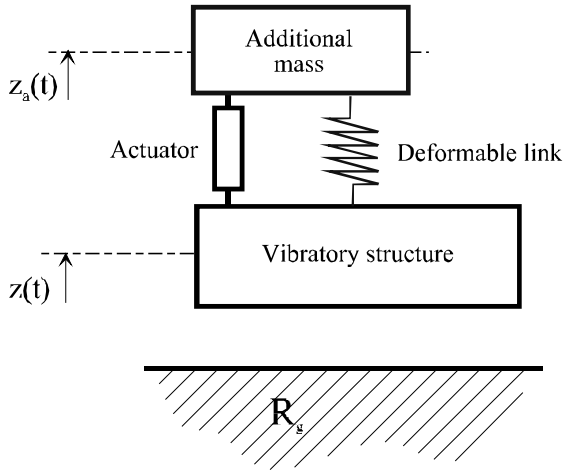

Figure 12.1. *Principle of an active resonator*

Two methods will be developed with an electromagnetic actuator and with a hydraulic actuator.

12.2.1. *Electromagnetic actuator*

There are several types of electromagnetic actuators whose working features affect functioning and tuning differently.

12.2.1.1. *Single stage resonator*

For this type of resonator, the principle of the single stage mechanical system is used (see Figure 12.2), whose displacement will be operated by an electromagnetic force.

The equation of the mass M_1 (permanent magnet) for small motion around its static position is given by:

$$M_1\,\ddot{x}_1 + c_1\,\dot{x}_1 + k_1\,x_1 = F_V(t) \qquad [12.1]$$

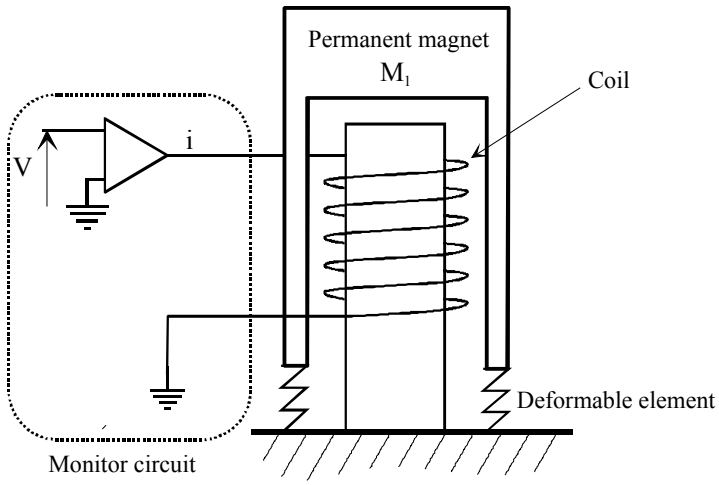

Figure 12.2. *Principle of a single stage system actuator*

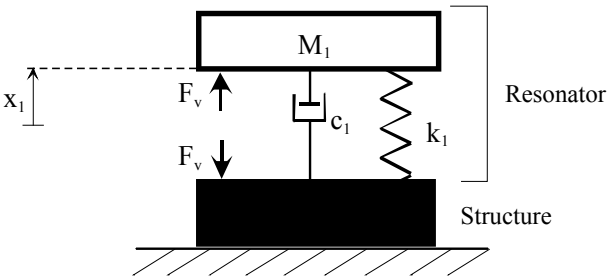

Figure 12.3. *Modeling of a single stage active resonator*

We assume that the actuator generates a harmonic control which we denote by:

$$F_V(t) = F_0 \cos(\omega t) \qquad [12.2]$$

Let:

$$\begin{aligned} F_V(t) &\rightarrow F_0\, e^{i\omega t} \\ x_1(t) &\rightarrow \bar{x}_1\, e^{i\omega t} \end{aligned} \qquad [12.3]$$

Based on equations [12.1] and [12.2], the displacement produced by the mass has the form:

$$\bar{x}_1 = \frac{1}{(k_1 - \omega^2\ M_1 + i\ c_1\ \omega)} F_0 \qquad [12.4]$$

The loads transmitted to the structure are given by:

$$F_T = c_1\ \dot{x}_1 + k_1\ x_1 - F_V \qquad [12.5]$$

If the complex function is:

$$\bar{F}_T = \frac{\omega^2\ M_1}{(k_1 - \omega^2\ M_1 + i\ c_1\ \omega)} F_0 \qquad [12.6]$$

The complex transfer function is defined by:

$$\bar{F}_T = \bar{H}(\omega)\ F_0 = H_0\ e^{i\varphi}\ F_0 \qquad [12.7]$$

where:

– H_0 is the module of transfer function,

– φ is the argument of transfer function.

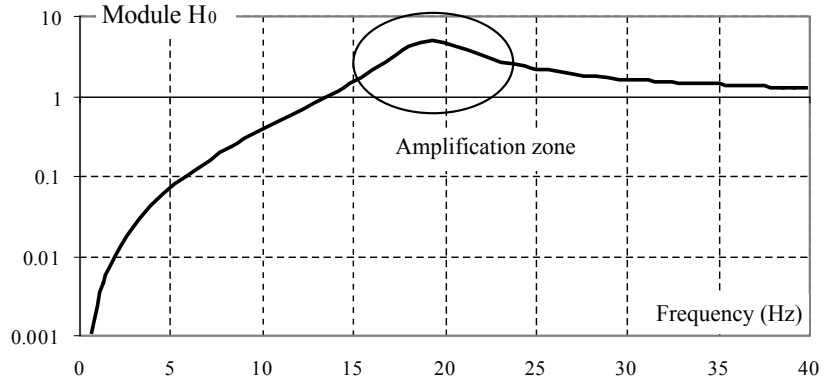

Figure 12.4. *Bode's diagram for the amplitude of the transfer function H(ω) of a single stage system*

The mechanical parameters (mass, stiffness) are chosen so that the magnetic loads remain small and compatible with an acceptable energy consumption (operation in the vicinity of the resonance point of the resonator to minimize the control loads). The natural frequency of the mass-spring system must be as close as possible to the frequency of vibrations that we want to control (see Figure 12.4).

The method of application is shown in Figure 12.5. The magnetic field generated by the permanent magnet generates a load in the winding, through which the electric current i flows, defined as follows:

$$F_V = B\ l\ i \qquad [12.8]$$

where:

– B is the magnetic flux density,

– i in the current in the winding,

– l is the total length of the coil wire.

By the principle of reaction, a load of the same amplitude but of opposite phase is exerted on the permanent magnet. The magnet has a flexible link with the structure, characterized by the stiffness k_1.

The electric current is generated at the natural frequency of the system which makes it possible to obtain the dynamic amplification (see equation [12.6]).

The advantage of such a system is that it offers a high load for a mass and low energy consumption.

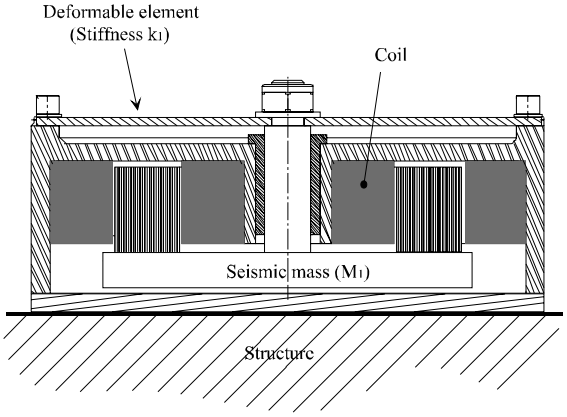

Figure 12.5. *Technology of a single stage resonator*

Another technology features two independent circuits generating two opposite loads, by means of the variable reluctance method (see Figure 12.6).

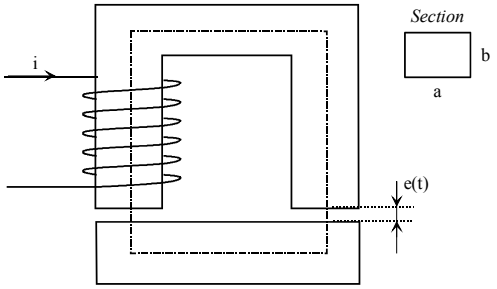

Figure 12.6. *Principle of variable reluctance*

Let:

– L_{m1} be the average length of the flow path on mass 1,

– L_{m2} be the average length of the flow path on mass 2,

– e be the length on flow paths in the air-gap.

According to Amper's law, the reaction of mass 1 on mass 2 is a function of the distance e:

$$F = \frac{\mu_0 \, S \, n^2}{4} \frac{I^2}{e^2} \qquad [12.9]$$

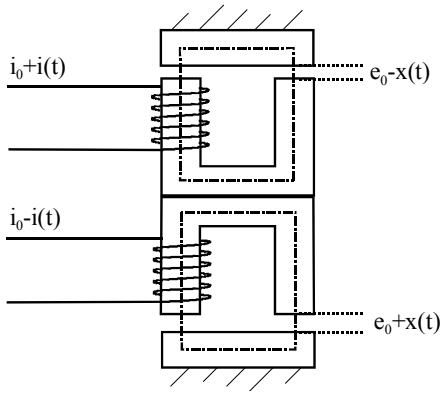

Figure 12.7. *Combination of two variable reluctances*

The total load produced by the actuator on the structure is thus:

$$F_V = \frac{\mu_0 \, S \, n^2}{4} \left(\frac{(i+i_0)^2}{(e_0 - x)^2} - \frac{(i-i_0)^2}{(e_0 + x)^2} \right) \qquad [12.10]$$

Assuming that x is small in comparison to e_0 and i is small in comparison to i_0, the load can be approximated as:

$$F_V = \mu_0 \, S \, n^2 \frac{i_0}{e_0^2} \left(i + \frac{i_0}{e_0} x(t) \right) \qquad [12.11]$$

Parameters i_0 and e_0 are chosen to create a system which is not sensitive to displacement x(t). This linearization can also be obtained with the help of the power amplifier, by estimating or measuring the values of x(t). The load F_V is thus proportional to the intensity i representing the linear control.

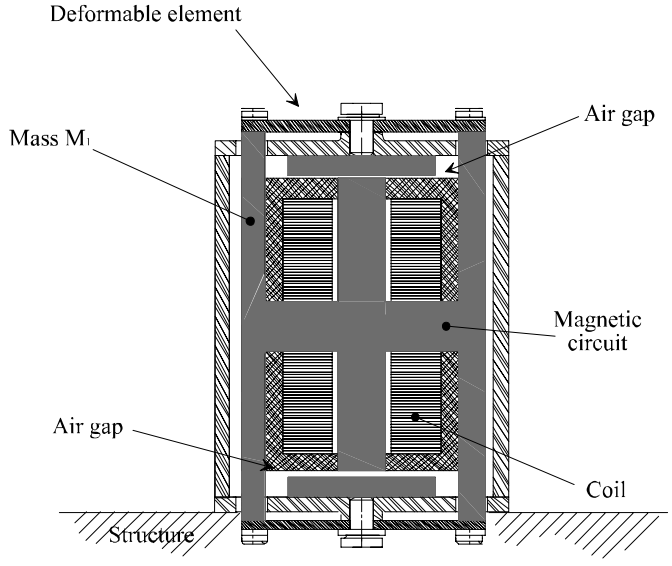

Figure 12.8. *Technology of a variable reluctance resonator*

12.2.1.2. *Two-stage electromagnetic resonator*

The principle of a two-stage electromagnetic resonator is shown in Figure 12.9.

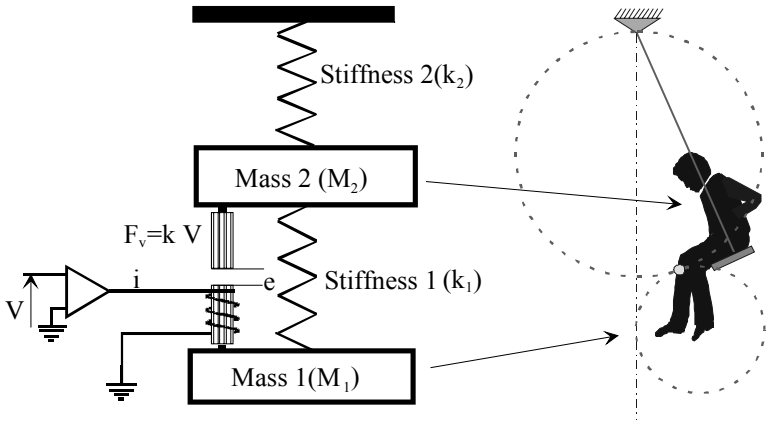

Figure 12.9. *Principle of a two-stage resonator*

This type of technology uses two masses called stages. The control force is introduced between the two masses by an electromagnetic load. The voltage control is fed to a power amplifier that generates the magnetic force F_V via the current in the coil.

The role of the amplifier is thus to ensure the law between the generated load F_V and the control voltage V is linear. For this technology, linearization is facilitated if the air gap e is small.

The control method consists of tuning the system (masses and stiffness) so that, at the control frequency, the force generated on the structure is amplified with respect to the force F_V, while maintaining a small relative displacement of the stages.

For this reason, we choose the parameters M_1, M_2 and k_2, so that the frequency of the set is close to the control frequency to take advantage of the dynamic amplification:

$$f_c \approx \frac{1}{2\pi}\sqrt{\frac{k_2}{M_1 + M_2}} \qquad [12.12]$$

The stiffness k_1 is chosen so that the second natural frequency of the system is be higher than the control frequency f_c. This setting provides a high amplification at the control frequency f_c, with little relative motion between the two masses.

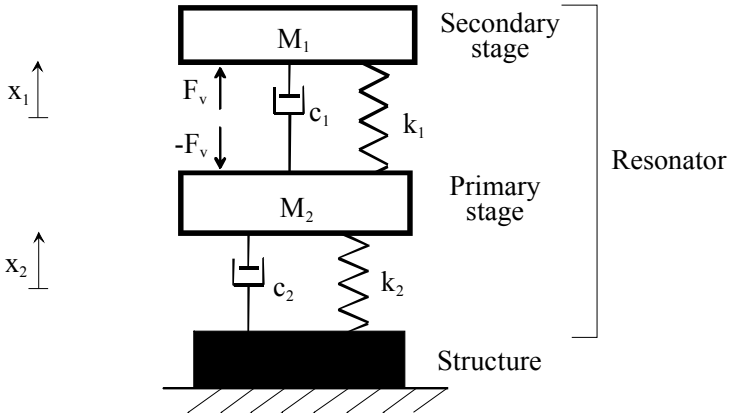

Figure 12.10. *Modeling of two-stage active resonator*

We will calculate the loads generated by the structure as a function of the control forces.

The resonator is controlled by the electrodynamic actuator. The equations of motion of masses 1 and 2 are:

$$\begin{cases} M_1\ \ddot{x}_1 + c_1(\dot{x}_1 - \dot{x}_2) + k_1(x_1 - x_2) = F_V \\ M_2\ \ddot{x}_2 + c_1(\dot{x}_2 - \dot{x}_1) + c_2\ \dot{x}_2 + k_1(x_2 - x_1) + k_2\ x_2 = -F_V \end{cases} \quad [12.13]$$

We assume that the actuator generates harmonic control:

$$F_V = F_0\ \cos(\omega\, t) \quad [12.14]$$

Thus:

$$\begin{cases} x_1(t) \to \overline{x}_1\ e^{i\omega\, t} \\ x_2(t) \to \overline{x}_2\ e^{i\omega\, t} \\ F_V(t) \to F_0\ e^{i\omega\, t} \end{cases} \quad [12.15]$$

The displacements generated by the actuator are such that:

$$\begin{cases} \bar{x}_2 = \dfrac{\omega^2\ M_1}{\left[(\bar{k}_1 + \bar{k}_2 - \omega^2\ M_2)\,(\bar{k}_1 - \omega^2\ M_1) - \bar{k}_1^{\,2} \right]} F_0 \\ \bar{x}_1 = \dfrac{\bar{k}_1}{(\bar{k}_1 - \omega^2\ M_1)} \bar{x}_2 + \dfrac{1}{(\bar{k}_1 - \omega^2\ M_1)} F_0 \end{cases} \quad [12.16]$$

where:

$$\bar{k}_1 = k_1 + i\ c_1\ \omega$$
$$\bar{k}_2 = k_2 + i\ c_2\ \omega$$

The loads transmitted to the structure are:

$$F_T = c_2\ \dot{x}_2 + k_2\ x_2 \quad [12.17]$$

or in the complex function:

$$\bar{F}_T = \frac{\bar{k}_2\ M_1\ \omega^2}{\left[(\bar{k}_1 + \bar{k}_2 - \omega^2\ M_2)\,(\bar{k}_1 - \omega^2\ M_1) - \bar{k}_1^{\,2} \right]} F_0 \quad [12.18]$$

We define the complex transfer function as:

$$\bar{F}_T = \bar{H}(\omega)\ F_0 = H_0\ e^{i\varphi}\ F_0 \quad [12.19]$$

where:

– H_0 is the module of the transfer function,

– φ is the argument of the transfer function.

Figure 12.12 shows the dynamic displacement of the masses for an excitation F_V depending on the frequency. At the control frequency, close to 19 Hz, the relative motion of the two masses is very low, which, considering the previous comment, facilitates the linearity of the control.

The usage of dynamic amplification makes it possible to significantly reduce the mass of the system.

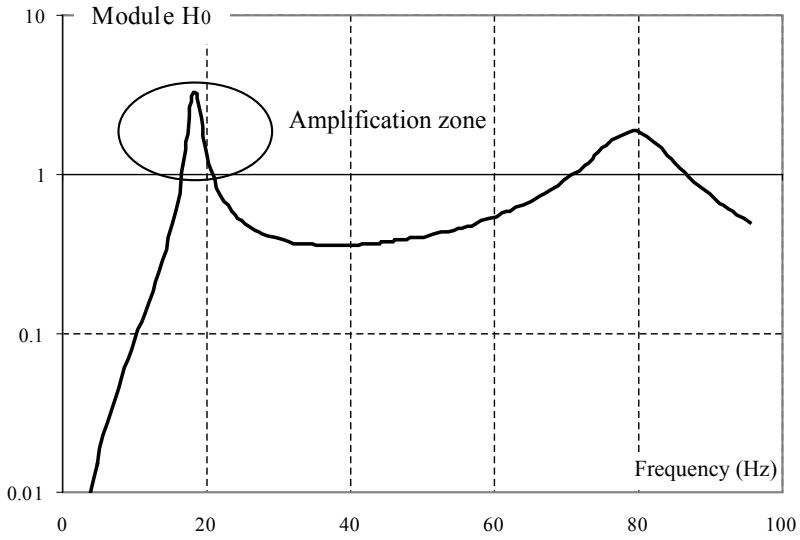

Figure 12.11. *Bode's diagram for the amplitude of the transfer function H(ω). Two-stage system*

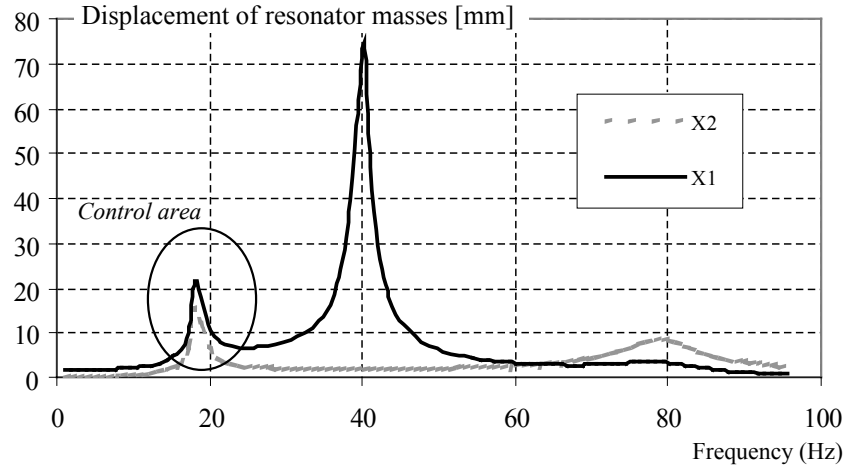

Figure 12.12. *Displacement of a two-stage resonator masses versus excitation frequency*

This resonator has the following advantages:

– the control is linear around the control frequency,

– the dynamic amplification helps generate very high loads with a very low control energy.

One of the technological systems is illustrated in Figure 12.13.

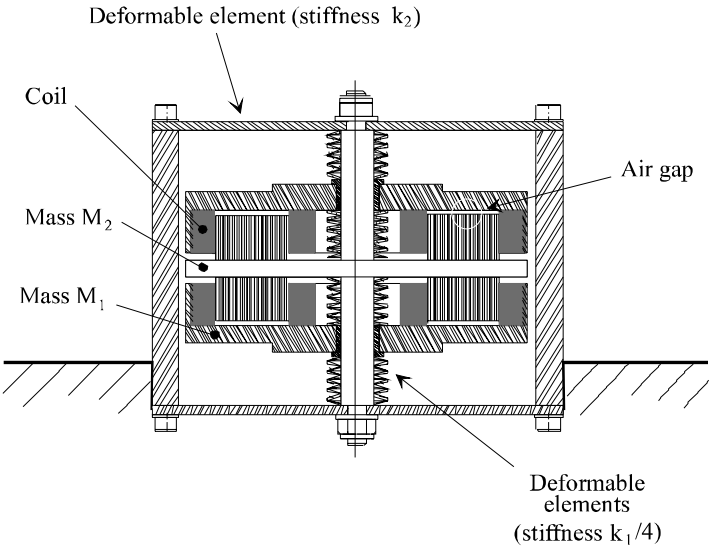

Figure 12.13. *Technology of a two-stage resonator*

12.2.2. *Hydraulic actuator*

12.2.2.1. *Technological principle*

The tail-shake phenomenon produces a high vibration level in the cockpit (see Chapter 9), and is characterized by an excitation band around 2 Hz with intermittent bursts. On most helicopters, the tail-shake phenomenon has been solved by making aerodynamic modifications, such as adding a fairing around the rotor shaft, modifying the covers, etc. We can also use an active technology.

The objective of this chapter is to show the application of a specific resonator installed in the tail boom. Its positioning is similar to that of the passive resonators presented in Chapter 10.

The design of the system is like that of a conventional passive resonator (see Chapter 10), but with a hydraulic actuator added. As indicated before, in this technique, the resonance peak of the structure due to aerodynamic excitation is replaced by an anti-resonance, but two new peaks are created.

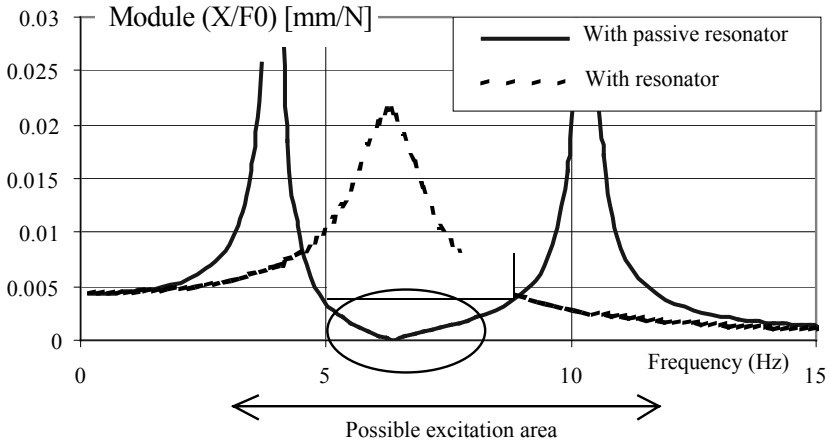

Figure 12.14. *Response of a structure with and without resonator*

The disadvantage of a passive resonator is that anti-resonance is a very sensitive phenomenon. A variation in the excitation frequency can shift the system back into a resonance area.

In the case of tail-shake, the excitation can cover an excitation range including the two resonance peaks of the structure with the resonator. The passive solution does not improve the situation. It is therefore necessary to use an active system that can adapt to the excitation.

Two technical solutions exist for introducing the energy necessary for vibratory control: either the actuator follows a displacement-based law (displacement control) or a load law is implemented (load control) (see Figure 12.15).

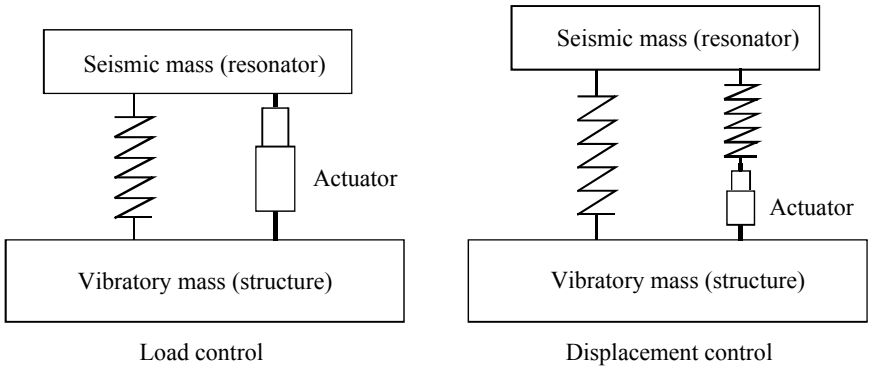

Figure 12.15. *Diagram of the active control system*

The displacement control has the advantage of not operating at anti-resonance. At anti-resonance the control is zero and the passive system is sufficient to control the vibrations. The load control requires a non-zero control at anti-resonance. In addition, load control is more technologically complex; therefore, displacement control was selected.

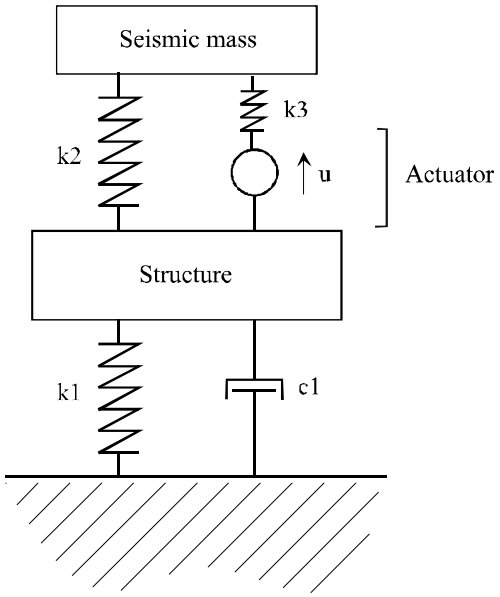

Figure 12.16. *Modeling of shifting piloting*

12.2.2.2. *Control algorithm*

To define the active control law, it is necessary to set up a control strategy. For this application the pole location method is used [CAR 00, LAN 93].

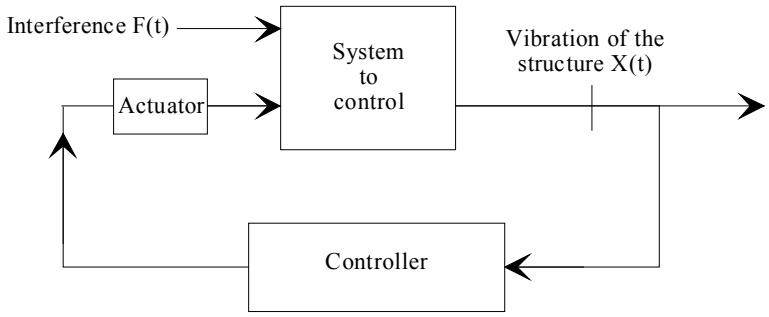

Figure 12.17. *Principle of closed loop control*

We try to place all the system poles in a closed loop, in the area that fulfills the performance and stability constraints. The disadvantage of this method is that it remains empirical for this type of application.

The transfer function of the acceleration of the structure with respect to the excitation is shown for the open and closed loop systems in Bode's diagram (see Figure 12.18).

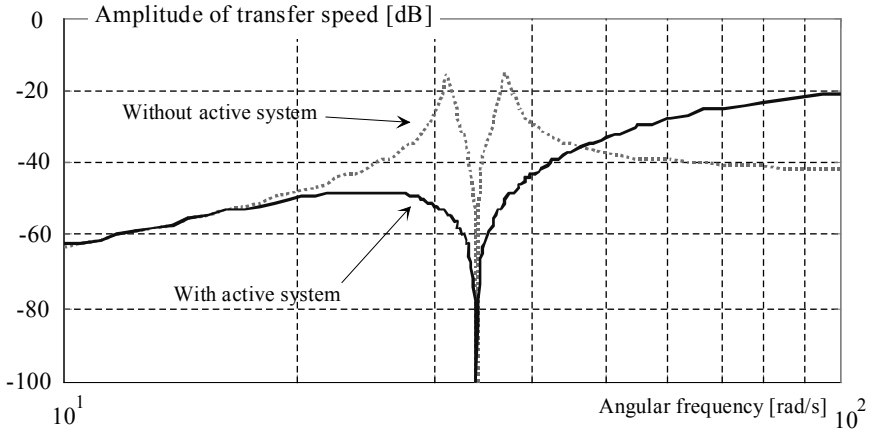

Figure 12.18. *Bode's diagram in open loop and closed loop*

The modes are well damped, since the resonance peaks have disappeared.

Note that, at high frequencies, the gain is higher than the gain of the open loop system.

One solution is to introduce a filter to cut out the high frequencies (roll off phenomenon). Industrial experience often shows that the actuators used have a very small bandwidth for high frequencies. Therefore, the observed gain is naturally reduced at high frequencies.

12.2.2.3. *Results of lab tests*

The efficiency of active controls can be confirmed in laboratory tests on models or in flight tests on real structures (see Figure 12.19).

The experimental results on models demonstrate the efficiency of active systems compared to passive systems or systems without resonators (see Figure 12.20).

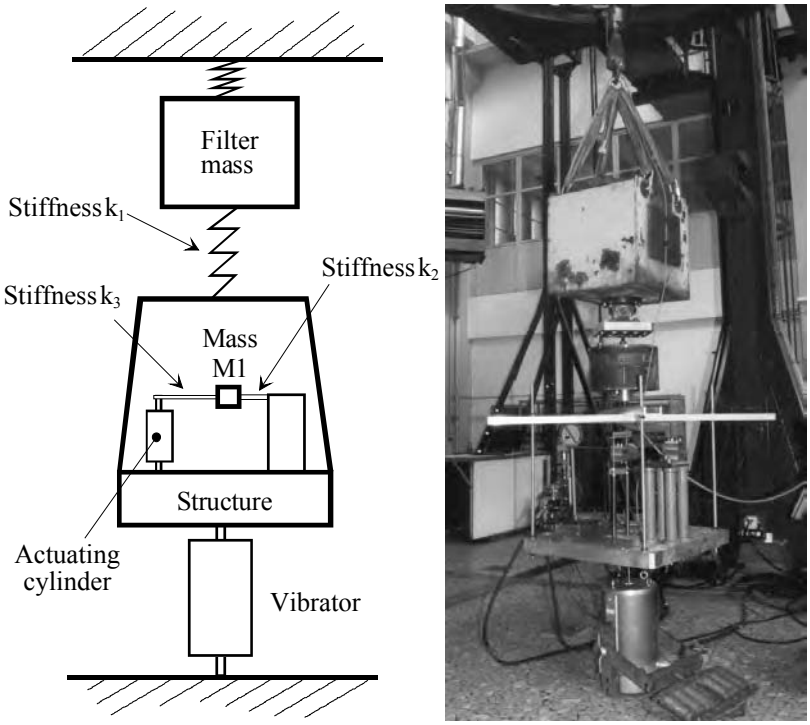

Figure 12.19. *Lab tests of the active system for tail-shake. Photo: Eurocopter*

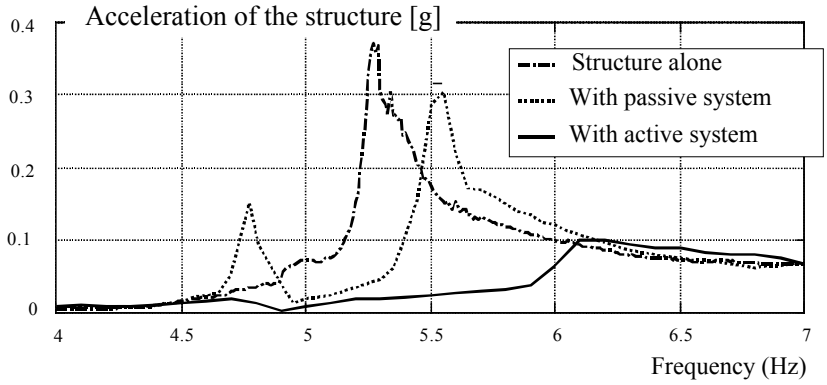

Figure 12.20. *Comparison of tests with active system and without system*

12.3. Active control through external loads

For certain applications, vibrations can be reduced by applying a technology based on external load generators.

In such cases, we can use a specific generating system or an actuator already installed on the structure.

We will now illustrate these two types of application with an example of a centrifugal generator and the usage of the anti-torque helicopter tail for active control.

12.3.1. *Mechanical load generator*

12.3.1.1. *Description of the mechanism*

The centrifugal generator uses unbalance to generate dynamic loads. The system requires the action generated to be unidirectional and the amplitude and the excitation frequency to be adjusted independently.

The generator has four rotating masses, whose centers of gravity are offset with respect to their axis of rotation (see Figure 12.21).

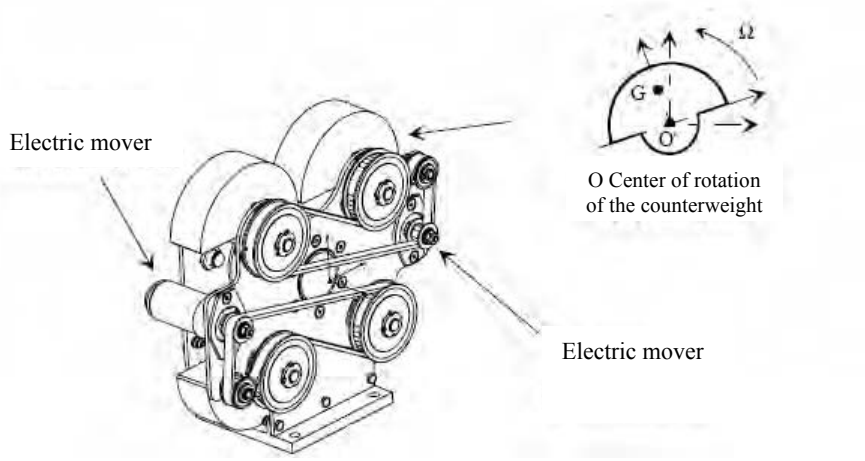

Figure 12.21. *Generator of centrifugal loads*

With four masses, it is possible to obtain the desired properties by acting on the rotation direction of the masses and their angular phase difference θ.

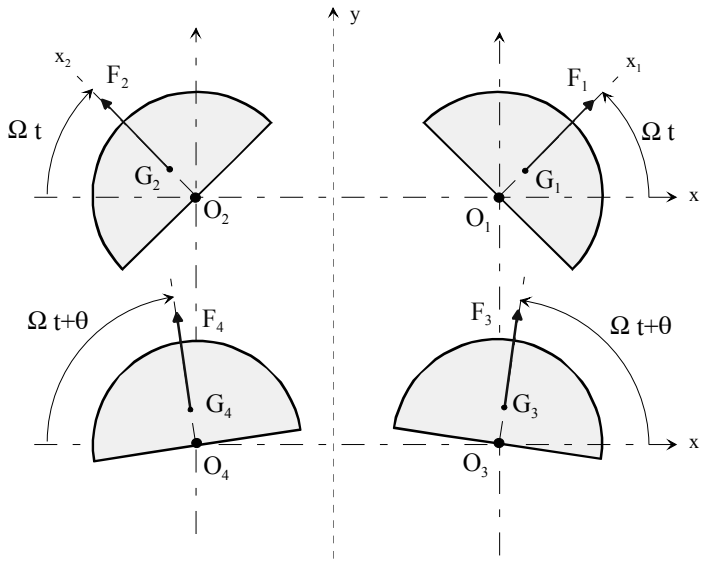

Figure 12.22. *Influence of four lead counterweights*

The load applied by the four counterweights on the structure is given by:

$$\vec{F}_T = \vec{F}_1 + \vec{F}_2 + \vec{F}_3 + \vec{F}_4 = 2m\, e\, \Omega^2 \left(\sin(\Omega\, t) + \sin(\Omega\, t + \theta)\right) \vec{y} \qquad [12.20]$$

where:

– m is the mass of a counterweight,

– e is the offset of the center of gravity from the center of rotation,

– Ω is the speed of rotation of the counterweights,

– θ is the phase difference between the upper counterweights and the lower counterweights.

This expression can be written as:

$$\vec{F}_T = 4\, m\, e\, \Omega^2 \sin(\Omega\, t) \cos\left(\frac{\theta}{2}\right) \vec{y} \qquad [12.21]$$

The excitation frequency is equal to the rotation frequency of the counterweights.

The excitation amplitude is determined by adjusting the phase difference θ between the upper and lower counterweights, so that the excitation amplitude varies independently of the excitation frequency.

12.3.1.2. *Positioning of the generator*

The position of the load generator is usually determined by analyzing the deformation of the structure, a complex process requiring finite element calculations. This will make it possible to identify the order of magnitude of the disturbing frequency and the place of nodes and antinodes of the mode to be processed.

This model is then reset again during vibration tests on the ground. In this phase (see Figure 12.23), the parameters are set with higher precision.

Figure 12.23. *Experimental modal identification of a complex structure. Photo: Eurocopter*

Once the model has been reset, we can predict the optimum location for installing the load generators.

The generators are integrated in the structure, as shown in Figure 12.24. A flight validation is then carried out to confirm their efficiency. The structure is excited by a constant amplitude control system at the control frequency.

The identification procedure verifies the influence of the loads injected to counter the vibrations in the structure. A good location for the generator guarantees a strong influence on the vibratory levels.

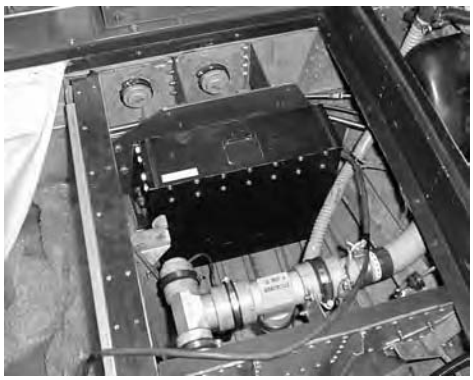

Figure 12.24. *Implementation of a generator on a prototype. Photo: Eurocopter*

The control algorithm manages the modulus and phase loads in order to minimize the vibrations. Two types of algorithms can be used: a temporal algorithm or a frequency algorithm.

The typical efficiency of the system is shown in Figure 12.25.

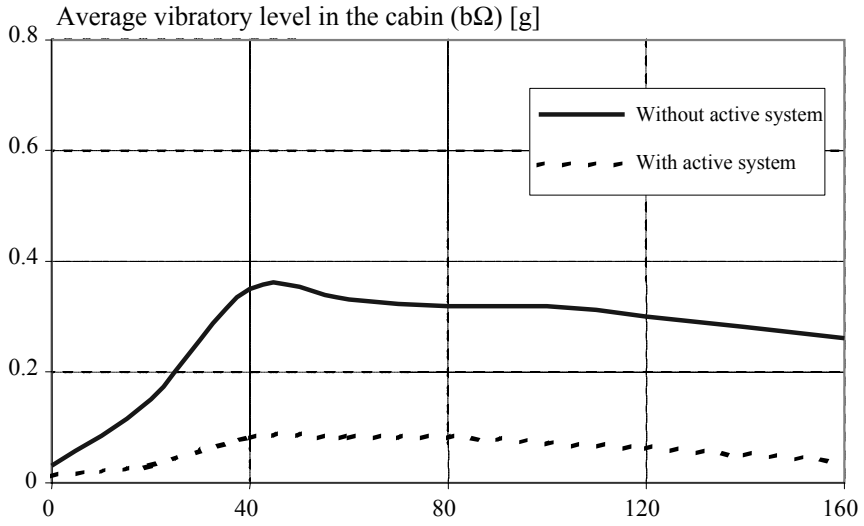

Figure 12.25. *Efficiency of the generator – measurements*

12.3.2. *Active control through the anti-torque rotor*

For certain structures, it is advantageous for vibration control to use actuators that are already installed. This solution is often economic as it avoids complications to the structure.

We will illustrate this solution for tail-shake control using the tail rotor (see Figure 12.26). The idea is to use the blade pitch variation to modify the aerodynamic loads and thus generate, through reaction, loads on the structure ΔT_Y. These loads will be superimposed on the loads T_Y generating the torque opposing the reaction torque created by the main rotor.

This actuator belongs to the helicopter and is thus a “free” element.

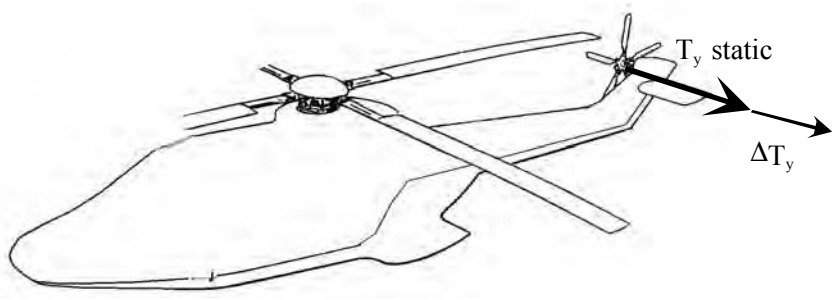

Figure 12.26. *Tail rotor used as an actuator for the active control of tail-shake. Illustration: C. Guarnieri*

The autopilot (AP) is used as a computer. Most helicopters are equipped with APs to facilitate the tasks of the pilot and comply with the various regulations in force. The active loop calculation for the tail-shake control can be included as a supplementary function for the autopilot.

The goal is to make sure that the elements in the control chain can operate in the range of frequencies that need to be controlled.

The tail-shake phenomenon, presented in Chapter 6, generates high vibrations in the cockpit, due to the excitation of the bending mode of the helicopter caused by the vortices from the main rotor.

In active control, the vibratory status of the system is measured and then a control law is defined for the tail rotor, using the autopilot control signal (see Figure 12.27).

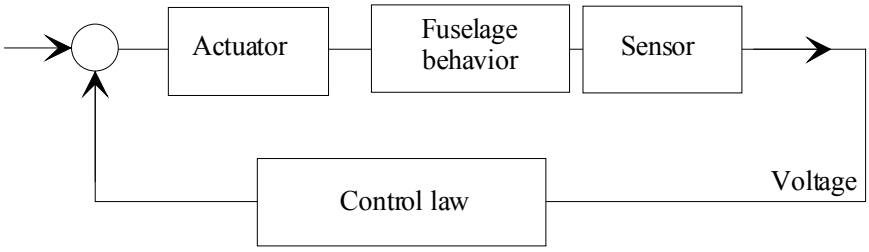

Figure 12.27. *Block diagram of the closed loop of the active control for tail-shake*

Vibrations can be measured in two different locations on the structure:

– on the tail boom with a strain gage,

– in the cabin, near the pilot seat, by an accelerometer.

The measured parameters are chosen in terms of simplicity, access and cost. The measured parameter chosen in this study is the sideways acceleration in the nose of the machine. The accelerometer is easy to install and the measuring system has a reasonable industrial cost.

Since this study was carried out in an industrial context, the phenomenon was identified directly on the helicopter in flight by exciting the tail rotor collective pitch (using the AP yaw channel) and by measuring the vibrations generated with the previously-mentioned sensor. In this phase, the transfer function used to adjust the control law is defined (see Figure 12.28).

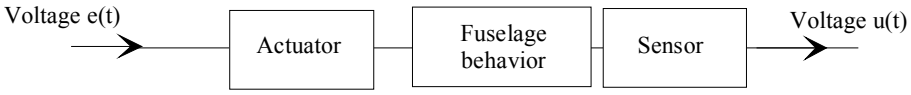

Figure 12.28. *Block diagram of the open loop identification*

For this analysis we will use complex variables.

Let:

$$e(t) \rightarrow \overline{E}\, e^{i\omega t}$$
$$u(t) \rightarrow \overline{U}\, e^{i\omega t} \qquad [12.22]$$

The transfer function is defined by:

$$\overline{U} = \overline{H}(\omega)\, \overline{E} \qquad [12.23]$$

The measured transfer function (see Figure 12.29) is like that of a second order single mode system. Hence, there is a peak at about 5.5 Hz.

The transfer function can be identified using traditional methods of modal analysis. Hence, the mathematical model used is:

$$\bar{H}(\omega) = \frac{G_{st}}{{\omega_0}^2 - \omega^2 + 2\, i\, \lambda\, \omega_0\, \omega} \qquad [12.24]$$

After identification, it is possible to establish a static gain G_{st} of 53 V/V, a natural frequency at 5.5 Hz and a damping ratio λ at 3%.

Once the open loop system is identified, the second phase consists of defining the active control strategy. The method must be sufficiently simple to be applicable to an industrial system, whilst being sufficiently efficient.

The system used here is based on the following observation: like all second order systems, the response lags the excitation by 90º.

Intuitively, an equalizer can be suggested, based on simple physical reasoning. In order to block the cabin vibrations, a voltage must be applied on the AP yaw signal with a 90º delay with respect to the acceleration. This voltage will generate acceleration opposed to the initial acceleration if we suppose that the system is linear.

We suggest an equalizer consisting of a *wash-out* associated with a phase shifter based on an 8^{th} order Butterworth filter (see Figure 12.30).

The wash-out has the role of eliminating the quasi-static component and the very low frequencies measured by the sensor. It imposes a phase lead of +15º at 5.55 Hz (see Figure 12.31). In order to have the –90º delay of the full equalizer, the phase shifter must provide a –105º delay at a frequency of 5.55 Hz.

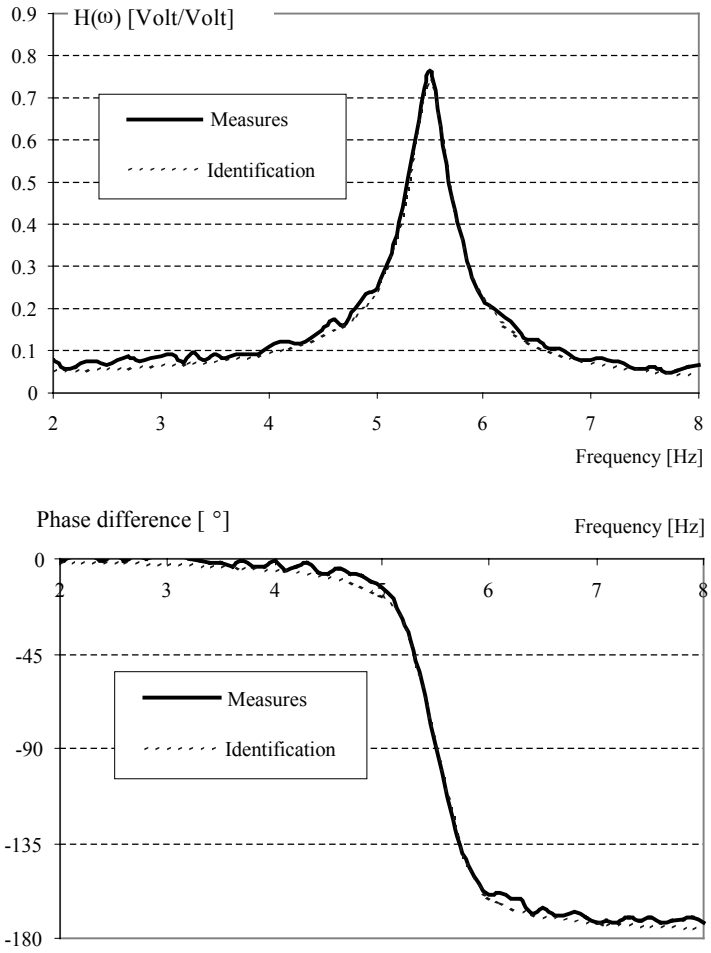

Figure 12.29. *Measured transfer function*

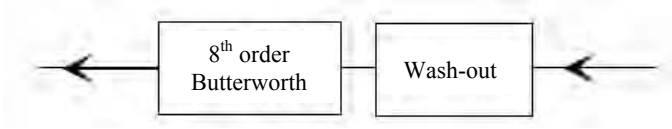

Figure 12.30. *Block diagram of the return loop*

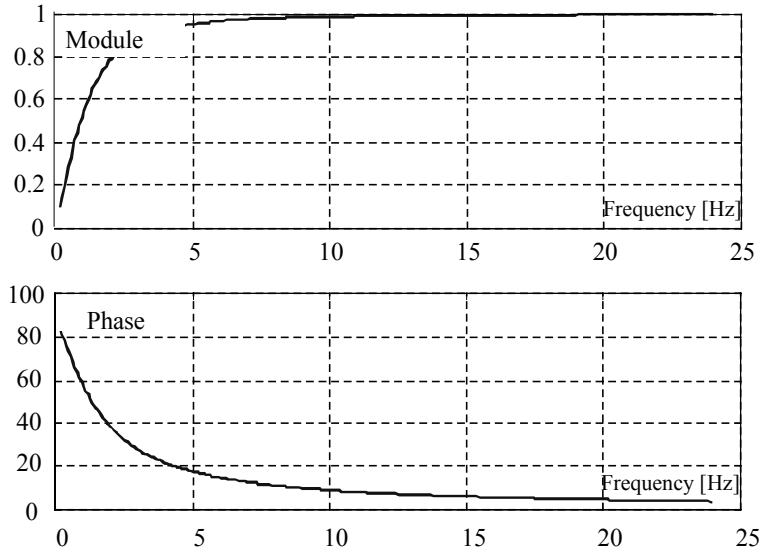

Figure 12.31. *Transfer function of the wash-out*

For a Butterworth filter, we can set a delay at a given frequency by choosing the cross-over frequency of the filter. For this, we use the linearity of the phase difference. Supposing:

$$\frac{F_c}{F_{def}} = \frac{-297}{\phi_x} \qquad [12.25]$$

To generate the –105º phase difference at a frequency of 5.55 Hz, we have to adjust the cross-over frequency of the filter to:

$$F_c = 5.55\left(\frac{-297}{-105}\right) = 15.69 \text{ Hz} \qquad [12.26]$$

The two elements of the equalizer are connected in series and the total result is given in Figure 12.33. Note that, at the frequency of 5.55 Hz, the equalizer produces a phase difference of –90º. The proposed equalizer gives a high gain in the range of frequencies from 2 to 17 Hz. It is important to make sure that in this range there are no other modes that can be disturbed by the proposed equalizer. The dynamic identification of the device using the yawing control showed that this was the case.

The third phase of the study consists of analyzing the influence of the equalizer in a closed loop, and thus finding an optimal setting. An analysis of measurements of the transfer function in flight makes it possible to analyze the performances (see Figure 12.34).

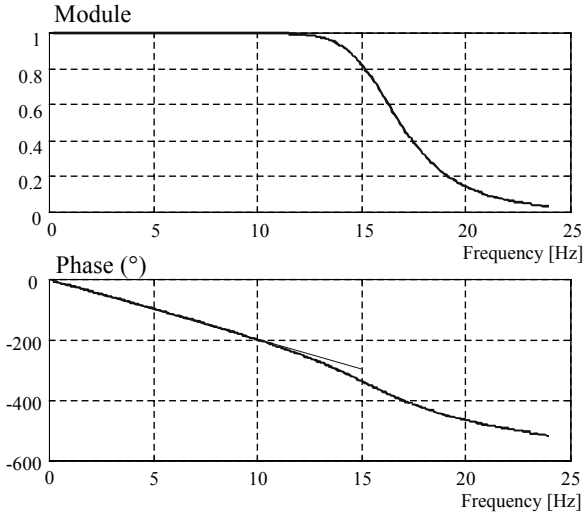

Figure 12.32. *Transfer function of the phase shifter (8th order Butterworth)*

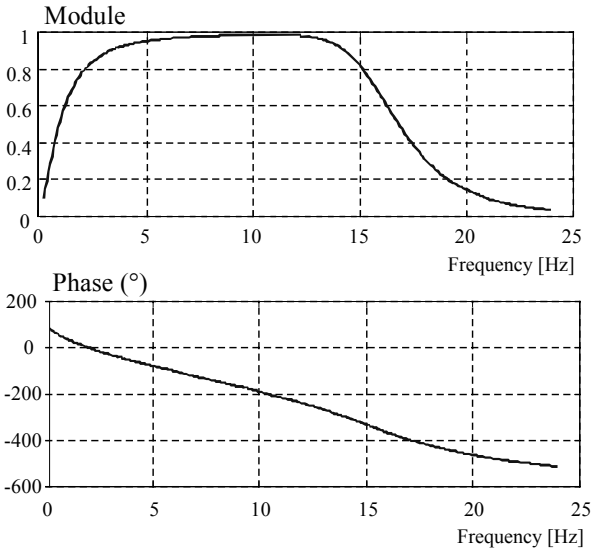

Figure 12.33. *Transfer function of the equalizer for a gain set to 1*

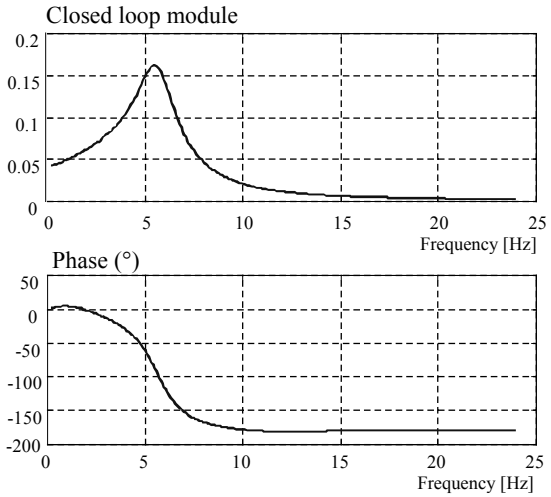

Figure 12.34. *Transfer function of the closed loop in flight*

Note that damping was increased by a factor of 5 in this setting configuration. These operations can also be analyzed by measuring the vibrations under the pilot seat (see Figure 12.35).

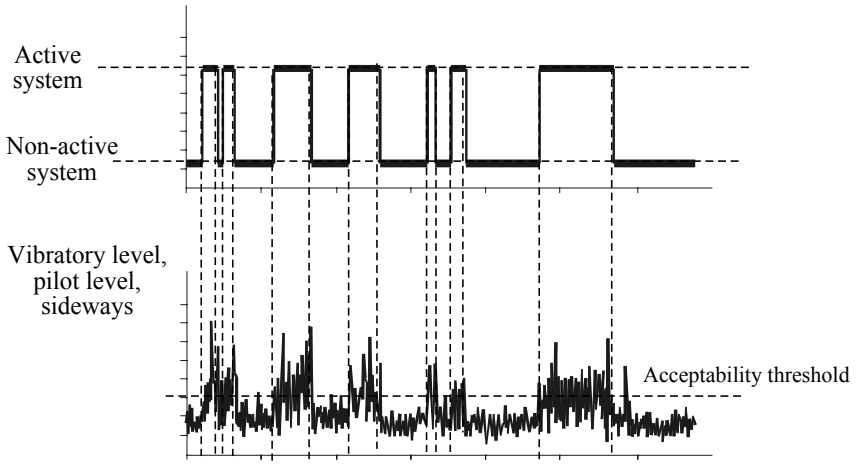

Figure 12.35. *Vibration measurements near the pilot seat*

Note that in the phases when the system is operating, the lateral vibrations under the pilot seat are significantly reduced (see Figure 12.35).

In the coupling loop, there is a non-linearity for the yawing booster control servoactuator, caused by the presence of a gap in a conventional servoactuator system.

Note that the electric order sent to the booster control is not fully transformed during the displacement. There is a dead zone estimated at +/–0.15 V.

The presence of this non-linearity reduces the efficiency of the system. Since this effect is difficult to physically eliminate, it has been preferable to model this behavior and to take it into account during the tuning of the system.

In fact, the dead zone of the control is modeled as in Figure 12.36.

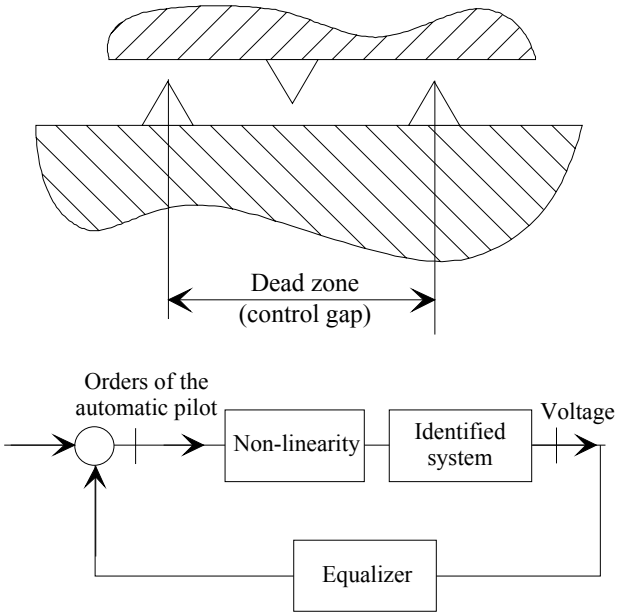

Figure 12.36. *Modeling of the non-linearity of the control*

Hence, if we introduce this non-linearity effect, it is possible to remake the simulations.

The system is less efficient when we allow for the control gap, and this new result is closer to the flight results.

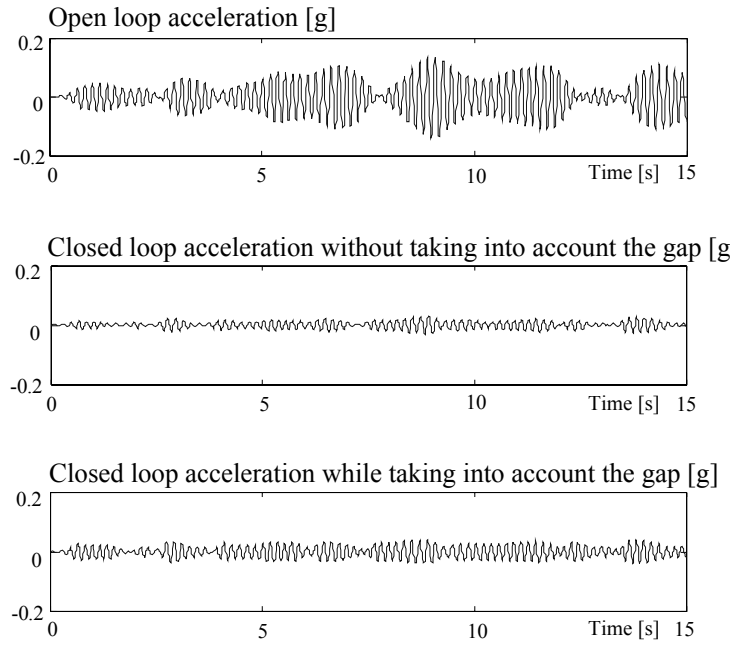

Figure 12.37. *Illustration of the non-linearity of the control*

Note also that the system can become unstable with a certain gain.

This part of the chapter discussed the industrial implementation of an active control system applied to a complex system. The conclusion is that it is necessary and possible to apply simple and efficient control laws.

During the phase in which we were looking for solutions, it was much easier to use an equalizer whose tuning was simple (8^{th} order Butterworth filter). During the phase of industrial development, it was much easier, for manufacture and production implementation, to decrease the order of the equalizer.

Chapter 13

Resonators

13.1. Introduction

In certain cases, it is easier and more efficient to locate anti-vibration systems near the vibration source. The idea is to create another source of vibrations which, if correctly tuned, will cancel out the original vibrations.

The principle is again to use the resonant mass system and its kinetic energy. These masses are coupled to the vibrating source either by kinematic coupling or via a very flexible link.

13.2. Kinematic coupling

13.2.1. *Pendular masses*

13.2.1.1. *Principle*

On certain helicopters, the blades are joined together on the hub at the hard point. Because of the multiple frequencies generated by the number of blades and rotational frequency, there is a risk of dynamic amplification, caused by the proximity of a blade mode to a rotor harmonic. This dynamic amplification may cause dynamic loads at the rotor hub, which are at the source of vibrations (see Chapter 3). In order to reduce these excitations, dynamic absorbers are positioned on the blades. Figure 13.1 shows the pendular system for absorbing the vertical blade vibrations (flapping) (see Chapters 3 and 4).

Figure 13.1. *Position of flapping pendulum. Photo: Eurocopter*

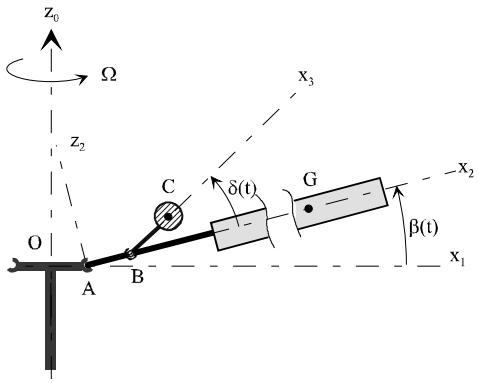

Figure 13.2. *Modeling of flapping pendulums*

13.2.1.2. *Modeling*

The model used to design the pendular system is illustrated in Figure 13.2.

Let:

$$\begin{aligned} \overrightarrow{OA} &= e\ \vec{x}_1 & \overrightarrow{AB} &= 1\ \vec{x}_2 \\ \overrightarrow{AG} &= r\ \vec{x}_2 & \overrightarrow{BC} &= d\ \vec{x}_3 \end{aligned} \qquad [13.1]$$

where:

– M is the mass of the blade,

– m is the flapping mass,

– I is the inertia of the flapping mass at its center.

If we first isolate the blade and flapping mass together and then the flapping mass alone, for small movements, we obtain the following equations of motion:

$$\begin{bmatrix} E & D \\ D & A \end{bmatrix} \begin{bmatrix} \ddot{\beta} \\ \ddot{\delta} \end{bmatrix} + \Omega^2 \begin{bmatrix} G & B \\ B & B \end{bmatrix} \begin{bmatrix} \beta \\ \delta \end{bmatrix} = \begin{bmatrix} C(t) \\ 0 \end{bmatrix} \qquad [13.2]$$

where:

$$\begin{aligned} A &= m\ d^2 & E &= I + m(1+d)^2 \\ B &= M\ d\ (e+l+d) & D &= M\ d(1+d) \\ G &= (M\ r\ (r+e) + m\ (e+l+d)\ (1+d)) \end{aligned} \qquad [13.3]$$

and:

– Ω is the speed of rotation,

– δ is the flap angle of the pendulum,

– β is the flap angle of the blade.

For a harmonic excitation of the form:

$$C(t) = C_0\ \cos(n\ \Omega\ t) \qquad [13.4]$$

we show that the response has the form:

$$\begin{cases} \delta(t) = \delta_0\ \cos(n\ \Omega\ t\ +\ \varphi_\delta) \\ \beta(t) = \beta_0\ \cos(n\ \Omega\ t\ +\ \varphi_\beta) \end{cases} \qquad [13.5]$$

The flap amplitude is defined by:

$$\beta_0 = \frac{\left(B - n^2 A\right) C_0}{\left[\left(G - n^2 E\right)\left(B - n^2 A\right) - (B - n^2 D)^2\right] \Omega^2} \qquad [13.6]$$

The response, for the n harmonics, is given in Figure 13.3.

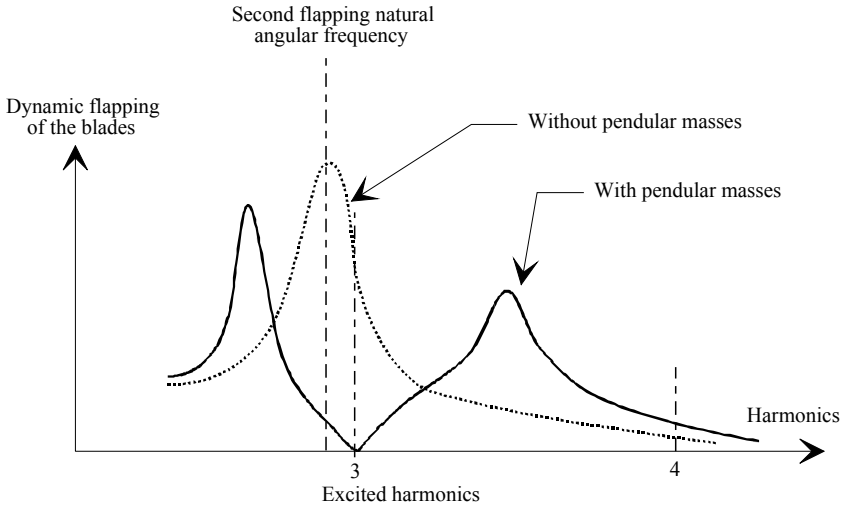

Figure 13.3. *Plot of the transfer function for blade flapping*

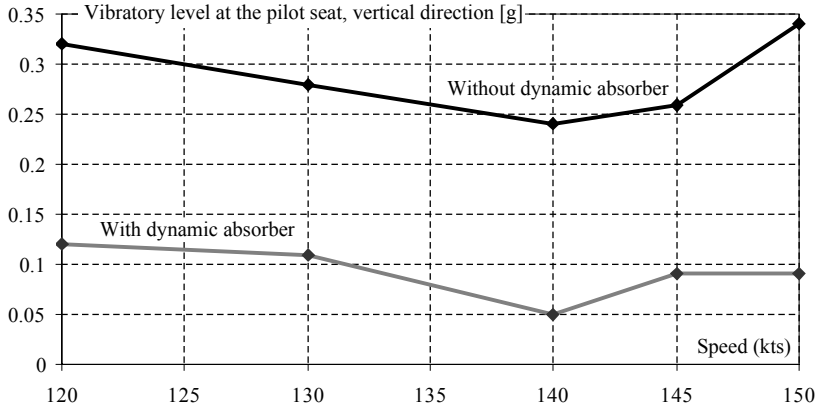

Figure 13.4. *Vibration measurements with rotor head pendulum*

The transfer function shows that the amplitude can be cancelled by choosing appropriately sized pendulums.

This condition requires that:

$$n = \sqrt{\frac{e + l + d}{d}} \qquad [13.7]$$

Without pendulums, the resonance angular frequency is:

$$\omega_r = \Omega \sqrt{\frac{M\ r(r+e)}{I}} \qquad [13.8]$$

13.2.1.3. *Analysis of the results*

The efficiency of the system (see Figure 13.4) is determined by measuring the vibrations in the cabin.

13.2.2. *Coplanar resonators*

This system is employed in certain devices to block the in-plane vibrations. Since the degree of freedom of the pendulums is in the plane of rotation, the principle is the same.

There are two types of resonators: a single wire and a two-wire resonator. The principle of the single wire resonator is shown in Figure 13.5.

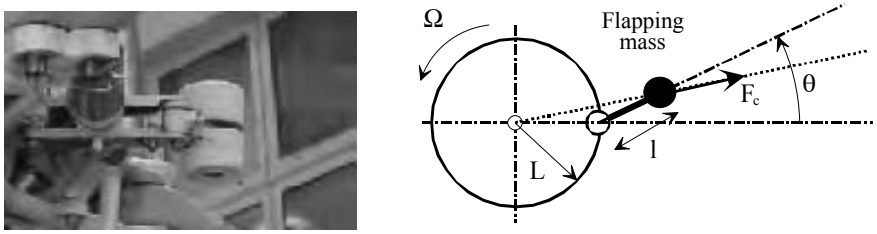

Figure 13.5. *Single wire resonator.*
Photo: Eurocopter

For this type of resonator, the angular frequency ω_p of the resonator must be matched to the harmonic n that we want to filter out in the rotating coordinates. This condition is expressed by:

$$\frac{\omega_p}{\Omega} = n = \sqrt{\frac{m1(1+L)}{\left(I + ml^2\right)}} \qquad [13.9]$$

where:

– m is the flapping mass,

– I is the inertia of the pendulum with respect to its hinge point,

– l is the lever arm of the pendulum,

– L is the distance of the pendulum with respect to the axis of rotation,

– Ω is the rotor speed.

In most practical applications on a helicopter with b blades, this type of pendulum is adjusted to the harmonics (b–1) Ω (see Chapter 3). This type of system is limited to a helicopter with a small number of blades.

Figure 13.6 shows that the pendulum can be adjusted for a harmonic of less than 3Ω. For higher harmonics, it will be necessary to reduce the inertia I, which also means decreasing the mass. The efficiency of the pendulum is thus diminished.

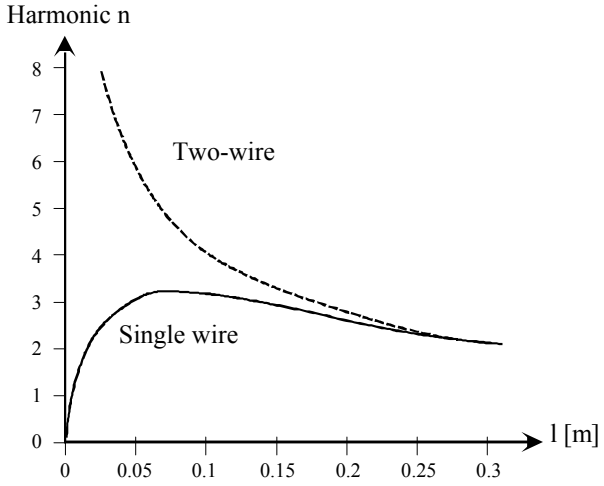

Figure 13.6. *Comparison between the adjustment capabilities of single wire and two-wire resonators*

In order to overcome this limitation, we will use a two-wire resonator whose working principle is illustrated in Figure 13.7.

The natural frequency ω of the two-wire resonator is independent of the mass and inertia, and depends only on geometric parameters.

$$\frac{\omega}{\Omega} = n = \sqrt{\frac{L-(D-d)}{D-d}} \qquad [13.10]$$

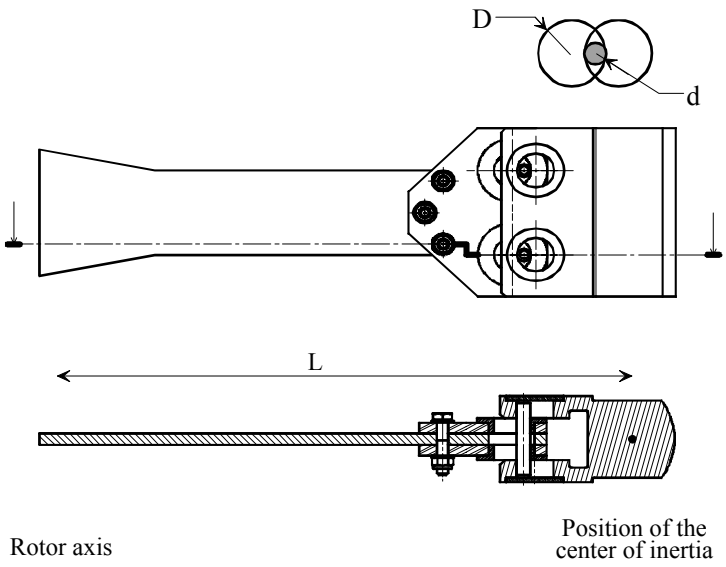

Figure 13.7. *Two-wire resonator*

As shown in Figure 13.6, this system can be tuned to higher harmonics than those of the single wire resonator.

13.3. Stiffness coupling

13.3.1. *Principle*

In a rotating structure, the stator is often excited by the rotor via, for example, inertial effects, such as unbalance, or other effects, such as the aerodynamic asymmetry of the blades or flaps.

The idea is to position a resonator on the rotor to generate loads that oppose the excitation loads.

The originality of this type of resonator is that the resonator is in a rotating system in order to control the vibrations on the non-rotating structure.

In the case of a helicopter, the resonant mass is positioned on the axis of the rotor hub. It is supported by three springs which allow it to vibrate in a plane perpendicular to the axis of rotation.

Figure 13.8. *Example of a two-wire resonator. Photo: Eurocopter*

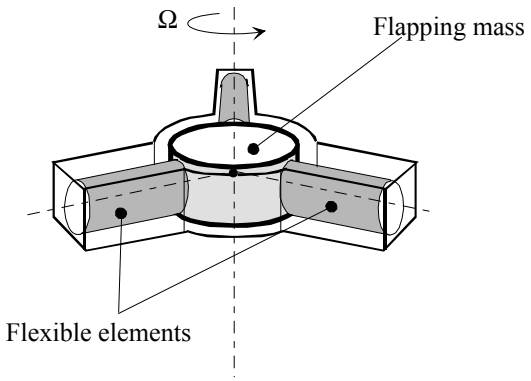

Figure 13.9. *Principle of the rotor head resonator*

Figure 13.10. *Implementation of a system at the rotor head. Photo: Eurocopter*

13.3.2. *Modeling*

The motion of the counterweight is mainly in-plane, so the system will generate in-plane loads to eliminate the in-plane vibrations.

The model necessary to determine the behavior of the system is shown in Figure 13.11.

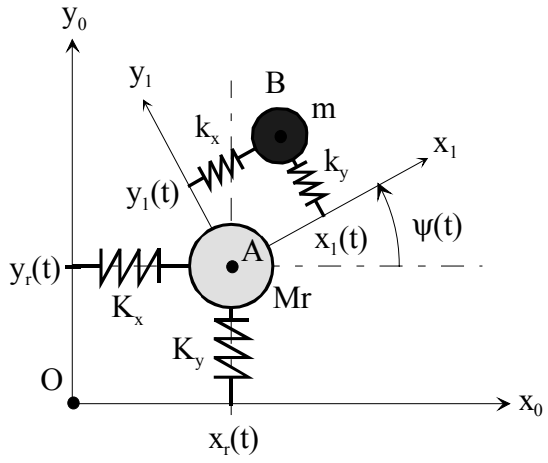

Figure 13.11. *Modeling of a rotor head resonator*

For this model, let:

– R_o be the frame of reference of the fuselage (Galilean relativity),

– R_1 be the frame of reference in the rotating system,

– M_r be the mass of the rotating part (rotor),

– m be the flapping mass of the resonator.

The system is designed for the phase in which the speed of rotation of the rotor is constant. We introduce the speed of rotation Ω:

$$\dot{\psi}(t) = \Omega \qquad [13.11]$$

We assume that the masses of the two bodies are concentrated masses. Lagrange equations will be used in order to establish the equations of the system.

We define a system S containing the rotor and the flapping mass. The calculation of the kinematic energy of the system is given by:

$$T(\Sigma / R_0) = T(\text{rotor} / R_0) + T(\text{counterweight} / R_0) \qquad [13.12]$$

or:

$$T(\Sigma / R_0) = \frac{1}{2} m \, \vec{V}^2_{B,2/R_0} + \frac{1}{2} M_r \, \vec{V}^2_{A,1/R_0} \qquad [13.13]$$

The speeds are calculated as follows:

$$\vec{V}_{A,1/R_0} = \left.\frac{d\overrightarrow{OA}}{dt}\right)_0 = \dot{x}_r \vec{x}_0 + \dot{y}_r \vec{y}_0 \qquad [13.14]$$

and:

$$\vec{V}_{B,2/R_0} = \left.\frac{d\overrightarrow{OB}}{dt}\right)_0 = \dot{x}_r \, \vec{x}_0 + \dot{y}_r \, \vec{y}_0 + \dot{x} \, \vec{x}_1 + \dot{y} \, \vec{y}_1 + x \, \dot{\psi} \, \vec{y}_1 - y \, \dot{\psi} \, \vec{x}_1 \qquad [13.15]$$

Thus, the kinetic energy is expressed by:

$$\begin{aligned} T\left(\Sigma/R_0\right) = \frac{1}{2}m\Big[& \dot{x}^2 + \dot{y}^2 + \dot{x}_r^2 + \dot{y}_r^2 + \left(x^2 + y^2\right)\Omega^2 + \ldots \\ & \ldots + 2\dot{x}_r(\dot{x} - y\Omega)\cos(\psi) + 2\dot{y}_r(\dot{y} + x\Omega)\cos(\psi) + \ldots. \\ & \ldots - 2\dot{x}_r(\dot{y} + x\Omega)\sin(\psi) + 2\dot{y}_r(\dot{x} - y\Omega)\sin(\psi)\Big] \\ & + \frac{1}{2}M_r\left(\dot{x}_r^2 + \dot{y}_r^2\right) \end{aligned} \qquad [13.16]$$

The external actions to be allowed for in this model are the actions of the springs, which are integrated via their potential function:

$$U(\text{spring}/R_0) = \frac{1}{2}\left(k_x\ x^2 + k_y\ y^2 + K_x\ x_r^2 + K_y\ y_r^2\right) \qquad [13.17]$$

The effects of the weight are negligible on the effects studied.

For each parameter, we can write with the help of Lagrange's formalism:

$$\frac{d}{dt}\left(\frac{\partial T\left(\Sigma/R_0\right)}{\partial q_i}\right) - \frac{\partial T(\Sigma/R_0)}{\partial q_i} + \frac{\partial U(\text{spring}/R_0)}{\partial q_i} = 0 \qquad [13.18]$$

The equation system obtained can be written as a matrix where:

$$X = \left\{x \quad y \quad x_r \quad y_r\right\}^T \qquad [13.19]$$

Then:

$$M\,\ddot{X} + C\,\dot{X} + K\,X = \left[0\right] \qquad [13.20]$$

where:

$$M = \begin{bmatrix} m & 0 & m\cos\psi & m\sin\psi \\ 0 & m & -m\sin\psi & m\cos\psi \\ m\cos\psi & -m\sin\psi & M_r + m & 0 \\ m\sin\psi & m\cos\psi & 0 & M_r + m \end{bmatrix} \qquad [13.21]$$

$$C = \begin{bmatrix} 0 & -2m\Omega & 0 & 0 \\ 2m\Omega & 0 & 0 & 0 \\ -2m\Omega\sin\psi & -2m\Omega\cos\psi & 0 & 0 \\ 2m\Omega\cos\psi & -2m\Omega\sin\psi & 0 & 0 \end{bmatrix} \quad [13.22]$$

$$K = \begin{bmatrix} k_x - m\Omega^2 & 0 & 0 & 0 \\ 0 & k_y - m\Omega^2 & 0 & 0 \\ -m\Omega^2\cos\psi & m\Omega^2\sin\psi & K_x & 0 \\ -m\Omega^2\sin\psi & -m\Omega^2\cos\psi & 0 & K_y \end{bmatrix} \quad [13.23]$$

For the obtained parametric transformation, the equations do not have constant coefficients and are strongly coupled. The following transformation of variables is applied:

$$\begin{cases} x(t) = \cos(\psi(t))u(t) + \sin(\psi(t))v(t) \\ y(t) = -\sin(\psi(t))u(t) + \cos(\psi(t))v(t) \end{cases} \quad [13.24]$$

Let:

$$X_1 = \{u \quad v \quad x_r \quad y_r\}^T$$

hence, we obtain:

$$M_1\,\ddot{X}_1 + C_1\,\dot{X}_1 + K_1\,X_1 = [0] \quad [13.25]$$

where:

$$M_1 = \begin{bmatrix} m & 0 & m & 0 \\ 0 & m & 0 & m \\ m & 0 & m + M_r & 0 \\ 0 & m & 0 & m + M_r \end{bmatrix} \quad [13.26]$$

$$C_1 = [0] \quad [13.27]$$

$$K_1 = \begin{bmatrix} k_x \cos^2\psi + k_y \sin^2\psi & (k_x - k_y)\sin\psi\cos\psi & 0 & 0 \\ (k_x - k_y)\sin\psi\cos\psi & k_x \cos^2\psi + k_y \sin^2\psi & 0 & 0 \\ 0 & 0 & K_x & 0 \\ 0 & 0 & 0 & K_y \end{bmatrix} \quad [13.28]$$

This new layout decouples the stiffness of the two sub-systems. Full decoupling of all stiffness parameters is achieved when k_x and k_y are equal.

This condition is verified if we take into consideration technological precautions related to the sizing of the springs.

In these conditions, the stiffness matrix is given by:

$$K_1 = \begin{bmatrix} k_x & 0 & 0 & 0 \\ 0 & k_x & 0 & 0 \\ 0 & 0 & K_x & 0 \\ 0 & 0 & 0 & K_y \end{bmatrix} \quad [13.29]$$

For the longitudinal in-plane motion, the equations can have the following form:

$$\begin{bmatrix} m & m \\ m & m + M_r \end{bmatrix} \begin{bmatrix} \ddot{u} \\ \ddot{x}_r \end{bmatrix} + \begin{bmatrix} k_x & 0 \\ 0 & K_x \end{bmatrix} \begin{bmatrix} u \\ x_r \end{bmatrix} = \begin{bmatrix} 0 \\ 0 \end{bmatrix} \quad [13.30]$$

Similarly, the lateral in-plane motion is given by:

$$\begin{bmatrix} m & m \\ m & m + M_r \end{bmatrix} \begin{bmatrix} \ddot{v} \\ \ddot{y}_r \end{bmatrix} + \begin{bmatrix} k_x & 0 \\ 0 & K_y \end{bmatrix} \begin{bmatrix} v \\ y_r \end{bmatrix} = \begin{bmatrix} 0 \\ 0 \end{bmatrix} \quad [13.31]$$

13.3.3. *Forced response of the system*

Assuming the rotor is subjected to an in-plane load of the form:

$$F(t) = F_0 \cos(\omega t) \quad [13.32]$$

Hence, the equation system is given by:

$$\begin{bmatrix} m & m \\ m & m+M_r \end{bmatrix}\begin{bmatrix} \ddot{u} \\ \ddot{x}_r \end{bmatrix}+\begin{bmatrix} k_x & 0 \\ 0 & K_x \end{bmatrix}\begin{bmatrix} u \\ x_r \end{bmatrix}=\begin{bmatrix} 0 \\ F(t) \end{bmatrix} \qquad [13.33]$$

The search for the forced solution is made in the complex plane. Let:

$$F(t) \rightarrow \overline{F}_0 e^{i\,\omega\,t},\ u(t) \rightarrow \overline{u}_0 e^{i\,\omega\,t},\ \overline{x}_r(t) \rightarrow \overline{x}_{r0} e^{i\,\omega\,t} \qquad [13.34]$$

Hence, we obtain:

$$\left(-\omega^2\begin{bmatrix} m & m \\ m & M_r+m \end{bmatrix}+\begin{bmatrix} k_x & 0 \\ 0 & K_x \end{bmatrix}\right)\begin{Bmatrix} \overline{u}_0 \\ \overline{x}_{r0} \end{Bmatrix}=\begin{Bmatrix} 0 \\ \overline{F}_0 \end{Bmatrix} \qquad [13.35]$$

The solutions of this system are:

$$\begin{cases} \overline{u}_0 = \dfrac{\overline{F}_0 m\omega^2}{(k_x - m\omega^2)(K_x-(M_r+m)\omega^2)-(m\omega^2)^2} \\ \overline{x}_{r0} = \dfrac{\overline{F}_0 (k_x - m\omega^2)}{(k_x - m\omega^2)(K_x-(M_r+m)\omega^2)-(m\omega^2)^2} \end{cases} \qquad [13.36]$$

13.3.4. *Analysis of the results*

We will try to cancel the vibrations at point A; in other words, we will try to ensure that $\overline{x}_{r0} = 0$ at all times.

$\overline{x}_{r0} = 0$, which implies that $k_x - m\omega^2 = 0$ if $\omega = \sqrt{\dfrac{k}{m}} = \omega_r$.

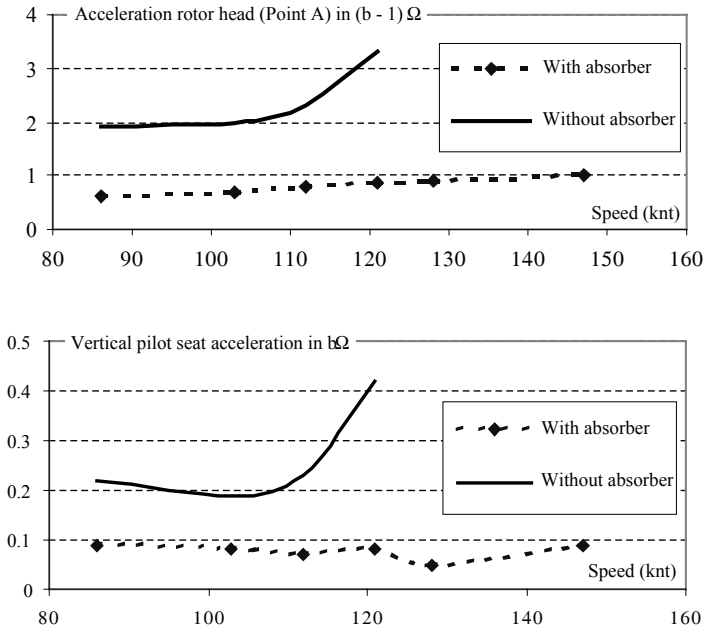

Figure 13.12. *Measured efficiency of the rotor resonator*

Hence, the displacement of the counterweights is:

$$\bar{u}_0 = \frac{\bar{F}_0 m\omega_r^2}{-(m\omega_r^2)^2} = \frac{\bar{F}_0}{m\omega_r^2} \quad \text{let} \qquad \bar{u}_0 = -\frac{\bar{F}_0}{k_x}$$

The "-ve" sign in the expression for $\bar{u}_0$ indicates that the anti-vibrator motion and the blade-induced excitation are of opposite phase (anti-resonance mode). The theoretical study of this simplified system showed that the opposite phase displacement of the resonator stopped the in-plane motion of the rotor for an excitation angular frequency $\omega = \omega_r$ (natural angular frequency of the resonator), and that, irrespective of the natural angular frequency of the structure ω_x:

$$\omega_x = \sqrt{\frac{K_x}{M_r}} \text{ or } \sqrt{\frac{K_y}{M_r}} \qquad [13.37]$$

Figure 13.12 shows the efficiency of such a system on a helicopter.

Chapter 14

Self-Adapting Resonators

14.1. Introduction

Self-adapting systems may be used to improve the performance of the passive systems described in the last chapter. Self-adapting systems are capable of adjusting to changes in the excitation frequency.

We will take the example of the hub resonator system presented in Chapter 13.

14.2. *Acting near the source: hub resonator*

The hub resonator of a helicopter consists of a flapping mass that vibrates in a plane perpendicular to the axis of rotation of the rotor. It is supported by three flexible elements indexed at 120º. The stiffness of these elements is designed so that the resulting anti-resonance corresponds to the excitation frequency. In this application, the stiffness is adjusted to eliminate, at a fixed point, the excitation at bΩ, where b is the number rotor blades and Ω the rotational speed of the rotor.

14.2.1. *Principle*

The principle of the self-adapting resonator is to add a mobile mass that slides along the rotor axis. The inertia of the assembly varies with the position z of the mass and thus the anti-resonance frequency also varies.

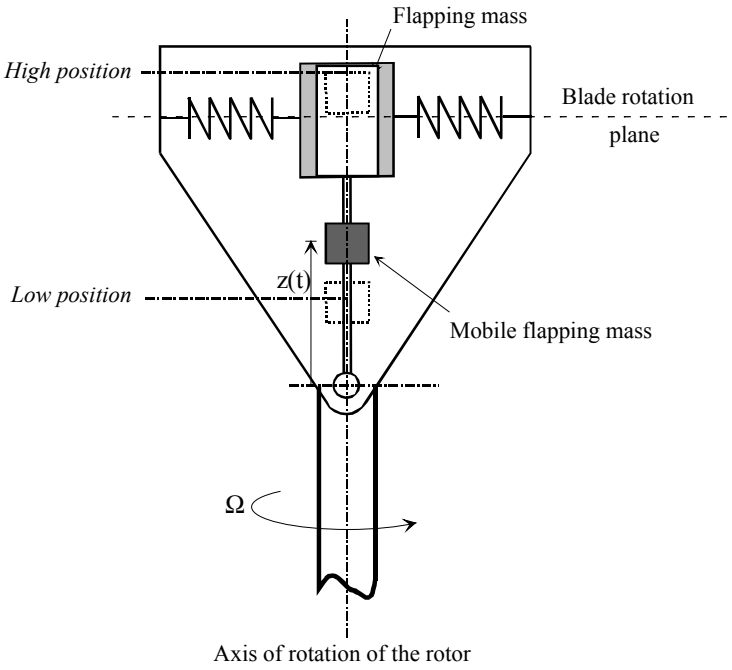

Figure 14.1. *Principle of self-adapting resonator*

By analyzing the vibratory level, it is possible to determine the required position of this supplementary mass, which is moved by an actuator.

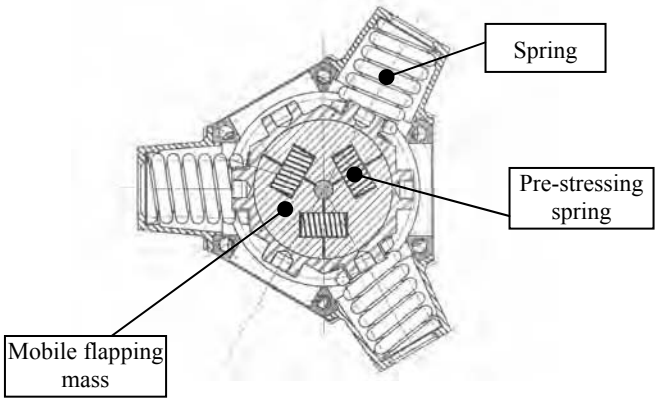

Figure 14.2. *Self-adjusting hub resonator*

The formulation of the system equations is based on the modeling outlined in Figure 14.3.

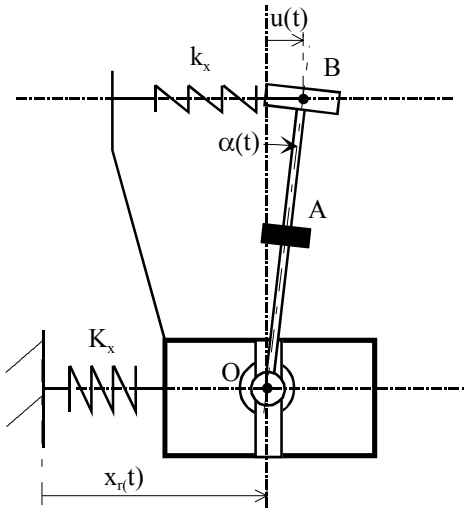

Figure 14.3. *Modeling of the hub for a self-adapting resonator*

Let:

– M_r be the equivalent mass of the structure,

– K_x be the equivalent stiffness of the structure,

– k_x be the in-plane stiffness of the resonator,

– m be the fixed mass of the resonator,

– μ be the mobile mass of the resonator.

Let:

$$d(OA) = z(t)$$
$$d(OB) = h \qquad [14.1]$$

In reality, the resonator balljoint has some degrees of movement. For small motion, the following equations of motion are obtained:

$$\begin{bmatrix} m_e & m_l \\ m_l & M_r + m + \mu \end{bmatrix} \begin{bmatrix} \ddot{u} \\ \ddot{x}_r \end{bmatrix} + \begin{bmatrix} k_x & 0 \\ 0 & K_x \end{bmatrix} \begin{bmatrix} u \\ x_r \end{bmatrix} = \begin{bmatrix} 0 \\ F(t) \end{bmatrix} \qquad [14.2]$$

where:

$$\begin{cases} m_e = m + \mu\left(\frac{z}{h}\right)^2 \\ m_l = m + \mu\left(\frac{z}{h}\right) \end{cases} \quad [14.3]$$

To cancel the fuselage displacement [x_r], the following condition must be satisfied:

$$k_x - \omega^2 m_e = 0 \quad [14.4]$$

The excitation angular frequency is $b\Omega$, which yields:

$$Z(\Omega) = h\sqrt{\frac{m}{\mu}}\sqrt{\left(\frac{k_x}{m\,(b\Omega)^2} - 1\right)} \quad [14.5]$$

where:

– b is the number of rotor blades,

– Ω is the rotational speed of the rotor.

By applying the relation, the law required to achieve anti-resonance at the harmonic b can be established versus the rotational speed Ω. It is seen that the law is almost linear in the system's operating range.

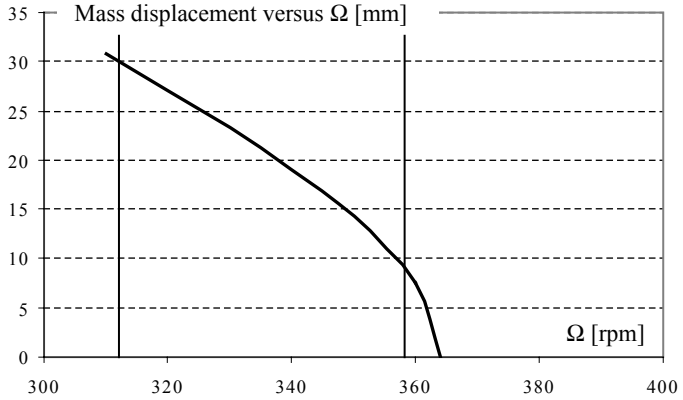

Figure 14.4. *Linearity of the anti-shaker hub absorber*

14.2.2. *Control algorithm*

The position of the mobile mass can be controlled in two ways: either by directly measuring the rotational speed Ω of the rotor, or by measuring the overall vibratory level of the structure and then searching, by dichotomy, for the optimum tuning (see Figure 14.5).

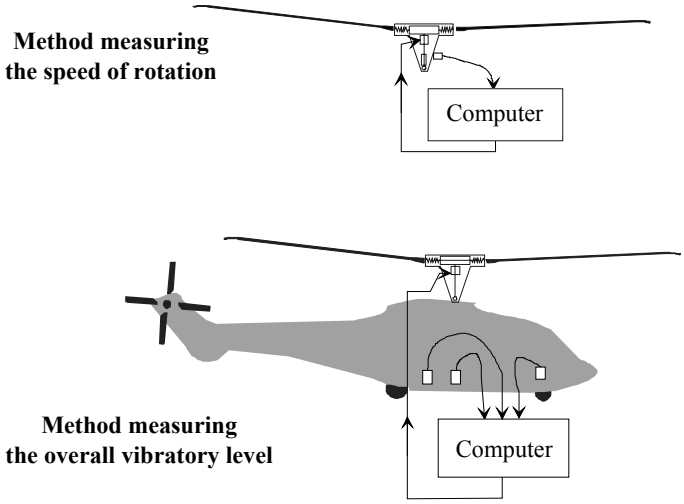

Figure 14.5. *Measuring systems for the self-adapting control of the hub absorber*

14.2.2.1 *Type 1 controller*

For the first method, we use the formulation [14.5]. We measure the rotor speed and the mass position to tune the resonator. The control will therefore be of the open-loop type.

14.2.2.2. *Type 2 controller*

For the second type of controller, the cabin vibrations are measured at different points. The overall vibratory level (OVL), which is based on a minimization criterion, is defined by the quadratic form:

$$\mathrm{OVL} = \sqrt{\frac{\gamma_1^2 + \ldots + \gamma_p^2}{P}} \qquad [14.6]$$

where γ_i is the acceleration in bΩ at the point number i.

The algorithm:

– calculates the vibratory level (OVL) based on p measures,

– displaces the mass in an arbitrary direction,

– analyzes the effect on the vibratory level,

– if the OVL increases, reverses the direction of displacement,

– if the OVL is still significantly high, repeats the process or otherwise stops it.

The displacement step is set experimentally after the efficiency of the system has been tested.

14.2.3. *Experiment*

A test bed can be used to analyze the performance of the Type II control algorithm (measurement of the OVL), as shown in Figure 14.6.

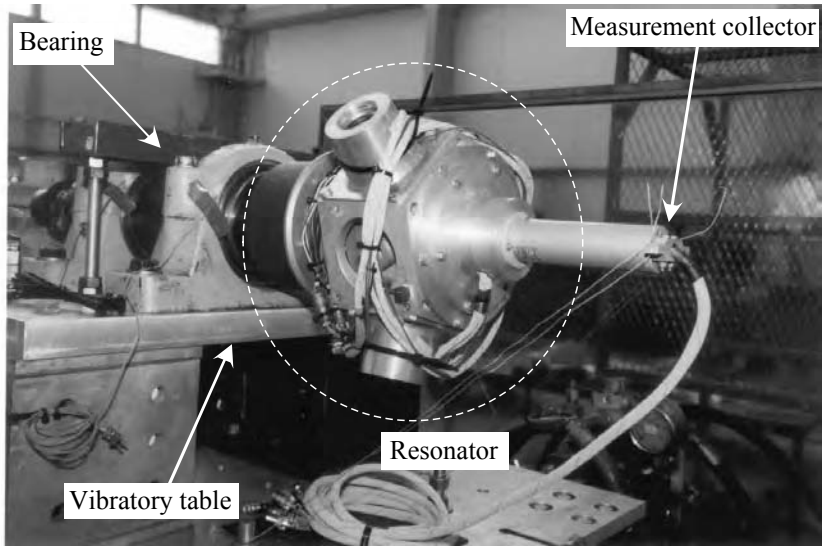

Figure 14.6. *Model of self-adapting head resonator. Photo: Eurocopter*

Figure 14.7 illustrates the efficiency of the system.

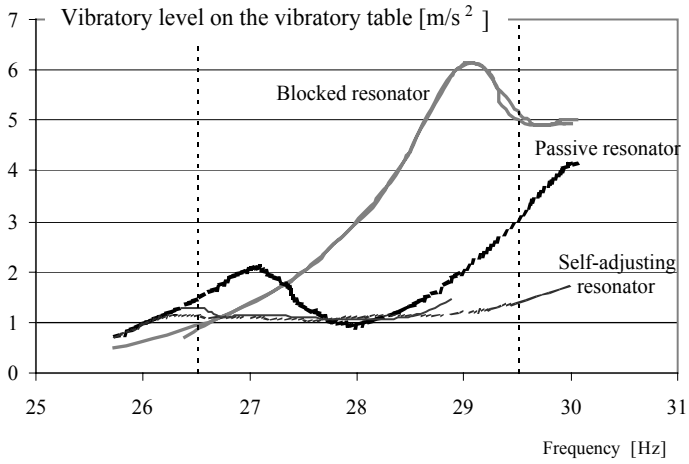

Figure 14.7. *Performance of a self-adapting system on a test bed*

Chapter 15

Active Systems

15.1. Introduction

The rotating part of a structure is a major source of vibrations (see Chapter 3). For some applications, it is possible to act directly on the source with the help of active systems but the actuators must be placed close to the source of the dynamic loads.

For a rotor whose vibrations are generated by the blades or flaps, it is then possible to create a vibratory source based on the behavior of the rotor.

The pitch of the blades on the main rotor of a helicopter can be controlled by a cyclic swashplate or a flap attached to the blade (see Chapter 4).

These controls, referred to as monocyclic, make the piloting of the helicopter possible, and use pitch variations with the following mathematical form:

$$\theta(t) = \theta_0 + \theta_{1c}\cos(\Omega t) + \theta_{1s}\sin(\Omega t) \qquad [15.1]$$

In Chapter 3 we showed that vibrations essentially come from dynamic loads in the rotor hinges, whose harmonics are (b – 1) Ω, (b Ω) and (b + 1) Ω.

– b is the number of blades,

– Ω is the rotation speed of the rotor.

To reduce these vibrations, the blade pitch incidence can be varied at the harmonic frequencies $(b-1)\Omega$, $b\Omega$ and $(b+1)\Omega$. These incidence variations will generate aerodynamic loads at the same harmonic frequencies.

In the last few years, new pitch controls have been created by adding higher order harmonics to the traditional monocyclic control.

This type of control, called "higher harmonic control", has the following form:

$$\theta(t)= \theta_0+ \theta_{1c} \cos(\Omega t)+ \theta_{1s} \sin(\Omega t) \text{ (monocyclic control)}$$

$$\ldots+ \sum_{n=2}^{k} \theta_{nc} \cos(n\Omega t) + \theta_{ns} \sin(n\Omega t) \text{ (higher harmonic control)} \qquad [15.2]$$

There are several methods for applying higher harmonic control to a rotor:

– the active system is in a fixed frame of reference and uses the classic cyclic swashplate (HHC, Higher Harmonic Control). With this system, the control can be introduced for vibrations at $(b-1)\Omega$, $b\Omega$, $(b+1)\Omega$, as shown in equation [15.3]:

$$\begin{aligned}\theta(t) = {} & \theta_0 + \theta_{1c} \cos(\Omega t) + \theta_{1s} \sin(\Omega t) \\ & \ldots + \theta_{b\Omega-1} \cos(\Omega t) + \theta_{b\Omega-1} \sin(\Omega t) \\ & \ldots + \theta_{b\Omega} \cos(\Omega t) + \theta_{b\Omega} \sin(\Omega t) \\ & \ldots + \theta_{b\Omega+1} \cos(\Omega t) + \theta_{b\Omega+1} \sin(\Omega t)\end{aligned} \qquad [15.3]$$

– the system is in a rotating frame of reference:

- by directly controlling the pitch individually for each blade (Individual Blade Control(IBC)),

- by using active flaps in the rotating frame of reference (Active Flaps).

The system in the rotating frame of reference has the advantage of being able to input controls, on the rotor, for all the rotor harmonics (see equation [15.2]).

15.2. Principle of the active system in the fixed frame of reference

15.2.1. *Principle*

The principle of higher harmonic control will be illustrated by an experimental system tested on the three-bladed Gazelle helicopter (see Figure 15.1) [ACH 86a, ACH 86b, KUB 93, POL 90, POW 78, ROE 93].

Figure 15.1. *Gazelle experimental helicopter equipped with higher harmonic controls. Photo: Eurocopter*

On a helicopter with a three-bladed rotor, the preponderant vibration frequency in the airframe is at 3Ω. These vibrations are caused by cyclic loads at a frequency of 3Ω about the rotor axis, transmitted directly to the airframe, and by loads at frequencies of 2Ω and 4Ω in the rotor plane, transmitted to the airframe, after transformation of the frame of reference, at a frequency of 3Ω (see Chapter 3).

Controls in series with the flight controls at a frequency of 3Ω generate loads at 2Ω, 3Ω and 4Ω on the rotor, which can be opposite in phase to the loads generating the vibrations (see Figure 15.2).

The role of the higher harmonic control system is to determine the transfer function between higher harmonic controls and the vibrations (variable according to the type of flight and the configuration of the device), so that the modulus and phase of each of the three optimal controls to be applied to the higher harmonic actuators can be calculated and the vibrations in the airframe decreased. The corresponding flowchart is shown in Figure 15.2.

The Fourier coefficients for the preponderant frequency (i.e. 3Ω) of the vibration measurements are extracted by harmonic analysis. Based on these data and on the knowledge of previous higher harmonic controls, the digital computer calculates the modulus and phases of the three higher harmonic controls. These values are transformed by the synthesizer into three sinusoidal signals at a frequency of 3Ω, and fed to the higher harmonic actuators.

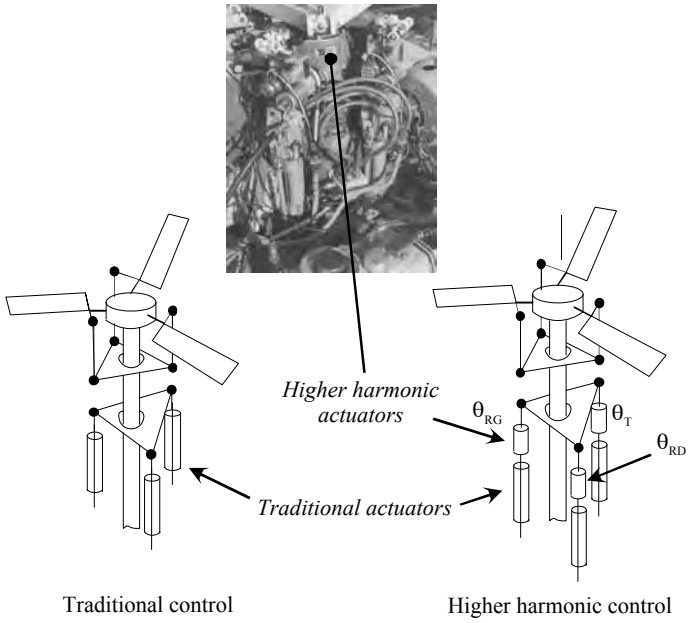

Figure 15.2. *Principle of higher harmonic control*

15.2.2. *Control algorithm*

There are several control algorithms. They are based on the linear representation of the transfer between higher harmonic controls and the vibrations of the airframe.

In a digital computer, calculation algorithms generate the optimal control vector θ, based on the vibration vector Z coming from the computer carrying out the harmonic analysis (the component of vibrations in 3Ω) (see Figure 15.3).

In order to obtain the lowest vibratory level, higher harmonic control must generate a vibratory level of the blades that opposes the natural level. The criterion

used is an overall vibratory level (OVL) corresponding to the root mean square of the 3Ω component measured by the system sensors:

$$OVL = \sqrt{\frac{Z_{accl}^2 + Z_{acc2}^2 + Z_{acc3}^2}{3}} \qquad [15.4]$$

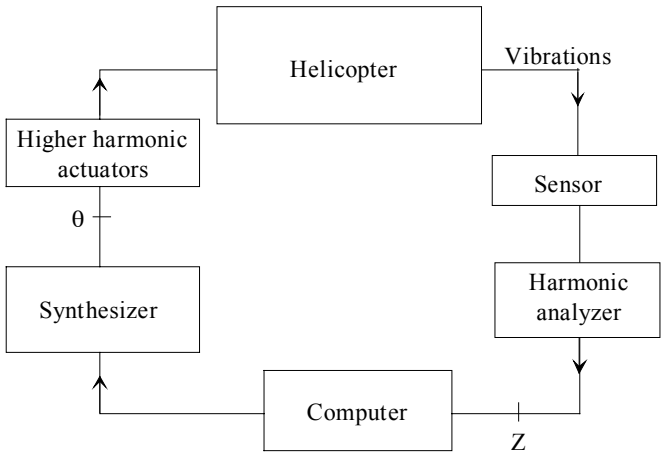

Figure 15.3. *Flowchart for calculating the higher harmonic control*

Sensors measure the vibratory levels (Z_{acc1}, Z_{acc2}, Z_{acc3}) at different points of the cabin.

At a given time t_k, a harmonic analyzer is used to identify the components of accelerations Z_i defined by:

$$\begin{aligned} Z_{ac1} &= Z_1 \cos(3\Omega t) + Z_2 \sin(3\Omega t) \\ Z_{ac2} &= Z_3 \cos(3\Omega t) + Z_4 \sin(3\Omega t) \\ Z_{ac3} &= Z_5 \cos(3\Omega t) + Z_6 \sin(3\Omega t) \end{aligned} \qquad [15.5]$$

To determine the control input to the rotor, it is necessary to identify the vibratory response of the structure to the control input θ by introducing the sensitivity matrix S, which is defined as follows:

$$Z_{k+1} = S\,\theta_k + Z_0 \qquad [15.6]$$

where:

– Z_0 is the vector of 2n Fourier coefficients at 3Ω, corresponding to n acceleration measurements without higher harmonic control,

– Z_{k+1} is the measuring vector at the pitch k+1, after higher harmonic control,

– θ_K is the vector of 6 Fourier coefficients at 3Ω corresponding to the controls applied to 3 actuators at the pitch k,

– S is the representative sensitivity matrix of the vibratory vector to the higher harmonic control vector (size: 2 lines, 3 columns).

The matrix is defined as follows:

$$\begin{pmatrix} Z_1 \\ Z_2 \\ Z_3 \\ Z_4 \\ Z_5 \\ Z_6 \end{pmatrix}_{k+1} = \begin{pmatrix} S_{11} S_{12} \text{ - - - - - - - } S_{16} \\ \\ \\ \\ \\ S_{61} \text{ - - - - - - - - - } S_{66} \end{pmatrix} \begin{pmatrix} \theta_1 \\ \theta_2 \\ \theta_3 \\ \theta_4 \\ \theta_5 \\ \theta_6 \end{pmatrix}_k + \begin{pmatrix} Z_1 \\ Z_2 \\ Z_3 \\ Z_4 \\ Z_5 \\ Z_6 \end{pmatrix}_0 \qquad [15.7]$$

After identifying the parameters of matrix S and calculating the optimal control vector θ, the digital computer sends higher harmonic signals to the blade pitch lever via booster controls.

The injected control is thus given by:

$$\begin{aligned} \theta_{RG} &= \theta_1 \cos(3\Omega t) + \theta_2 \sin(3\Omega t) \\ \theta_{RD} &= \theta_3 \cos(3\Omega t) + \theta_4 \sin(3\Omega t) \\ \theta_T &= \theta_5 \cos(3\Omega t) + \theta_6 \sin(3\Omega t) \end{aligned} \qquad [15.8]$$

where (see Figure 15.2):

– θ_{RG} is the left roll input,

– θ_{RD} is the right roll input,

– θ_T is the pitch input.

The control algorithm:

– identifies the matrix S at all times since it depends on the flight conditions and the configuration of the device. The identification of Z_0 is not required, provided the optimal control is calculated iteratively using the local model [15.6];

– calculates the optimal control vector θ_k.

The control vector θ_k is calculated at each step by minimizing a quadratic criterion (see Chapter 9).

15.2.3. *Experiment*

This system was tested on the Gazelle 349 helicopter. The experimental results showed a high reduction of the natural vibration level in all flight phases.

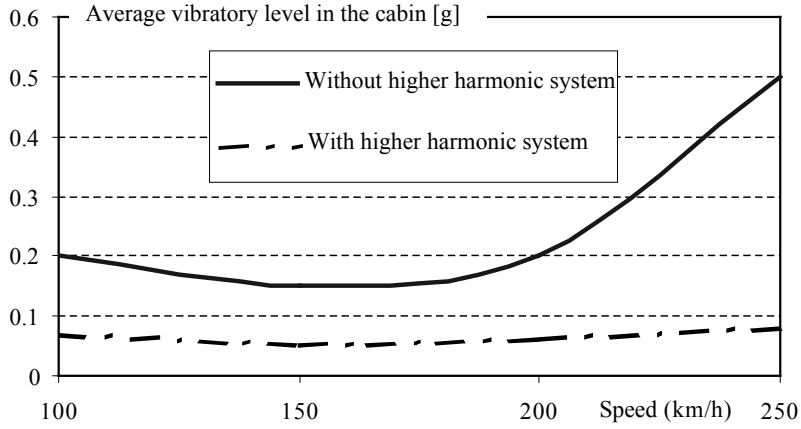

Figure 15.4. *Results from flights with higher harmonic control*

The performance comparison between the active vibration control system and the passive suspension of the Gazelle 349 shows that, for equivalent vibration levels, the active system is more efficient than the passive system.

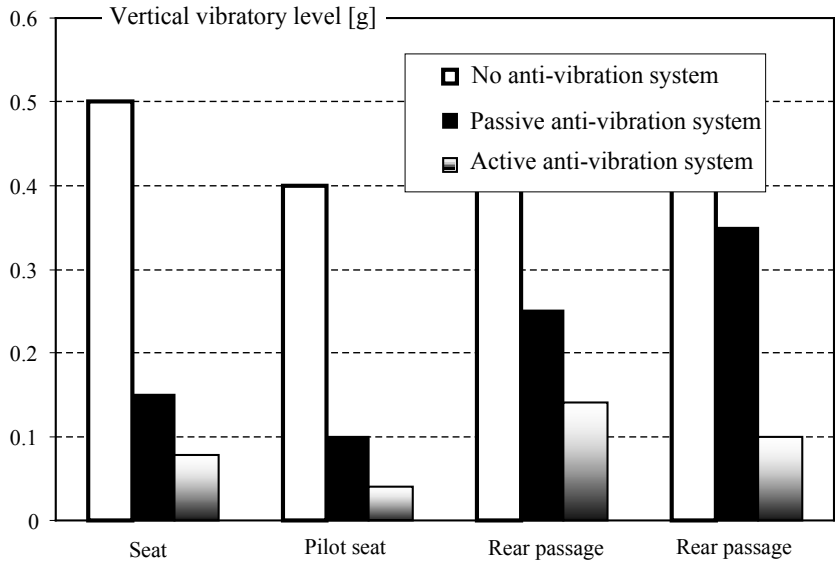

Figure 15.5. *Comparison with a passive anti-vibration system*

15.2.4. *Conclusions*

A higher harmonic control system is specific to the helicopter. Through direct action on the blade pitch control, the system minimizes the vibrations induced in the structure. When tested on the Gazelle 349 helicopter, a 90% decrease of the natural vibratory level was achieved in all the flight phases.

For a three-bladed helicopter, higher harmonic control can:

– reduce the aerodynamic stall of the blades, and thereby minimize the power required in forward flight, or increase the rotor lift to match the flight phase,

– decrease the impulsive noise due to blade interaction.

15.3. Principle of the active system in a rotating frame of reference

15.3.1. *Introduction*

A second method of actively controlling the rotor is control in a rotating frame of reference. With this control, it is possible to manage the vibrations, the acoustic

emissions, and the performance of rotors with more than three blades. We will present two technological systems developed with active blade control:

– the IBC (Individual Blade Control), [BEB 02, KUB 92, KUB 93, NIE 94, PRE 92, ROT 01, SCH 97, SCHI 98, SCHO 98, SPE 91, SWA 94, SWA 95, TEV 95],

– blades with piezoelectric actuator flaps.

The external noise is mainly due to the acoustic emission of the blades, called Blade Vortex Interaction (BVI) noise and created in flight by the interaction of the vortex created by the tip of a blade with the passage of the next blade. This usually happens during the landing of a helicopter, when it descends in its own wake.

Some vibrations transmitted by the rotor – especially at low frequencies (< 100 Hz) – are felt by passengers. They are generated by the vibrations of the helicopter blades. The most uncomfortable of these vibrations are at frequencies of $(b - 1)\Omega$, $b\Omega$ and $(b + 1)\Omega$.

Figure 15.6 presents two blade pressure curves measured on two flight configurations. The first plot, during a descent at 65 kts, highlights the peak pressures characteristic of BVI noise that produce blade click. The second plot in forward level flight at 110 kts shows the pressure components at higher harmonic frequencies (3Ω, 4Ω and 5Ω) that generate vibratory load on the blades, i.e. the source of the vibrations.

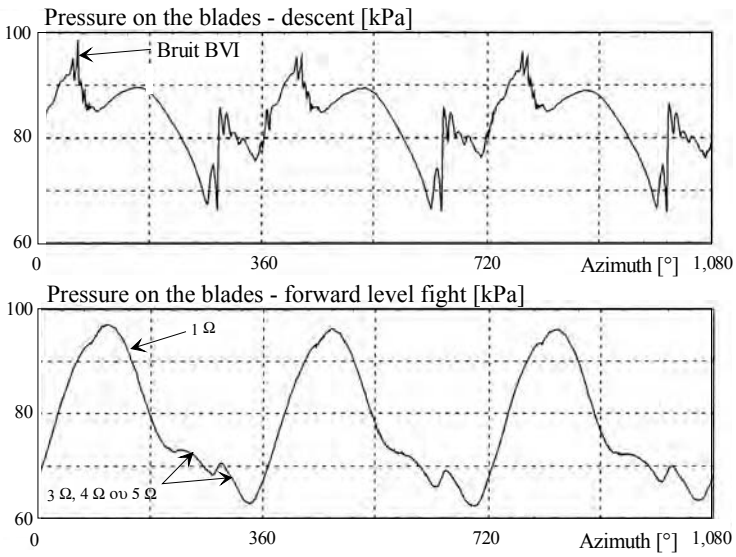

Figure 15.6. *Measurements of the pressure on a blade (BO105 SI)*

We will now present two technological systems which were developed with active blade control:

– individual blade control (IBC),

– blades with piezoelectric actuator flaps.

15.3.2. *Individual blade control*

15.3.2.1. *Principle*

The principle of the IBC system is individualized active control of the helicopter blades using hydraulically driven actuators. The actuators replace the traditional pitch links and act so that every blade can induce a rotor hub load capable of canceling out the natural excitation loads of the rotor.

15.3.2.2. *Design*

The demonstrator using hydraulically operated booster controls is called the BO105 S1 (see Figure 15.7).

Figure 15.7. *IBC BO105 S1 demonstrator in flight.*
Photo: Eurocopter Deutschland

The control system is divided into two groups:

– the hydraulic pump and the electronic equipment installed in the helicopter's cabin,

– the hydraulic actuators with their sensors placed in the rotating system.

This control system is operated by an embedded digital computer and a high-tech signal processing system for data transfer between the rotating system and the non-rotating system. A monitoring system consisting of bending strain gauges installed on the blades and on the mast, blade pressure sensors, microphones installed on the landing gear and several accelerometers makes it possible to control the vibratory load of the hub and the external noise. The IBC system thus works in a closed loop. A safety concept has been developed to satisfy the civil airworthiness requirements.

15.3.2.3. *Hydraulic actuators of the IBC system*

The actuators replace the traditional links between the pitch lever and the cyclic swashplate and are integrated in the main flight control system.

Figure 15.8. *IBC hydraulic actuator. Photo: Eurocopter Deutschland*

The working stroke of the piston can be controlled independently for each actuator over a blade incidence range of $^{+}/_{-}$ 1.1°. To further improve the bandwidth of the four actuators, each is equipped with a local position feedback loop in the time domain ("inner loop"). The piston position is measured by a position sensor inside each actuator. In addition, for control and safety reasons, each actuator is also equipped with a piston speed sensor and an axial force sensor.

15.3.2.4. *Implementation*

The strategies used to control BVI noise and vibrations are different and not correlated; hence, to decrease both at the same time would imply pursuing two objectives, which are not necessarily compatible. The architecture of the system is

therefore based on two task loops, connected in parallel: one in charge of controlling the BVI noise and the other in charge of controlling the vibrations. We will present here the vibration control system.

All the tests conducted in flight on the BO105 S1 showed that the loads applied to the hub and the vibrations of the airframe can be efficiently controlled by the IBC system.

Figure 15.9 shows the variations versus time of the vertical vibrations near the copilot seat of the BO105, both without IBC input and with IBC inputs of limited authority. A spectral analysis revealed a significant decrease in the measured 4Ω vibrations thanks to an open loop IBC (IBC frequency of 4Ω, pitch amplitude of 0.4º).

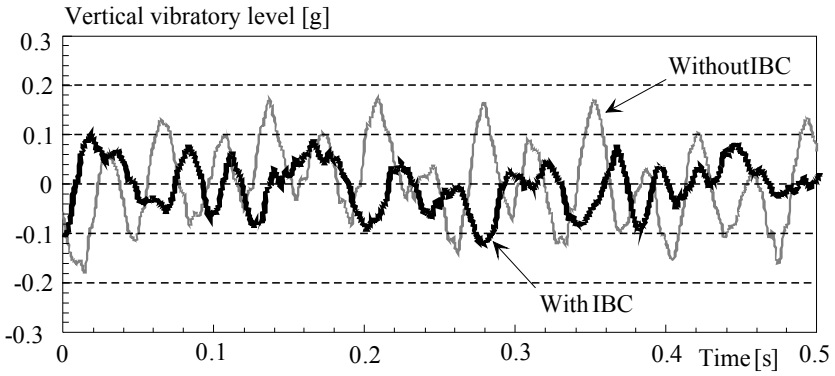

Figure 15.9. *Vertical vibrations near the copilot seat with and without IBC*

15.3.3. *Individual control by servo-flaps*

15.3.3.1. *Principle of the rotor with blade flaps operated by piezoelectric actuators*

The principle of this rotor is to actively control the blade lift using trailing edge flaps (see Figure 15.10). The main objective is to induce an appropriate hub response load which opposes the blade loads at the rotor harmonic frequencies. This system must also be able to decrease the BVI noise level [ROT 01].

Figure 15.10. *Trailing edge flaps with piezoelectric actuators on the blade. Photo: Eurocopter Deutschland*

The control input frequency varies from 0 to 6Ω depending on the desired application and the number of blades. The amplitude of this control is sufficient for most of the desired applications. In case of power loss, the behavior and stiffness of the actuator must be guaranteed. The flaps are operated by piezoelectric actuators with mechanical force amplification.

15.3.3.2. *Technological solutions*

15.3.3.2.1. Position and size of the flaps

The way in which the trailing edge flaps decrease the noise and the vibrations depends on the reaction of the blade, i.e. on the flap chord, the control frequency and the blade torsional stiffness. Hence, for a large flap chord and high blade torsional stiffness, we obtain a direct lift effect through flap deflection. On the other hand, a small flap chord and low blade torsional stiffness induce a flap servo effect equivalent to a blade twisting moment (see Chapter 4). At low control frequencies, the two effects are in opposition. At frequencies higher than the first twist natural frequency, the two effects are in-phase.

We show that extending the flap chord over 15% of the blade chord does not significantly improve the blade reaction, and requires more electric power for the actuator.

Another important factor is the radial position of the flap. According to a study, for an optimum decrease of the BVI noise, the flap must be positioned as close as possible to the tip of the blade. Because of its tapered shape, however, the flap cannot be positioned at the blade tip but at a maximum radius of 4.9 m (0.89 R).

In addition, the radial position of the flap influences the response. When the center of the flap is positioned at 4.6 m (0.83 R), the response is minimal, as shown

in Figure 15.11. The lift effect and the servo effect on the hub moments at 4Ω (for 3Ω flap activation, 5º amplitude) are presented separately (see Chapter 4). For the blade parameters chosen at the radial position of 4.6 m, the two effects have the same amplitude, but are of opposite signs.

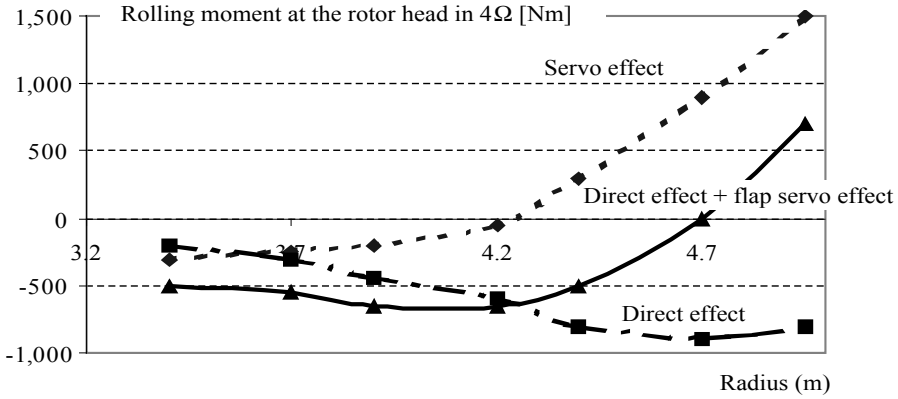

Figure 15.11. *Effects of the radial position of the flap*

The results for other dynamic rotor loads (not presented) are similar. As such, the 4 m position (0.73 R), where the two effects have the same sign, is preferred for vibration control.

15.3.3.2.2. Actuators

The rotor active control requires high-performance and robust actuators. The flap actuator must be able to handle high mechanical loads and it must be small for integration on the blade. It must also offer good efficiency and control. A piezoelectric actuator made of ceramics with mechanical force amplification was chosen (see Figure 15.12), because it can withstand the centrifugal loads and has sufficient stiffness in the event of electrical power loss.

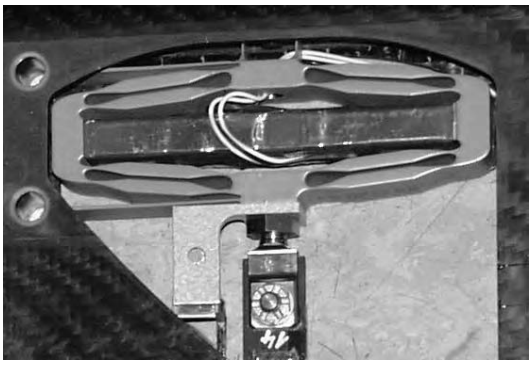

Figure 15.12. *Piezoelectric actuator made of ceramics. Photo: Eurocopter Deutschland*

A ceramic piezoelectric material converts the electric energy directly into mechanical movement, within the dynamic limits of the system used.

15.3.3.2.3. Implementation

The full flap system consists of three identical units, each 0.3 m long. Each unit has a pair of actuators, which are installed near each other on the blade trailing edge between the radial positions of 3.8 m and 4.7 m. Each flap unit consists of a carbon fiber box structure inserted through the trailing edge between the top and bottom layers of the blade.

For each flap unit, a pair of actuators, positioned as close as possible to the blade leading edge, acts via rods to transmit the load to the flap.

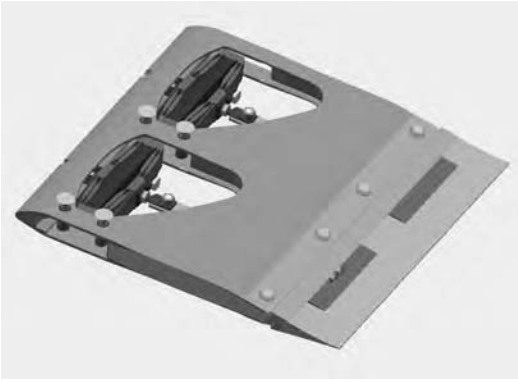

Figure 15.13. *Flap unit*

The ceramic actuators used in the blades generate a 100 μm displacement. A 10-factor amplification system in the direction of the blade chord is therefore required to move the flap to its required position.

The current studies on intelligent materials could be used to modify the blade twists, e.g. use of shape memory materials.

Bibliography

[ACH 86a] ACHACHE M., POLYCHRONIADIS M., "Development of an Experimental System for Active Control of Vibrations on Helicopters", *12th European Rotor Aircraft Forum*, Germany, September 1986.

[ACH 86b] ACHACHE M., POLYCHRONIADIS M., "Higher Harmonic Control Flight Test of an Experimental System on the SA 349 Research Gazelle", *American Helicopter Society Forum*, Washington, 1986.

[AGA 86] AGATI P., BREMONT Y., DELVILLE G., *Mécanique du solide*, Dunod, Paris, 1986.

[ALL 89] ALLONGUE M., KRYSINSKI T., "Validation of new general aerospatial aeroelastic rotor model through the wind tunnel and flight test data", *46th AHS annual forum*, Washington, USA, 1989.

[BEB 02] BEBESEL M., ROTH D., "Reduction of BVI Noise on Ground – In-flight Evaluation of Closed-Loop Controller", *28th European rotorcraft forum*, Bristol, UK, 17-20 September 2002.

[BIE 92] BIELAWA R., *Rotorcraft – Structural dynamics and aeroelastic*ity, IAA Education series, Washington D.C., 1992.

[BIG 95] BIGRET R., FERON J.-L., *Diagnostic*, *maintenance disponibilité des machines tournantes*, Masson, 1995.

[BLE 77] BLEVINS R.D., *Flow-induced vibrations*, Van Nostrand Reinhold company, New York, 1977.

[BRA 80] BRAUN D., "Development of Antiresonance Force Isolators for Helicopter Vibration Reduction", *6th European Rotorcraft and Powered Lift Aircraft Forum*, Bristol, UK, September 1980.

[BRA 82a] BRAUN D., "Development of Antiresonance Force Isolators for Helicopter Vibration Reduction", *AHS*, vol. 27, no. 4, p. 37-44, October 1982.

[BRA 82b] BRAUN D., "Ground and flight tests of a passive rotor isolation system for helicopter vibration reduction", *Eighth European Rotorcraft Forum*, Aix-en-Provence, 31 August-3 September 1982.

[BRU 84] BRUN R., *Science et technique du moteur diesel industriel et de transport*, Vol. 1 and 2, Technip Editions, 1984.

[BRU 02a] BRUN-PICARD D., MALBURET F., CARMONA J.C., "Perspectives du contrôle actif des déformations et des vibrations en usinage à grande vitesse", *ICMAS 2002 – International Conference on Manufacturing Systems*, Bucharest, Romania, 10-11 October 2002.

[BRU 02b] BRUN-PICARD D., MALBURET F., "Contrôle actif des vibrations, ce qui marche et ce qui ne marche pas", *Deuxièmes assises "Machines et Usinage à Grande Vitesse"*, Lille, France, 2002.

[CAR 00] CARMONA J.C., MAZZONI D., SCHUSTER P., "A new feedback approach in active noise control robust pole placement control", *Active Control in Mechanical Engineering*, AA Balkema Rotterdam Brookfield, L. Jezequel (ed.), p. 73-84, 2000.

[CAV 00] CARDIN V., "Practical examples of new technologies in dynamics as applied to Eurocopter products", American Helicopter Society, *56th Annual Forum*, Virginia Beach, 2000.

[COY 96] COYLE S., *The art and science of flying helicopters*, Iowa State University Press/Ames, 1996.

[DES 76] DESJARDINS R.A., HOOPER W.E., "Rotor Isolation of the Hingeless Rotor BO105 and YUH-61 Helicopters", *2nd European Rotorcraft and Powered Lift Aircraft Forum*, Buckeburg, FRG, September 1976.

[DES 78] DESJARDINS R.A., HOOPER W.E., "Antiresonance Rotor Isolation for Vibration Reduction", *American Helicopter Society 34th Annual Forum*, Washington DC, May 1978.

[EDF 70] EDF, Vibrations et équilibrage des systèmes tournants, technical bulletin, no. 79, 1970.

[FEN 68] FENG C.C., The measurement of vortex-induced effects in flow stationary and oscillating circulator and D-section cylinder, M.A. Sc. Thesis, University of British Columbia, 1968.

[FER 01] FERRER R., AUBOURG P.A., KRYSINSKI T., BELLIZZI S., "New methods for rotor tracking and balance tuning and defect detection applied to Eurocopter products", *American Helicopter Society 57th Annual Forum*, Washington, 2001.

[FLA 66] FLANNELLY W.G., "The Dynamic Anti-Resonant Vibration Isolator", *American Helicopter Society 22nd Annual Forum*, Washington DC, May 1966.

[FUL 97] FULTON M.V., ORMISTON R.A., "Hover Testing of a Small-Scale Rotor with On-Blade Elevons", *Proceedings of the 53rd Annual Forum of the American Helicopter Society*, Virginia Beach, Virginia, 29 April-1 May 1997.

[GAL 00] GALLAGHER F., "Flight testing Kaman Aerospace Corporation's composite main rotor blade", *Presented at the American Helicopter Society 56th Annual Forum*, Virginia Beach, Virginia, 2-4 May 2000.

[GES 99] GESSOW A., MYERS C.G. Jr, *Aerodynamics of the helicopter*, College Park Press, 1999.

[GOH 95] GOHRING E., VON GLASNER E.C., POVEL R., SCHUTZNER P., "Intelligent suspension systems for commercial vehicles", *Active control in mechanical engineering*, *international symposium MV2*, p. 13-25, Hermès, 1995.

[GOO 00] GOODMANN ROBERT K., THOMAS DR., MILLOTT A., "Design, Development, and flight testing of the active vibration control system for the SIKORSKY S-92", *AHS Forum Virginia Beach*, Virginia, 2-4 May 2000.

[HAL 80] HALMES D.R., "Live Liquid Inertia Vibration Eliminator", *36th American Helicopter Society Annual Forum*, Washington, 1980.

[HAL 81] HALMES D.R, "Total Main Rotor Isolation System", *AHS Northheast Region National Specialist Meeting on Helicopter Vibration*, Hartford, Connecticut, November 1981.

[HEG 83] HEGE P., GENOUX G., "The Sarib vibration absorber", *9th European rotorcraft and powered lift aircraft forum*, September 1983.

[KER 68] KER WILSON W., *Devices for controling vibrations*, Chapman & Hall, 1968.

[KUB 92] KUBE R., ACHACHE M., NIESL G., SPLETTSTÖßER W.R., "A Closed Loop Controller for BVI Impulsive Noise Reduction by Higher Harmonic Control", *48th Annual Forum of the American Helicopter Society*, Washington DC, June 1992.

[KRY 98] KRYSINSKI T., FERULLO D., ROURE A., "Helicopter vibration control methodology and flight test validation of a self-adaptive anti-vibration system", *24th European Rotorcraft Forum*, Marseille, 15-17 September 1998.

[KUB 93] KUBE R., "Simultaneous Vibration and BVI Noise Feedback for Closed Loop Higher Harmonic Control", *European Rotorcraft Forum*, Italy, September 1993.

[LAC 79] LACZKOWSKI R., *Wywazanie elementow wirujacych*, WNT, Warsaw, 1979.

[LAN 86] LALANNE M., BERTHIER P., DER HAGOPIAN J., *Mécanique des vibrations linéaires*, Masson, 1986.

[LAN 93] LANDAU I.D., CYROT C., REY D., "Robust control design using combined pole placement – sensitivity function shaping method", *European Control Conference*, Groningen, Holland, 1993.

[LAN 97] LALANNE M., FERRARIS G., *Rotordynamics Prediction in Engineering*, Wiley & sons, 1997.

[LEG 68] LEGRAND F., *Rotorcraft National Aeronautics and Space*, Administration Washington DC NASA TT F-11, 530, April 1968.

[LIB 98] LIBERATOIRE E.K., *Helicopters before helicopters*, Kriegier Publishing Company Malabar, Florida, 1998.

[LIE 66] LIENHARD J.H., "Synopsis of lift, drag and vortex frequency data for Rigid circular cylinders", Washington State University, College of Engineering, *Research Division Bulletin 300*, 1966.

[NIE 94] NIESL G., SWANSON S.M., JACKLIN S.A., BLAAS A., KUBE R., "Effect of Individual Blade Control on Noise Radiation", *AGARD Aeroacoustics Conference*, Berlin, October 1994

[ORM 01] ORMISTON R.A., "Aeroelastic considerations for rotorcraft primary control with on blade elevons", *American Helicopter Society 57th Annual National Forum*, Washington, DC, 9-11 May 2001.

[ORM 91] ORMISTON R.A., "Can Smart Materials Make Helicopters Better", presented at the *4th Workshop on Dynamics and Aeroelastic Stability Modeling of Rotorcraft Systems*, College Park, Maryland, November 19-21, 1991.

[ORM 98] ORMISTON R.A, FULTON M.V., "Aeroelastic and Dynamic Rotor Response with On-Blade Elevon Control", *24th European Rotorcraft Forum*, Marseilles, September 1998.

[OUZ 62] OUZIAUX R., *Mécanique appliquée*, Dunod, 1962.

[PAR 88] PARSZEWSKI Z., *Drgania i dynamika maszyn*, WNT, Warsaw, 1988.

[POL 90] POLYCHRONIADIS M., "Generalized Higher Harmonic Control Ten Years of Aerospatial Experience", *16th ERF*, Glasgow, September 1990.

[POW 78] POWER E.R., HAMMOND R.W., "On Method for Application of Harmonic Control", *4th ERF*, Stresa, September 1978.

[PRE 92] PRESS W.H., TEUKOLSKI A., VETTERLING W.T., FLANNERY B.P., *Numerical Recipes*, Cambridge University Press, 2nd ed., 1992.

[RAH 88] RAHNEJAT H., *Multi-Body Dynamics Vehicles*, *Machines and Mechanisms*, Professional Engineering Publishing Limited, London and Bury St Edmunds, UK, 1988.

[RAH 98] RAHNEJAT H., *Multi-body dynamics vehicles*, *machines and mechanisms*, Professional Engineering Publishing Ltd, London and Bury St-Edmunds, UK, 1998.

[RIC 92] RICHARD L., "Bielawa Rotary Wing Structural Dynamics and Aeroelasticity", *AIAA Education Series*, 1992.

[RIT 76] RITA A.D., MCGARVEY J.H., JONES R., "Helicopter Rotor Isolation Evaluation utilizing the Dynamic Antiresonant Vibration Isolator", *American Helicopter Society 32nd Annual Forum*, Washington DC, May 1976.

[ROE 93] ROESCH P., ALLONGUE M., ACHACHE M., "Towards Generalized Active Control of Helicopters", *European Rotorcraft Forum* , Italy, September 1993.

[ROT 01] ROTH D., DIETERICH O., BEBESEL M., PONGRATZ R., "Individual Blade Root Control Demonstration – Recent Activities", *27th European Rotorcraft Forum*, Moscow Russia, 11-14 September 2001.

[SCH 97] SCHIMKE D., JÄNKER P., BLAAS A., KUBE R., SCHEWE G., KEßLER C., "Individual Blade Control by Servo-Flap and Blade Root Control – A Collaborative

Research and Development Programme", *23rd European Rotorcraft Forum*, Dresden, Germany, September 1997.

[SCHI 98] SCHIMKE D., ARNOLD U.T.P., KUBE R., "Individual Blade Root Control Demonstration – Evaluation of Recent Flight Tests", *54th Annual Forum of the American Helicopter Society*, Washington DC, 20-22 May, 1998.

[SCHO 98] SCHÖLL E., GEMBLER W., BEBESEL M., SPLETTSTÖßER W.R., KUBE R., PONGRATZ R., "Noise Reduction by Blade Root Actuation – Analysis of Flight and Wind Tunnel Tests", *24th European Rotorcraft Forum*, Marseille, 15-17 September 1998.

[SEI 92] SEITZ G., KRYSINSKI T., "Overview of TIGER Dynamics", *American Helicopter Society 48th Annual Forum*, Washington DC, June 1992.

[SIM 96] SIMIU E., SCANLAN R.H., *Wind Effects on Structures: an Introduction to Wind Engineering*, a Winley-Interscience Publication, John Wiley & Sons, 1996.

[SMI 99] SMITH MICHAEL R., REDINGER W. SCOTT, "The Model 427 Pylon isolation system", *55th AHS Annual Forum*, Montreal, Quebec, Canada, 25-27 May 1999.

[SPE 91] SPLETTSTÖßER W.R., SCHULTZ K.-J., KUBE R., BROOKS T.F., BOOTH E.R., NIESL G., STREBY O., "BVI Impulsive Noise Reduction by Higher Harmonic Pitch Control: Results of a Scaled Model Rotor Experiment in the DNW", *17th European Rotorcraft Forum*, September 1991.

[STA 89] STAPLE A.E., "An Evaluation of Active Control of Structural as a Means of Reducing Helicopter Vibrations", *15th European Rotorcraft Forum*, September 1989.

[STA 90] STAPLE A.E, WELLS D.M., "Development and Testing of an Active Control of Structural Response System for the EH 101 Helicopter", *16th European Rotorcraft Forum*, September 1990.

[SWA 94] SWANSON S.M., JACKLIN S.A., BLAAS A., KUBE R., NIESL G., "Individual Blade Control Effects on Blade-Vortex Interaction Noise", *50th Annual Forum of the American Helicopter Society*, Washington DC, May 1994.

[SWA 95] SWANSON S.M., JACKLIN S.A., BLAAS A., NIESL G., KUBE R., "Acoustic Results From a Full-Scale Wind Tunnel Test Evaluating Individual Blade Control", *51st Annual Forum of the American Helicopter Society*, Fort Worth, TX, May 1995.

[SWO 84] SWOBODA B., *Mécanique des moteurs alternatifs*, Technip, 1984.

[TAY 88] TAYLOR R.B., "Helicopter vibration reduction by rotor blade modal shaping", United Technologies Research Center, *38th annual forum of the AHS*, Anaheim, CA, May 1988.

[TEC 83] PAUTHENET R., *Théorie du magnétisme*, Techniques de l'ingénieur, traité génie électrique, D 175, 1983.

[TEC 84] HABERMANN H., *Paliers Magnétiques*, Techniques de l'ingénieur, traité génie mécanique, B 5 345, 1984.

[TEC 96] GUIMBRETIERE P., *Joints homocinétique*, Techniques de l'ingénieur, traité génie mécanique, B 5 815, 1996.

[TEC 97] GUIMBRETIERE P., *Joints de Cardan*, Techniques de l'ingénieur, traité génie mécanique, B 5 810, 1997.

[TEC 00] BLANC H., *Dynamique des rotors: Analyse des régimes de fonctionnement*, Technique de l'ingénieur, Traité génie mécanique, BM 5 123, 2000.

[TEV 95] TEVES D., NIESL G., BLAAS A., JACKLIN S., "The Role of Active Control in Future Rotorcraft", *21st European Rotorcraft Forum*, St. Petersburg, Russia, 30 August-1 September, 1995.

[TOU 92] TOUZET C., *Artificial Neural Networks: Introduction to Connectionism*, EC2, Paris, 1992.

Index